Competitive and Sustainable Growth (GROWTH) Programme

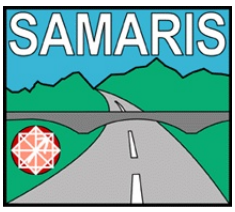

SAMARIS

Sustainable and Advanced MAterials for Road InfraStructure

WP 14: HPFRCC (High Performance Fibre Reinforced Cementitious Composites) for rehabilitation

Deliverable D18 – Part A

Report on tests of UHPFRC in the laboratory - Part A

	Name and signature	Date
Drafted:	Katrin Habel **K. Habel** **E. Denarié**	**15.11.2004**
Reviewed:	**Aleš Žnidaric, Richard Woodward, Pierre Rossi**	**21.01.2005**
Verified:		
Validated:	**n.a.**	
	Approved by SAMARIS Management Group:	**01.02.2005**

Table of contents

List of figures

List of tables

Part I
Foreword and acknowledgements

1 Foreword and acknowledgements

This report is the second of a series covering all aspects necessary to the implementation of UHPFRC (Ultra High Performance Fibre Reinforced Concretes) for the rehabilitation of reinforced concrete structures, within the framework of work package (WP) 14 "HPFRCC for rehabilitation" of project SAMARIS. The other reports are:

- D13 - Report on preliminary studies for the use of HPFRCC for the rehabilitation of road infrastructure components
- D22 - Report on tests of UHPFRC in the field
- D26 - Modelling of UHPFRC in composite structures
- D25 - Specifications for the use of corrosion inhibitors and UHPFRC for rehabilitation of highway structures
- D31 - Guidelines on selection of innovative materials for the rehabilitation of highway structures.

Contributors to WP 14 are: MCS-EPFL (contractor and WP leader), LCPC - Dr. P. Rossi (contractor), and TRL - Dr. R. Woodward (contractor).

The original concept of application of UHPFRC for the rehabilitation of reinforced concrete structures was proposed at MCS, by Prof. Dr. E. Brühwiler, in 1999.

The works at MCS-EPFL are performed under the lead of Dr. E. Denarié (WP 14 leader) and Prof. Dr. E. Brühwiler (Director of MCS-EPFL).

Dr. Pierre Rossi of LCPC-France, inventor of CEMTECmultiscale® and worldwide known expert of Fibre Reinforced Concretes, proposed the original UHPFRC recipes used in this study and the concepts for their tailoring to the specific applications of rehabilitation.

→ *This report is the first part of Deliverable D18. It covers a first extensive series of tests on UHPFRC (material CM0[1]) and concrete materials as well as UHPFRC-Concrete composite structural members, mainly focused on composite beams. All results mentioned in this report are from Dr. Katrin Habel.*

→ The *second part of deliverable D18 (part B), due in September 2005 will cover following aspects:*

- *permeability tests on undamaged and damaged UHPFRC materials (material CM0[1]).*
- *second extensive series of structural tests on UHPFRC-concrete composite beams, walls and slabs (materials CM1 and CM2[1]).*
- *delayed behaviour at early age, from TSTM (Temperature-Stress Testing Machine) test set-up (material CM2[1]).*

Lausanne, 15 November 2004 Dr. Emmanuel Denarié

1. See Appendix U and deliverable D13 for definitions of materials.

Part II
Introduction

2 Motivation and context

This test report describes the experimental program that was conducted within the scope of the research project on “Structural behaviour of elements combining Ultra-High Performance Fibre Reinforced Concretes (UHPFRC) and reinforced concrete” [Habel04]. The objectives of the research were to *investigate performance and structural behaviour of composite “UHPFRC-concrete” members* and to *provide a better knowledge of UHPFRC properties.*

UHPFRC have a high potential of application in structures. They belong to the group of High Performance Fibre Reinforced Cement Composites (HPFRCC) (Figure 2.1). HPFRCC are Fibre Reinforced Concretes (FRC) that exhibit strain-hardening under uniaxial tension. In addition, UHPFRC are characterized by a dense matrix and have consequently a very low permeability when compared to HPFRCC and normal strength concretes. However, their properties are still poorly known.

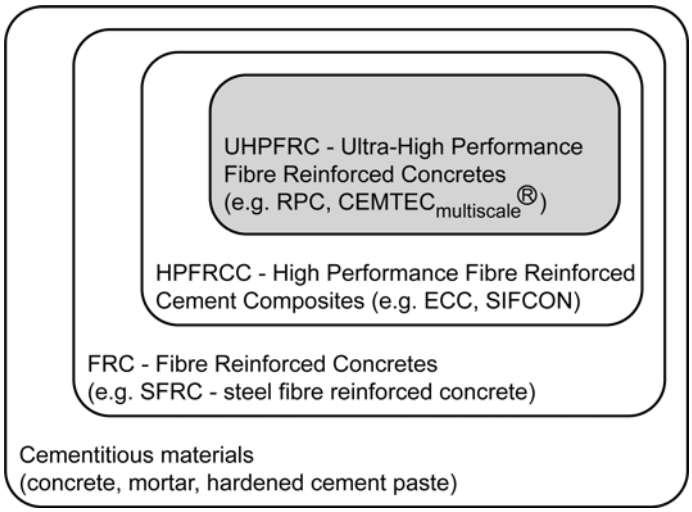

FIGURE 2.1: Definition of UHPFRC

The conceptual idea of this research project was to combine UHPFRC and normal strength concrete in order to enhance existing and new structures made of cementitious materials. *Composite “UHPFRC-concrete” elements* are appropriate for new constructions and conservation of existing structures. UHPFRC should be used in parts of the structures that are exposed to detrimental substances or that have to transfer high mechanical loads, for example at points of concentrated load introduction or when an existing structure has to be strengthened without increasing its dead load. Their field of application is illustrated by the example of a road bridge deck (Figure 2.2): crash barrier and deck overlay are made of UHPFRC (without water proofing membrane), while the rest is built of normal strength reinforced concrete. Crash barrier and deck overlay are exposed to detrimental substances (e.g. de-icing salts containing chlorides) and require a high resistance against the ingress of these substances in order to guarantee sufficient durability. Moreover, the crash barrier is a massive element with a high cracking risk at early age. The dimensions of the crash barrier and early age cracking risk are reduced due to the outstanding mechanical properties of UHPFRC in terms of resistance and energy dissipation. Composite “UHPFRC-concrete” elements are a new kind of structures and their performance and structural behaviour have to be studied experimentally.

3 Objectives

The main objectives of the experimental campaign are to *investigate the structural behaviour of composite elements made of UHPFRC and concrete* and to *characterize the material properties of the cementitious materials, in particular of the UHPFRC.*

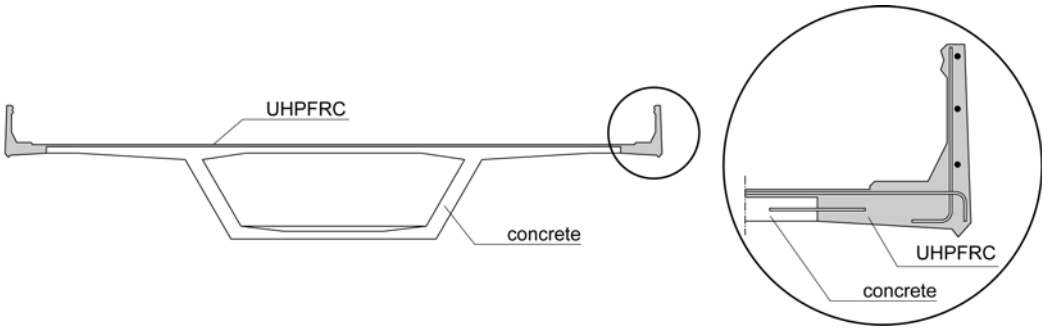

FIGURE 2.2: Composite "UHPFRC-concrete" bridge deck

As UHPFRC are a relatively new group of cementitious materials, many of their material properties are still little known. Furthermore, UHPFRC are materials with specifically tailored properties that differ from each type of material. Thus, it is essential to *investigate the properties of the UHPFRC* (a type of CEMTEC$_{multiscale}$® [Rossi02]) used in this research. The material tests should also give information about the relation between thermal and hygral changes and deformation: Attention is drawn to the *early age behaviour* of the UHPFRC when the major part of deformations occurs.

The *feasibility* of composite elements made of UHPFRC and concrete during their whole life cycle is aimed to be investigated. As the material properties of UHPFRC and concrete are different, a *good structural behaviour* has to be proven. Furthermore, it is important to investigate whether the advantageous properties of the UHPFRC can be exploited in composite structural elements during the whole range of possible action effects during the service life of the structure - at early age, long term and at fracture. Early age behaviour is extremely important, since the major part of damage due to internally provoked deformations occurs during this period and the risk of damage is high. Another objective is to better *understand the physical mechanisms* of the deformations. Deformations and cracking at long term as well as flexural creep are aimed to be studied on the beams. Finally, the *fracture behaviour* is investigated with bending tests with regard to cracking, deformations and force evolution.

The composite elements are chosen to cover a wide range of possible applications: thin UHPFRC layers for protection function and thicker UHPFRC layers with and without reinforcement for additionally increased resistance.

4 Test program

4.1 Material tests

Material tests were carried out to characterize the UHPFRC and the concrete properties. As UHPFRC are rather new materials, their properties were not well known. So, the material tests allowed to discover and to describe its material properties. Also tests on the concrete were conducted.

The following tests were carried out and are described in Part III of this report:

- The *characterization of the fresh UHPFRC* included the determination of the air content and the density, the fibre content and the workability. Furthermore, the ambient temperature and the temperature of the fresh concrete were measured (Section 6).
- The *heat of hydration* was evaluated with tests in semi-adiabatic moulds. The adiabatic temperature rise due to the heat of hydration was deduced from the tests (Section 7).
- Measurements of the *relative humidity* (RH) were carried out on UHPFRC specimens in order to estimate its self-desiccation (Section 8).

- The evolution in time of strength and the modulus of concrete under *uniaxial compression* were determined on cylinders. The tests were executed by the LMC (Section 9).
- The behaviour in *tension* was determined with uniaxial tensile tests. The evolution in time of strength, pre-and post cracking behaviour and fracture energy were evaluated (Section 10).
- *Basic and drying shrinkage* in combination with *creep* tests (under compression) were carried out with regard to the time-dependent behaviour of the specimens. Cylinders were installed in a chamber with controlled climatic conditions. *Free and restraint autogenous shrinkage* tests were performed on the UHPFRC at early age at the university Laval, Québec, Canada (Sections 11 to 13).
- The *reproducibility* of the UHPFRC was tested for each batch. For this, prismatic specimens were tested in bending and in compression. The results were treated statistically (Section 14).
- The *adherence* of the interface zone was measured on cylinders drilled out of composite "UHPFRC-concrete" blocks. The contact surface of the concrete was prepared by hydro-jetting in the same way than the contact surface for the beam tests (Section 15).

4.2 Testing of structural elements

The behaviour of composite "UHPFRC-concrete" elements is described in Part IV. 15 full-size bending beams with a length of 5.40 m were investigated consisting of an old layer of reinforced concrete that was more than 5 months old during testing and a new layer made of UHPFRC. The contact zone of the concrete was prepared by hydrojetting.

The *deformational behaviour* of the beams was measured from the casting of the UHPFRC layer for 11 to 12 weeks (Section 18). So, the *early age behaviour* of the composite elements was observed and conclusions could be drawn of the *long term behaviour.* After the early age and long term tests, the beams were submitted to four-point-bending tests to investigate their *fracture behaviour* (Section 19).

The *parameters* of the tests were the thickness of the UHPFRC layer h_U, the presence of reinforcement in the UHPFRC layer $A_{s,U}$ and the static system. Three different thicknesses (h_U = 3, 5, 10 cm) for the UHPFRC layer were investigated. Additional reinforcement $A_{s,U}$ was placed in the UHPFRC layer of half of the beams with thicknesses of the UHPFRC layer of 5 and 10 cm. The reinforcement ratio of the additional reinforcement was $\rho_{s,U}$ = 2% of the UHPFRC section. A statically determinate and a statically indeterminate system were investigated. The statically determinate system consisted of beams with cantilevers on each side and the statically indeterminate system of three span beams. Half of the statically determinate beams were subjected to flexural creep after 28 days. The creep loading induced a constant moment in the central span of the beams and tensile stresses in the UHPFRC layer.

During the early age and long term tests, the temperature of the beams was *measured* with thermocouples. Two of the beams were also equipped with humidity sensors. The deformations were followed with LVDTs and two optical deformation sensors that were placed in the central span of the beams. Furthermore, the cracking of the beams was followed visually. During the fracture tests, the deformations were measured with LVDTs and the optical deformation sensors. The crack openings were followed visually and with Ω-gages that were placed on the upper side and on the sides of the beams.

Part III
Material characterization

5 Material composition

5.1 Concrete

The concrete was a B45/35, mixed by the plant “Sables et Graviers Tinterin SA” in Tentlingen. Its composition and the details of the cement are given in Tables 5.1 and Table 5.2. The aggregates were mainly “hard” and “medium hard” [Hammerschlag01].

TABLE 5.1: Concrete composition

	type	**theoretical weight**	**weight [kg/m^3]**
Cement	CEM I 42.5, Vigier	350 kg/m^3	346.7
Aggregates	0/4		968.2
	4/8		96.9
	8/16		945.3
Plasticizer	SIKA Viscocrete 2	0.5 M-%	1.73
Water			137.1
w/c			0.40

TABLE 5.2: CEM I 42.5, Vigier, properties (mean values 2001)

Mineralogical composition	
C_3S	59.9% ± 5.2%
C_2S	17.1% ± 3.9%
C_3A	7.1% ± 0.9%
C_4AF	9.6% ± 0.8%
Specific Surface (fineness of Blaine)	2731 ± 181 cm^2/g
Heat of Hydration	
1 day	263 J/g
3 days	333 J/g
5 days	340 J/g
7 days	345 J/g
Time of the beginning of setting (at 20 °C)	186 ± 24.6 min.
Compressive Strength	
at 2 days	23.2 ± 2.2 MPa
at 28 days	51.7 ± 3.4 MPa

5.2 UHPFRC

The used UHPFRC was a kind of CEMTEC$_{multiscale}$® with one kind of steel fibres, developed at the LCPC [Rossi02]. CEMTEC$_{multiscale}$® is an ultra-high performance concrete consisting of cement, silica fume, fine sand, superplasticizer and water (Tables 5.3 and Table 5.4).

The cement is a CEM I 52.5 N with a high quantity of silicates, produced by Lafarge. The sand is very fine with an average grain size of 0.3 mm, and a maximum grain size of 0.5 mm. It also contains a high amount of silicates. The silica fume is very pure with 93.5% of SiO_2 from the zirconium producing industry. The steel fibres are short (l_f = 10 mm) with an aspect ratio l_f/d = 50. Their tensile strength is high so that the fibres are pulled out of the cementitious matrix and do not break.

TABLE 5.3: UHPFRC composition

	type	**weight**
Cement	CEM I 52.5 N CE PM-ES-CP2 NF, Lafarge, Le Teil	1051.1 kg/m^3
Sand	Sand of Fontainebleau, MN 30 (∅ < 0.5 mm)	732.5 kg/m^3
Silica Fume	SEPR (median diameter: 50 µm, specific surface: 12 m^2/g, SiO_2: 93.5%)	273.3 kg/m^3
Steel fibres	straight, l = 10 mm, ∅ = 0.2 mm	468.0 kg/m^3
Superplasticizer	Chrysofluid OPTIMA 175	total: 35.1 kg/m^3
		wet: 24.6 kg/m^3
		dry: 10.5 kg/m^3
Additional water		164.6 kg/m^3
Total water		189.2 kg/m^3
w/c		0.18
w/(c+SF) = w/b		0.14

The UHPFRC had a very low water/binder-ratio (0.14) and a very dense matrix. The water was not sufficient for complete hydration of the cement. The theoretical degree of hydration of the UHP-FRC was approximately 31% [Jensen01, Waller00]. So, a part of the cement grains acted as inert filler. The low water content required the addition of a superplasticizer to ensure sufficient workability of the material. The used UHPFRC was designed to be self-compacting.

TABLE 5.4: CEM I 52.5 N CE PM-ES-CP2 NF, Lafarge (mean values, 12/02)

Mineralogical composition	
C_3S	73.4%
C_2S	10.0%
C_3A	4.0%
C_4AF	5.8%
Specific Surface (fineness of Blaine)	3400 cm^2/g
Heat of Hydration	
12 hours	185 J/g
Time of the beginning of setting (at 20 °C)	185 min.
Compressive Strength	
at 2 days	28.0 MPa
at 28 days	63.0 MPa

6 Characterization of the fresh material

6.1 General

The density and the air content of the fresh concrete were determined with a pressure-type air meter. The temperature of the concrete was measured with a thermocouple of type K. The ambient climatic conditions (T, RH) were recorded with a data logger of type HAENNI, Opus I. The workability of the concrete was determined with the slump test after [SIA162/1]. The workability of the self-compacting UHPFRC was determined with the inverted slump test by using a turned standard cone of the slump test [Neville95]. The cone was filled, lifted and the spread was measured.

6.2 Results

6.2.1 Concrete

The tests of the fresh concrete were carried out at Element AG under the same conditions as the structural elements that were exposed to at an ambient temperature of 5.5 °C (Table 6.1). The ambient conditions were characteristic for a day in february. However, the temperature was very low and the hydration of the concrete was delayed. All the specimens for the concrete characterization were stored at this low ambient temperature, only the beams for the structural tests were heated during the night to accelerate the hydration process.

The workability of the concrete was medium and not, as originally intended, high. As the concrete in the beams was compacted with a vibrating table, the concrete of the beams was well compacted and of good quality.

TABLE 6.1: Properties of the fresh concrete and the environment

	Type of test	**Result**
density	pressure-type air meter	2460 kg/m^3
slump test	ISO 4109	7 cm (medium workability)
temperature of the concrete	thermocouple, type K	10 °C
ambient temperature	HAENNI, Opus I	5,5 °C
ambient RH	HAENNI, Opus I	75%

6.2.2 UHPFRC

Tests on fresh UHPFRC were carried out on several mixes (Table 6.2). The density and the air content were determined with a pressure-type air meter having a volume of 8 litres (Figure 6.1a). The density was higher than for traditional concrete due to the high steel fibre content of the material.

TABLE 6.2: Properties of the fresh UHPFRC and the environment

	Type of test		**Result**
density	pressure-type air meter		2’749 kg/m^3 (A18)
			2’712 kg/m^3 (A53)
air content	pressure-type air meter		2.5% (A18)
			3.8% (A53)
workability	inverted slump test (20 min. after water addition)		70.5 cm (A18)
			73.0 cm (A27)
	(1 hour after water addition)		57.0 cm (A18)
temperature of the concrete	thermocouple, type K	Series 1 (A01_19)	28.5 °C ± 1.2
		Series 2 (A20_58)	24.4 °C ± 0.8
		Series 3 (A60_71)	22.4 °C ± 0.6
ambient temperature	thermocouple, type K	Series 1 (A01_19)	23.4 °C ± 0.7
		Series 2 (A20_58)	17.6 °C ± 1.3
		Series 3 (A60_71)	18.0 °C ± 0.9

The workability was tested with an inverted slump test (Figure 6.1b) or simply controlled visually. The material was directly taken from the mixture of two batches mixed in succession and put together for casting. The UHPFRC was always self-compacting. There was a loss of workability in the first hour after casting. Therefore, two batches were the maximum to be mixed in succession and

a) *b)*

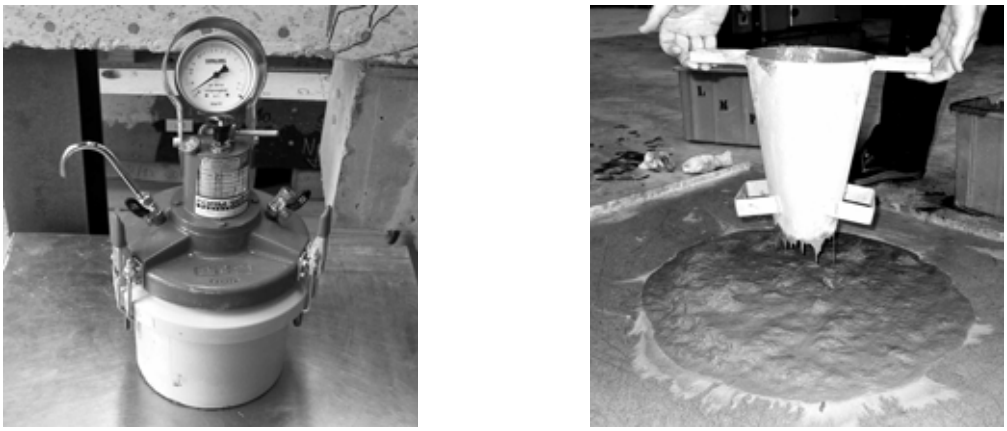

FIGURE 6.1: a) Air meter, b) inverted slump test of the UHPFRC

cast together. The casting was always rather fast (maximum duration: 15 min. for two batches), so, no loss of workability could be visually observed during casting.

The first series (A01_19) was cast in summer (july 02), whereas the two others (A20_58, A60_71) were cast in winter (november 02, february 03). The ambient temperature and the temperature of the fresh concrete were different for the different seasons. For A20_58 and A60_71, the same ambient temperature of the two mixes was observed, the temperature of the fresh concrete, however, was lower for series 3. This may be due to a lower reactivity of the constituents of the UHPFRC (cement, superplasticizer), since the mixing procedure and the mixer were the same.

7 Heat of hydration

7.1 General

The chemical reaction of cement hydration is exothermal, therefore, heat is liberated during the hardening of concrete. The resulting temperature changes lead to deformations in the material. The major part of the heat liberation occurs before setting when the material is still soft. Cooling occurs when the hydration rate slows down and tensile stresses build up in case of restraint. The more heat is liberated, the higher is the maximum temperature and the stresses in case of restraint.

The heat of hydration was measured with semi-adiabatic moulds (Figure 7.1) [Bernard00, Charif98]. The temperature evolutions of concrete cylinders placed in an insulated mould and of cylinders in a cardboard mould at ambient temperature were measured during approximately one week after casting. The ambient temperature was also measured. The heat of hydration was calculated on the basis of these measurements. The thermal losses of the moulds had been measured previously and a heat transfer coefficients had been determined to π_T = 083 W/(m^{2}K) for the insulated moulds and to π_T = 8 W/(m^{2}K) for the cylinders in the cardboard moulds.

Several models exist to describe the temperature rise in concrete: The Danish model is an empirical model, developed by the Danish cement industry EQ. 7.1 [Roelfstra89]. The Danish model describes well the evolution of the heat of hydration for traditional concretes. When the setting is too much retarded as this was the case for UHPFRC, the model does not apply.

FIGURE 7.1: Semi-adiabatic moulds (picture from [Bernard00])

$$H_{hydr}(M(t)) = H_T \cdot e^{-\left(\frac{a}{M(t)}\right)^b} \qquad \textit{(EQ 7.1)}$$

with M(t) [hours]: maturity of the concrete at time t, H_T [kJ/m^3]: total heat of hydration, H_{hydr} (M(t)) [kJ/m^3]: released heat at a given maturity, a, b [-]: parameters.

The adiabatic temperature rise may also be calculated directly with the method, proposed by RILEM TC119-TCE [RILEM97]. This method allows to determine the adiabatic temperature rise on the basis of semi-adiabatic tests. The adiabatic temperature of the cementitious material at the time t is given by EQ. 7.2. The integral of EQ. 7.2 is treated with a step-by-step method, with the area under the integral being calculated directly with the trapezoidal rule for each time step.

$$T_{ad}(t) = \left(1 + \frac{C_{cal}}{C_s}\right) \cdot \left(T_s(t) + \int_0^t a(t)dt\right) \qquad \textit{(EQ 7.2)}$$

$$\text{with} \quad a(t) = \frac{\pi_t(T_s - T_a)}{C_{cal} + C_s}$$

with t: time [h], T_{ad}(t): adiabatic temperature at time t [°C], C_{cal}: apparent heat capacity of calorimeter [J/K], C_s: heat capacity of the sample [J/K], T_s(t): temperature of the sample [°C], a(t): coefficient of temperature loss [K/h], π_T: coefficient of heat loss [J/(h K)], T_a: temperature at the boundary [°C]

7.2 Results

7.2.1 Concrete

The heat of hydration was measured with the semi-adiabatic moulds placed next to the beams, outside the hall at the Element AG. The outside temperature during testing was low (Figure 7.2). Two cardboard cylinders (l = 32 cm, ∅16 cm) were placed in the moulds and two cardboard cylinders next to the moulds. Figure 7.2a shows the temperature development in the moulds and Figure 7.2b the temperature development in the cardboard cylinders. The test served to fit the models for the heat of hydration (Table 7.3).

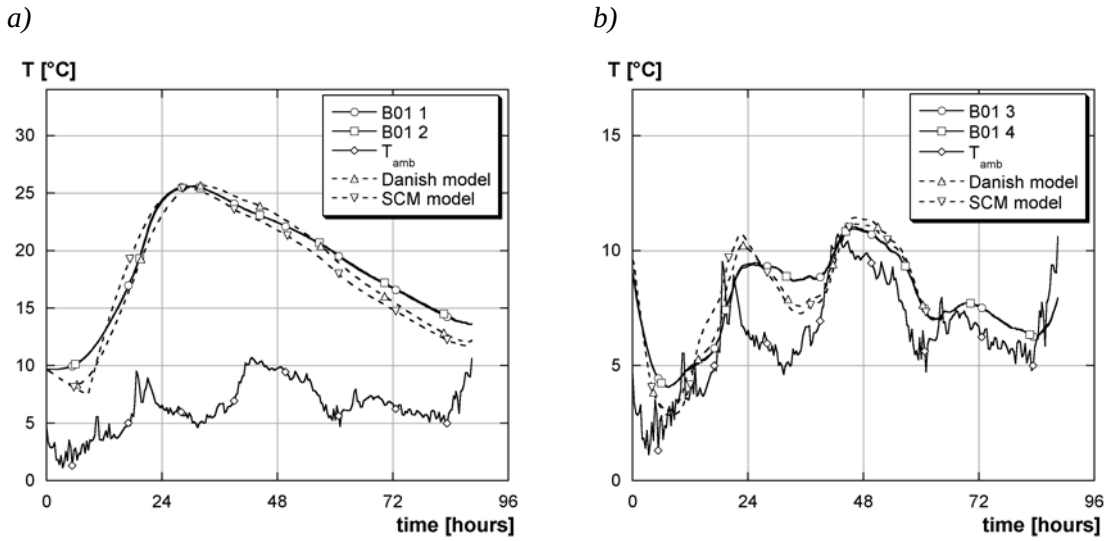

FIGURE 7.2: Temperature development and simulation of the concrete cylinders a) in the semi-adiabatic moulds and b) in the carton moulds

TABLE 7.3: Heat of Hydration models (B01)

c_T	[kJ/m^{3}K]	2'200	SCM			Danish model		
λ_T	[W/m K]	2.4	a	[h^{-1}]	0.06	a	[h]	16
H_T	[kJ/m^3]	120'000	d	[h]	5	b	[-]	1.09

As the cylinders were stored at low temperatures, the activation energy was probably different to the one developed in the beams, which were heated during setting. Since the first test structural test series started at an age of 5 months of the concrete substrate, the adjusted models shown in Figure 7.2 and Table 7.3 were considered to be sufficiently exact to describe the properties of the concrete substrate before and during the structural testing.

7.2.2 UHPFRC

The heat of hydration was measured for batch A68 with the semi-adiabatic moulds (Figure 7.3a). The maximum temperature in the semi-adiabatic moulds was 75 °C at 37 hours after casting; the maximum temperature in the cylinders was 33 °C after 36.5 hours. The temperature rise of the UHPFRC was higher than for the concrete, since the cement content of the UHPFRC was higher and the cement was a CEM I 52.5 N (higher fineness of Blaine). The dormant period of the UHPFRC was approximately 24 hours. This is typical for cementitious materials with high amounts of superplasticizer.

Since the heat of hydration of the UHPFRC can not be accurately modelled with the Danish model because of the long dormant period, the adiabatic temperature rise was calculated with the method proposed by RILEM TC119-TCE (Figure 7.3b). The adiabatic temperature of the UHPFRC was determined to be 117 °C after 7 days (168 h).

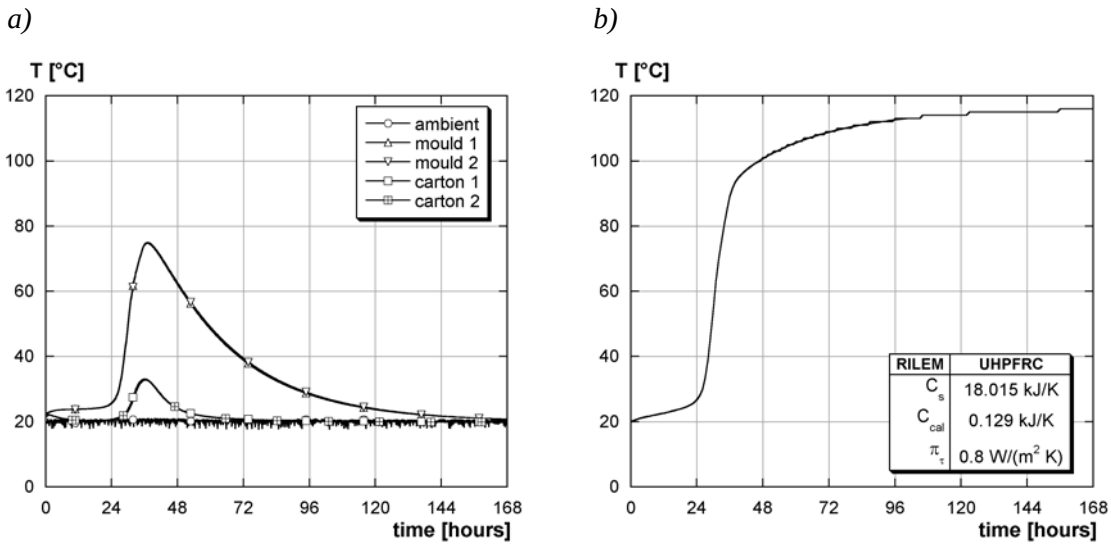

FIGURE 7.3: a) Temperature evolution of the UHPFRC during testing), b) adiabatic temperature rise (A68)

The thermal capacity and the thermal conductivity were also estimated from the semi-adiabatic tests by numerical simulation with MLS. The thermal capacity was c_T = 2800 kJ/(m^3 K), the thermal conductivity λ_T = 3.0 W/(m K).

8 Relative humidity evolution in the UHPFRC

8.1 General

The moisture content in cementitious materials is influenced by the hydration reaction, for which water is necessary to create the hydration products and by moisture exchange with its environment. The reduction of the moisture content due to hydration leads to a reduction of the RH in the specimen when the water available for hydration is not sufficient for complete cement hydration. This is the case for cementitious materials for low water/binder-ratios as UHPFRC. As the hydration is strong during early age, the major part of RH change occurs during the first 10 days. This internal RH-change induces shrinkage deformations that can be high (see Section 12).

8.2 Test set-up

The internal RH-change of the UHPFRC was measured with ROTRONIC sensors recording temperature and RH. The sensor was placed in a cylindrical UHPFRC specimen with the thickness of the UHPFRC around the sensors being 1 cm (Figure 8.1a). The thickness was small in order to minimize the temperature increase of the UHPFRC during hydration. The sensor was put into the specimen immediately after casting. The metal mould was additionally sealed with plastic foils to minimize the moisture exchange between the specimen and its environment. RH and temperature were recorded with data loggers.

8.3 Results

The RH was constant at 100% until 1.36 days (33 hours) (Figure 8.2). Then, it decreased to 90% after 5 days. The further decrease of the RH was lower, but it continued monotonously. The maximum temperature due to heat of hydration was 20.6 °C at 1.46 days (35 hours). The temperature rise was 0.8°C. The effect of the heat of hydration on the temperature was observed until 2.5 days when the temperature had decreased to the ambient temperature.

The period when the RH was 100% may be divided into two parts: The first part was the dormant period when no major chemical reactions occurred in the UHPFRC; in the second part, the hydration

a) *b)*

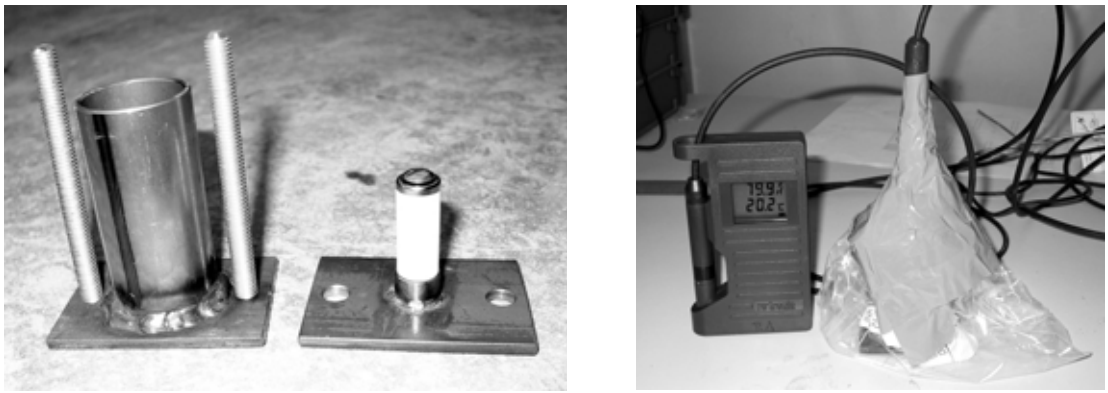

FIGURE 8.1: Test set-up of the RH measurements: a) mould, b) measuring system

a) *b)*

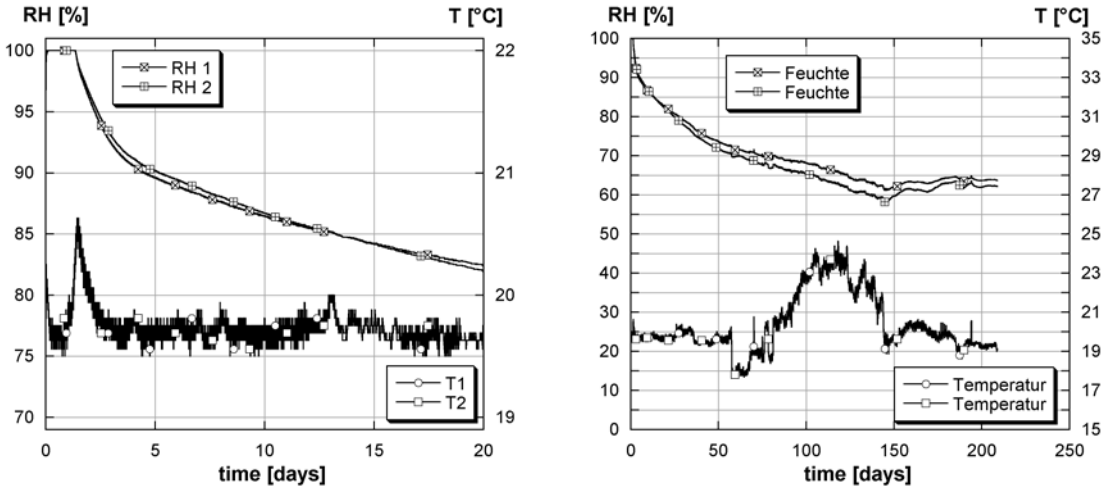

FIGURE 8.2: Evolution of the RH (A70): a) early age, b) long term

reaction began and there was enough water available for hydration that no capillary pressure built up. The transition between the first and the second period was the moment when the temperature began to rise at 1.2 days.

The RH decreased strongly until approximately 4 days. Then, it decreased constantly at a lower rate. The strong decrease may be explained with the high hydration rate at early age. At higher ages, the RH decrease was due to a slow hydration reaction and to drying to the surface, since the specimens were probably not completely sealed. At early age, however, the internal drying exceeded the external drying and the measurements were attributed to internal drying as a consequence of the hydration reaction.

9 Compression properties

9.1 General

Tests on cylinders and on cubes were used to investigate the compressive strength and the secant modulus of elasticity at 30% of the compressive strength. The test were performed at different ages between 4 and 365 days in order to investigate the evolution of the properties as a function of time.

The development of the material properties can be described by different models. The first model is from de Schutter [DeSchutter96] and considers the degree of reaction ξ as state variable. This

model describes well the material properties during the first five days after casting (EQ. 9.1) [Bernard00].

$$p(\xi(t)) = p(\xi = 1) \cdot \left(\frac{\xi - \xi_0}{1 - \xi_0}\right)^c \qquad \textit{(EQ 9.1)}$$

with ξ [-]: degree of reaction, $p(\xi)$: value of the considered property at a given degree of reaction, ξ_0 [-]: hydration threshold, c [-]: parameter.

The second model [Charif98] is adapted from the CEB-FIP model [CEB204] and describes the development of strength and modulus in EQ. 9.2 as a function of maturity. It reproduces well the evolution of strength for an age of more than five days after casting [Bernard00].

$$p(M(t)) = p(M = 28 \text{ days}) \cdot e^{s \cdot b\left(1 - \sqrt{\frac{28}{M(t)}}\right)} \qquad \textit{(EQ 9.2)}$$

with M(t) [days]: maturity of the concrete at time t, p(M): value of the considered property at a given maturity, s [-]: parameter characterizing the kinetics of the cement, b [-]: parameter

Both models are used to describe the evolution of the mechanical properties in concrete - the de Schutter model for the early age behaviour and the CEB-FIP model for the long term behaviour.

9.2 Testing and results

9.2.1 Concrete

Cubic specimens with a side length of 15 cm were tested in the laboratory of Element AG at the age of 3 and 28 days. The tests at 3 days were used to determine whether the beams had sufficiently hardened to be transported to the EPFL. These cubes were stored next to the beams. The cubes which were tested at an age of 28 days were kept at 20 °C. The cylindrical specimens (∅16 cm, l = 32 cm) were stored next to the beams during the first four days. Afterwards, they were stored in a water basin at 20 °C. The compressive strength and the Young's modulus (secant modulus at 30% of f_{cc}) were determined at the LMC at an age of 28, 90 and 365 days (Table 9.3 and Table 9.4) after the procedure described in the Swiss norm SIA 162/1, test n° 3 [SIA162/1].

TABLE 9.3: Compressive strength of the concrete

age [days]	f_{cc} [MPa]			f_{cm} [MPa]	specimen	curing
3	35.6	36.9	36.0	36.2 ± 0.7	cube 15 cm	next to the beams
28	51.1	52.4	49.8	51.1 ± 1.3	cube 15 cm	at 20 °C
28	40.6	50.0	47.6	46.1 ± 4.9	cyl. ∅ 16 cm	next to beams, water basin
90	49.2	55.0	52.4	52.2 ± 2.9	cyl. ∅ 16 cm	next to beams, water basin
365	55.1	63.4	63.5	60.7 ± 4.8	cyl. ∅ 16 cm	next to beams, water basin

The resistance of the cubes and the cylindrical specimens varied due to the different shape of the specimens. The strength of the cubic specimens was 10% higher than of the cylindrical specimens. The cylindrical specimens were stored in water at a temperature of 20 °C after demoulding at an age of 5 days. The cubic specimens remained in the formwork until testing at 20 °C.

TABLE 9.4: Modulus of elasticity of the concrete

age [days]	E_{cc} [GPa]			E_{cm} [GPa]	specimen	curing
28	37.25	35.55	40.65	37.81 ± 2.59	cyl. ∅ 16 cm	next to beams, water basin
90	40.20	39.00	38.70	39.30 ± 0.79	cyl. ∅ 16 cm	next to beams, water basin
365	41.80	41.20	41.80	41.60 ± 0.34	cyl. ∅ 16 cm	next to beams, water basin

The compressive strength on the cylinders was 46 MPa at 28 days and 61 MPa at 365 days (1 year). The secant modulus was 37.8 GPa and 41.8 GPa at 28 and 365 days respectively. The early age behaviour of the concrete was less important, since the age of the concrete at the beginning of the structural tests on the beams was more than 5 months. Therefore, only the CEB-FIP model was considered to model the evolution of the compressive strength and the secant modulus of the concrete. Figure 9.1 shows the test results and the mean values of each age of the compressive and the secant modulus test as well as the parameters of the CEB-FIP and its evolution in time.

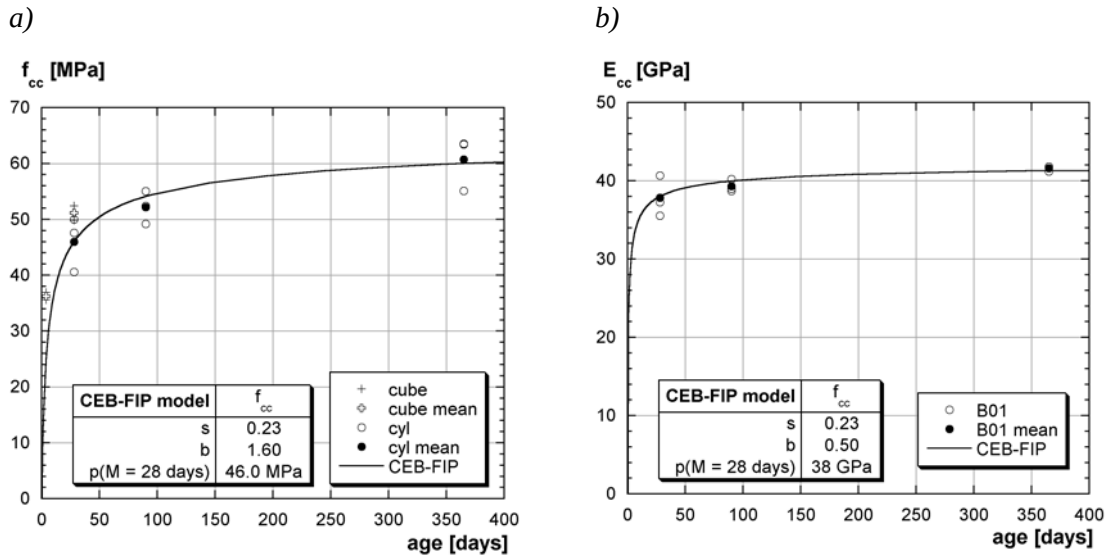

FIGURE 9.1: a) Evolution of the compressive strength, b) evolution of the secant modulus of elasticity of the concrete

The volumetric mass of the concrete was also determined during the tests to 2.45 kg/dm^3.

9.2.2 UHPFRC

Cylindric specimens. The compressive strength and the secant modulus of elasticity were determined on cylinders (∅11 cm, l = 22 cm) at the LMC after [SIA 162/1]. The cylinders were stored in the humid chamber after demoulding until testing.

The average compressive strength at 28 days was 168 MPa and the secant modulus 48.1 GPa (Table 9.5 and Table 9.6). The specimen did not fracture suddenly during tests, but were hold together by the steel fibres (Figures 9.2). The strength increased until approximately 90 days (Figures 9.3). Then, the values became virtually constant, since no further increase was observed between 90 and 365 days. The stable values suggest that the hydration process stopped or became very slow at approximately 90 days.

The de Schutter model describes well the evolution at early age (Figures 9.3a and 9.4a). The CEB-FIP model, used to describe the evolution at long term, fits well for UHPFRC lower than 90 days, but overestimates the strength at 365 days (Figures 9.3b and 9.4b). Therefore, compressive strength and secant modulus at 28 or 90 days may be assumed to be the final values.

FIGURE 9.2: Failure mode of a cylindric specimen,

TABLE 9.5: Compressive strength of the UHPFRC

age [days]	f_{Uc} [MPa]			f_{Ucm} [MPa]	specimen	batch	curing
3	131.4	127.0	122.6	127.0 ± 4.4	cyl. ∅11 cm	A45	stored in the humid chamber at the LMC
8	145.6	134.0	136.2	138.6 ± 6.2	cyl. ∅11 cm	A45	stored in the humid chamber at the LMC
15	162.5	132.0	148.0	147.5 ± 15.3	cyl. ∅11 cm	A45	stored in the humid chamber at the LMC
28	174.6	166.6	164.7	167.8 ± 4.3	cyl. ∅11 cm	A16	stored in the humid chamber at the LMC
	163.0	167.4	170.4			A45	
91	183.5	174.2	164.0	173.9 ± 9.8	cyl. ∅11 cm	A16	stored in the humid chamber at the LMC
365	156.6	166.6	178.0	167.1 ± 10.7	cyl. ∅11 cm	A16	stored in the humid chamber at the LMC

Prismatic specimens. Tests were conducted on prismatic specimens (7.2*7.2*21cm^3) to investigate the whole force-displacement curve in compression of the UHPFRC. These tests demand high stability during testing which was achieved by using a stiff test set-up and by adjusting the control parameters of the testing machine. The tests were displacement controlled and performed on a 1000 kN universal testing machine (Schenck 1000 kN). The specimen was placed between two 10 cm thick steel plates (Figure 9.5). LVDT (A) measured the displacement between the steel plates and was the LVDT that controlled the test. The deformations of the specimen were recorded with three LVDTs (B) that were fixed on rings. The rings were placed at a distance of 11 cm in the middle of the specimen. The used LVDTs had a range of ±5 mm and a precision of 1 μm. The tests were performed at a displacement rate of 0.1 mm/min.

Two tests were conducted on the prismatic specimens at 28 days. Figure 9.5b shows the stress-strain diagram of the two specimens. The stresses were calculated by dividing the measured force by

TABLE 9.6: Young's modulus the UHPFRC

age [days]	E_{cc} [GPa]			E_{cm} [GPa]	specimen	batch	curing
3	37.60	39.60	38.60	38.60 ± 1.00	cyl. ∅11 cm	A45	stored in the humid chamber at the LMC
8	45.00	42.60	43.80	43.80 ± 1.20	cyl. ∅11 cm	A45	stored in the humid chamber at the LMC
15	51.40	52.40	49.80	48.50 ± 3.70	cyl. ∅11 cm	A16	stored in the humid chamber at the LMC
	47.70	42.00	48.00			A45	
28	49.20	49.10	46.00	48.10 ± 1.80	cyl. ∅11 cm	A45	stored in the humid chamber at the LMC
91	52.60	53.60	53.70	53.30 ± 0.60	cyl. ∅11 cm	A16	stored in the humid chamber at the LMC
365	50.8	53.0	50.7	51.50 ± 1.30	cyl. ∅11 cm	A16	stored in the humid chamber at the LMC

a) *b)*

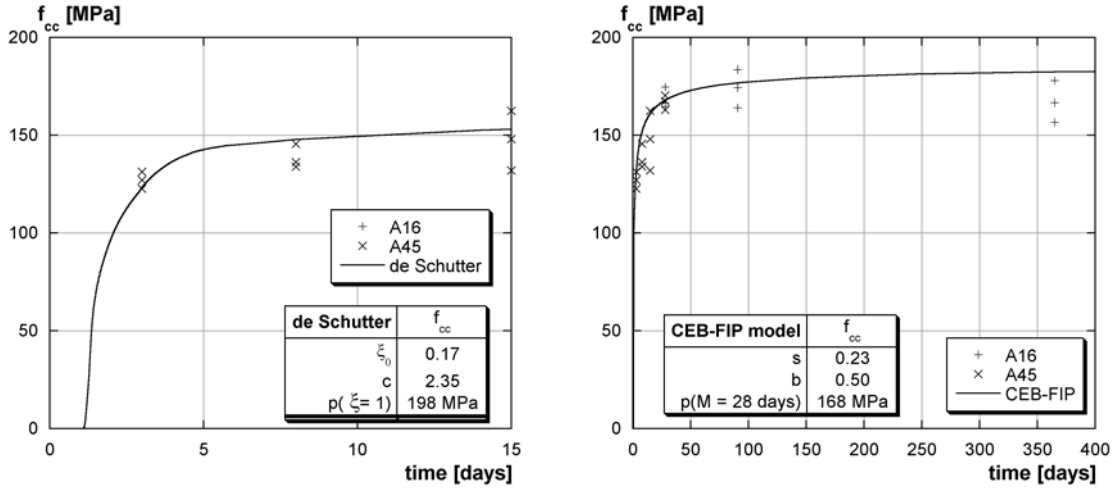

FIGURE 9.3: Evolution of the compressive strength: a) de Schutter model, b) CEB-FIP model

a) *b)*

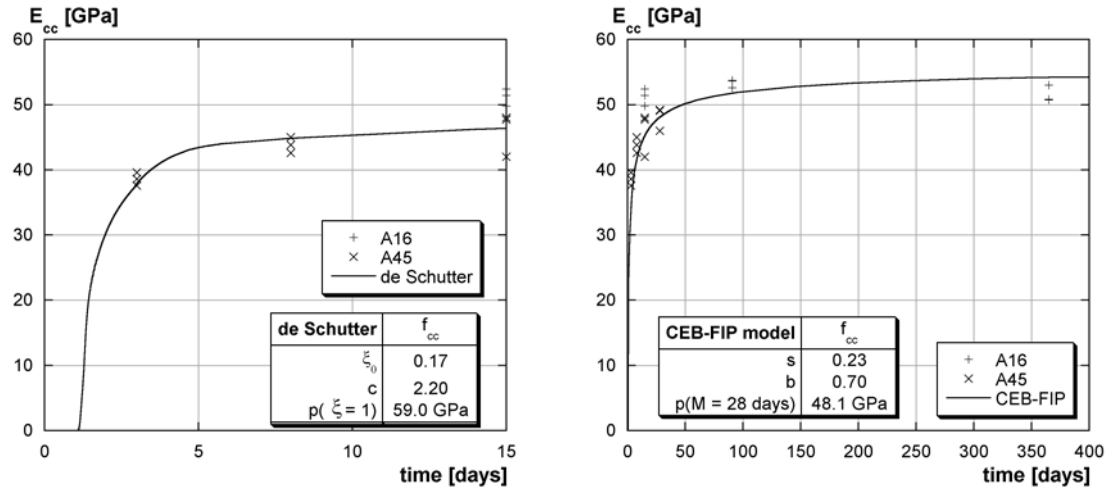

FIGURE 9.4: Evolution of the secant modulus: a) de Schutter model, b) CEB-FIP model

a) *b)*

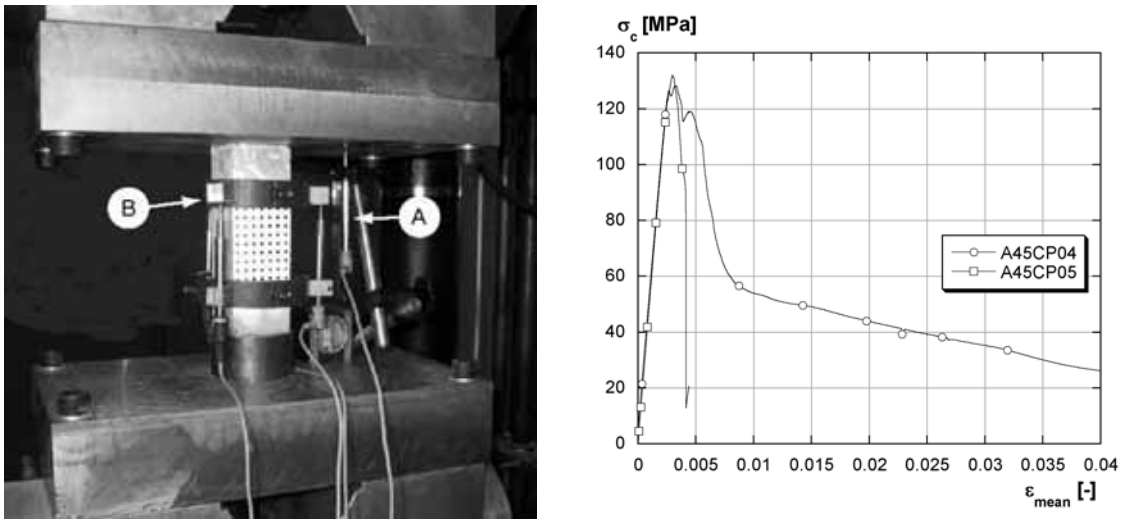

FIGURE 9.5: Prismatic specimens: a) test set-up ((A) LVDT that controlled the test, (B) ring with 3 LVDTs to measure the deformations), b) test results

the cross section of the specimen (7.2*7.2 cm^2). The deformation was the mean value of the three LVDTs, divided by the base length of 11 cm. The compressive strength of the specimens was 130 MPa and was more than 10% lower than the strength of the cylindric specimens. This may be due to the cross section (quadratic instead of circular) and to the increased ratio l/d = 3 instead of l/∅ = 2 when compared to the cylinders. However, the tests were performed to investigate the overall compressive behaviour, e. g. mainly the behaviour near the compressive strength and after the peak of the compressive strength was reached. The results show that the stress-strain curve was linear-elastic until approximately 95% of the compressive strength. The stress decreased rapidly after having passed the peak. The pre-peak behaviour was identical for the two specimens, but the post-peak behaviour was different. A45CP05 exhibited a very strong stress decrease which was characterized by instabilities at the descending branch. The test set-up was not sufficiently well controlled to obtain the post-peak behaviour. During the testing of A45CP04, no instabilities were observed: The stress decreased strongly until a stress of 60 MPa where a change of the slope occurred. Afterwards, the stress decreased slowly with increasing strain.

The compressive behaviour shows a strong stress decrease after the maximum of the compressive strength. At approximately 50% of the compressive strength, the slope changes and the stress decreased slowlier. This means that few energy was released during the first part of the descending branch, but more during the second part. The UHPFRC did not fracture completely when the peak was reached, but was still hold together by the steel fibres. Therefore, more energy was needed to obtain a complete fracture of the specimen.

10 Tension properties

10.1 General

The tensile behaviour is evaluated with uniaxial tensile tests to obtain the whole force-displacement curve before the formation of localized macrocracks and beyond the force-CMOD curve. A stiff testing device is developed to avoid stresses due to bending in the specimen. As the test is deformation-controlled, pre- and post-peak behaviour can be investigated.

10.2 Experimental Setups

Uniaxial tensile tests were conducted (Figure 10.1a) on an universal testing machine (capacity: 1000 kN). They were closed-loop displacement-controlled by the mean value of two LVDTs fixed

on the specimen (Figure 10.1a, d). The ends of the specimen were built-in to ensure a stiff test set-up. The glue (Figure 10.1b, d) filled out the space between the specimen (Figure 10.1b, c) and the surrounding metallic pieces (Figure 10.1b, a and b). However, there was no adherence between the glue and the metallic pieces. Here, the stress transfer was guaranteed by interlocking in order to ensure a uniform stress transfer. The test was designed for plates with a cross-section of 20*5 cm^2 at the supports.

a) *b)*

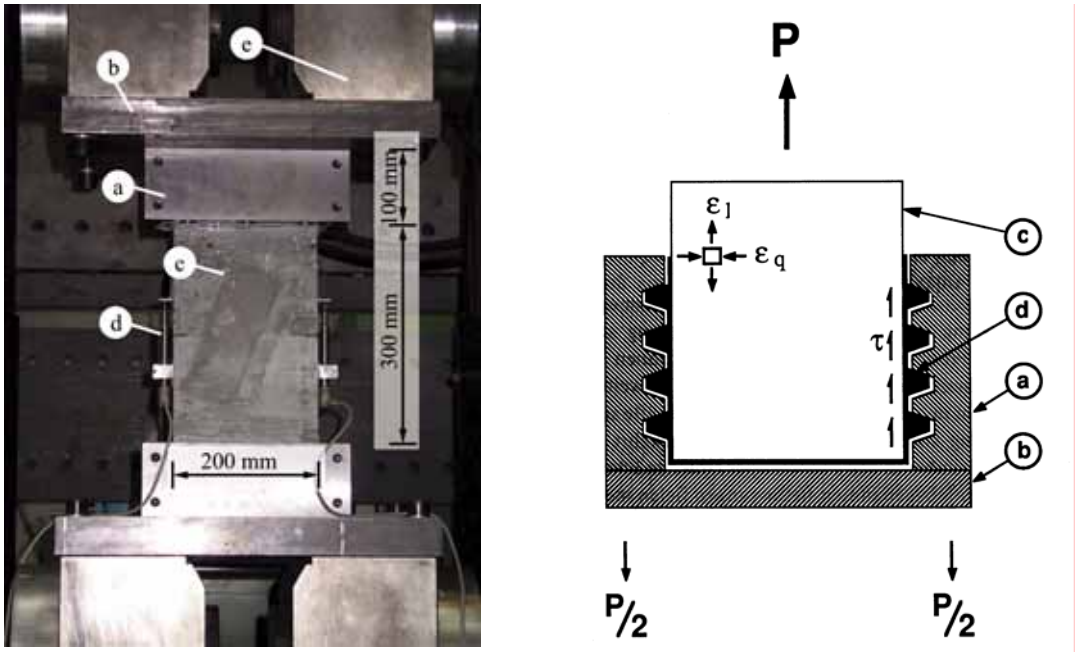

FIGURE 10.1: ***a)*** *Set-up of the uniaxial tensile test: a) surrounding metallic pieces with interlocking, b) base plate, c) specimen, d) LVDT, e) testing machine;* ***b)*** *force introduction at the end of the specimen from [Helbling87]: a) surrounding metallic pieces with interlocking, b) base plate, c) specimen, d) glue*

The tensile strength of the concrete was measured on cylindrical specimens (∅11 cm, h = 21 cm), having a constant section to avoid stress concentration due to notches. The tests were force-controlled with a rate of 3 kN/min.

10.3 Results

10.3.1 Concrete

The tensile strength of the concrete was determined at several ages (Table 10.1). Five cylinders (∅11 cm, h = 21 cm) were tested at each age. At 28 and 84 days, several cylinders failed at the glued surface and gave a lower boundary for the tensile strength. At 449 days, no failure occurred at the glue and represented the value of the tensile strength.

TABLE 10.1: Tensile strength - cylindrical tests

age [days]	**f_{ct} [MPa]**					**f_{ctm} [MPa]**	**specimen**
28	3.61	2.77*	3.57*	3.52*	3.62*	3.42 ± 0.36	cyl. ∅ 11 cm
84	3.39*	3.17*	3.27	3.92*	-	3.44 ± 0.33	cyl. ∅ 11 cm
449	4.53	4.73	5.11	5.06	3.95	4.68 ± 0.47	cyl. ∅ 11 cm
* failure at the glued surface							

The evolution of the tensile strength was modelled with the CEB-FIP model. All test results were considered for the fit of the model. Figure 10.2a shows the comparison between the test results and the CEB-FIP model. All test results as well as the mean values are drawn for each age of the testing; the parameters of the CEB-FIP model are also given in the diagram.

a) *b)*

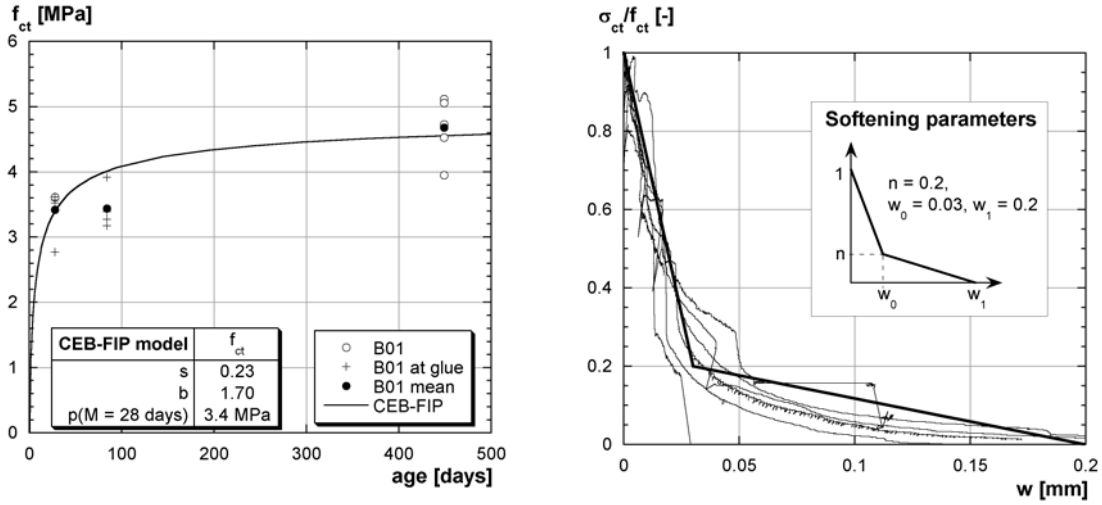

FIGURE 10.2: a) Evolution of the tensile strength (tests on cylinders), b) softening parameters of the concrete (B01)

The whole force-displacement curves under tension were determined with the uniaxial tensile test on notched prismatic specimens (5*20*5 cm^3). Tensile tests were conducted at 28 days and 365 days of the concrete and the softening curve was deduced on the basis of these results (Figure 10.2b). The specific fracture energy was approximately 120 J/m^2.

10.3.2 UHPFRC

The tensile behaviour of the UHPFRC was investigated on notched specimens (50*20*5 cm^3) at 4, 8, 14, 28 98 and 365 days. Furthermore, six tests were conducted on dogbone specimens to determine the secant modulus of the undamaged specimen. The tests were displacement-controlled with the mean value of the two lateral LVDTs at a rate of 0.6 mm/h. The base of the controlling LVDTs was 10 cm for the notched specimens and 34 cm for the dogbone specimens. The length was chosen to span the whole cracking zone of the specimens in which cracking was likely to occur.

Table 10.2 gives an overview over the test results that were determined with notched specimens. The only exception was the modulus at 28 days that was studied for notched and dogbone specimens. The stresses $f_{Ut,max}$ and $f_{Ut,1st}$ were calculated by dividing the maximum force and the force at the first cracking (at the end of the linear-elastic zone at the beginning of the test) by the reduced section at the notch (16*5 cm^2). $E_{notched}$ is an estimation of the secant modulus during the linear-elastic part at the beginning of the test, since no cycles were conducted to determine its value. The secant modulus was also investigated on the dogbones specimens ($E_{dogbone}$) with a constant reduced cross-section (15*5 cm^2). Here, the secant modulus was determined with three cycles between approximately 5 and 50% of σ_{1st}. Finally, the fracture energy was also investigated. The detailed results can be found in Tables A.1 and Table A.1 in Appendix A.

Stress-displacement curve. The *stress-displacement curves* of the notched specimens at 28 days are shown in Figure 10.3a. The displacement represents the mean displacement measured with the LVDTs over a length of 10 cm. A stress rise was observed until a displacement of approximately 0.25 mm. Then, the stress decreased monotonously until the fracture of the specimen. The stress rise was characterized by a steep linear-elastic stress rise. A sudden decrease in the slope was observed at a stress of 9.1 MPa. No localized cracks were observed with the naked eye on the specimen and

TABLE 10.2: Test results of the uniaxial tensile tests on notched specimens (UHPFRC)

age [days]	number of specimens	$f_{Ut,1st}$ [MPa]	$f_{Ut,max}$ [MPa]	$E_{notched}$ [GPa]	$E_{dogbone}$ [GPa]	G_F [kJ/m^2]
4	3	5.8	7.1	37.4	-	9.9
8	3	5.6	5.8	37.3	-	7.9
14	2	7.6	7.6	39.1	-	11.2
28	5	9.1	11.0	41.0	-	20.2
28	2	-	-	-	53.5	-
98	3	11.2	12.7	45.8	-	23.8
365	3	10.2	12.9	45.3	-	24.2

the stress continues to increase. This part of the curve can be represented in a stress-strain diagram (Figure 10.3b). At the maximum stress, a localized crack formed leading to the fracture of the specimen. Here, the LVDTs measured the crack mouth opening displacement of the localized crack.

The *mean curve* of the test results is also traced in Figure 10.3. A domain of hardening was observed until a deformation of approximately 0.28%. The stress-displacement curves of all tests can be found in Figures A.2 to A.13 in Appendix A.

a) *b)*

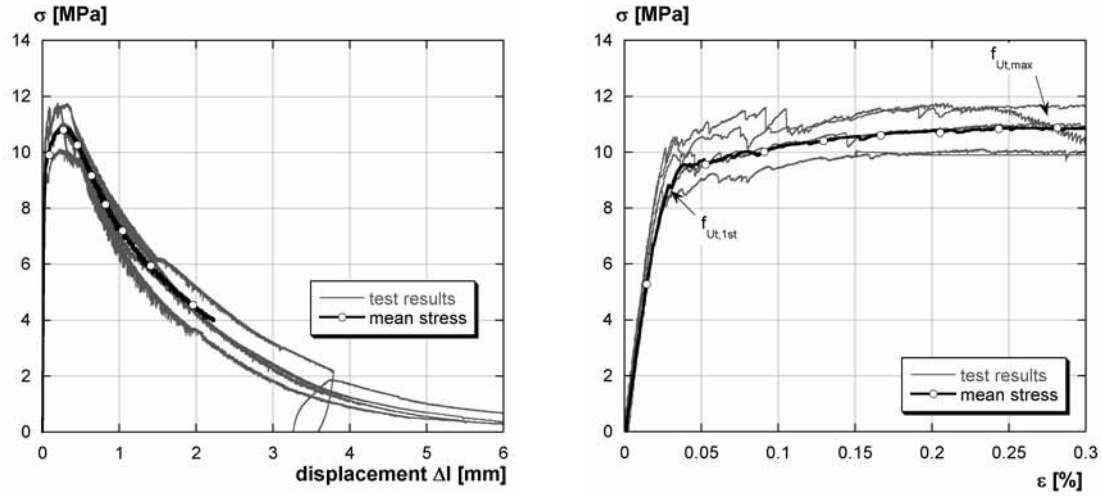

FIGURE 10.3: Tensile behaviour of the uniaxial tensile tests (at 28 days): a) stress-displacement curve, b) stress-strain curve before cracking

The *crack paths* of the UHPFRC did not go straight from one notch to the other. The crack paths can be found in Figures A.14 to A.45 in Appendix A. The assumption to take the reduced section of the notched specimen as crack surface did not apply to all specimens. The crack surface was often bigger and the stress lower. However, since it was difficult to estimate the surface, the assumption is a simple way to calculate the tensile parameters for UHPFRC. The variability of the UHPFRC was high at an age of 4 days (Figures A.2, A.3 in Appendix A). This may be due to the different fracture surfaces (Figures A.14, A.15 in Appendix A). Therefore, the mean values of Table 10.2 were higher at 4 days than at 8 days.

The *eccentricities* during testing were determined by four LVDTs fixed near the edges two on the front side and two at the same places on the back side of the specimen, as shown in Figure 10.4a (A). They were *small* and remained at approximately 0.04 mm at the maximum force between the 4 LVDTs fixed on the specimen and at 0.11 mm during softening near the end of the test (Figure 10.4b).

a) *b)*

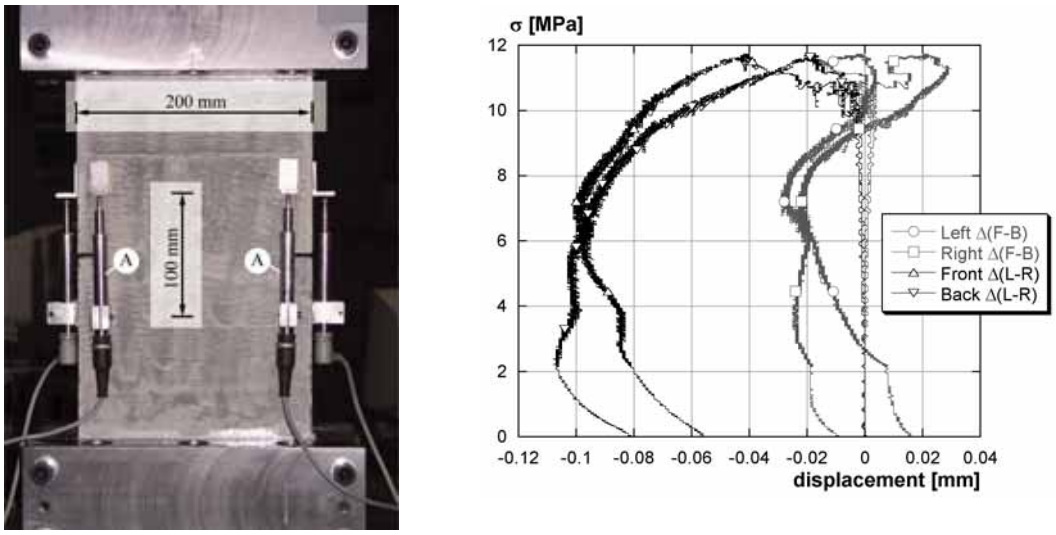

FIGURE 10.4: a) Position of the LVDTs (A) during the uniaxial tensile test, b) eccentricities for specimen A18T03 (tested at 28 days) (F: front side, B: backside, L: left side, R: right side)

Evolution of the tensile properties in time. The evolution in time of the parameters of the tensile behaviour was modelled with the CEB-FIP and the de Schutter model (Section 9.1). As the de Schutter model describes well the early age properties, the model parameters were fitted with the test results for 4, 8, and 14 days. The CEB-FIP model was fitted with all the test results.

TABLE 10.3: Model parameters for uniaxial tension (UHPFRC)

Model		$f_{Ut,1st}$	$f_{Ut,max}$	$E_{notched}$	$E_{dogbone}$	G_F
CEB-FIP	s	0.23	0.23	0.23	0.23	0.23
	b	1.6	1.6	0.72	0.72	1.5
	p(M=28 days)	9.2 MPa	11 MPa	41 GPa	53.4 GPa	20.0 kJ/m^2
de Schutter	ξ_0	0.17	0.17	0.17	-	0.17
	c	8.5	8.5	2.2	-	8.5
	p(ξ_0=1)	19.1 MPa	21.2 MPa	52 GPa	-	30 kJ/m^2

Figure 10.5a shows the evolution of $f_{Ut,max}$ and $f_{Ut,1st}$ at early age and the fit of the de Schutter model; Figure 10.5b shows the evolution of $f_{Ut,max}$ and $f_{Ut,1st}$ at long term and the fit of the CEB-FIP model. The properties increased until 90 days and then became virtually constant. The same evolution was observed for the evolution of the secant moduli $E_{notched}$, $E_{dogbone}$ and the fracture energy G_F (Figures A.46 to A.52 in Appendix A). It can be concluded that the hydration slowed down to a very small rate at approximately 90 days. This may be explained with the low water/ binder-ratio and the low permeability of the UHPFRC that hindered water to penetrate into the specimen.

Secant modulus. The secant modulus on a constant section $E_{dogbone}$ was found to be 30% higher than the secant modulus on the notched specimens $E_{notched}$. The two moduli can be described with the same model parameters. Therefore, the model parameters were fitted on the notched specimens. Then, the models were applied to $E_{dogbone}$.

Evolution of the secant modulus. The secant modulus was measured at different displacements of the LVDT by means of cyclic tests to determine the Young's modulus with increasing cracking (and damage) of the specimen.

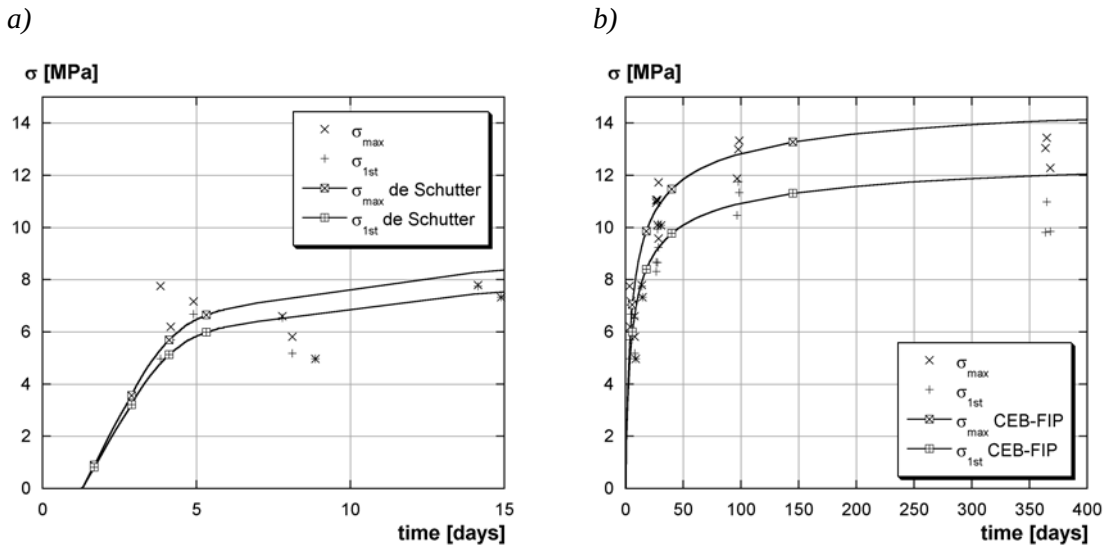

FIGURE 10.5: Tensile strength of the UHPFRC: a) comparison to the de Schutter model, b) comparison to the CEB-FIP model

Cyclic tests were conducted on three notched specimens at 4, 8 and 28 days. Figure 10.6 shows the evolution of the modulus in function of the displacements of the LVDTs. The secant moduli E_{secant} are normalized by the first secant modulus $E_{secant0}$ measured during the linear elastic stress rise at the beginning of the test and represents the secant modulus for the undamaged specimen.

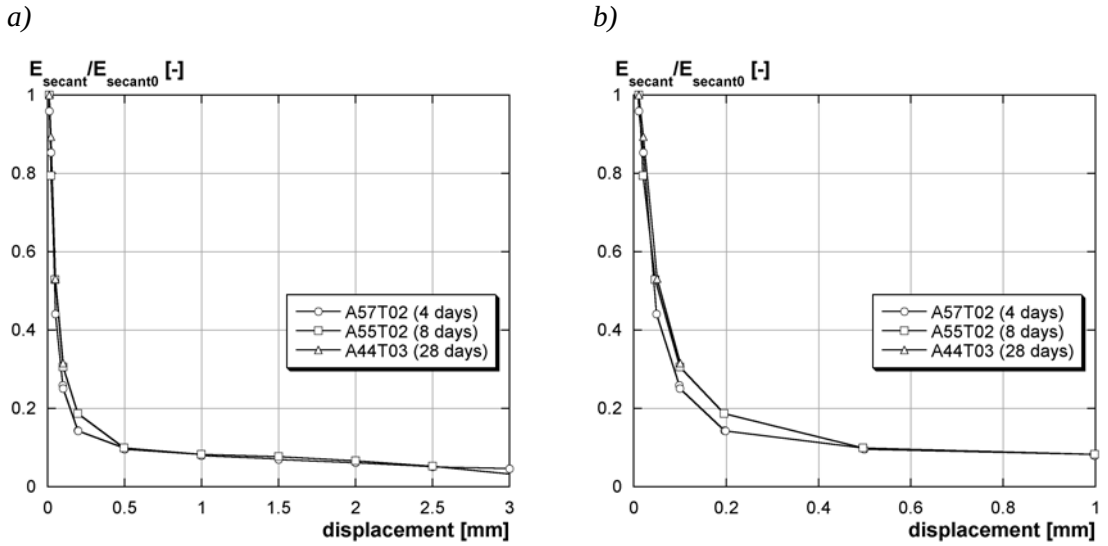

FIGURE 10.6: Evolution of the normalized secant modulus during testing; a) whole diagram, b) detail

A strong decrease of the secant modulus was observed until 0.2 mm. At 0.2 mm, the secant modulus was at 15% of its initial value. Thus, the significant decrease occurred during the hardening domain of the material. The decrease of the secant modulus indicated progressive damage of the matrix of the specimen. The secant modulus decreased slightly for displacements that were higher than 0.2 mm. This indicates that the UHPFRC matrix was completely damaged in the crack and that the force was transferred by the fibres. The fibres were pulled out gradually to the fracture of the specimen. The secant modulus measured at a displacement of 3 mm was at 10% of the initial modulus $E_{secant0}$.

Summary. The uniaxial tensile tests show that the UHPFRC had a high fracture energy. A hardening domain could be distinguished until a strain of 0.28% on the notched specimens and of 0.1% in the dogbone specimens. Afterwards, softening occurred until the fracture of the specimen. The first

cracking strength and the maximum tensile strength were $f_{Ut,1st}$ = 9.1 MPa and $f_{Ut,max}$ = 11 MPa respectively at 28 days for the notched specimens which was approximately three times higher than for the concrete. The evolution of the secant modulus shows that the matrix was mainly damaged during the hardening domain. The softening zone was characterized by the pull-out of the steel fibres in a completely damaged matrix at the crack.

11 Free shrinkage tests

11.1 Test set-up

Shrinkage was measured on 2 drying and 2 sealed cylinders (∅11 cm, l = 22 cm) (Figure 11.1). The cylinders were kept in the climatic tent under constant ambient conditions (RH ≈ 40%, T ≈ 20 °C). The sealed cylinders were isolated with two layers of self-adhesive aluminium which was a very good moisture barrier [Toutlemonde96]. Two rings were fixed with three screws each on the specimens with at a distance of 15 cm [Clement01]. A LVDT (HBM, W1T3, ±1 mm, precision: ±1 μm, recorded with an UPM60) measured the relative displacement between the rings.

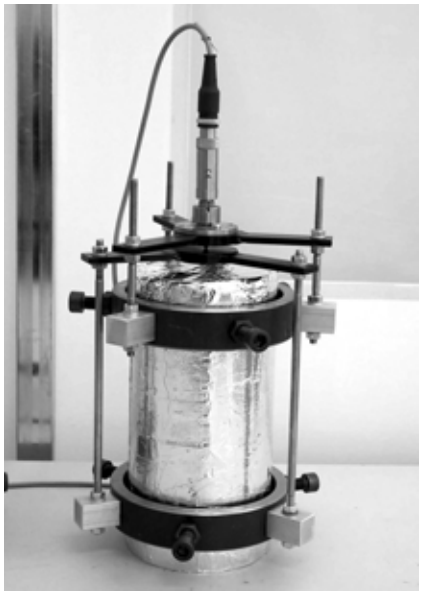

FIGURE 11.1: Test set-up of the free shrinkage tests

11.2 Results

11.2.1 Concrete

The cylinders were prepared for the shrinkage tests 22 hours after casting. The humidity barrier was put on directly after the cardboard cylinder had been removed. The measurements starts 23 hours after casting. The measurements show a strong increase of deformation until an age of 80 days (Figure 11.2a). Then, the increase of deformation slowed down and stabilized after approximately 365 days. The deformations of the sealed specimens were four times lower than those of the drying specimens. The shrinkage deformation days was 800 μm/m for the drying specimens and 150 μm/m for the sealed specimens at 365.

11.2.2 UHPFRC

The UHPFRC specimens were prepared two days after casting. The cardboard formwork of the cylinders had been removed 4 hours before the start of the measurements. The cylinders were stored

in water in the period between the removal of the formwork and the preparation of the specimens. The measures started 54 hours after casting.

The shrinkage deformation of the UHPFRC increased strongly until an age of approximately 90 days (Figure 11.2b). At this age, the deformation of the sealed specimens was 350 μm/m and 400 μm/m for the drying specimens. Then, the shrinkage deformation increased very slowly.

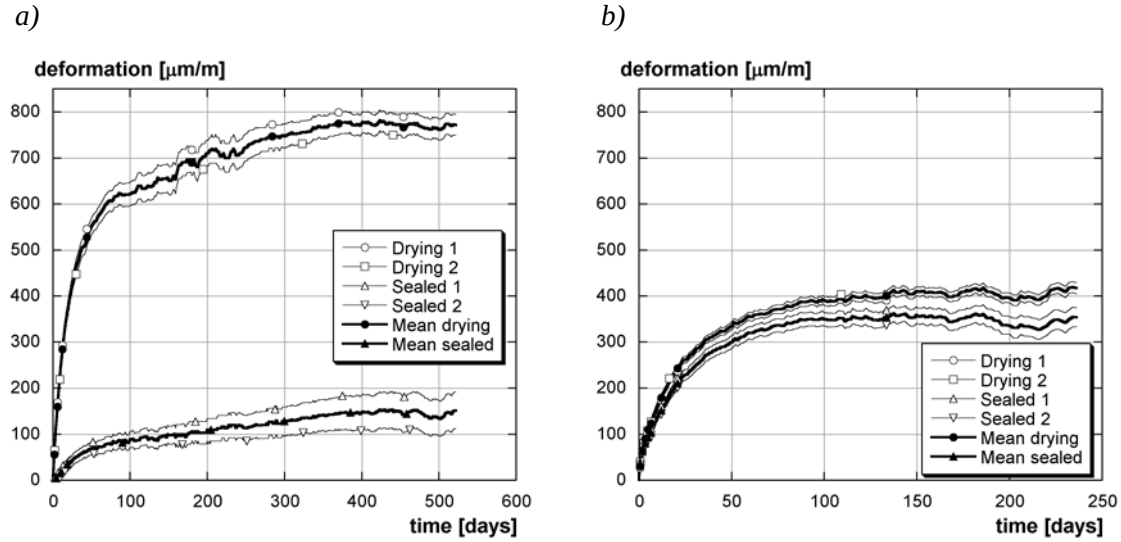

FIGURE 11.2: Shrinkage deformation of a) B01and b) A45

The difference between the sealed and the drying shrinkage was small. The main difference was observed during the first 20 days and indicates small moisture exchange with the surroundings. At early age, this difference may be due to the hardening material. At the beginning, the permeability of the material seems to be higher, since the hydration reaction was still creating the dense matrix.

12 Free and restrained autogenous shrinkage of the UHPFRC at early age

12.1 General

Free and restrained shrinkage tests were performed at the university LAVAL in Québec, Canada, by M. Bouhlel, B. Zuber and B. Tamtsia Taboue (CRIB, under direction of Prof. J. Marchand) in order to investigate autogenous shrinkage and viscoelasticity at early age.

The test set-up consists of two moulds: one to measure free shrinkage and the second to measure stress evolution due to the restraint of shrinkage. Thus, viscoelasticity can be deduced by comparing the two tests. Linear deformation in horizontal direction is measured during testing. The test is designed in a way that deformations and stresses can be measured from the moment when the material exhibits a small stiffness. The test set-up is shown in Figure 12.1, further details can be found in [Charron03], who improved the test to its present state.

The deformations are measured with two LVDTs for each specimen. The deformation in the specimen is obtained by the difference of the two LVDTs of one specimen and by dividing the difference by the base length of 75 cm. In the free shrinkage test, the deformations of the sealed specimen are recorded. In the restrained shrinkage test, also called “discretized restrained shrinkage” DRS [Charron02], the deformations and the stresses in the specimen were measured. When the stress reaches the stress limit of 0.01 MPa, i.e. the material has sufficiently hardened to sustain a stress of 0.01 MPa, the system to control deformations is activated: the deformations are free until they reach the threshold value of $\Delta\varepsilon_{limit}$ = 6 μm/m. Then, they are reset by zero and the stresses in the specimen increase. This process is shown in Figure 12.2. Discretized restrained shrinkage means

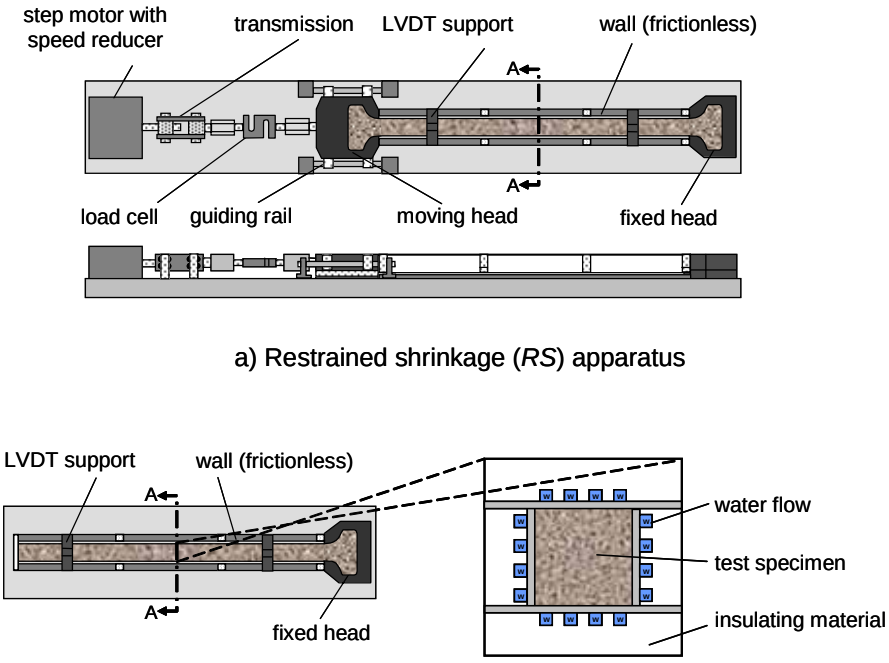

FIGURE 12.1: Conceptual illustration of the discretized restrained shrinkage (DRS) test setup (from [Charron02])

that the stress is increased in steps: between two steps, the stress is constant and creep curves develop. The deformation / stress increments at each step are used to deduce the elastic modulus.

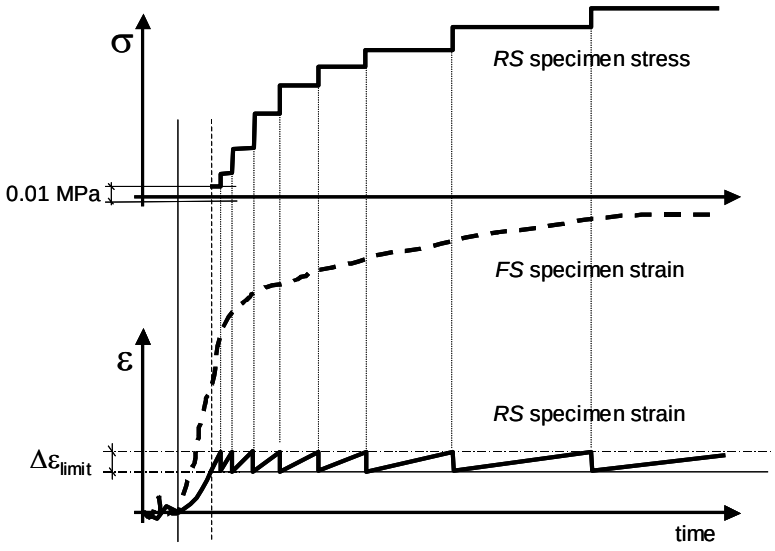

FIGURE 12.2: Test procedure of the DRS test (from [Charron02])

The test-set up is equipped with a temperature control consisting of pipes around the specimen in which water circulates and cools or heats the specimen. The small cross-section of the specimen (5*5 cm) leads to a small temperature gradient (< 0.1 °C) in the specimen.

12.2 Test program

The test program consisted of three tests on the investigated UHPFRC: two at isothermal conditions at 20 °C and one without temperature control. The temperature of the surrounding was approximately 20 °C, thus, the temperature in the test without temperature control was also expected to be approximately 20 °C at the beginning and the end of the test.

12.3 Test results

Several problems occurred during testing. Unfortunately, not all necessary information was available to clarify all uncertainties of the test results. In the first test, the temperature control of the specimen should had been controlled by a temperature sensor placed in the specimen. However, this system did not work and the bath was controlled by its internal temperature sensor at 20 °C. Thus, the temperature in the specimen varied approximately 1.5 °C (20.5 °C ±0.75 °C). The temperature sensors in the specimen were not well calibrated during the second and the third test (the test at ambient temperature and the second isothermal test) and were adjusted by making hypotheses on the initial temperature (20 °C). Finally, during the second isothermal test, the control of the test did not work during 15 and 27 hours and the beginning of setting was not controlled. Furthermore, the recording of one of the LVDTs of the free shrinkage tests was far to high and indicated a problem during data acquisition. As the problems during testing were not entirely known and the uncertainties of the measurements could not be controlled, this test was not treated any further.

Thus, *only the results of one isothermal test at 20 °C (the first test) and the test at ambient temperature are discussed*. Their test results were presented in Figures 12.3 and 12.4 respectively: The displacements measured with the LVDTs in the free and the restrained shrinkage tests are shown in Figures a). The displacements were zeroed at the beginning of the test (after the casting of the specimens). The deformations, calculated by the difference of each pair of LVDTs which was divided by the base length, are traced in Figures b).

Figures c) and e) show the free shrinkage curve, the “shrinkage + creep” curve deduced from the DRS test and the creep curve, deduced by subtracting the “shrinkage + creep” curve from the free shrinkage curve. Compression creep at very early age and the tensile creep are shown in Figures c), while only tensile creep is traced in Figures e).

Figures d) show the evolution of the stress in the DRS test and the moduli of elasticity calculated for each load step. It must be noted that the moduli were rough estimations that were calculated on a deformation $\Delta\varepsilon_{limit}$ = 6 μm/m and a small load steps (< = 0.5 MPa). Moreover, the deformation rate was slow with 3 μm/m/min.

The temperature evolution in the centre and at the side of the specimen as well as the temperature in the bath were traced in Figures f). It can be seen that the temperature difference in the specimen remained always below 0.5 °C. However, a temperature rise of 1 to 1.5 °C was observed in the specimens at approximately 30 hours. Thus, the isothermal test was not a real isothermal test and shows nearly the same temperature evolution than the test at ambient temperature. Therefore, both tests can be directly compared and treated in the same way.

The results of the two tests were in good agreement with a scatter of 15% between the two tests: The free autogenous shrinkage amounted to 300 to 350 μm/m after 168 hours (Figures 12.3e and 12.4e). The tensile creep deformation was evaluated to 160 to 250 μm/m; the difference in the values was explained by the stress history that varied for the two tests. The creep deformation was depending on the stress in the specimen and was not a specific creep curve.

The stresses rise to 4.2 and 3.9 MPa respectively at the end of the test at 168 hours (Figures 12.3d and 12.4d). The moduli of elasticity increased strongly in stiffness from 30 to 72 hours and evolved slowly afterwards. The high scatter of the moduli in Figure 12.4e may be explained by the imprecise way of deducing this parameter.

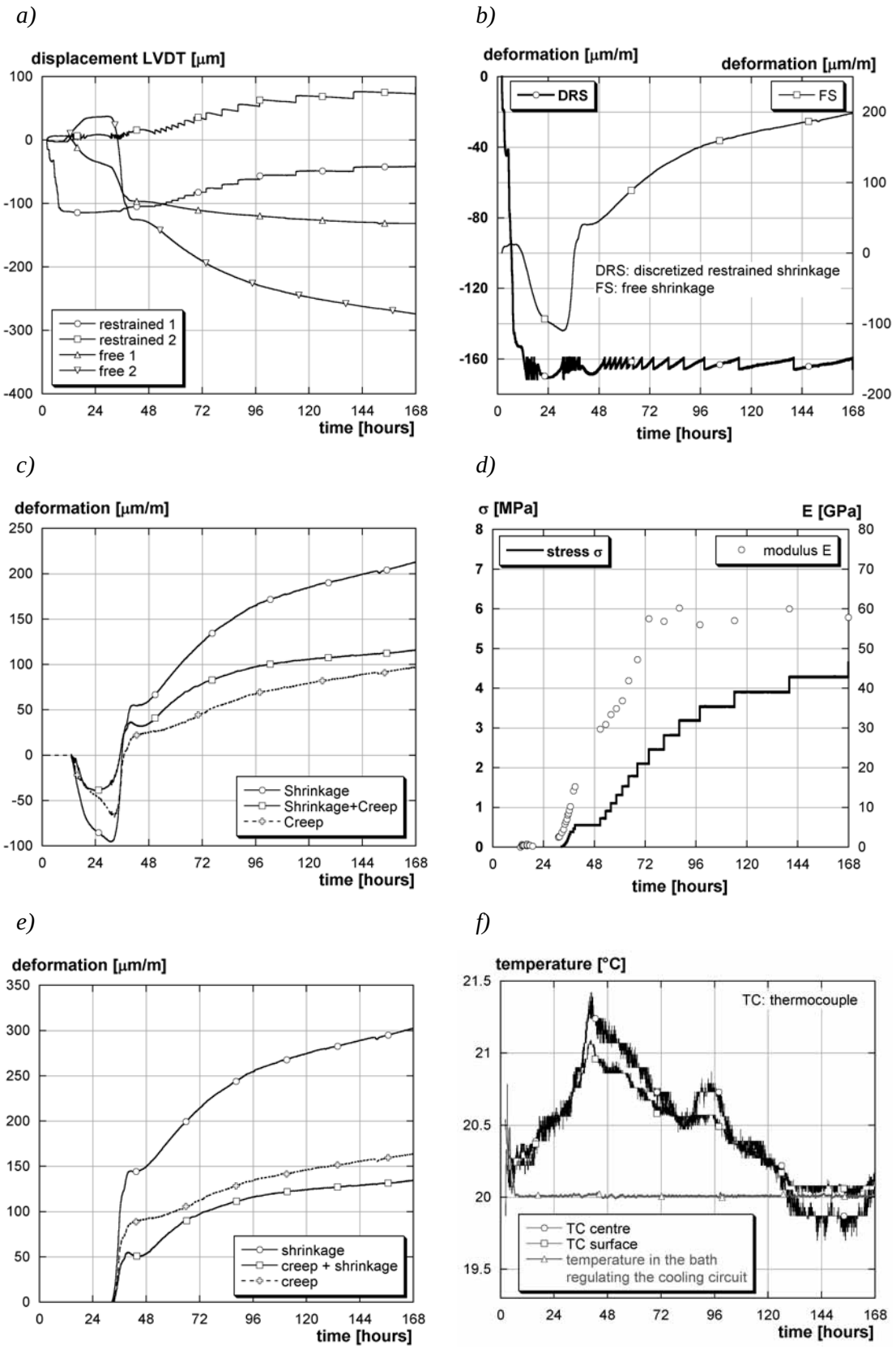

FIGURE 12.3: Test results of the isothermal DRS test at 20 °C: a) raw displacements of the LVDT, b) deformations in the free and restrained shrinkage test, c) free shrinkage, creep + shrinkage, and calculated creep curve, d) stress and calculated secant modulus, e) free shrinkage, creep + shrinkage, and calculated creep curve under tension, f) temperature evolution in the specimen and in the bath that supplied the temperature control of the specimen

a)

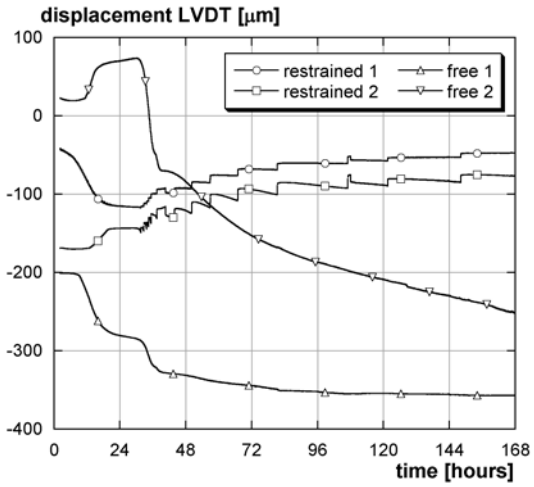

b)

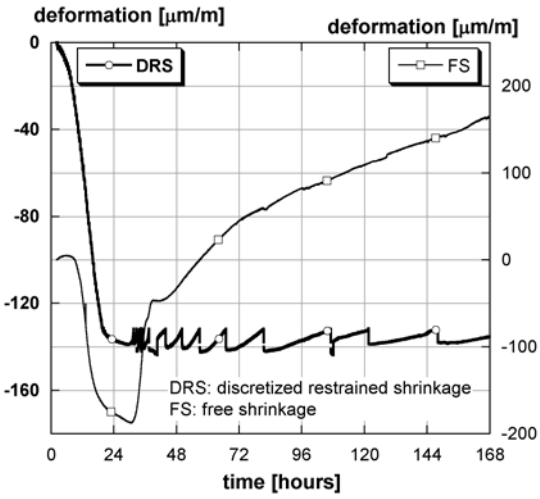

c)

no creep in compression was observed and the figure was identical to e)

d)

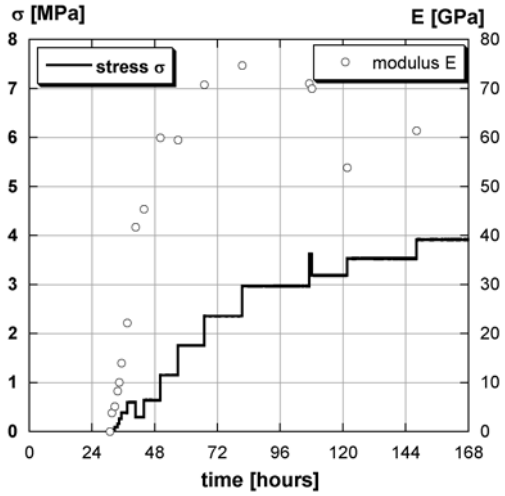

e)

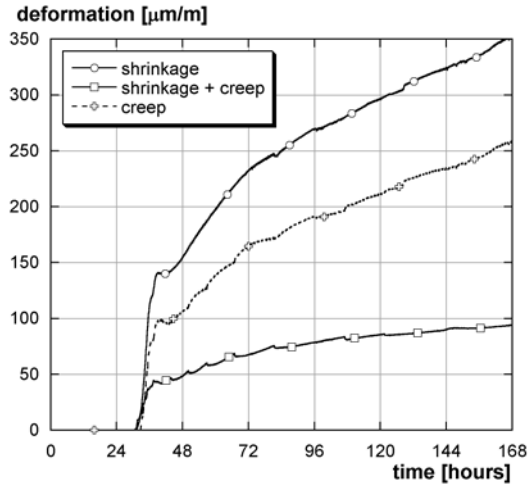

f)

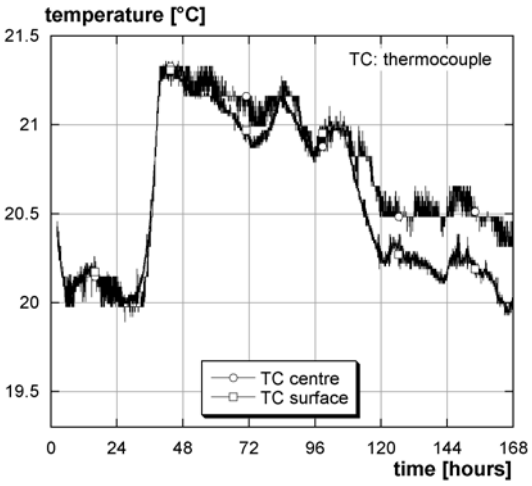

FIGURE 12.4: Test results of the isothermal DRS test without temperature control: a) raw displacements of the LVDT, b) deformations in the free and restrained shrinkage test, c) free shrinkage, creep + shrinkage, and calculated creep curve, d) stress and calculated secant modulus, e) free shrinkage, creep + shrinkage, and calculated creep curve under tension, f) temperature evolution in the specimen (temperature sensors probably not calibrated)

13 Compression creep

13.1 General

Compression creep tests were conducted on cylinders in a climatic chamber at 20°C ± 1 °C and a RH of 60% ± 5%. In parallel, the shrinkage deformation was measured. For each configuration, deformations were measured on two sealed and two drying specimens with a dial gage (Compac, Geneva, type 556 E, nominal accuracy: ± 1 μm) (Figure 13.1). The real precision of the gage was below this value, since temperature influences (heating of the gage with the hands during measurements) and the manual data acquisition led to errors.

a) *b)*

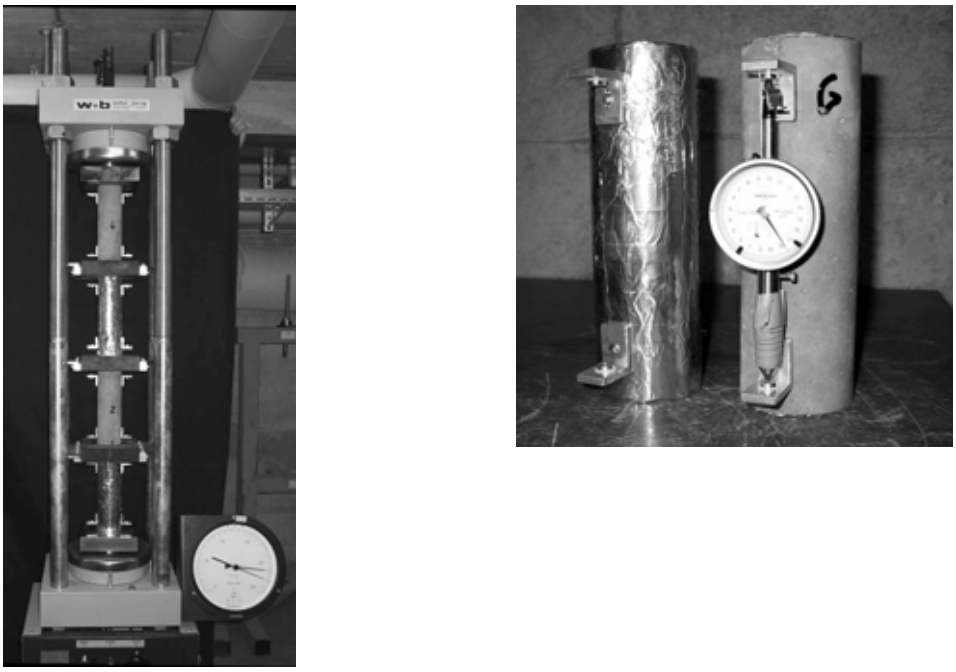

FIGURE 13.1: a) Creep test set-up, b) free shrinkage specimens with dial gage (UHPFRC)

The cylinders were stored in water until 30 minutes before the start of the test. Then, the pieces for the measuring device were fixed on the cylinders and two layers of self-adhesive aluminium were applied to seal the cylinders. So, water exchange with the environment was prevented [Toutlemonde96].

13.2 Results

13.2.1 Concrete

The compressive creep tests of the concrete were conducted on cylinders (∅11 cm, l = 22 cm). The load level was approximately 25% and 50% of the compressive strength f_{cc} at 28 days, corresponding to stresses of 11.5 MPa and 23 MPa respectively. The initial temperature of the cylinders was approximately 27 °C at the beginning of the test. The creep tests started at a concrete age of 137 days.

Figure 13.2 shows the creep compliance of the concrete. A significant difference was observed for the drying and the sealed specimens. The creep compliance of the sealed specimens - the basic creep - was nearly constant, while the creep compliance of the drying specimens increased monotonously. A constant slope developed after approximately 15 days.

The measurements on the sealed specimens were imprecise due to the measuring system. The measuring points were glued on small aluminium angles. The angles were fixed with screws and

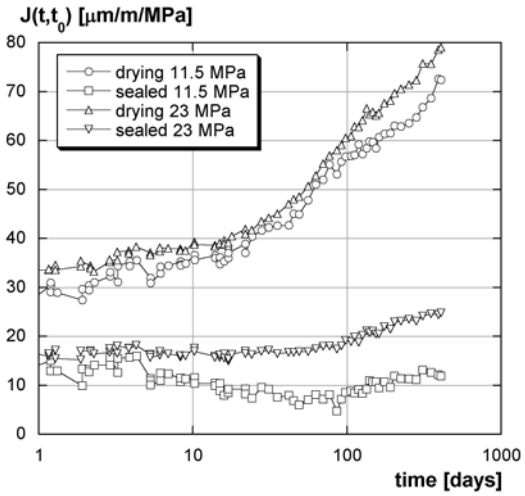

FIGURE 13.2: Creep compliance of the concrete (B01)

plastic dowels to the specimen. An interaction between the dowels and specimens occurred during the first seven days of testing. This interaction apparently only occurred in the sealed specimens. Therefore, the absolute values of the sealed specimens were probably higher than measured. Furthermore, the specimen temperature at the beginning of the test also distorted the measured values in the beginning of the tests.

13.2.2 UHPFRC

The cylindrical specimens (∅6.9 cm, l = 22 cm) were loaded at an age of 6 days with a compressive stress of 34 MPa and 58 MPa. Considering a compressive strength at 3 days of 127 MPa (Chapter 9.2.2), the load corresponded to 27% and 46% of the compressive strength at the beginning of the test. The creep measurements started during the early age of the concrete when the material properties still change.

Figure 13.3 shows the creep compliance of the UHPFRC specimens. No distinction can be made between the drying and the sealed specimens. The mean creep compliance of the specimens was 50 µm/m/MPa after 250 days. The slope of the creep compliance was constant, until it became virtually constant at 50 µm/m/MPa after approximately 90 days.

a) *b)*

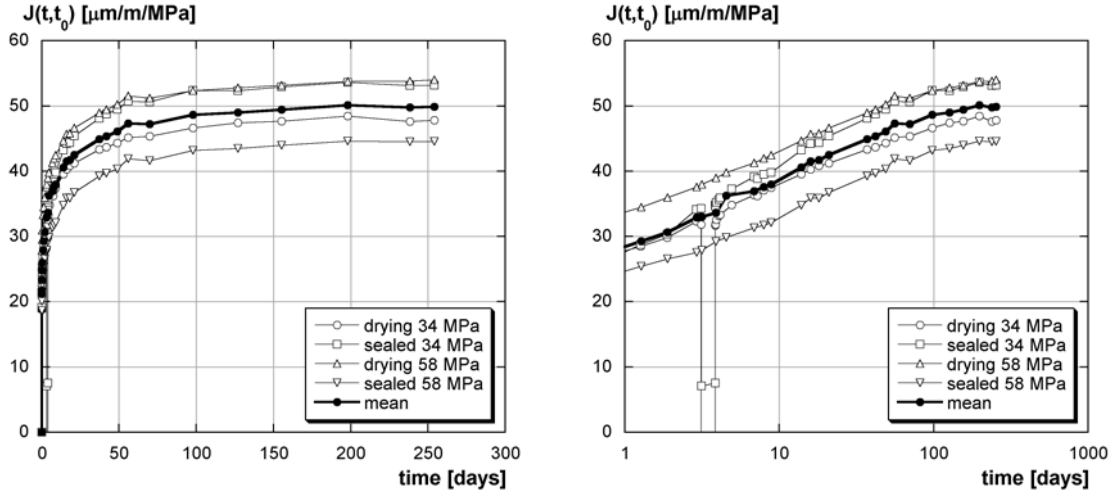

FIGURE 13.3: Creep compliance of the UHPFRC

The measurements were imprecise. The system of the fixation of the measuring points with plastic dowels and screws may have moved at the early age. Furthermore, some cylinders of the column with a load of 34 MPa were not plane and started to move in the testing device. Eccentricities were created leading to unequal deformations in the specimens. Therefore, the column with 34 MPa was unloaded 3 days after loading and the cylinders were adjusted. Afterwards, the column was reloaded. Small eccentricities still existed in the columns with 34 MPa. Despite of the problems during testing, the measurements of the UHPFRC were exploited. It was obvious that the measurements were imprecise, but the order of magnitude of the results was correct.

14 Reproducibility of the UHPFRC

14.1 General

Compressive and flexural tests on prisms (4*4*16 cm^3) were used to evaluate the reproducibility and the quality of the UHPFRC batches. The size was chosen to minimize the material used for these tests. Furthermore, the size corresponds to the standard test size for cement pastes [EN196/1], so, standardized test set-ups could be used (Figure 14.1). As the UHPFRC has a very fine matrix (biggest aggregate diameter: 0.5 mm) and quite short steel fibres (l = 10 mm) and the casting procedure was always the same, the tests indicated well the quality and the reproducibility of the material.

a) *b)*

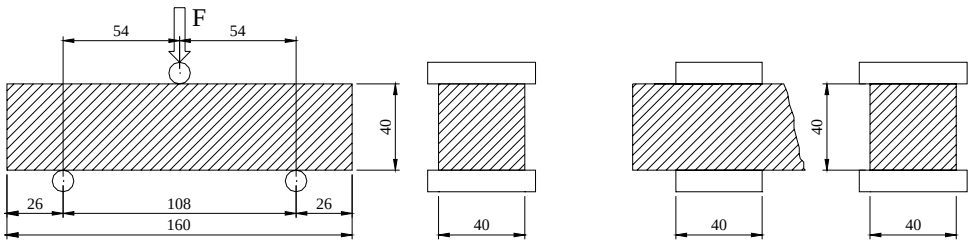

FIGURE 14.1: Test set-up for the prisms: a) flexural test, b) compressive test

The prisms were first broken in two halves with the flexural test (rate: 150 min./40 mm (position) at the W&B 200 kN). Then, compressive tests were conducted on each prism half (rate: 1 mm/min. (position), Schenck 1000 kN). The upper side of the prisms during casting was on the side during testing.

14.2 Results

Three prisms were cast from each batch. The tests on the prisms were conducted at 28 days. They were statistically treated to evaluate the reproducibility of the UHPFRC. The box plots show that there were nearly no outliers in the data (Figure 14.2). Compressive strength f_{Uc} decreased form series to series. The flexural strength f_{Ufl} of the first two series (A01_19, A20_58) was nearly identical, but it was lower for the last series (A60_71).

A normal law was applied for each series and for all the prisms (Figure 14.3, Table 14.1). Table 14.1 shows the number of specimens considered for each series, the mean, the standard deviation and the coefficient of determination (R^2) for the fit of the normal distribution. As the coefficient of determination was always higher than 0.94, the normal distribution can describe the test data.

The decrease in strength of series A60_71 may be explained with the aging of the constituents of the UHPFRC. The cement and super plasticizer were purchased before the first and the second series. It was possible that during the storage in the structural laboratory hall, chemical or physical

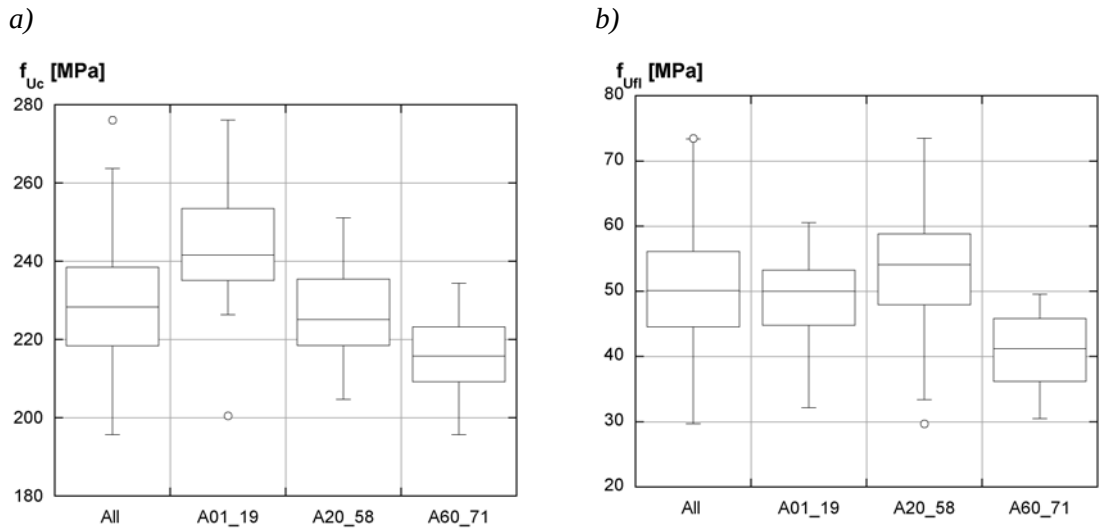

FIGURE 14.2: Box plot of the a) compressive strength and b) the flexural strength

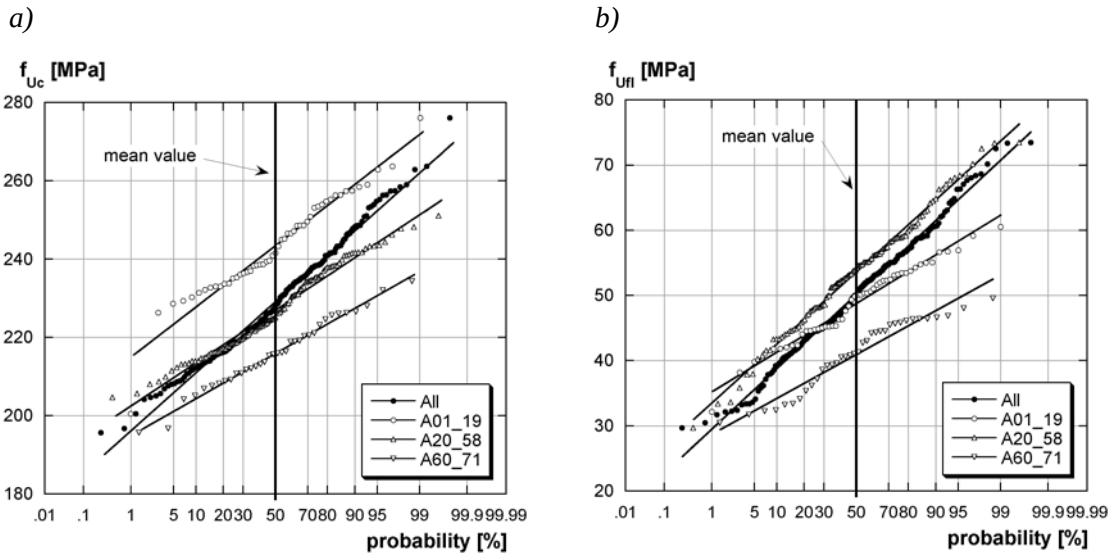

FIGURE 14.3: Normal distribution of the a) compressive strength and b) the flexural strength

TABLE 14.1: Results of the tests on the prisms

name	casting period	no. prisms [-]	flexural strength f_{Ufl} mean value [MPa]	flexural strength f_{Ufl} standard deviation [MPa]	flexural strength f_{Ufl} R^2	compressive strength f_{Uc} mean value [MPa]	compressive strength f_{Uc} standard deviation [MPa]	compressive strength f_{Uc} R^2
A01_19	07/02	51	48.8	5.9	0.97	240	10	0.95
A20_58	11/02	117	53.6	8.6	0.99	227	11	0.98
A60_71	02/03	36	40.9	5.4	0.94	216	9	0.99
	Total	204	50.2	8.8	0.99	229	14	0.99

processes led to an alteration of the material. The fresh concrete temperature of the second series (A20_58) was higher than the one of the third series (A60_71) for the same average ambient temperature (6). This may also be a sign of a reduced binder reactivity due to an alteration of the constituents during mixing of the third series.

15 Adherence tests

15.1 Uniaxial tensile tests

The tensile resistance in the interface zone was tested with uniaxial tensile tests on cylindrical specimens with a diameter of 5.45 cm (Figure 15.1a). The average height of the concrete was 15 cm and the one of the UHPFRC 10 cm. The specimens were drilled out of a composite block of 50*50 cm^2 consisting of concrete and $CEMTEC_{multiscale}$®. The surface of the concrete was prepared by hydrodemolition. The block was prepared exactly the same way as the beams of the structural testing. The tests were conducted on an universal testing machine (W&B, 200 kN) at a rate of 0.12 mm/min. (350 min. for 40 mm).

a) *b)*

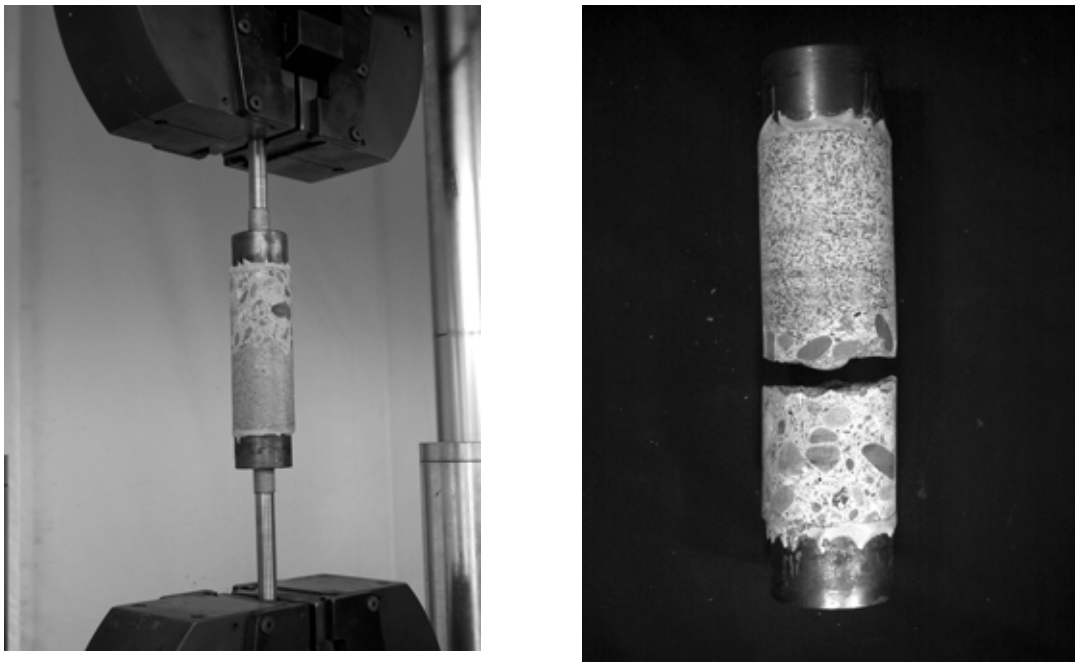

FIGURE 15.1: a) Test setup of the adherence tests (ø 5.45 cm), b) typical fracture (AR15)

The adherence strengths of all specimens are shown in Table 15.1. All specimens failed near the contact surface in the concrete (0 to 2 cm from the interface). Hydrodemolition seems to induce damage into the concrete. This damaged zone had a thickness of about 2 cm. The failure surface of the specimens was often at the interfacial transition zone (ITZ), i.e. the zone between aggregate and cement paste. Low failure values were often due to a high percentage of ITZ-failure. The high variability of the results may be due to the small diameter of the specimens when compared to the aggregate size. All the specimens failed mainly in the concrete and to a minor part (≈ 5 to 10%) at the contact surface (Figure 15.1b). The mean tensile strength at the interface was 2.49 MPa ± 0.39 MPa, approximately 75% of the concrete tensile strength. The apparent tensile strength of the concrete during the adherence tests was lower than the one measured with the uniaxial tensile tests on plain concrete specimens (Chapter 10.3.1). No dependency on the age of the concrete was observed.

The failure in the concrete may also be due to bending effects during cracking as a consequence of the different stiffnesses of the materials. As the test set-up was flexible (articulations at the ends), the crack started at one side of the specimen and so, a bending moment was introduced to the specimen.

TABLE 15.1: Interface tensile strength of the adherence tests in uniaxial tension

age B01 [days]	$f_{ct,I}$ [MPa]									$f_{ctm,I}$ [MPa]	specimen
182	2.58	1.50	2.48	2.24	2.82	2.76	1.81	2.34	2.34	2.32 ± 0.43	∅ 5.45 cm
197	2.74	2.28	2.37	2.82	2.01	2.61	3.04	2.83		2.59 ± 0.34	∅ 5.45 cm
459	2.10	2.17	2.72	2.13						2.28 ± 0.30	∅ 8.60 cm
533	2.69	3.12	2.90	2.75	2.62					2.82 ± 0.20	∅ 8.60 cm

15.2 Wedge splitting tests

The behaviour of the interface was also investigated with the Wedge Splitting Tests (WST). Therefore, specimens were sawn out of a block (50*50 cm^2) consisting of concrete and CEMTEC-$_{multiscale}$® (Figure 15.2a). The tests were conducted on an universal testing machine with a maximum force of 200 kN (Walter & Bai). They were deformation controlled by the mean value of the upper LVDTs at a rate of 0.24 mm/min. (Figure 15.2b). The crack mouth opening displacement (CMOD) was measured with the lower LVDTs.

a) *b)*

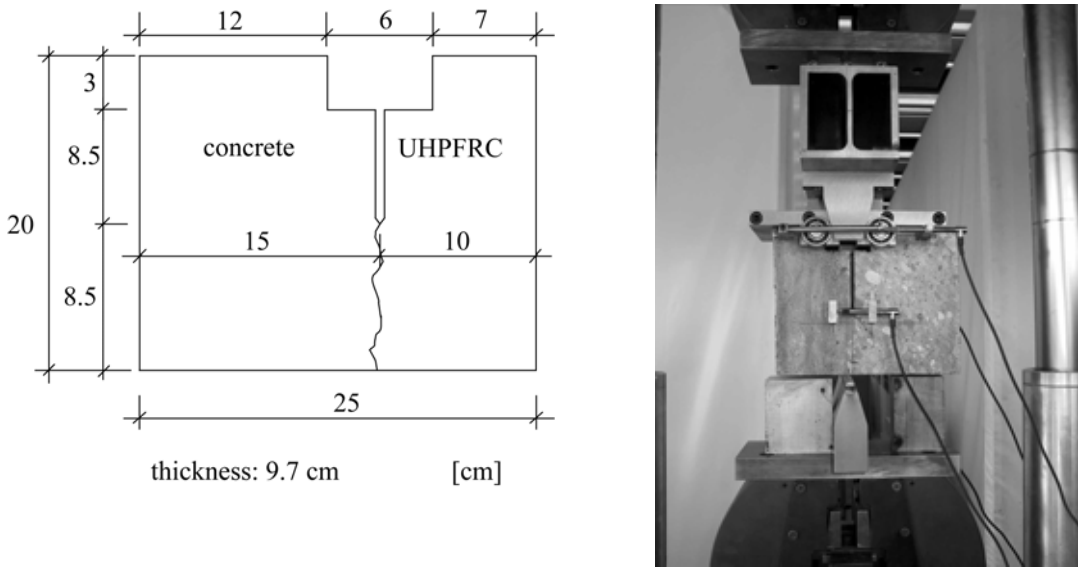

FIGURE 15.2: a) Dimensions, b) test set-up of the WST specimens

Figure 15.3 shows the horizontal force in relation of the CMOD. Different maximum forces were measured during the tests. The variability may be explained with the crack path. As the interface had a high roughness, the notch can not be sawn exactly at the interface. Therefore, the end of the notch was sometimes totally in the concrete, sometimes it passed partially in the UHPFRC. As the tensile strength and fracture energy of the UHPFRC were much higher than for the concrete, the maximum force was influenced even by very small parts of UHPFRC at the crack path. The crack deviates always into the concrete, where it passes mainly through the ITZ. However, it goes also through some aggregates. The cracks did not follow the contact zone between CEMTEC$_{multiscale}$® and concrete indicating good adherence at the contact zone.

The strong influence of the UHPFRC on the maximum force of the WST tests complicates considerably the interpretation of the WST tests. The high roughness of the interface makes it impossible to deduce an adherence strength at the interface zone. The WST test is therefore not adapted to determine the interface strength of hydrojetted surfaces with their high rugosity when the two cementitious materials have significantly different mechanical properties.

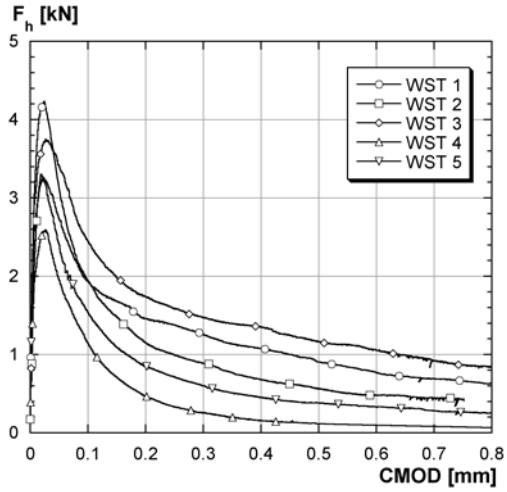

FIGURE 15.3: Force- CMOD diagram of the WST tests

16 Summary of the material characterization

The material tests were conducted on a normal strength concrete and on a type of CEMTEC$_{multi-scale}$®. The reproducibility of the UHPFRC was good, i.e. the standard deviations of the flexural and compressive strengths of all batches was approximately 15%. The properties of the two materials are summarized in Table 16.1.

The advantages of the UHPFRC when compared to the concrete were:

- the casting technology, (the UHPFRC was self-compacting, the concrete had to be vibrated)
- the high compressive strength,
- the significantly improved tensile properties, (the tensile strength was 3 times higher than of concrete; the fracture energy 150 times higher; furthermore, hardening behaviour until a deformation of 2.5 ‰ was observed on the notched specimens.),
- the low permeability. (The low permeability was measured with the Torrent test on the beams (Section 19.4.5).) It was indirectly observed by the deformations of the free shrinkage specimens, where an important difference between the sealed and the drying specimens was observed for the concrete, while it was small for the UHPFRC.)

However, the UHPFRC had also disadvantageous properties when compared to the concrete:

- The heat of hydration was higher, however, the consequences for early age deformations are small, since UHPFRC is foreseen for an application in slender elements.
- The strong self-desiccation at early age caused higher autogenous shrinkage in the UHPFRC, but the overall shrinkage of UHPFRC is comparable and even smaller than for normal strength concretes.

It can be concluded that the UHPFRC had significantly improved properties when compared to the normal strength concrete. However, the contraction due to internal thermal and hygral changes (mainly at early age) was higher than for normal strength concrete. The higher deformations may lead to higher stresses in case of restraint or gradients which may be balanced by the high strengths and the hardening behaviour in tension. Therefore, the interaction between stresses and strength must be evaluated to estimate if the advantageous properties of the UHPFRC can be exploited in structural elements or if damage is caused.

The tests of the adherence strength at the interface zone show that the contact surface between UHPFRC and concrete can be prepared such that no fracture occurred exactly at the contact surface. The fracture always occurred in the concrete at 0 to 3 cm from the interface. The adherence strength was 2.5 MPa, approximately 75% of the concrete tensile strength.

TABLE 16.1: Summary of the properties of the concrete and the UHPFRC

Property		**UHPFRC**	**concrete**
Fresh material (Section 6)		self-compacting	vibrated
Heat of hydration (Section 7)	$T_{adiab,final}$	117 °C	75 °C
Humidity (Section 8)		90% after 5 days	- (not measured)
Compressive properties (28 days) (Section 9)	f_{cc}	168 MPa (cyl. ∅11 cm, 28 days)	46 MPa (cyl. ∅11 cm, 28 days)
	E_{cc}	48.1 GPa (cyl. ∅11 cm, 28 days)	37.8 GPa (cyl. ∅11 cm, 28 days)
Tensile properties (28 days) (Section 10)	f_{ct}	10.9 MPa (notched plates, 28 days)	3.4 MPa (cyl. ∅11 cm, 28 days)
	G_F	21'000 J/m^2, hardening (notched plates, 28 days)	120 J/m^2 (28 days)
	strain-hardening	2.8‰ (notched plates, 28 days)	no strain-hardening
Shrinkage[a] (Section 11)	drying	400 μm/m (365 days)	700 μm/m (365 days)
	autogenous	350 μm/m (365 days)	100 μm/m (365 days)
Shrinkage at early age (Section 12)	autogenous	325 μm/m (7 days)	- (not measured)
Restrained shrinkage at early age (Section 12)	autogenous	σ = 4.2 MPa (after 7 days), relaxation of approximately 40%	- (not measured)
Compression creep[b] (Section 13)	drying	50 μm/m/MPa (after 90 days), stabilization after 90 days	55 μm/m/MPa (after 90 days), no stabilization after 365 days
	sealed		
Evolution of the material properties		The material properties became virtually constant after 90 days.	The material properties still evolve after 365 days.

a. The measurements started one day after setting.

b. The compression creep tests started at 137 days for the concrete and at 6 days for the UHPFRC.

Part IV
Structural Testing on Composite Beams

17 General

The aim of the structural testing was to investigate the structural behaviour of composite structural elements made of UHPFRC and reinforced concrete. The reinforced concrete substrate simulates an existing structural element, while the UHPFRC was added as new material. The differences in the material properties of UHPFRC and concrete may lead to deformations and cracking in the composite element. Therefore, it is essential to prove that the combination "UHPFRC-concrete" is appropriate, i.e. there are no deformational incompatibilities and the advantageous properties of UHPFRC are exploited.

Different configurations for slender composite beams were tested: Thin UHPFRC layers were designed to protect the existing concrete structure, while thicker UHPFRC layers with and without additional reinforcement were designed to increase the ultimate resistance of the structure and to protect the existing structure. So, the influence of the thickness of the UHPFRC layer and the degree of reinforcement in the UHPFRC layer were investigated in the experimental campaign. The degree of restraint was varied by the different thicknesses of the UHPFRC layer and by two different static systems: a statically determinate and a statically indeterminate system. Some of the statically determinate beams were loaded 4 weeks after having cast the UHPFRC layer to investigate flexural creep in the beams.

The structural behaviour of composite structural elements was investigated by means of early age and long term tests and fracture tests.

Early age and long term tests. The UHPFRC deforms as a consequence of the hydration reaction and associated hygral and thermal variations. These deformations occur mainly at early age, but continue also in the long term. When UHPFRC is used in combination with concrete to form composite elements, the UHPFRC causes deformations in the whole composite element. In case of restraint or gradients, stresses build up in the structural element and may lead to cracking. The early age and long-term tests were conducted to describe quantitatively and qualitatively deformations and cracking of the beams as well as to estimate th stress level.

Fracture tests. Fracture tests were carried out on the structural elements after the long term tests. The fracture tests were conducted to answer the following questions:

- What was the ultimate resistance of the beams?
- How did the stiffness of the beams develop during the fracture test?
- Is the fracture of the beams announced by large deformations?
- Have cracks formed during the long term tests? Do these cracks influence stiffness and ultimate resistance during the fracture tests?
- How did the cracks propagate under pure bending? Is there debonding at the interface did the beams behave in a monolithic way until fracture? were there many small cracks or some large cracks? How many localized macrocracks occur? How did the crack openings develop?

18 Experimental program

18.1 Test specimens

Old layer. The structural tests were conducted on 15 "UHPFRC-concrete" beams with a length of 540 cm. The concrete substrate had a section of b*h = 30*17 cm (Figure 18.1a) with a thickness of the cover concrete of 2 cm. The width of the section was chosen with regard to the UHPFRC layer: Since the fibre length of the UHPFRC was 1 cm, 30 cm were assumed to lead to a representative fibre distribution in the element. The concrete cover of 2 cm was removed from the upper surface by hydrojetting in order to prepare the contact surface between concrete and UHPFRC. The thickness

of the concrete substrate was fixed to 15 cm after hydrojetting. Standard bridge decks in Switzerland have a thickness of approximately 22 cm [Broquet99]. Considering hydrojetting of 5 to 7 cm on existing bridge decks, a thickness of the concrete substrate of 15 to 17 cm would remain.

The reinforcement of the concrete substrate consists of steel bars with f_{sy} = 500 MPa (S500) (Figure 18.1a). The stress-strain curve of the rebars can be found in [Guandalini04]. The lower reinforcement ($A_{s,low}$) was chosen to ensure that the tensile stresses due to the positive moments were transferred without fracture of the beams. The upper reinforcement had a reinforcement ratio of ρ =0.83%. Stirrups were placed in beams. They had smaller distances near the supports of the statically indeterminate beams than in the statically determinate beams to take up the force introduced into the supports. The reinforcement drawings can be consulted in Appendix C.

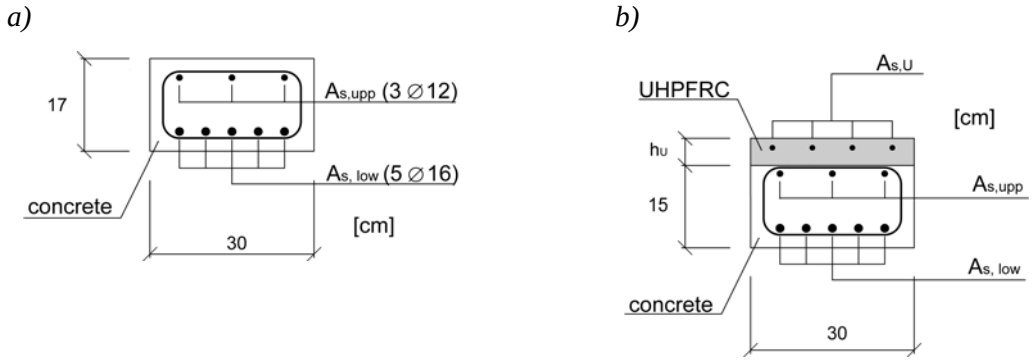

FIGURE 18.1: a) Section of the concrete substrate, b) section of the composite element

18.2 Test parameters

- *Thicknesses of the UHPFRC layer* of 3, 5 and 10 cm were chosen. So, the final section of the beam was 18, 20 and 25 cm for thicknesses of the UHPFRC layer of h_U = 3, 5 and 10 cm respectively (Figure 18.1b).
- Additional *reinforcement* was placed in half of the beams with h_U = 5 and 10 cm with a ratio of $\rho_{s,U}$ = =$A_{s,U}/(b \cdot h_U)$ = 2%.
- The *degree of restraint* was essential for the stress level in the structure during the early age and long term tests. The higher the degree of restraint, the higher were the stresses in the structure. Usual degree of restraints are 0.40 to 0.60 [Bernard00]. High degrees of restraint are obtained by using a statically indeterminate systems. A choice had to be made between the degree of restraint and the deformations of the structure. Two different static systems were used in this experimental campaign: statically determinate beams and statically indeterminate beams with three spans. The 10 statically determinate beams and the 5 statically indeterminate beams differed only in the static system, but not in the general beam configuration. The ratio of longitudinal reinforcement was equal for all beams (Figure 18.1).
- The *flexural creep* behaviour was investigated on half of the statically determinate beams that were loaded 28 days after the casting of the UHPFRC layer.

  An overview over the tested beams and their parameters is given in Table 18.1.

18.3 Test program

The beams were tested in three series, since there was not enough space in the structural hall for a simultaneous testing of all the beams. The detailed program can be found in Appendix B.

Early age and *long term tests* as well as *fracture tests* were conducted. During the long term tests, deformations of the beams and their temperature evolution were measured. The measurements started before the casting of the UHPFRC layer and last until an age of the UHPFRC layer of 80 days. The beams subjected to flexural creep were loaded after 28 days and remained loaded for 7 weeks. Afterwards, the creep recovery was measured for at least 2 days. After the long term tests,

TABLE 18.1: Parameters of the beams

Name	Static system	h_U	Reinf.	Loading	Moment due to loading	Degree of restraint at 28 days
I3	determinate	30 mm	-	-	-	0.51
I3L	determinate	30 mm	-	1015 kg	9.1 kNm	0.51
H3	indeterminate	30 mm	-	-	-	0.76
I5	determinate	50 mm	-	-	-	0.44
I5L	determinate	50 mm	-	750 kg	6.8 kNm	0.44
I5R	determinate	50 mm	4 ∅ 10	-	-	0.44
I5RL	determinate	50 mm	4 ∅ 10	750 kg	6.8 kNm	0.44
H5	indeterminate	50 mm	-	-	-	0.67
H5R	indeterminate	50 mm	4 ∅ 10	-	-	0.67
I10	determinate	100 mm	-	-	-	0.44
I10L	determinate	100 mm	-	1605 kg	14.4 kNm	0.44
I10R	determinate	100 mm	4 ∅ 14	-	-	0.44
I10RL	determinate	100 mm	4 ∅ 14	1605 kg	14.4 kNm	0.44
H10	indeterminate	100 mm	-	-	-	0.53
H10R	indeterminate	100 mm	4 ∅ 14	-	-	0.53

the fracture behaviour was investigated with four-point-bending tests, inducing a constant negative bending moment in the central span and tensile stresses in the UHPFRC layer.

18.4 Preparation of the concrete substrate

18.4.1 Casting

The concrete substrate of the beams was cast at the prefabrication company Element AG in Tafers (Fr) the 7th February 2002 in the afternoon at an average ambient temperature of 6 °C. The formwork consisted of laminated timber beams (thickness 10 cm) that were fixed on a metallic vibrating table (Figure 18.2a). The formwork was stiff and had a high accuracy. The 5 statically indeterminate beams were cast in the hall, while the 10 statically determinate beams were cast outside under a shelter. The temperature in the hall was higher than outside, however, the doors of the hall were open during the day. The temperature evolution of the concrete substrate and the ambient temperature were measured during the first four days after the casting of the concrete substrate.

The vertically and horizontally fixed supports of the statically indeterminate beams were incorporated into the concrete substrate. Hollow tubes were placed in the concrete section for the restraint of vertical displacements. Steel plates with dowels were placed at the supports for the horizontal restraint (Figure 18.2b, see also reinforcement drawings in Appendix C). The steel plates were put on the vibrating table without any fixation and moved during the casting between 0 and 8 mm. These eccentricities were compensated during testing.

Due to the low ambient temperature, the curing of the fresh concrete was extremely important: The beams were covered with a plastic sheet and an thermally isolating cover. The statically indeterminate beams were heated with warm air that was introduced with two pipes between the plastic sheet and the isolating cover. The heating of the beams was turned on one hour after casting and turned off after 10 hours, the next morning at 7:00 am. The heating was turned on a second time: for the statically determinate beams on friday at 4:00 pm. to 6:00 pm., and for the statically determinate beams from 9:00 am. to 4 pm. Covers and formwork were removed after 85 hours (after 3 1/2 days, on Monday, 11.2.2002) and the beams were stored under a shelter at Element AG until their transport to the EPFL on Tuesday afternoon (12.2.2002).

a) *b)*

FIGURE 18.2: a) Formwork of the statically determinate beams (before casting), b) vertically and horizontally fixed support before casting

18.4.2 Storage

The concrete substrata were stored in the structural hall at an average temperature of 22 °C and a RH of 47% (Figure 18.3). An epoxy resin (SIKA Sikafloor-156) was applied twice (Thursday, 14.2.2002 and Friday, 15.2.2002) on the sides of the beams in order to obtain drying only in vertical direction.

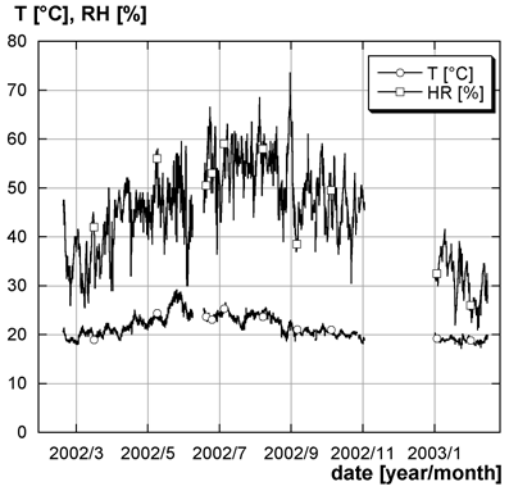

FIGURE 18.3: Temperature and RH in the structural hall

18.4.3 Preparation of the interface

The concrete cover of 2 cm was removed by hydrojetting from the upper side of the beam. The hydrojetting was performed by the company Hubert Etter et fils SA outside the structural hall may, 14th and 15th 2002 (Figure 18.4). A robot with a turning jet at high pressure (2500 bar, 35 l/min. of water) was used. The pressure probably provoked bending cracks at the bottom of the beams. The cracks formed always at the position of a stirrup. The last 10 cm of one end of the beams were not hydrojetted to protect the cables of the sensors in the beams (see Section 18.6.2). Afterwards, the beams were stored again in the structural hall. As the epoxide resin layer was partially removed during hydrojetting, two new layers were applied (16./17.5.2002).

FIGURE 18.4: Hydrojetting of the beams

18.5 Casting of the UHPFRC layer

The UHPFRC layer was cast in the structural hall of the EPFL. Therefore, a concrete mixer (EIRICH R08 W, 75 l) with a maximum capacity for 47 l of UHPFRC was used. The concrete substrates were installed in the climatic tents (T = 20 °C, RH = 40%) at least 3 days before casting, and the supports of the statically indeterminate beams were fixed. The formwork was fixed with clamps on the concrete substrate. The measuring systems were installed and started to record one day before casting. So, deformations and temperatures were measured during casting. The tents had to be removed during casting, since the skip was lifted with the overhead crane. The upper side of the concrete beams, the future interface, was moistened two times before casting, approximately one hour before casting and just before casting. So, the difference of RH between the UHPFRC and the concrete substrate was decreased and the concrete substrate did not pump too much water from the UHPFRC layer.

a) *b)*

FIGURE 18.5: a) Formwork of the statically indeterminate beams, b) casting of the UHPFRC

The first test series consisted of six beams of the test series with h_U = 5 cm. The quantity of UHPFRC was too big for one batch, so two batches were cast in succession. The first batch was kept in the skip and covered with a plastic foil. The second batch was poured in the skip and was slightly mixed with the first one with a steel bar. Then, a beam was cast in one go. The second test series, six beams with h_U = 10 cm, was cast with a central joint. Two batches were always mixed together. As four batches were needed for each beam, a joint was situated in the middle of the beam. The casting procedure can be seen in Figures 18.6 and 18.7. The casting of each part started in the middle of the beam to avoid having the end of the batch, where fibre concentrations sometimes occurred, in the

a) *b)*

FIGURE 18.6: Beams with h_U = 10 cm: a) joint, b) casting of the joint

centre of the beam. The third series consisted of three beams with h_U = 3 cm. The casting procedure was equal to the one of the first series (h_U = 5 cm).

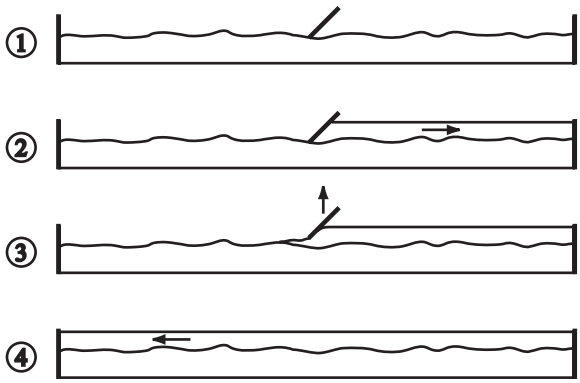

FIGURE 18.7: Casting procedure of the beams with h_U = 10 cm

The UHPFRC always showed good workability and no signs of segregation. Fibre accumulations occurred at the end of the batches. As the end of the batch was always situated at the end of the beams, the mechanical properties in the beams were not changed due to these accumulations.

The climatic tents were installed over the beams immediately after casting, and the air conditioning was turned on approximately one hour after casting. The formwork of the UHPFRC layer was removed after approximately 5 days (cf. Appendix B). Afterwards, two layers of the epoxide resin were applied to the sides of the beams to hinder moisture exchange with the environment.

18.6 Long term tests

18.6.1 Test set-up

The long term tests were also designed to investigate the early age of the UHPFRC layer of the composite beams. Therefore, beams and measuring systems were installed before the casting of the UHPFRC layer.

The statically determinate beams had one fixed and one pin support with a central span of 240 cm and cantilevers of 150 cm (Figure 18.8, Figures 18.9a). After 28 days, the climatic tent was removed to load half of the beams with boxes filled with lead to investigate the creep behaviour of the beams. The boxes were put on neoprene sheets at a distance of 30 and 90 cm from the ends of the beams. First, the box near the fixed support was put on the beams with the overhead crane. Under

the box, the beam was supported with a hydraulic lift to avoid a reversal of the beam during the asymmetric loading. Then, the second box was put on the beam and the hydraulic lift was removed. Afterwards, the climatic tent was put again over the beams. The loading of the beams took one hour. The lead boxes were removed after seven weeks with the inverse procedure of the loading. The creep recovery was measured for two days for the first series and five days for series 2 and 3. The measurements were stopped after approximately 12 weeks, and the beams were prepared for the fracture tests.

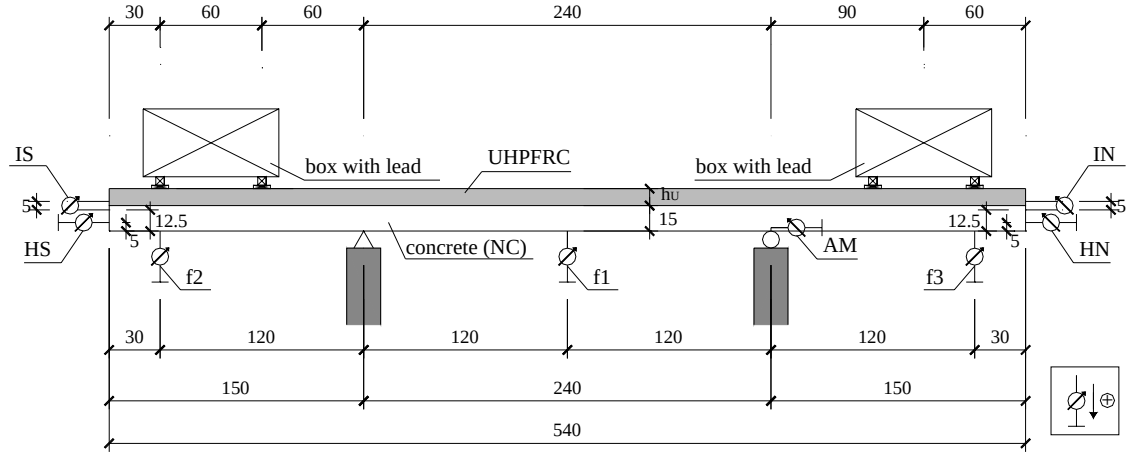

FIGURE 18.8: Test set-up of the statically determinate beams (in [cm])

a) *b)*

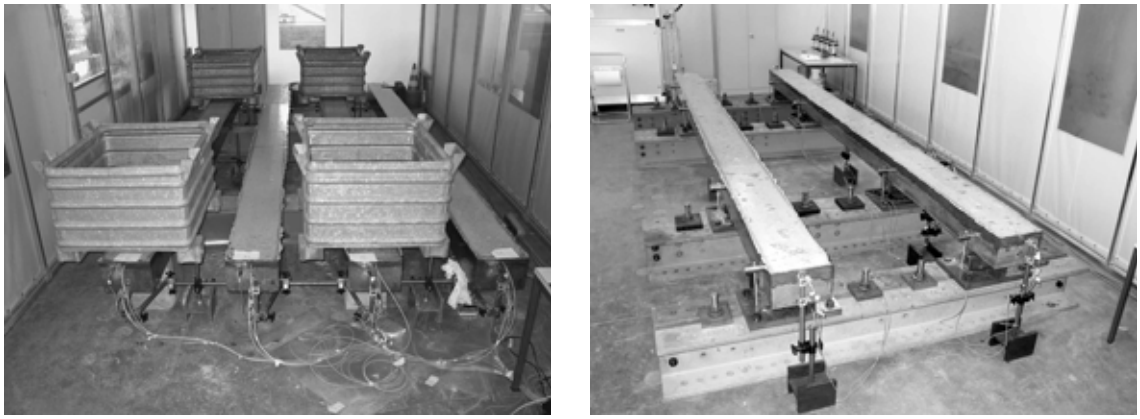

FIGURE 18.9: a) Statically determinate beams with load, b) statically indeterminate beams

The statically indeterminate beams had four supports (Figures 18.9b and 18.10). The two central supports were at the same position as the supports of the statically determinate beams (Figure 18.11a). These supports were supposed to restrain vertical and horizontal deformations. The vertical displacements were hindered with prestressed rods, the horizontal displacements with steel plates prestressed to the base steel profiles that were also anchored by prestressed bars in the floor of the structural hall. The restraint in vertical direction worked very well, however, the restraint in the horizontal direction worked only partially, since the system was not sufficiently stiff. Two supports were placed at 30 cm from the ends of the beams (Figure 18.11b). These supports were only fixed in the vertical direction. Their horizontal displacements were only restrained by friction due to the pre-stress of the rods. The supports were fixed before the casting of the UHPFRC layer. The supports were loosened at the end of the tests and the recovery was measured for series 2 and 3 (h_U = 3 and 10 cm).

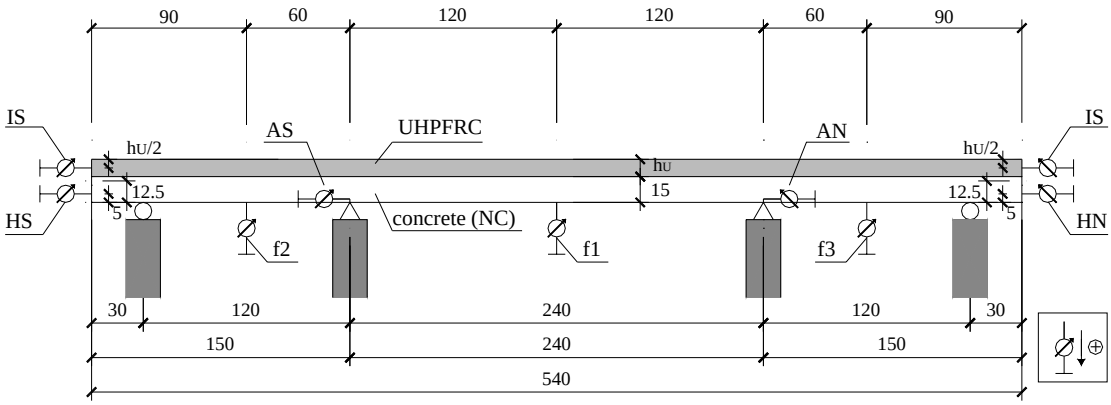

FIGURE 18.10: Test set-up of the statically indeterminate beams (in [cm])

a) *b)*

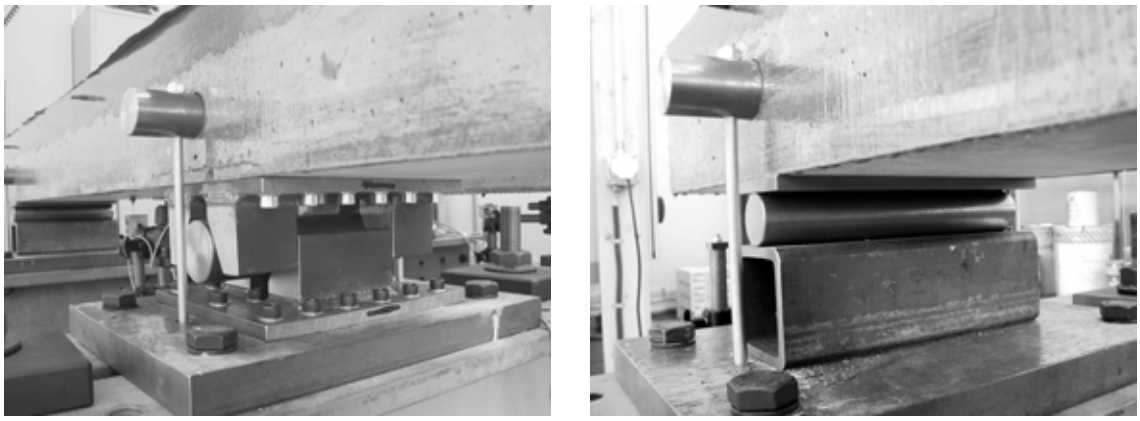

FIGURE 18.11: Supports of the statically indeterminate beams: a) central support, b) support at the ends

A temperature of 20 °C and a RH of 40% were the imposed climatic conditions in the tents (Appendix E). The stability of the temperature during testing was high with a variation of approximately ± 1 °C. The RH was more difficult to keep constant: The highest variations were observed for the first test series (h_U = 5 cm) during which a RH up to 60% was measured. The air conditioning was re-adjusted after the first series and the variations of the RH were smaller in the following: The RH of the tent with the statically indeterminate beams varied for the test series 2 and 3 (h_U = 10 cm and 3 cm) between 25 and 50% and in the tent with the statically determinate beams between 30 and 40%. The wall of the climatic tents was made of a membrane and variations of the climatic conditions in the structural hall were not always balanced by the air conditioning in the tents. Thus, the air condition had to be adjusted for the different seasons. The maintenance of a stable RH did not work as well as expected.

18.6.2 Measured data

The concrete substrate was equipped with two *thermocouples* (TC_{low}, TC_{upp}) and an *optical deformation sensor* (ODS L), the UHPFRC layer with a thermocouple (TC_U) and an optical deformation sensor (ODS U) (Figure 18.12 and Appendix B). The optical deformation sensors were of type SOFO and measured the mean deformation of the central span of the beam over a length of 200 cm. The thermocouples (type K) recorded the temperature in the beam at 50 cm from one end of the beams,

The measurements of the ODS were well adapted to follow the early age behaviour of the composite beams, since one sensor (ODS U) was placed in the UHPFRC and a second one (ODS L) in the concrete. The ODS can measure the deformations of cementitious materials from a degree of

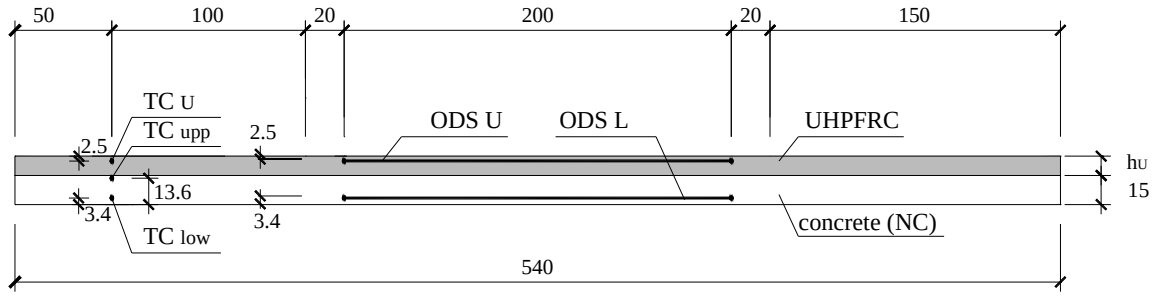

FIGURE 18.12: Instrumentation of the ODS and the thermocouples (in [cm])

hydration of 0.01 [Glisic00]. However, the measured deformations were not only dependent on the stiffness of the sensor, but also on parasite factors that can cause restraint, as for example, the fixation of the ODS on the rebars. The ODS U of the beams with h_U = 5 cm and 10 cm were fixed on transversal rebars. For the beams with reinforcement in the UHPFRC layer, the rebars were also fixed on these transversal rebars. The reinforcement stiffened the system and in these beams, the early age deformations of the UHPFRC were entirely measured with the ODS. The ODS U of the beams with h_U = 3 cm were fixed with threads. Here, the system was very elastic, so that the ODS measurements approached the deformations of the early age UHPFRC. Even if the deformations in the UHPFRC layer could not be followed exactly during the first day, the measurements indicated the order of magnitude of the deformations. Shortly after the beginning of the hardening of the UHPFRC, ODS U started to measure the exact deformations of the beams.

The *deflections* of the beam, the horizontal displacement of the supports, the horizontal displacements at the end of the beams and the relative displacement between the concrete and the UHPFRC layer at the ends of the beams were measured with LVDTs (Figures 18.8 and 18.10). Data acquisition of the LVDTs was performed with an UPM100 (HBM) for the statically determinate beams and an UPM60 (HBM) for the statically determinate beams. The ambient climatic conditions (T, RH) were recorded in the tents with HAENNI Opus 1.

The *air permeability* of the cover concrete was measured at the end of the long term tests on the beams with h_U = 5 cm with the Torrent test [Torrent92] (Figure 18.13a). The air permeability was measured on the upper side for the UHPFRC and on the lower side for the concrete. The electrical resistivity was measured with the Wenner test (Figure 18.13b) giving indirectly information about the RH in the concrete.

a) *b)*

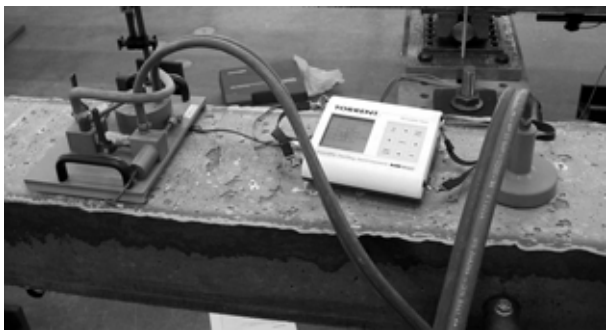

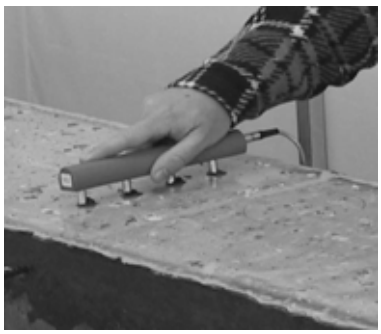

FIGURE 18.13: a) Set-up of the Torrent test, b) Wenner test

18.7 Fracture tests

18.7.1 Test set-up

After the long term tests, fracture tests were conducted on the beams at an age of the UHPFRC layer of approximately 90 days. The beams were tested with a set-up that respects the same geometry as the statically determinate beams during the long term tests (Figure 18.14). A constant negative bending moment was introduced into the central span of the beams, so that the UHPFRC layer was under tension.

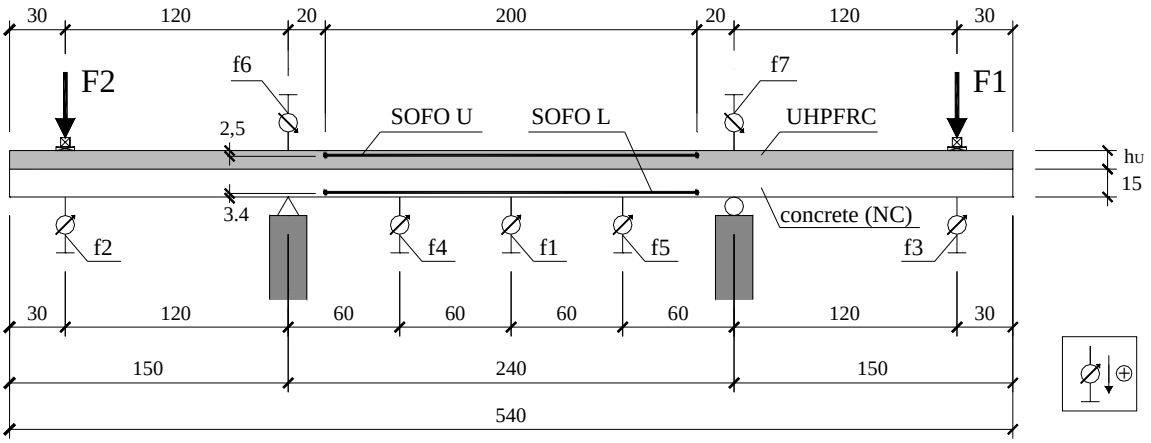

FIGURE 18.14: Test set-up of the fracture tests (in [cm])

Two hydraulic jacks (capacity: 200 kN) were placed at 30 cm from the ends of the beams, their lever arm was 1.20 m. The displacement of the jack at the force F2 was controlled by a LVDT measuring the displacement of the jack. Both jacks were connected to the same hydraulic pumps and had therefore the same pressure (and force). As only one jack was controlled directly with the LVDT, the displacements under the two jacks were different after the formation of localized macrocracks. The displacement rate of the jack was fixed to 0.45 hours/mm (26 min./cm).

The beams were loaded until the upper rebars in the concrete substrate ($A_{s,upp}$) yielded and then unloaded. Two beams (I10RL**,** I3) were loaded until fracture of the rebars ($A_{s,upp}$ and for the beam I10RL also $A_{s,U}$).

18.7.2 Measured data

LVDTs (f1 to f7) measured the deflections of the beams (Figure 18.14, see also Appendix B) and the ODS (ODS L, ODS U) the mean deformation of the beams in the central span over a length of 200 cm. Ω-gages were fixed on the upper side and on the sides of beams to follow the crack openings (drawings of the position of the Ω-gages in Appendix D). The force under the hydraulic jacks was recorded with force sensors (F1, F2).

19 Results

19.1 General behaviour of the composite beams

19.1.1 Statically determinate beams

Typical mid-span deflection curves (f1) of a loaded and a non-loaded statically determinate beams are shown in Figure 19.1. The time was zeroed at the moment when the deflection reached its minimum at early age.

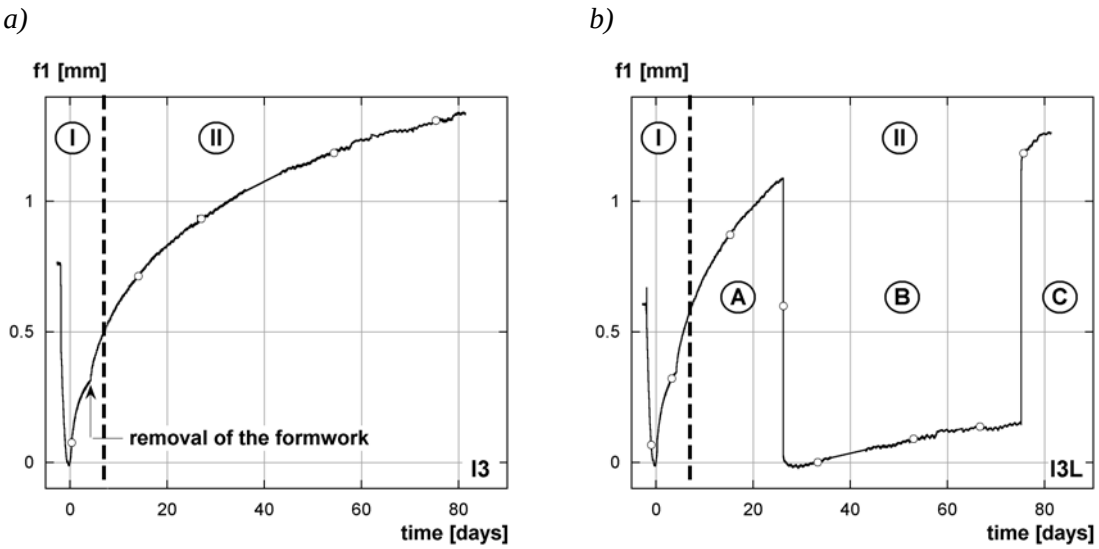

FIGURE 19.1: Typical time-deflection (f1) curves: a) of a non-loaded beam (I3), b) of a loaded beam (I3L)

Two main phases were distinguished:

I. *Early age* was a period of approximately 7 to 9 days governed by the hydration reaction. The hydration reaction was exothermal and water consuming. In the case of UHPFRC, the hydration reaction provoked heat release and self-desiccation leading to deformations in the UHPFRC and therefore in the whole beam. There was no clear transition between early age and long term, as the hydration reaction did not stop suddenly.

II. *Long term*: When the major part of the hydration reaction was finished, the evolution of the material properties and of the deformations slowed down.

After 28 days, some of the statically determinate beams were loaded with lead boxes to simulate the bending creep behaviour under a constant load with the UHPFRC being under tension (Figure 19.1b). Three phases were distinguished:

A. First, the beam remained unloaded.

B. The beam was loaded with lead boxes 28 days after the casting the UHPFRC layer.

C. The lead boxes were removed 49 days (7 weeks) later.

The deflection decreased during approximately the first 2 days after the casting of the UHPFRC layer (until time zero) and increased monotonously afterwards. The loading of the beams decreased the deflections considerably and reduced the slope of the curve. At unloading, the deflection increased again, and creep recovery occurred.

Figure 19.2a shows the deformations recorded with the ODS for beam I3. ODS U in the UHPFRC layer showed a strong contraction, ODS L in the concrete substrate slight expansion. The deformations measured with ODS U were more than 5 times higher than those of ODS L

Figure 19.2b shows the curvature κ_{ODS} of the beams I3 and I3L. The curvature was calculated with the deformations of the ODS (EQ. 19.1) and represents the mean curvature in the central span

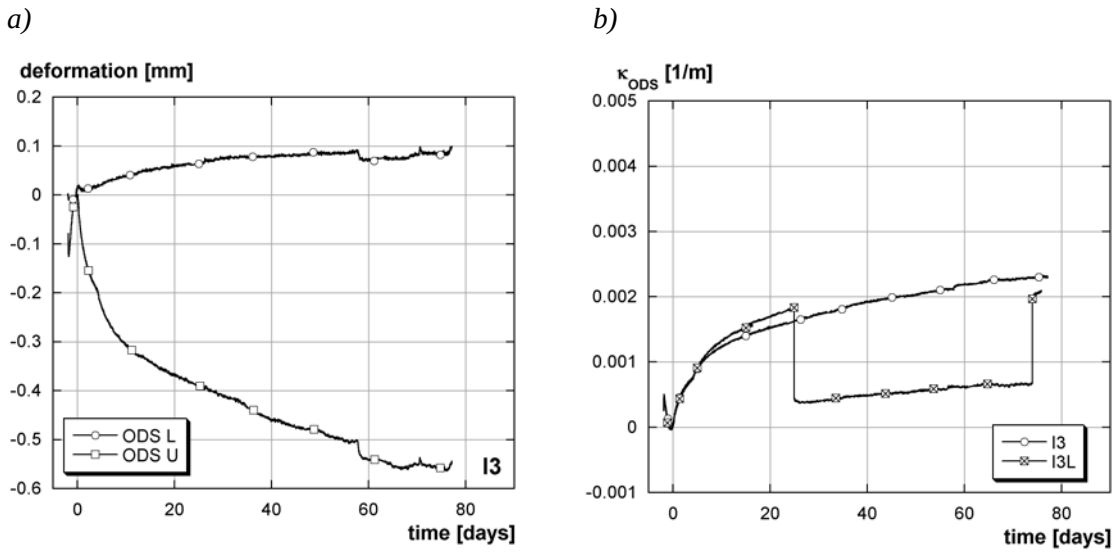

FIGURE 19.2: a) ODS deformations (I3), b) curvature (I3, I3L) of the statically determinate beams

of the beams (over a length of 200 cm). The curvature showed the same overall behaviour as the deflections.

$$\kappa_{ODS} = \frac{\text{ODS U} - \text{ODS L}}{d} \qquad \textit{(EQ 19.1)}$$

with κ_{ODS}: curvature [1/m], ODS U, ODS L [m/m] and d: distance between ODS U and ODS L [m].

19.1.2 Statically indeterminate beams

A typical time-deflection curve of the statically indeterminate beams is shown in Figure 19.3a. The long term testing of the statically indeterminate beams was divided into two periods (Figure 19.3a):

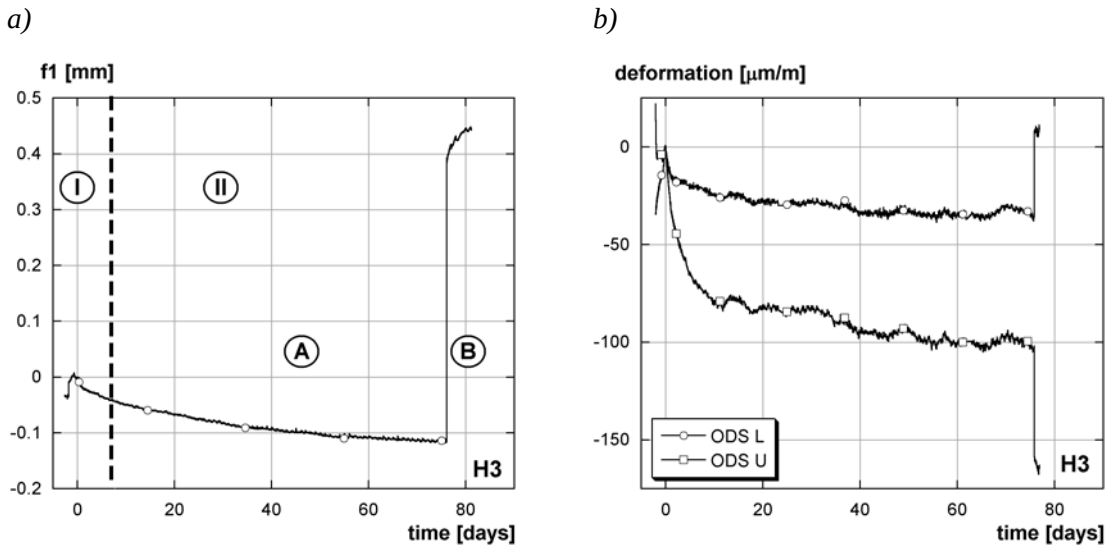

FIGURE 19.3: a) Typical time-f1 curve of a statically indeterminate beam (H3), b) deformations of the ODS (H3)

I. the *early age* during the first 7 to 9 days after casting the UHPFRC layer,

II. the *long term* with two periods:

A. The behaviour of the statically indeterminate beam until an age of the UHPFRC layer of approximately 80 days.

B. The recovery of the beam after the removal of the external supports and the horizontal fixation of one of the internal supports, i.e. the beam became statically determinate.

The deflection rate during the long term tests was small when compared to the recovery after the loosening of the supports indicating that the restraint in the beam due to the statically indeterminate system worked well.

The deformations measured with the ODS (ODS U, ODS L) had the same overall behaviour as the deflections (Figure 19.3b). The deformations of the ODS in the UHPFRC layer (ODS U) were higher than the deformations of the ODS in the concrete substrate (ODS L). Both ODS measured a decrease in deformation. Only when the beams became statically determinate, the deformations of ODS L increased and those of ODS U decreased.

19.2 Early age of the concrete substrate

The temperature evolution in the concrete substrate was measured during the first four days after casting (Figure 19.4). The statically indeterminate beams (H) were cast and stored in the hall at an ambient temperature between 10 and 18 °C. The temperature in the beams increased to 34 to 38 °C in the beams due to the heating periods. The statically determinate beams (I) were cast and stored under a shelter outside the hall at an ambient temperature between 5 and 10 °C. Here, the temperature in the beams increased to 24 to 28 °C. The concrete cooled down to the ambient temperature after approximately 2.5 days.The temperature evolution of the concrete substrate at early age can be consulted in Appendix F.

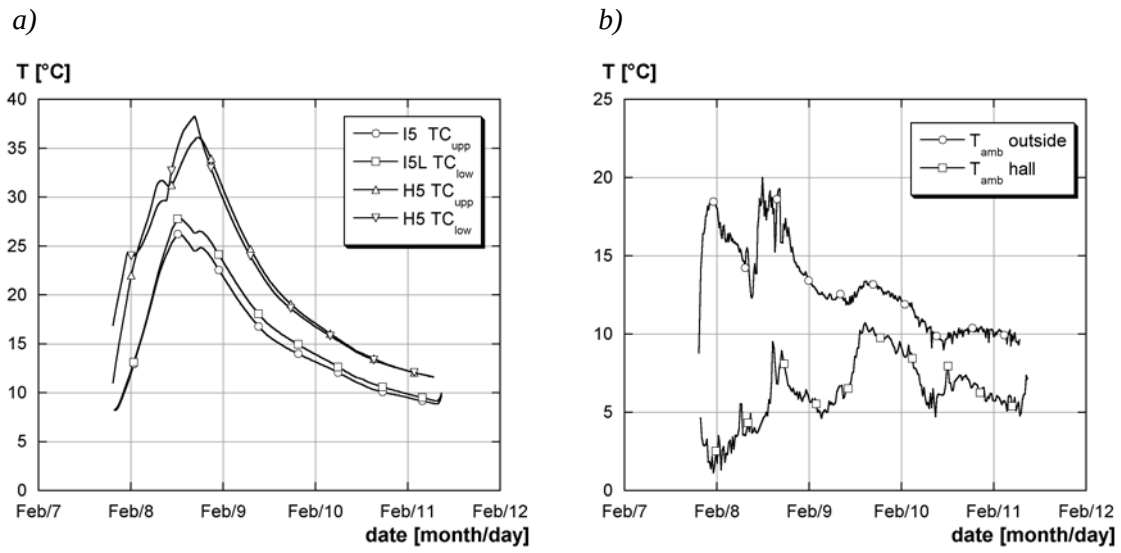

FIGURE 19.4: a) Temperature evolution at the early age of the concrete substrate of I5 and H5, b) ambient temperature during the early age of the concrete substrate

The beams were transported to the EPFL 5 days after casting, after having been stored at ambient temperatures of approximately 10°C for 2 days. The beams were kept in the structural hall at the EPFL at a temperature of approximately 20 °C (see Figure 18.3). The hydration reaction was thermally activated and reduced at low temperatures. The external heating of the beams accelerated the hydration reaction at the early age, but, the storage of the beams at the low temperatures slowed down the hydration reaction, until the beams were stored at 20 °C. As the period when the beams were subjected to low ambient temperatures was only 1.5 days and the first series of the long term testing started at an age of the concrete substrate of 5 months, the low temperatures during the two days should not have significantly influenced the evolution of the concrete properties.

19.3 Early age of the UHPFRC layer

19.3.1 Temperature evolution of the early age of the UHPFRC layer

The temperature evolution due to the hydration reaction of the UHPFRC was measured with thermocouples (Figure 19.5), placed at three depths in the section (see Figure 18.12). As the thermocouple in the UHPFRC layer (TC_U) was placed at approximately 2.5 cm from the upper surface, it did not necessarily record the maximum temperature in the cross-section for the beams. The results of the measurements are given in Appendix G

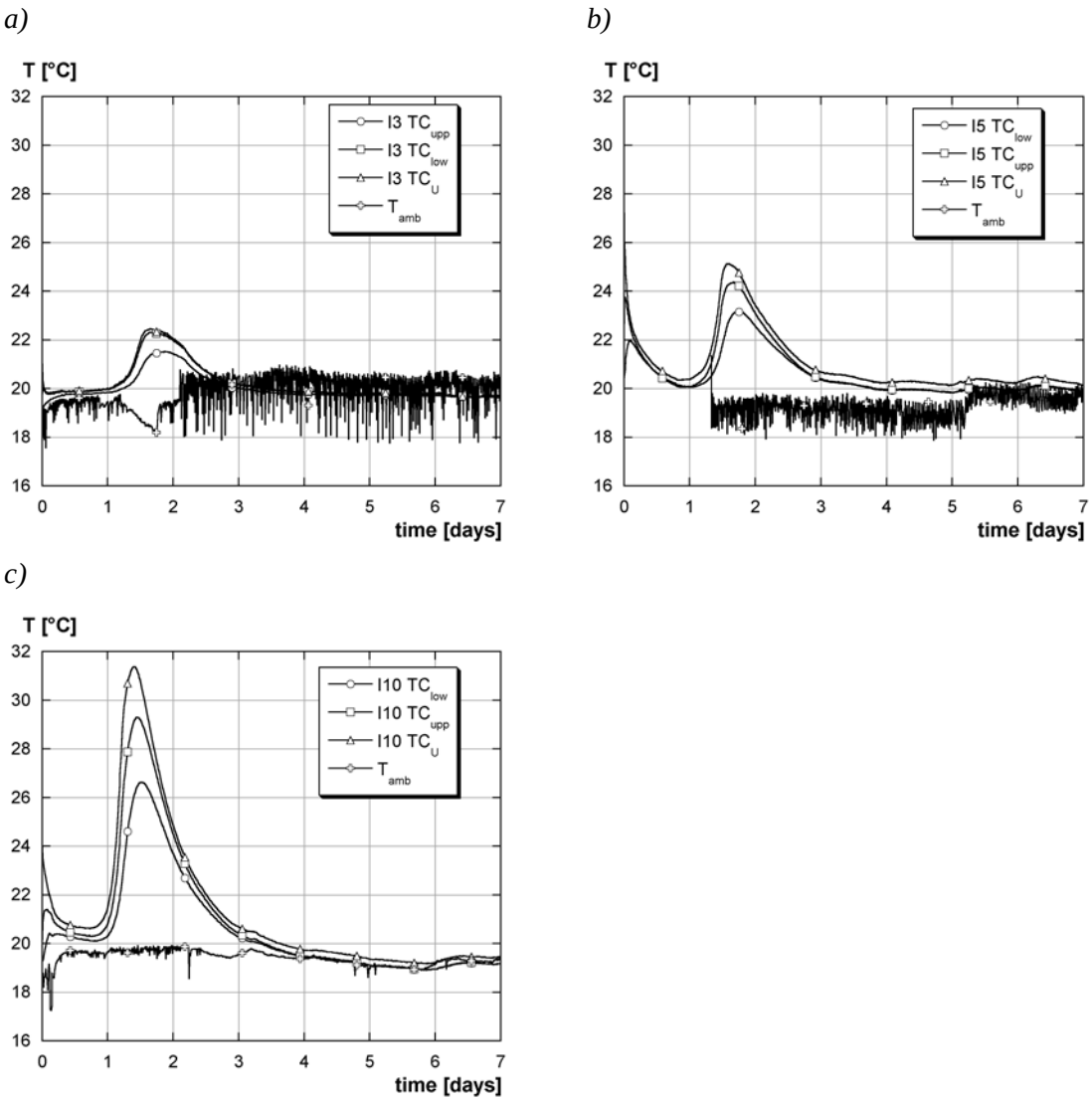

FIGURE 19.5: Temperature evolution at the early age of the UHPFRC layer: a) h_U = 3 cm, b) h_U = 5 cm, c) h_U = 10 cm

The *temperature* of the UHPFRC at casting was approximately 25 °C, depending on the test series and the ambient temperature during casting (see Section 6.2.2). Then the UHPFRC cooled down to the ambient temperature. After approximately one day, the temperature increased until it reached its maximum after 1.5 days. A temperature decrease followed down to the ambient temperature.

The *temperature gradient* in the composite beam led to deflections.The magnitude of the gradient was dependent on the thickness of the composite element and of the relation between the depths of the concrete substrate and the UHPFRC layer. The highest gradient was observed for h_U = 10 cm,

i.e. the elements with the biggest UHPFRC section and therefore the highest temperature rise during hydration.

19.3.2 Deformations at the early age of the composite beams

Statically determinate beams. At early age, the high rate of the hydration reaction led to temperature and RH changes inducing deformations in the composite elements. Figure 19.6a shows the *deflections* of beam I5 at early age. The time was zeroed when the beam was cast. The deflections of the beam increased instantly during casting when the dead weight of the UHPFRC was added to the beam. The increase of deformations continued until approximately one day after casting. Then, the deformations decreased. A small increase was observed with its peak after approximately 1.5 days. Afterwards, the deformations decreased continuously. The mid-span deflection f1 and the cantilever deflections f2 and f3 had the same appearance.

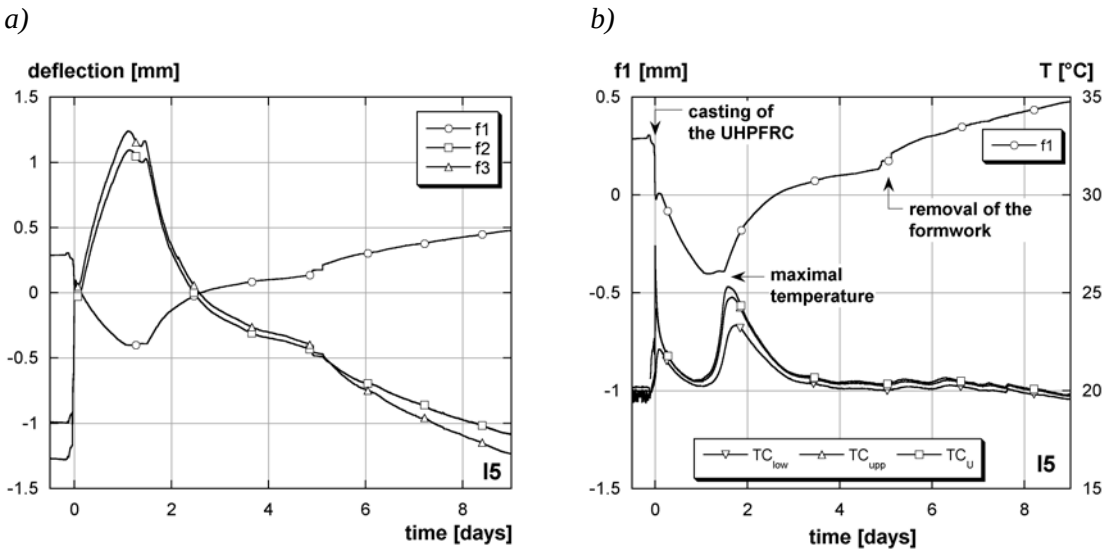

FIGURE 19.6: Early age deformations: a) deflections (I5), b) deflection f1-temperature (I5)

Part of the early age deflections was explained by the *temperature evolution* in the beams (see Section 19.3.1). Deflection f1 decreased during casting, i.e. the beam went up in the middle. Immediately after casting, a small increase of the deflection occurred having its maximum when TC_{low} was at its maximum. The cooling of the beam down to the ambient temperature during the first day induced a decrease in deflection. Deflection f1 increased only slightly during the temperature rise of the beam (at approximately 1 day). A maximum occurred just before the maximum temperature was reached. Finally, the deflection increased during the temperature decrease.

The *temperature differences* were shown in Figure 19.5 for the different thicknesses of the UHPFRC layer (see also Appendix G). The curves were zeroed when the UHPFRC layer was cast. The temperature of the UHPFRC increased during mixing. The dormant period was 1 day. During this period, the temperature of the UHPFRC cooled nearly down to the surrounding temperature (T_{amb}).

The *dormant period* was influenced by the thickness of the UHPFRC layer and was 1.1 days (26.5 hours) for the beams with h_U = 3 cm, 1 day (24 hours) for the beams with h_U = 5 cm and 0.85 days (20 hours) for the beams with h_U = 10 cm. The long dormant period was due to the high amount of superplasticizer in the UHPFRC and has to be considered during construction, since the material stays soft during more than 24 hours.

The *maximum temperature* (measured with TC_U) was 22.3 °C at 1.8 days (43.5 hours) for the beams with h_U = 3 cm, 25.1 °C at 1.6 days (38.5 hours) for the beams with h_U = 5 cm and 30.8 °C at 1.4 days (33.5 hours) for the beams with h_U = 10 cm. The temperature of the concrete substrate also increased during the hydration reaction of the UHPFRC layer. The maximum temperature (meas-

ured with TC_{low}) was 21.5 °C for the beams with h_U = 3 cm, 23 °C for the beams with h_U = 5 cm and 26.5 °C for the beams with h_U = 10 cm. The *temperature difference* between the thermocouples TC_{low} and TC_U was 0.8 °C for the beams with h_U = 3 cm, 2 °C for the beams with h_U = 5 cm and 5 °C for the beams with h_U = 10 cm. The maximum temperature occurred first in the UHPFRC layer, approximately 3 hours later at TC_{upp} and another 2 hours later at TC_{low}.

Figure 19.7a shows the deformations of the ODS for the beam I5 with the time zeroed at the casting of the UHPFRC. The deformations measured with ODS U were higher than those of ODS L. During the first 3 days, the deformations of ODS L were significantly influenced by the temperature changes in the beam. A period of contraction (during 0.2 days) was followed by an increase of deformation until approximately 1.7 days. After approximately 1 day, a small intermediate maximum occurred. After having reached the overall maximum after 1.7 days, the deformations decreased monotonously.

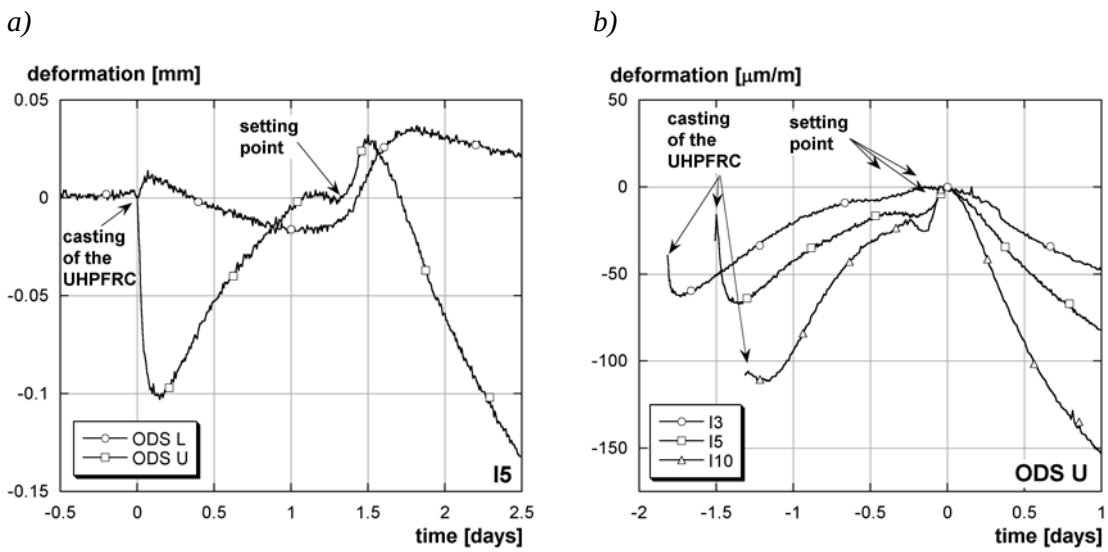

FIGURE 19.7: Early age deformations; a) ODS (I5), b) setting point of the beams

The evolution of ODS U for the different thicknesses of the UHPFRC layer h_U is shown in Figure 19.7b (time zeroed on the maximum value of ODS U during the heat of hydration). The smallest deformations were measured for the beams with h_U = 3 cm, the highest for the beams with h_U = 10 cm. The period between the minimum of the deformation shortly after casting and the maximum at time zero was the shortest for h_U = 10 cm and the longest for h_U = 3 cm. The deformations followed approximately the temperature evolution at early age (see Section 19.3.1).

The time span between maximum and minimum deformations was approximately 0.3 days (Figure 19.7b, about 1.5 days after casting cf. Figure 19.7a). It may be interpreted as the setting point of the UHPFRC. At the maximum, the autogenous shrinkage due to the water consumption during hydration became important and was superimposed to the thermal deformations. At this moment, the hydration reaction was strong and the material hardened.

Statically indeterminate beams. The early age deflections of the statically indeterminate beams are shown in Figure 19.8a. At casting, the dead weight of the UHPFRC layer was applied and the deflections increased instantly. The mid-span deflection f1 increased afterwards and rose to a maximum after approximately 1.5 days. The increase of deformation corresponds to a lowering of the mid-span deflection f1. The deflections f2 and f3 in the end spans were exactly opposite to the central span deflection f1, but showed the same overall behaviour as f1.

By comparing the deflection f1 with the temperature changes, the same overall behaviour was observed (Figure 19.8b). The only difference occurred at 1.2 days when the deflection described a small hook with a maximum and a minimum, while the temperature increased monotonously. This hook is attributed to the superposition of the thermal deformations and the autogenous shrinkage

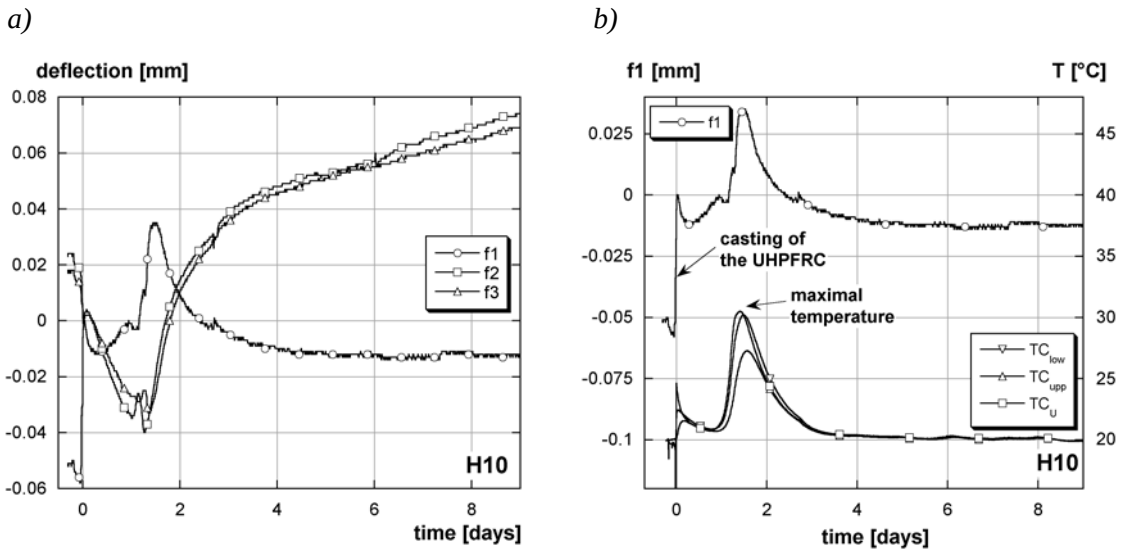

FIGURE 19.8: Early age deformations: a) deflections (H10), b) deflection f1-temperature (H5)

that became important shortly after the hydration reaction started off strongly after the dormant period.

The measurements of the ODS showed similar behaviour for both ODS (Figure 19.9a) at early age. The decrease in deformation of ODS U until approximately 0.2 days was high and did not reflect accurately the deformation of the UHPFRC layer, since the UHPFRC was still too soft. After approximately 0.2 days, the orders of magnitude of the deformations of ODS U and ODS L were similar, and both ODS measured precisely the deformations.

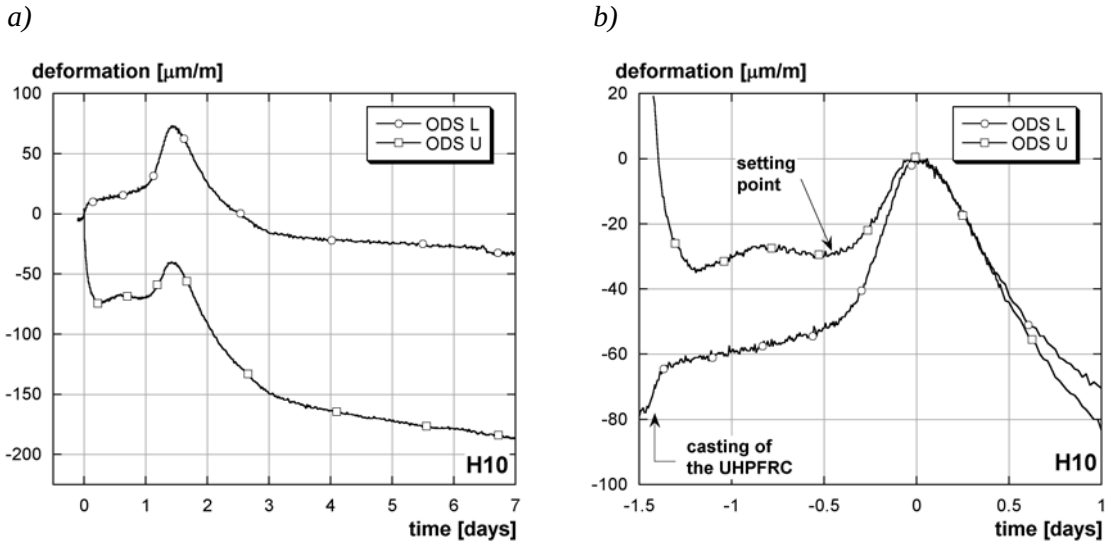

FIGURE 19.9: Early age deformations: a) ODS (H10), b) setting point (H10)

The deformations were lower in the UHPFRC layer (ODS U) than in the concrete substrate before the maximum temperature was reached (Figure 19.9b, time zero: when the maximum deformation due to the heat of hydration occurred). After the maximum deformations (at time zero), the deformation rate of the UHPFRC became higher than of the concrete substrate.

The influence of the superposition of the deformations of autogenous shrinkage and temperature evolution was also observed with ODS U at approximately 0.8 to 0.5 days before the maximum deformation due to the heat of hydration was reached. The end of the hook may be interpreted as the setting point of the UHPFRC, since from this moment on, the deformations of the ODS had similar appearance, indicating monolithic behaviour of the composite beam.

19.4 Long term tests

The results for all beams during the long-term tests are given in Appendices H to N.

19.4.1 Statically determinate beams

Horizontal deformations. The horizontal deformations of the beams were followed with the ODS and the LVDTs at the end of the beams (HS, HN) and at the pin supports (AM). The horizontal deformations HS and HN did not give clear results. The LVDTs were sometimes touched during the tests, leading to distorted results. Furthermore, the deflections of the beams led to inclined ends of the beams and to relative vertical and horizontal displacements between the LVDT and the measuring point on the beam. Therefore, the results of the LVDTs HS and HN were not exploited further.

Figure 19.10 shows the horizontal deformations at the pin support. The displacements at the pin supports decreased monotonously during the tests. At 75 days, values of -0.42 mm for I3, -0.58 mm for I5 and -0.8 mm for I10 were reached (Figure 19.10a). The displacements were higher for higher thicknesses of the UHPFRC layer. Reinforcement in the UHPFRC layer decreased the displacements of the supports (Figure 19.10b). The effect of the reinforcement on the displacements was more pronounced for the beams with h_U = 10 cm than for those with h_U = 5 cm.

a) *b)*

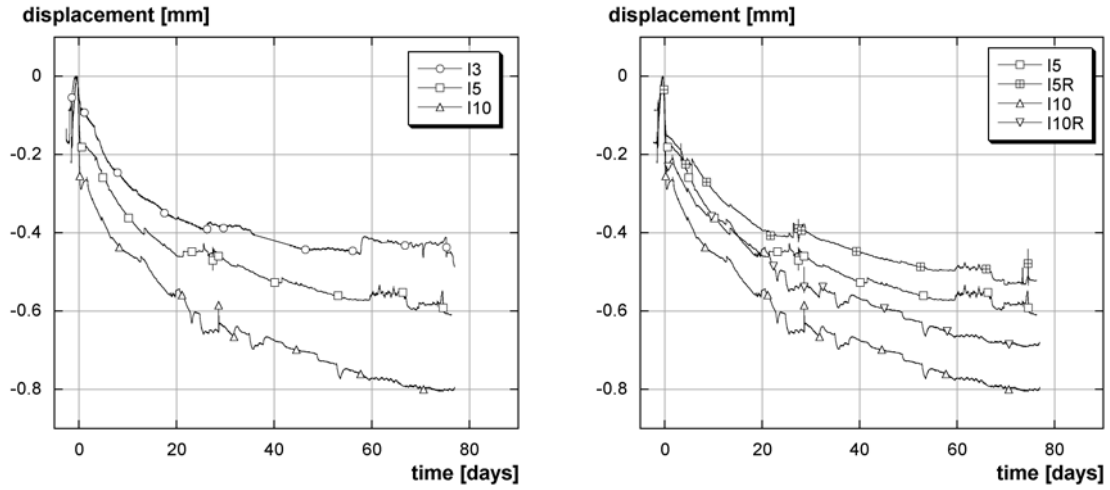

FIGURE 19.10: Horizontal displacements of the supports (statically determinate beams): a) I3, I5, I10, b) I5, I5R, I10, I10R

The axial deformations of the central span of the beams were also measured with the ODS. The elongation is calculated with EQ. 19.2 and represents the mean axial deformation in the central span.

$$\varepsilon_{ODS} = \frac{ODS\ U + ODS\ L}{2} \qquad \textit{(EQ 19.2)}$$

with ε_{ODS}: elongation [μm/m], ODS U, ODS L [μm/m].

The elongation of the beams was negative, i.e. the beams contracted during testing (Figure 19.11). The higher the thickness of the beams, the stronger was the contraction of the beams: At 75 days, the deformation was -120 μm/m for I3, -170 μm/m for I5 and -200 μm/m for I10. The beams with reinforcement in the UHPFRC layer (I5R, I10R) showed lower elongations than the beams without $A_{s,U}$ (I5, I10). No significant effect of the loading on the horizontal deformations was observed (Figure 19.11).

a) *b)*

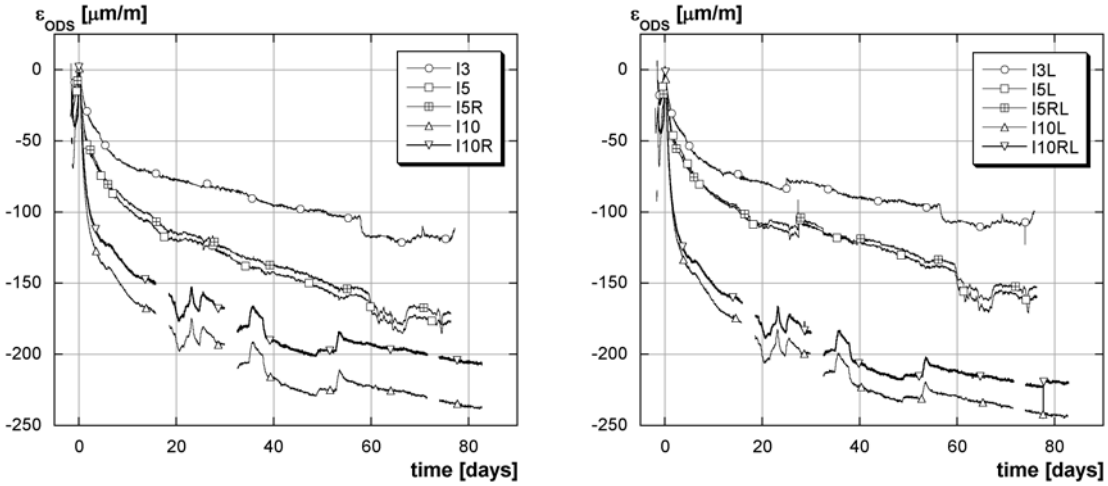

FIGURE 19.11: Elongation (ODS) of the statically determinate beams: a) without loading, b) with loading

Influence of the reinforcement. The influence of the reinforcement $A_{s,U}$ on the deformations of the beams during the long term tests is shown in Figure 19.12. The deformations of the beams with $A_{s,U}$ (I5R, I10R) were smaller than those for beams without $A_{s,U}$ (I5, I10), but both beams had the same overall behaviour. The difference in deformations was small for h_U = 5 cm (Figure 19.12a). Here, no difference in deformation occurred in the lower part of the concrete section (ODS L) and the deformations in the UHPFRC layer (ODS U) were barely higher for the beams without $A_{s,U}$.

a) *b)*

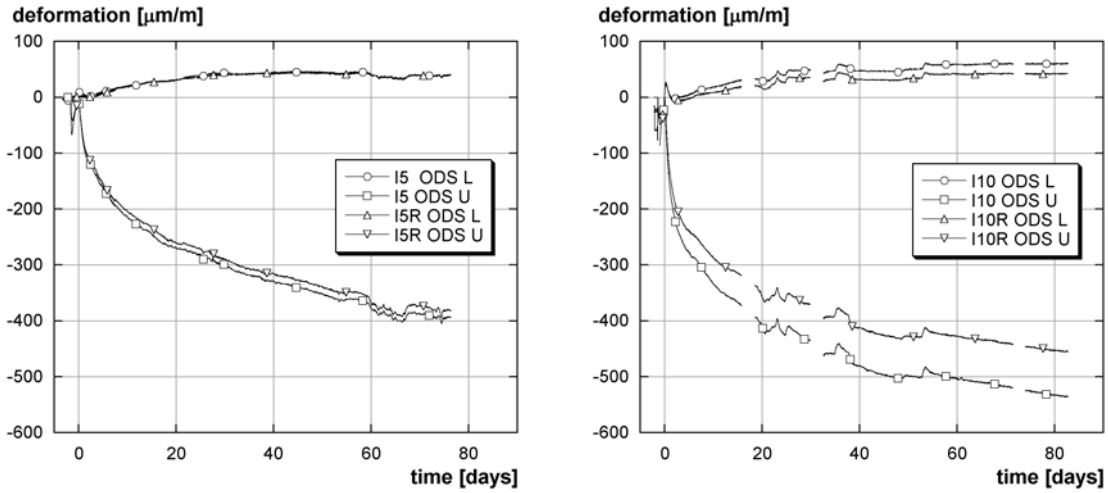

FIGURE 19.12: Influence of the reinforcement-ODS deformations: a) h_U = 5cm, b) h_U = 10 cm

The decrease of deformation due to $A_{s,U}$ was higher for the beams with h_U = 10 cm (Figure 19.12b). The difference in deformation was pronounced for ODS U, but was also measured with ODS L.

The same tendency was observed on the deflections at mid-span (f1) and at the cantilevers (f2) (Figure 19.13a) as well as on the curvature of the beams (Figure 19.13b). The influence of reinforcement was higher for the beams with h_U = 10 cm (I10, I10R) than for h_U = 5 cm (I5, I5R). At the end of the long term tests, the curvature of the beam without $A_{s,U}$ (I10R) was approximately 20% higher than for the beam with $A_{s,U}$ (I10).

The presence of $A_{s,U}$ reduced the deformations. The differences were small for the beams with h_U = 5 cm and significantly higher for h_U = 10 cm. The reinforcement layers $A_{s,U}$ and $A_{s,upp}$ were

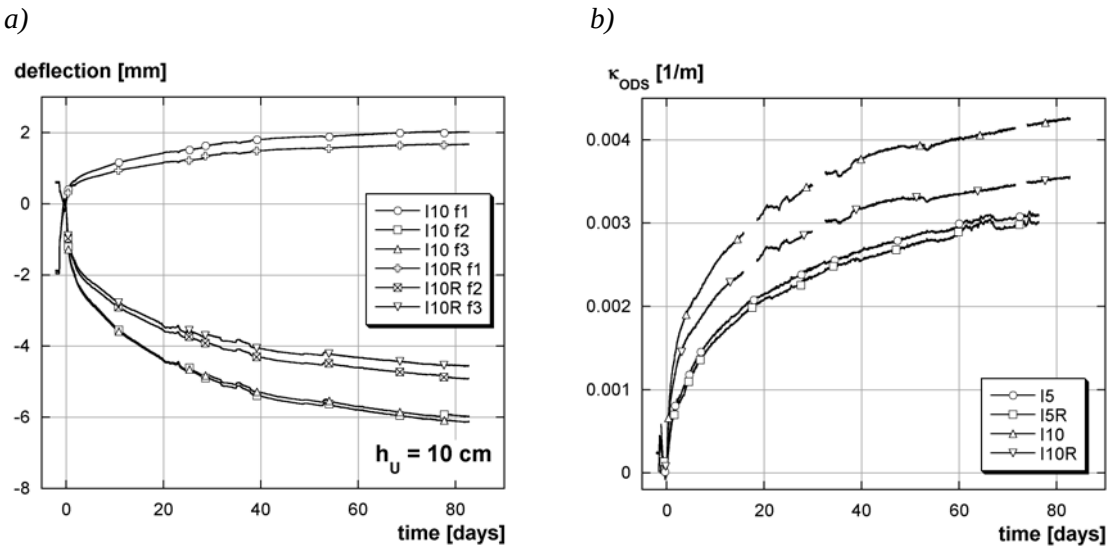

FIGURE 19.13: Influence of the reinforcement: a) h_U = 10 cm-deflection, b) curvature

close (distance: 4 cm) in the beam with h_U = 5 cm (I5R). Here, the reinforcement $A_{s,upp}$ had a strong influence on the UHPFRC layer. The additional layer $A_{s,U}$ did not increase the restraint of the UHPFRC layer considerably, and the difference in deformations was small. The reinforcement $A_{s,U}$ had a strong influence on the beams with h_U = 10 cm. The space between the reinforcement layers $A_{s,U}$ and $A_{s,upp}$ was higher (distance: 8.5 cm). $A_{s,U}$ was situated near the upper surface of the UHPFRC layer and worked as restraint on the UHPFRC layer and the deformations of the UHPFRC layer were partially restrained from the two sides.

The diagrams of the influence of reinforcement in the UHPFRC layer during the long-term tests are given in Appendix K.

Influence of the thickness of the UHPFRC layer. Three different thicknesses of the UHPFRC layer were tested during the long term test (h_U = 3, 5 and 10 cm). The highest mid-span deflections were observed for the beams with h_U = 10 cm and the lowest for h_U = 3 cm (Figure 19.14a). The overall behaviour of the beams was identical for all thicknesses.

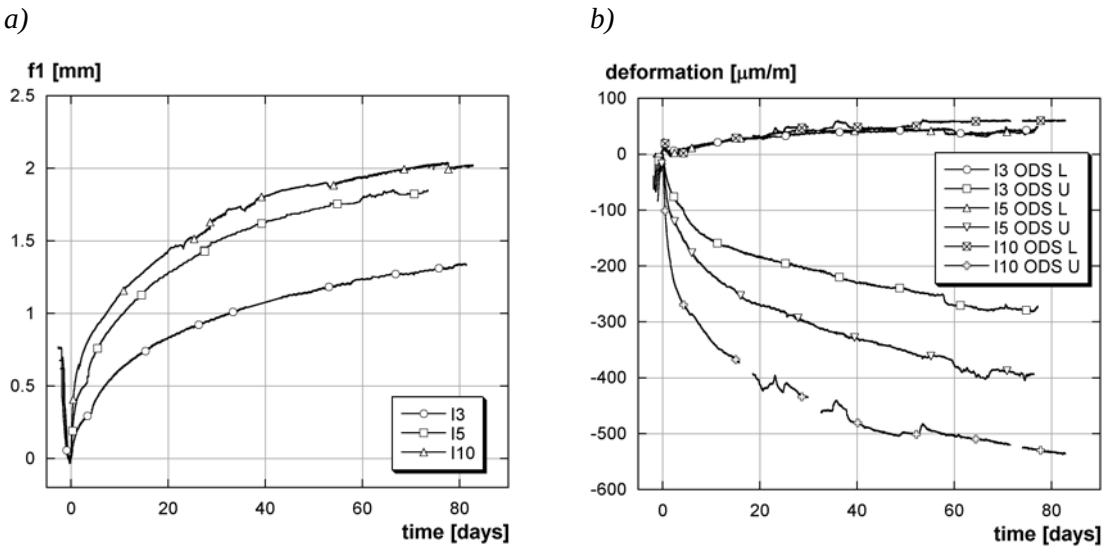

FIGURE 19.14: Influence of the thickness of the UHPFRC layer (statically determinate beams without $A_{s,U}$): a) deflection f1, b) ODS deformations

The measurements of the ODS show that the differences of deformations occurred mainly in the UHPFRC layer (Figure 19.14b). The deformations of the ODS, placed in the concrete substrate (ODS L), were identical, whereas differences were observed in the UHPFRC (ODS U): the deformations of ODS U were nearly two times higher for the beams with h_U = 10 cm (I10) than for the beams with h_U = 3 cm (I3).

Curvature and elongation, calculated from the ODS, also confirm that the deformations of the thicker beams were higher than of the thinner beams (Figure 19.15). The curvature of the beams with h_U = 10 cm (I10) was nearly 1.5 times higher than of the beams with h_U = 5 cm (I5) and nearly 2 times than for the beams with h_U = 3 cm (I3). The overall contraction of the beams was two times higher for I10 than for I3.

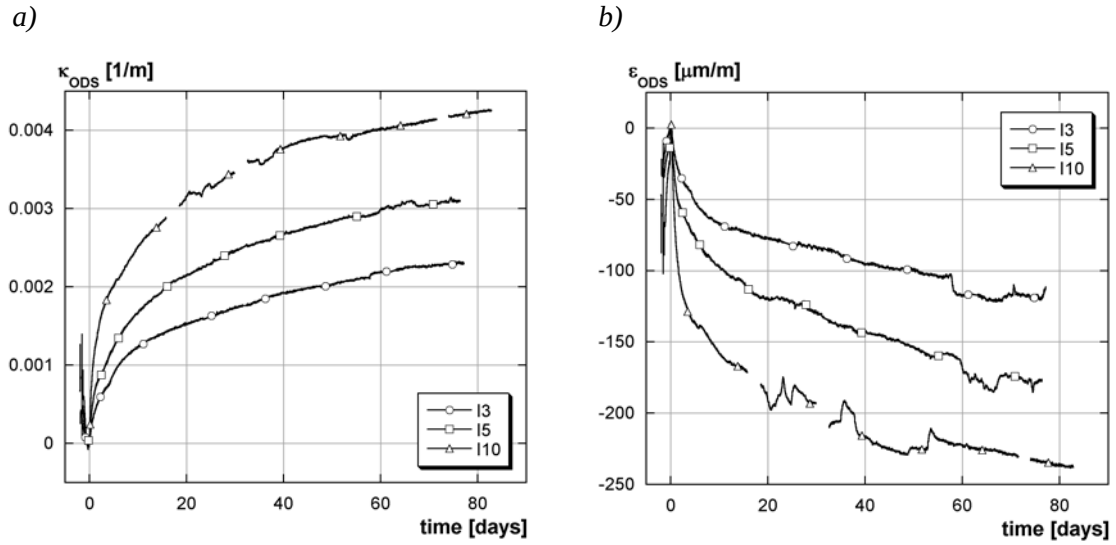

FIGURE 19.15: Influence of the thickness of the UHPFRC layer (statically determinate beams without $A_{s,U}$): a) curvature, b) elongation

Beams with reinforcement in the UHPFRC layer ($A_{s,U}$) were made only for h_U = 5 and 10 cm. Curvature and elongation of the beams with $A_{s,U}$ and h_U = 10 cm (I10R) were higher than for the beams with h_U = 5 cm (I5R) (Figure 19.16a and b), however, the difference was smaller than for the beams without $A_{s,U}$ (I5, I10).

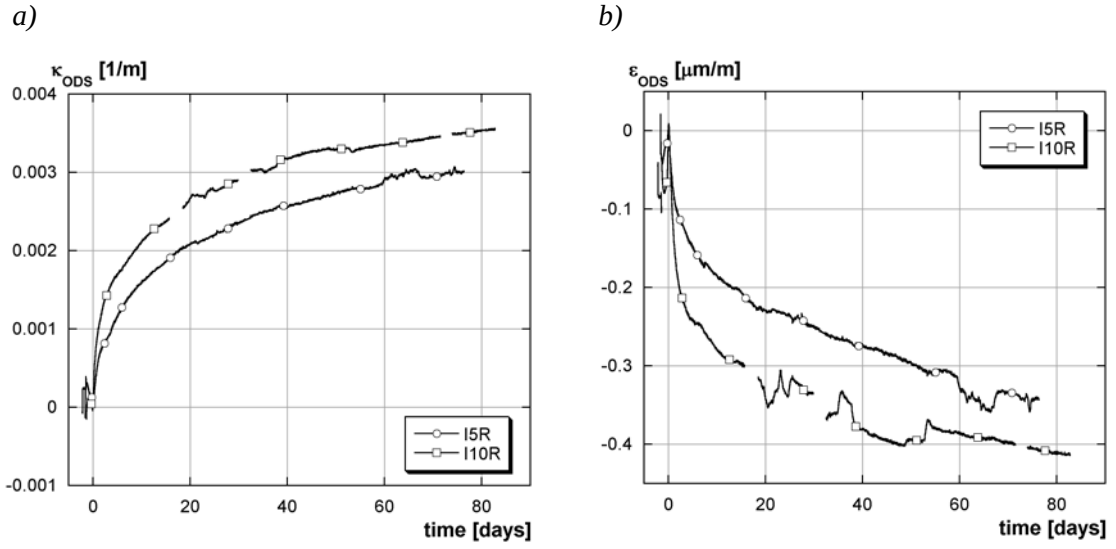

FIGURE 19.16: Influence of the thickness of the UHPFRC layer (statically determinate beams with $A_{s,U}$): a) curvature, b) elongation

The thickness of the UHPFRC layer (h_U) influenced considerably the deformations. The higher the thickness of the UHPFRC layer, the higher were the deformations. The major part of the deformations occurred in the UHPFRC layer (Figure 19.14b). The thicker the UHPFRC layer, the more important was its influence on the composite beams. The deformations of the UHPFRC due to internal thermal and hygral changes exerted higher influence on the concrete substrate.

Reinforcement in the UHPFRC layer ($A_{s,U}$) decreased the difference of deformation for different thicknesses. The reinforcement imposed additional restraint of the UHPFRC deformations which was higher for thicker UHPFRC layers.

The influence of the thickness is illustrated with diagrams in Appendix L.

Flexural creep. Flexural creep behaviour was investigated during the long term tests. Half of the statically determinate beams were loaded with lead boxes 28 days after the casting of the UHPFRC layer and remained loaded for 49 days (Figure 18.8). There was always a loaded and a non-loaded beam of the same configuration. The non-loaded beams were only deformed by RH-changes and by consequences of the progressive hydration. The loaded beams were additionally deformed by an elastic and a creep contribution. The creep deformations were obtained by comparing the non-loaded and the loaded beams (EQ. 19.3 and Figure 19.17).

$$\varepsilon_{cc}(t, t_0) + \varepsilon_{ci}(t_0) = \varepsilon_c(t, t_0) - \varepsilon_{cs}(t) \qquad \textit{(EQ 19.3)}$$

with $\varepsilon_{cc}(t,t_0)$: creep deformation, $\varepsilon_{ci}(t_0)$: elastic deformation due to the load, $\varepsilon_c(t,t_0)$: total deformation, measured on beam that was loaded at time t_1, $\varepsilon_{cs}(t)$: shrinkage deformation of the non-loaded beam.

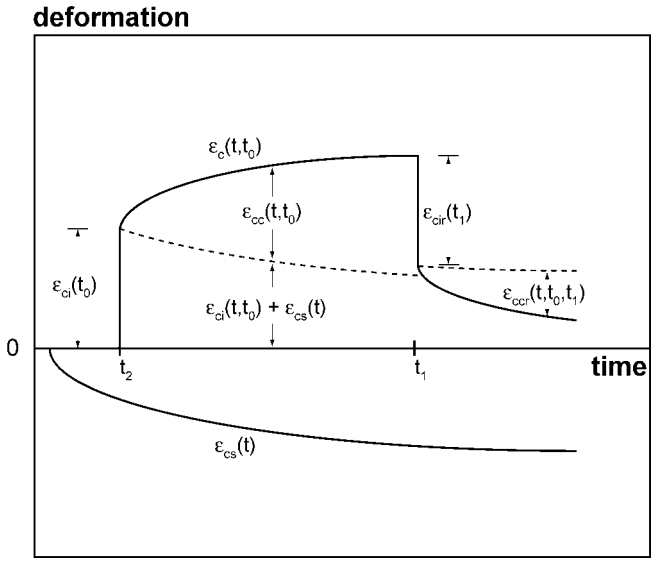

FIGURE 19.17: Definition of the creep deflections (after [Bernard00])

The *load level* was fixed in relation to the theoretical additional tensile stresses in the upper fibre of the UHPFRC layer. The additional tensile stresses due to loading were 4.5 MPa for the beams I5 and I5R and 6.0 MPa for the beams I3, I10 and I10R. The stress distribution due to loading was superimposed to the stress state in the beam due to internal thermal and hygral changes that had already provoked tensile stresses in the composite beam prior to the loading.

Creep deformations. Figure 19.18a shows the *creep deflections* in the central span (f1) and near the ends of the beams (f2, f3). The creep curves were calculated by subtracting the deformations of the

unloaded beam from the loaded beam of the same configuration. This method contains uncertainties: The deformations before loading of two identical beams were not exactly the same, therefore, the difference of the deformations of the two beams did not give the exact creep deformation. The time was zeroed when the load was applied. The elastic deformation due to the load was 3.2 mm for f2 and f3 and -1.1 mm for f1. The deflections increased monotonously until the end of the loading after 49 days. The unloading of the beams was characterized by the reversal of the elastic deformation and the creep recovery. The residual deflections expressed the non-elastic part of the deformation.

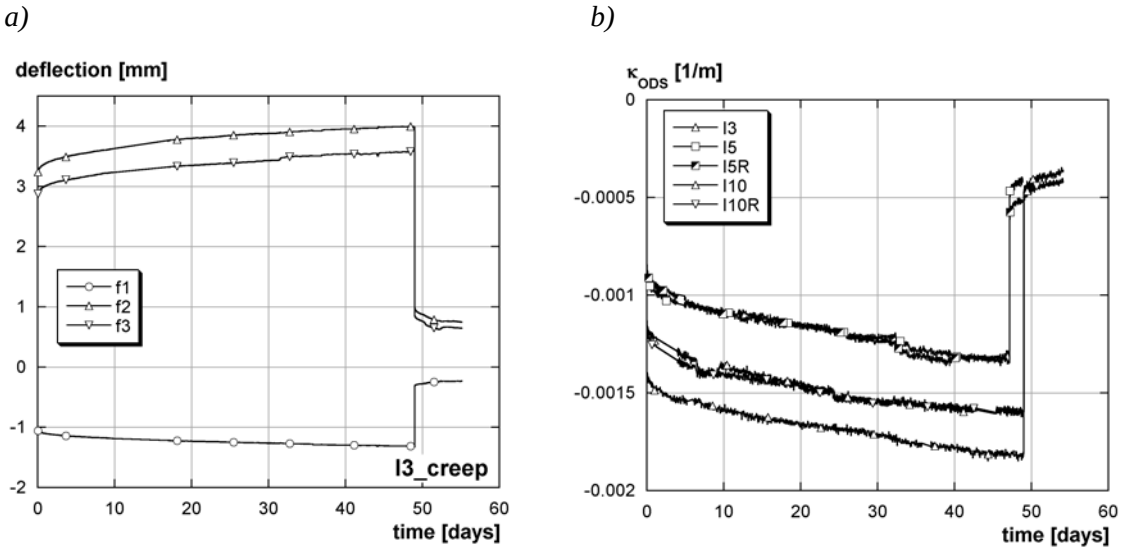

FIGURE 19.18: a) Creep deflections f1, f2, f3 of I3, b) comparison of the curvature κ_{ODS} of the beams

The creep deformations were also observed with the *curvature* (Figure 19.18b): The curvature decreased due to the loading, since the already deformed beams were straightened under loading. The creep deformations of beams I5 and I5R were the lowest, followed by I10 and I10R. The creep curvature decreased most for beam I3. The load level of I5 and I5R was the lowest explaining the lowest curvature decrease. The stiffness of beams I10 and I10R was higher than for I3 which had the highest decrease in creep curvature.

Creep compliance. The creep compliance $J(t,t_0)$ of the beam was calculated for the deflections. The creep compliance describes the creep strain per unit stress, independent on load and stiffness (EI). So, the different beam configurations could be compared on the basis of the creep compliance. The definition of the creep compliance is given in EQ. 19.4:

$$\varepsilon_{cc}(t, t_0) + \varepsilon_{ci}(t, t_0) = \left(\frac{1}{E_{ci}(t_1)} + \frac{1}{E_{cc}(t, t_0)}\right) \cdot \sigma = J(t, t_0) \cdot \sigma \qquad \textit{(EQ 19.4)}$$

with $\varepsilon_{cc}(t,t_0)$: creep deformation [µm/m], $\varepsilon_{ci}(t,t_0)$: elastic deformation due to the load [µm/m], $E_{cc}(t,t_0)$: creep modulus [MPa], $E_c(t)$: elastic modulus [MPa], σ: stress [MPa], $J(t,t_0)$: creep compliance function [µm/m/MPa].

The elastic deflections were calculated for linear elastic material behaviour (EQ. 19.5, EQ. 19.6).

$$\text{for f1: } f1_{ci} = -0.648 \cdot 10^6 \cdot \frac{F}{E_c I} \qquad \textit{(EQ 19.5)}$$

$$\text{for f2, and f3: f2, f3}_{ci} = 1.674 \cdot 10^{6} \cdot \frac{F}{E_c I} \qquad \textit{(EQ 19.6)}$$

with f1, f2, f3: deflections [mm], F: creep load [kN], E_c: elastic modulus [MPa], I: moment of inertia [mm^4], $J(t,t_0)$: creep compliance [µm/m/MPa].

The creep compliance was deduced from the elastic deformations (EQ. 19.7, EQ. 19.8)

$$\text{for f1: } J(t, t_0) = -\frac{1}{E_{mean}} \cdot \frac{(E_c I)_{total}}{0.648 \cdot F} \cdot 10^{-6} \cdot (f1_{cc}(t, t_0) + f1_{ci}(t, t_0)) \qquad \textit{(EQ 19.7)}$$

$$\text{for f2 and f3: } J(t, t_0) = \frac{1}{E_{mean}} \cdot \frac{(E \cdot I)_{total}}{1.674 \cdot F} \cdot 10^{-6} \cdot (f2, f3_{cc}(t, t_0) + f2, f3_{ci}(t, t_0)) \qquad \textit{(EQ 19.8)}$$

with $J(t,t_0)$: creep compliance [µm/m/MPa], E_{mean}: average elastic modulus of the beam section, $(EI)_{total}$: stiffness of the beam section, F: creep load [kN], f1, f2, $f3_{cc}(t,t_0)$: creep deflections [mm], f1, f2, $f3_{ci}(t,t_0)$: elastic deflections [mm].

As the elastic moduli of the UHPFRC and the concrete were different, the stiffness of the element had to be calculated for the whole section ($(EI)_{total}$), considering the difference between the moduli. The creep function was obtained by a division by the mean elastic modulus E_{mean} which was calculated considering the proportions of the UHPFRC and the concrete section.

Figure 19.19a shows the mean value of the creep compliances for *deflections* f2 and f3 for each configuration. The compliance of all the beams was of the same magnitude. The lowest creep compliance was found for I3, which had the lowest initial value as well as the lowest slope. The beams with h_U = 5 and 10 cm had approximately the same initial values and the same slope. Figure 19.19b shows the creep compliance for the central span deflection f1. The creep compliances of I3, I10 and I10R were lower than those of I5, I5R. The curve of I3 had the lowest slope, which may be explained with the age of the UHPFRC (at an UHPFRC age of 28 to 77 days). During this period, the material properties of the UHPFRC still changed. The compression creep tests (Chapter 13) showed that the creep deformations of the UHPFRC increased strongly until an age of 90 days and were higher than those of the concrete during this period. Therefore, the creep deformations of the UHPFRC were dominant for the beam deformations. Since the beams with h_U = 3 cm had the thinnest UHPFRC layer, the influence of the UHPFRC on the beam was remote and the creep deformations were the lowest. The creep compliances for deflections f1, f2, f3 for each beam configuration can be found in Appendix M (Figures M.1 to M.5).

By comparing Figure 19.19a and b, it can be stated that the creep compliance for I5 and I5R were identical (cf. Appendix M, Figures M.2 and M.3). The creep compliances of I3, I10 and I10R were higher for the deflections at the end of the beams (f2, f3) than in the middle of the beams. This indicates that the central span deflection was smaller than its calculated deflection calculated with the theory of elasticity. As the loads were applied at the ends of the beams, the lower central span deflection may indicate damage in the UHPFRC layer near the supports. I3, I10 and I10R had a higher load level than I5 and I5R. However, no significant influence of the load level on the kinetics of the creep compliances was observed.

The creep compliance of I5R was higher than for I5; that of I10R lower than for I10. This may be due to the uncertainties which were induced by subtracting the deformations of the unloaded beam from the loaded beam.

a) *b)*

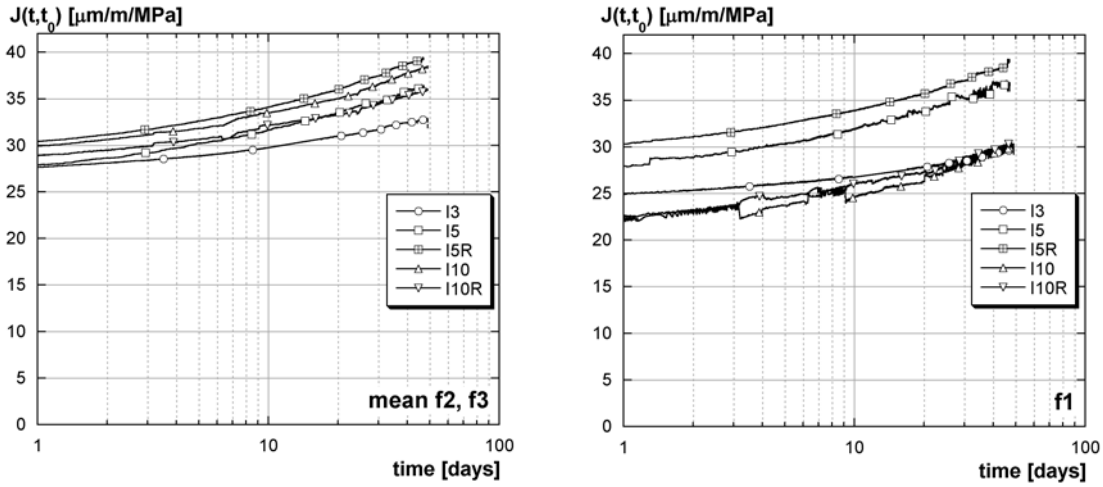

FIGURE 19.19: Creep compliance: a) mean value of deflections f2 and f3, b) deflection f1

The creep compliance curves are convex in a logarithmic time scale (Figure 19.19), i.e. the creep deformations did not stabilize during the testing period, but increased continuously. This curvature of the compliances may be attributed to microcracking in the tension chord, i.e. in the UHPFRC layer. As the creep tests had only been conducted for 49 days, no statements can be made about a possible and probable stabilizing of the creep deformations.

The creep deformations are given in Appendix M.

Creep recovery. The creep recovery was measured for time spans between 1.8 and 6 days. The unloading of the beams was treated as negative loading [Bernard00] and recovery compliances $J(t,t_1)$ were calculated the same way as the creep compliances.

Figures 19.20 shows the creep and the recovery compliances for beams I3 and I5R which were representative for the two load levels. The recovery compliances were lower than the creep compliances. The elastic deformations during unloading were smaller than during loading. This may be attributed to a higher stiffness of the beams at the end of the creep tests. The mechanical properties of the UHPFRC still evolved during the period of the creep tests (28 to 77 days).

a) *b)*

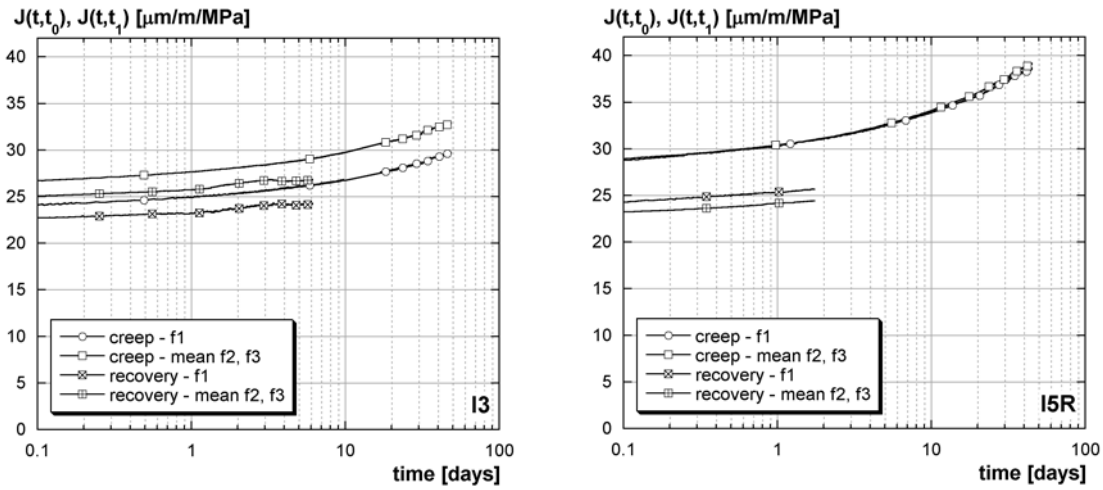

FIGURE 19.20: Recovery compliance: a) mean value of deflections f2 and f3, b) deflection f1

The difference between creep and recovery compliance was small for beams I5 and I5R, but significantly higher for beams I3, I10 and I10R. The higher load level for beams I3, I10 and I10R probably induced microcracking into the beams and residual deformations remained after unloading.

The recovery compliances were measured over a short time span. Thus, it was impossible to predict the recovery and to draw significant conclusions from the recovery compliance. The recovery compliances and the comparison between creep and recovery compliances are given in Appendix M (Figures M.6 to M.15).

Crack pattern. The cracks visible with the naked eye that occurred during the long term tests on the upper side of the beams were traced on the beams (see also Appendix N). The observations gave the following results:

- Cracks formed mainly during the first 14 days after casting. After approximately 28 days, nearly no more cracks formed. Most of the beams had very few cracks after the long term tests. The most sensible period to cracking was the early age of the UHPFRC layer.
- The cracks were mainly orientated perpendicular to the axis of the beams. However, cracks in axial direction were also observed on some of the beams. The axial cracks were shrinkage cracks due to the restraint in transversal direction; the perpendicular cracks were governed by the stress state in axial direction. As the length of the beams was much higher than their width, the degree of restraint was much higher in axial than in transversal direction. The axial cracks indicate that the casting procedure influenced the fibre orientation. More steel fibres were orientated in axial direction. Therefore, cracks in axial direction occurred even when the stresses perpendicular to the axis were lower than in axial direction.
- Zones with more cracks were found on two of the beams with h_U = 5 cm. These crack zones were probably in relation with the casting procedure and the workability of the UHPFRC, since these zone did not correspond to the zones in which the highest stresses occurred.
- All the observed cracks were surface cracks. The upper surface of the beams was characterized with pores that were created by the air that had risen to the surface when the material was still soft. These air bulbs are typical for self-compacting concrete. Furthermore, the upper surface was subjected to drying after 6 days when the plastic foils were removed. So, the tensile resistance of the surface of the UHPFRC was probably lower than the measured tensile strength. As the highest tensile stresses occurred at the upper side of the elements, surface cracking occurred.
- No new cracks formed due to the loading of the beams after 28 days. The applied loading for the flexural creep tests was not high enough for the formation of visible cracks in the UHPFRC.
- No significant influence of the reinforcement on the cracking was observed. The additional restraint due to the reinforcement did not provoke stresses in the UHPFRC that were higher than the first cracking strength of the material.

19.4.2 Statically indeterminate beams

Horizontal deformations. The deformations of the statically indeterminate beams were recorded with LVDTs and ODS. The horizontal deformations of the LVDTs, placed at the end of the beams, were not exact, since the measured values were a superposition of pure horizontal deformations and the deflections of the beams. As the LVDTs HS and HN were placed at 2 cm from the lower side of the beams, the horizontal displacements of HS and HN were underestimated. The LVDTs IS, IN were placed at 2 cm from the upper side of the beams. Here, the displacements were overestimated. Furthermore, debonding was not considered. The LVDTs at the supports (AS, AN) measured the horizontal deformations at the lower side of the supports.

Figure 19.21a shows the horizontal displacements at the end of the beams and at the supports for beam H3. The displacements of the supports AS and AN decreased during the test to a value of -0.08 mm at the end of the tests. Their overall behaviour was the same as for AS and AN. However,

the deformations of IS and IN were approximately 2.5 times higher than those of HN and HS. The decrease of the deformations indicated a contraction of the beam during the tests.

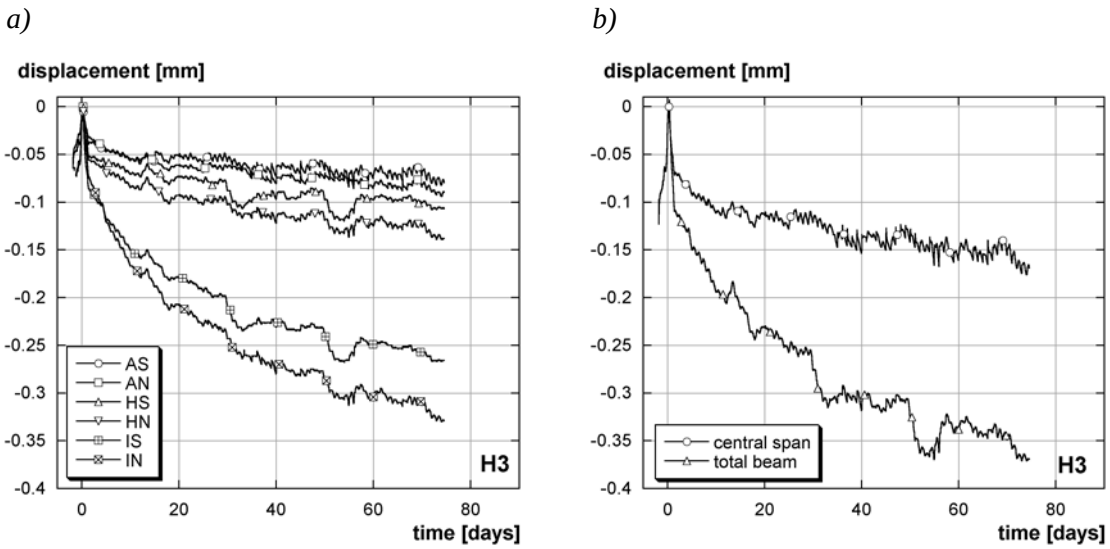

FIGURE 19.21: Horizontal displacement - H5R: a) AS, AN, HS, HN, b) central and total span

Figure 19.21b shows the deformations of the central span and the whole beam for H3. The values were calculated from the measurements of the LVDT. The deformations of the central span were the sum of AS and AN, indicating the horizontal displacement between the supports at the lower side of the beams. The total deformation of the beam was calculated by EQ. 19.9 with the values of HS, HN, IS and IN as well as the LVDTs placed to measure debonding (ISdir, INdir).

$$\text{total beam} = \frac{\text{HS} + (\text{IS} - \text{ISdir})}{2} + \frac{\text{HN} + (\text{IN} - \text{INdir})}{2} \qquad \textit{(EQ 19.9)}$$

After 75 days, the deformation in the central span was -0.15 mm (63 μm/m), the deformation of the total beam -0.35 mm (65 μm/m), nearly the same as the value for the central span.

Figure 19.22 illustrates the influence of the different thicknesses of the UHPFRC layer and of reinforcement in the UHPFRC layer ($A_{s,U}$) on the horizontal deformations. Figure 19.22a shows the deformations of the central span of the beams measured with the LVDTs AS and AN; Figure 19.22b the elongation measured with the ODS. The reinforcement only had an influence for the beams with h_U = 10 cm: the beams with $A_{s,U}$ contracted slightly less. The thickness had a strong influence on the horizontal deformations. The displacements of the supports after 75 days were -0.17, -0.3 and -0.47 mm for h_U = 3, 5 and 10 cm respectively (Figure 19.22a). The elongations (in mm), measured with the ODS (Figure 19.22b), were slightly lower than the deformations at the supports. However, the measuring length of the ODS (200 cm) was lower than the distance between the central supports (240 cm).

The beams contracted due to the shrinkage of the UHPFRC layer. Reinforcement in the UHPFRC layer ($A_{s,U}$) did not significantly influence the horizontal deformations. The thickness of the UHPFRC layer (h_U) influenced strongly the horizontal deformations. The thicker the UHPFRC layer, the higher were the horizontal deformations.

The horizontal deformations showed that the horizontal restraint of the central span of the statically indeterminate beams was weak. The central span with a length of 240 cm was 2.25 times shorter than the total length (540 cm); the deformations of the total beam were 2.33 times higher than those of the central span. The ratio of the deformations was slightly higher than the ratio of the lengths. It can be concluded that the horizontal deformations of the beam were nearly constant over

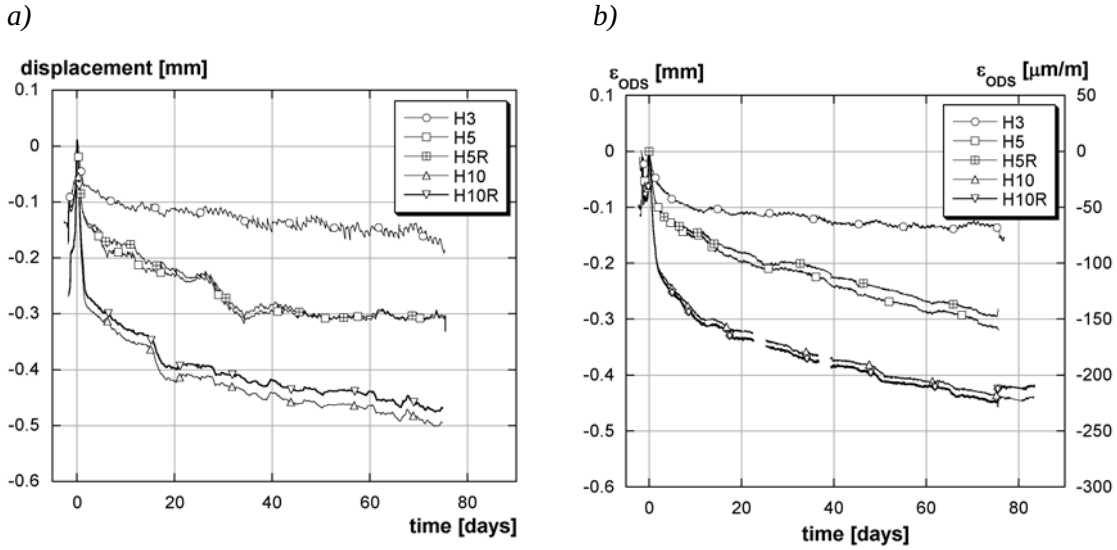

FIGURE 19.22: a) Horizontal displacements AS+AN, b) elongation (ODS) of the statically indeterminate beams

the whole length of the beam. The horizontal restraint of the central supports was small, e. g. the additional restraint of the static system was nearly completely due to the vertical restraint.

Influence of the reinforcement. The influence of the reinforcement on the deflections of the statically indeterminate beams is shown in Figure 19.23 for h_U = 5 and 10 cm (H5R, H10R). The end span deflections f3 were smaller for the beams with reinforcement in the UHPFRC layer ($A_{s,U}$). The mid-span deflection of the beam with a h_U = 5 cm and $A_{s,U}$ (H5R) was smaller than for the beam without $A_{s,U}$ (H5). However, the mid-span deflections of the beams with h_U = 10 cm were higher for the beam without reinforcement in the UHPFRC layer (H10).

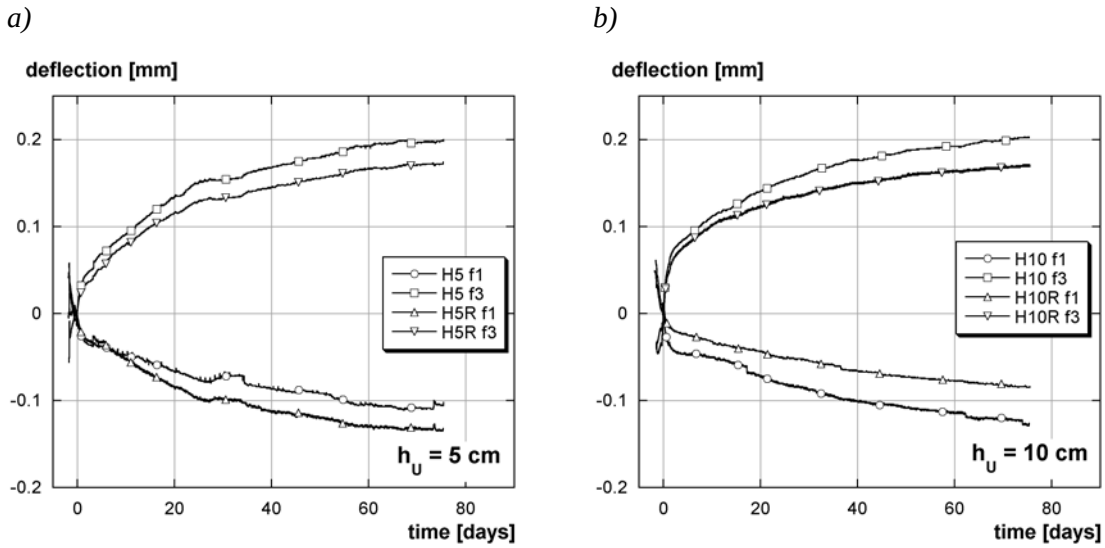

FIGURE 19.23: Influence of the reinforcement - mid-span deflections: a) h_U = 5 cm, b) h_U = 10 cm

The measurements of the ODS are shown in Figure 19.24. The deformations of the ODS in the concrete substrate were identical for the beams with and without $A_{s,U}$. The measurements of the ODS in the UHPFRC layer (ODS U) showed an influence of the reinforcement. The deformations of ODS U were higher for the beams without $A_{s,U}$ for h_U = 5 cm, while the deformations of ODS U were lower for the beams without $A_{s,U}$ for h_U = 10 cm.

The difference of the measurements between the beams with h_U = 5 cm and with h_U = 10 cm may be explained with different degrees of damage in form of microcracking of the UHPFRC layer:

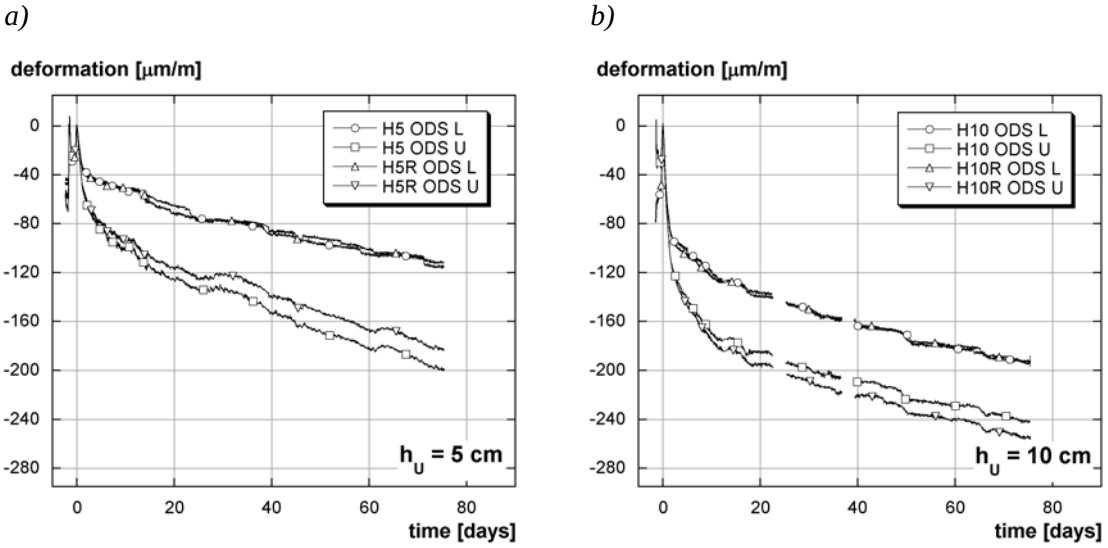

FIGURE 19.24: Influence of the reinforcement: ODS deformations: a) h_U = 5 cm, b) h_U = 10 cm

The beams with h_U = 10 cm (H10R) had thicker rebars ($A_{s,U}$) in the UHPFRC layer (∅14 mm, compared to ∅10 mm for h_U = 5 cm, H5R). Furthermore, the tensile stresses in the UHPFRC layer were probably higher for the beams with h_U = 10 cm, since the temperature elevation was higher at early age and the deformations were more restrained due to the difference in the reinforcement $A_{s,U}$. The interaction between rebars and UHPFRC caused probably damage in form of microcracking in beam H10R. This damage led to higher deformations in H10R when compared to H10. Less microcracks had probably formed in beam H5R than in H10R. The reinforcement of the UHPFRC layer increased the stiffness, and its deformations were lower than those of beam H5.

The influence of the reinforcement is also given in Appendix K.

Influence of the thickness of the UHPFRC layer. The influence of the thickness was observed with the deformations ODS U (Figure 19.25a): The deformations of the beams with h_U = 10 cm (H10) were more than two times higher than for the beams with h_U = 3 cm (H3). The influence of the thickness of the UHPFRC was most important for the axial deformations of the beams. The mid-span elongation, measured with the ODS, were the highest for h_U = 10 cm and the lowest with h_U = 3 cm. The impact of the thickness was here even bigger than for ODS U.

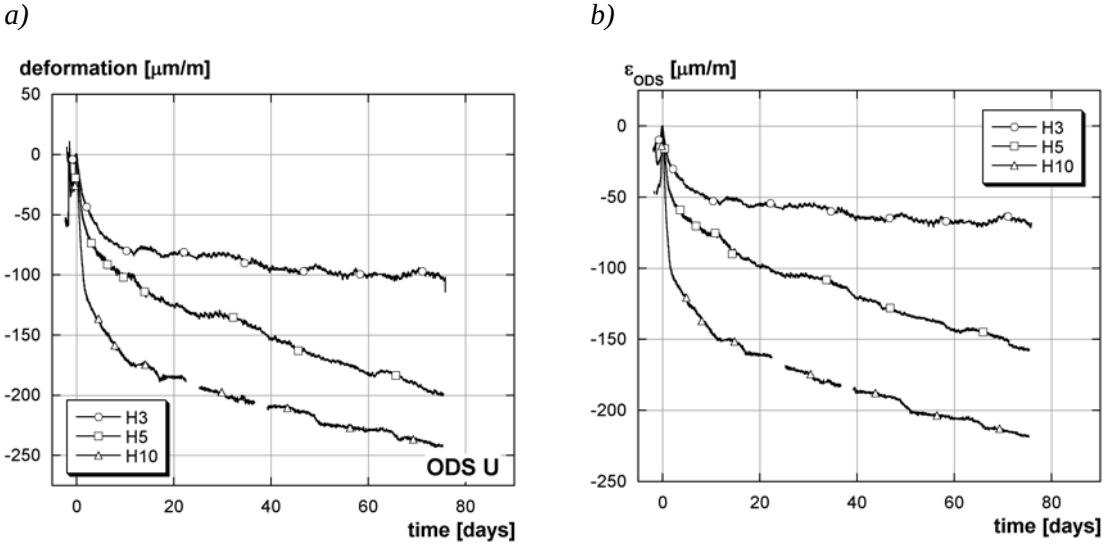

FIGURE 19.25: Influence of the thickness of the UHPFRC layer (statically indeterminate beams without $A_{s,U}$): a) deformation ODS U, b) elongation

However, the thickness of the UHPFRC layer did not significantly influence the mid-span deflection f1 and the curvature (Figure 19.26a and b). The curvature of the beams was nearly identical for the three different thicknesses until an age of 20 days. Afterwards, the curvature for the beams with h_U = 10 cm remained constant, whereas the curvatures for h_U = 3 and 5 cm continued to increase beyond an age of approximately 30 days. The highest increase was observed for h_U = 5 cm and reflected the gradual increase of deformation of ODS U (Figure 19.25b).

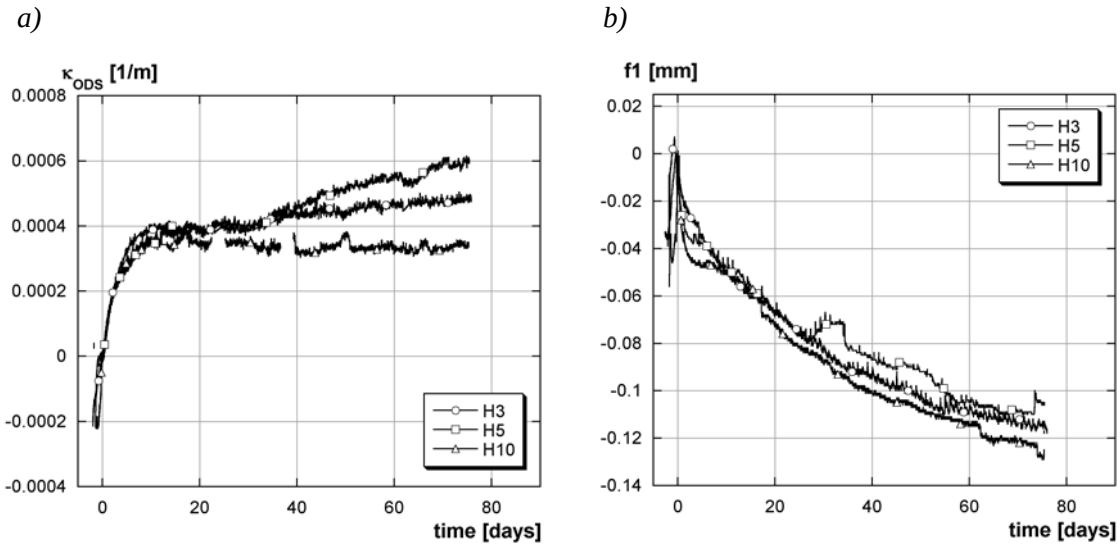

FIGURE 19.26: Influence of the thickness of the UHPFRC layer (statically indeterminate beams without $A_{s,U}$): a) curvature, b) deflection f1

The influence of the thickness of the UHPFRC layer was mainly observed for the horizontal deformations. No significant influence of the thickness occurred on the deflections. Theses differences may be explained by the restraint. It was aimed to restrain horizontal and vertical deformations with the supports of the beams (cf. Figure 18.10 on page 49). The vertical restraint worked well, therefore, no significant differences were observed in the deflections. The horizontal restrain, however, did not work well and horizontal deformations occurred, depending on the thickness of the UHPFRC layer. The force, induced by the restraint, depended on the section of the UHPFRC layers and horizontal restraint may be seen as a system with a resort. The thicker the UHPFRC layer, the higher was the force and the higher the axial deformations.

The diagrams of the influence of the thickness of the UHPFRC layer can be consulted in Appendix L.

Crack pattern. The observations of the visible cracks during the long term tests result in following statements (see also Appendix N):

- Cracks formed mainly during 14 days after casting. After approximately 28 days, nearly no more new cracks occurred.
- The cracks were mainly orientated perpendicular to the axis of the beams At the end of the long term tests, the space between the cracks was 10 to 20 cm. The cracks, perpendicular to the axis, did not go over the whole width of the beam. They were mainly situated in the central 15 cm of the width of the beams.
- The observed cracks were surface cracks, except for two cracks of beam H3. Here, two perpendicular cracks went from one side to the other side and penetrated deeper into the UHPFRC layer.
- The beams with reinforcement in the UHPFRC layer $A_{s,U}$ (H5R, H10R) showed more cracks than the beams without $A_{s,U}$ (H5, H10). The additional restraint was high enough to build up stresses that led to visible cracks.

19.4.3 Comparison of the static systems

Deflections. The difference between the statically determinate and indeterminate beams were observed by the deflections (Figure 19.27). The mid-span deflections f1 of the statically determinate beams were more than 10 times higher than of the statically indeterminate beams. Moreover, the deflections f1 had positive values for the statically determinate beams and negative values for the statically indeterminate beams, i.e. the mid-span of the statically determinate beams lowered, whereas it rose for the statically indeterminate beams (Figure 19.28). The supports of the statically indeterminate beams were removed after approximately 77 days, leading to an increase in the mid-span deflection, i.e. to a lowering at the mid-span. Without vertical restraint at the supports, the former statically indeterminate beams curled the same way as the statically determinate beams. However, the recovery of the deflections after the removal of the beams did not reach the deflections of the statically determinate beams.

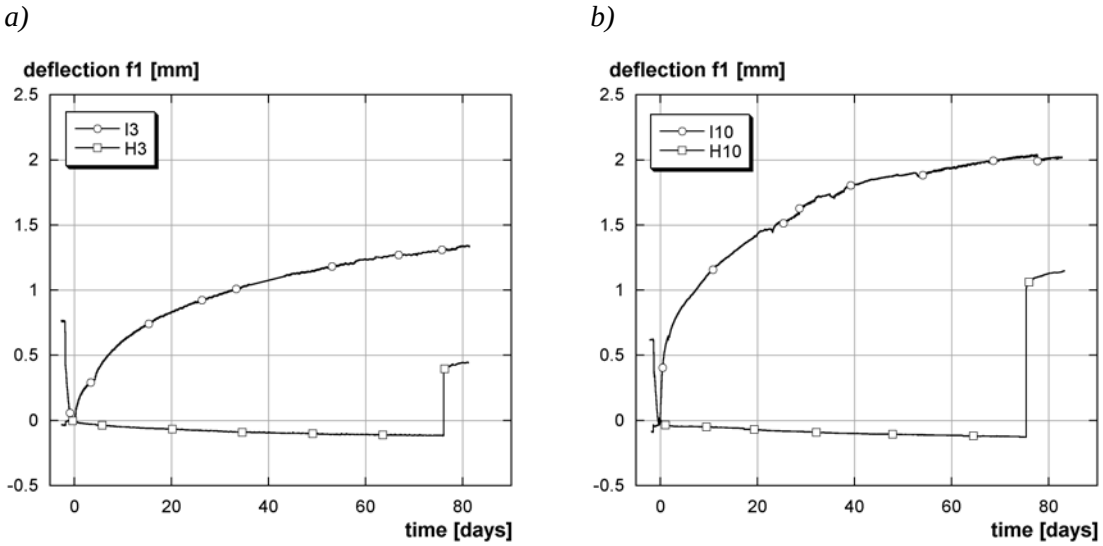

FIGURE 19.27: Influence of the static system a) h_U = 3 cm, b) h_U = 10 cm

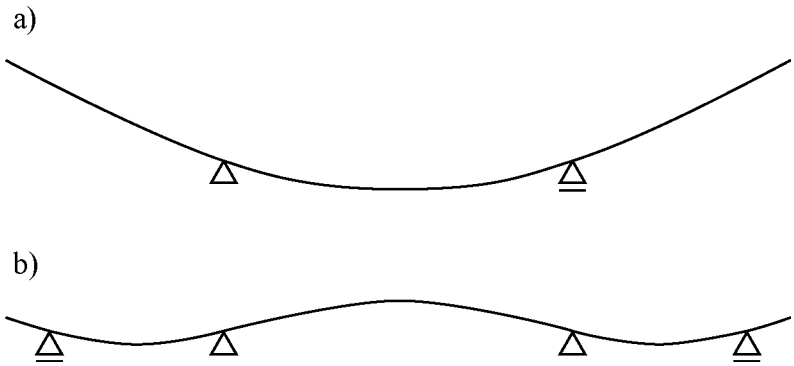

FIGURE 19.28: Deformations of the beams during the long term tests: a) statically determinate beams, b) statically indeterminate beams (deflections were not scaled in the figure)

Measurements of the ODS. The deformations of the ODS L in the concrete substrate increased for the statically indeterminate beams and decreased for the statically determinate beams (Figure 19.29a). The thickness of the UHPFRC layer influenced significantly the deformations of ODS L for the statically determinate beams, while the difference of ODS L of the statically indeterminate beams was smaller. All ODS U, placed in the UHPFRC layer, measured a decrease in deformation (Figure 19.29b). The deformations were approximately 2.5 times higher for the statically determinate beams than for the statically indeterminate beams. The measurements of both ODS

showed that the deformations remained smaller for the statically indeterminate beams after the removal of the supports than those of the statically determinate beams. The deformations did not recover fully and indicate inelastic deformations during the long term tests.

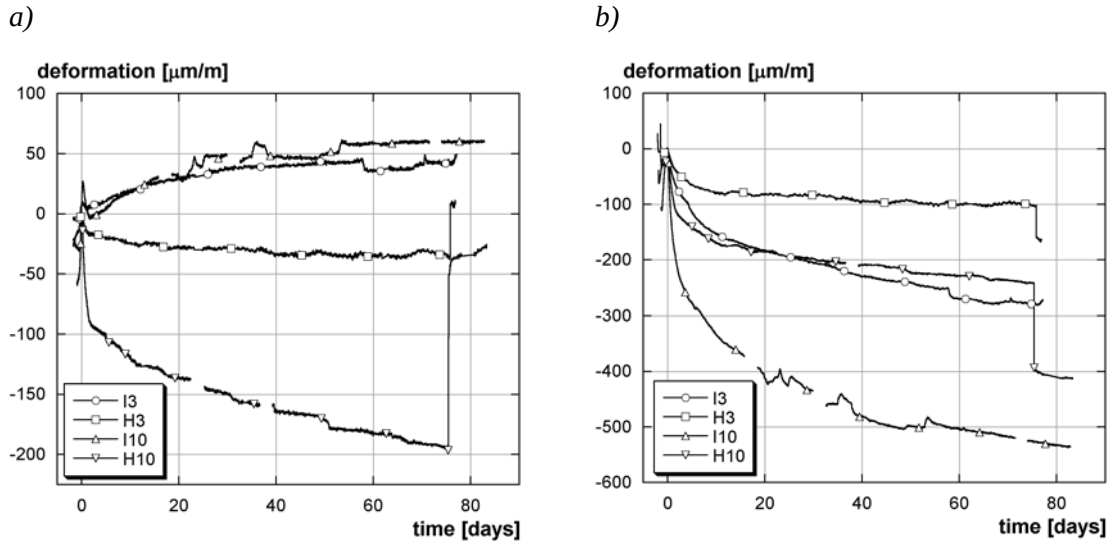

FIGURE 19.29: Influence of the static system a) ODS L, b) ODS U

The curvature, calculated on the basis of the measurements of the ODS, increased monotonously for all beams (Figure 19.30a), being significantly higher for the statically determinate beams. The curvature of the statically determinate beams increased monotonously until the end of the long term tests. The curvature of the statically indeterminate beams increased until approximately 10 days and then remained virtually constant.

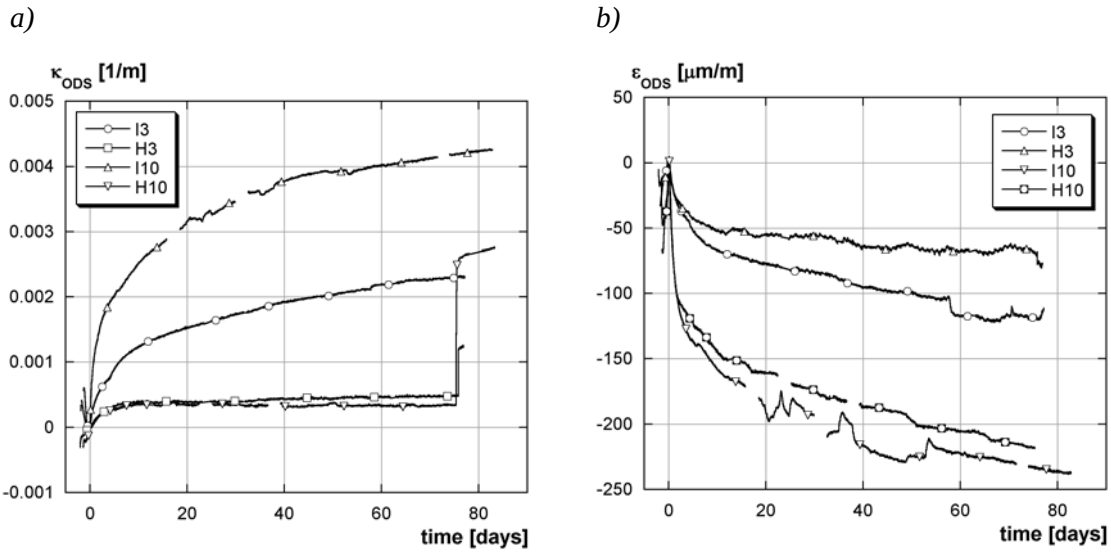

FIGURE 19.30: Influence of the static system a) curvature, b) elongation

The elongation or axial deformation, calculated from the measurements of the ODS, was also higher for the statically determinate beams (Figure 19.30b). However, the horizontal deformations were more sensible to the thickness of the UHPFRC layer than to the change of the static system.

Crack pattern. More visible cracks were found on the statically indeterminate beams after the long term tests. The cracks of the statically determinate beams were mainly due to the casting procedure and the workability of the material, while the cracks on the statically indeterminate beams were more orientated indicating that higher stresses were induced because of the higher degree of

restraint. For the beam H3, the bending cracks penetrated more profoundly into the material and caused damage to the UHPFRC layer.

19.4.4 Cracking in the interface zone

The measurements of interface cracks were performed with the LVDTs IS and IN, placed at the interface on the ends of the beams to measure the relative displacement between UHPFRC and concrete layer (see Figure 18.8). LVDT IS measured on the side of the beam, where the 10 cm had not been hydrojetted, LVDT IN on the side that was hydrojetted to the end. This system was used for the statically determinate beams and for the statically indeterminate beams with h_U = 3 cm. As the LVDTs measured the relative displacement between the old and the new layer on the sides of the beams, the LVDTs were only fixed on the beams after the removal of the formwork several days after the casting of the UHPFRC layer. Therefore, no conclusions can be drawn about early age interface cracking.

Figure 19.31 shows the measurements of the LVDTs IS and IN for the beams with h_U = 3 cm. The displacements of the LVDTs IS were higher than those of the LVDTs IN. The relative displacement between the layers was approximately 0.03 mm after 80 days, with the exception of I3 IS, where the final displacement was 0.04 m. No significant difference was observed between the statically determinate (Figure 19.31a) and indeterminate (Figure 19.31b) beams. LVDT I3 IS increased suddenly at a time of approximately 5 days, and LVDT H3 IS after approximately 60 days, indicating sudden crack growth at the interface. The displacement H3 IN increased until approximately 15 days and became smaller afterwards. The damage at the interface seems to reach a constant level after 15 days and no further interface damage was induced during the testing.

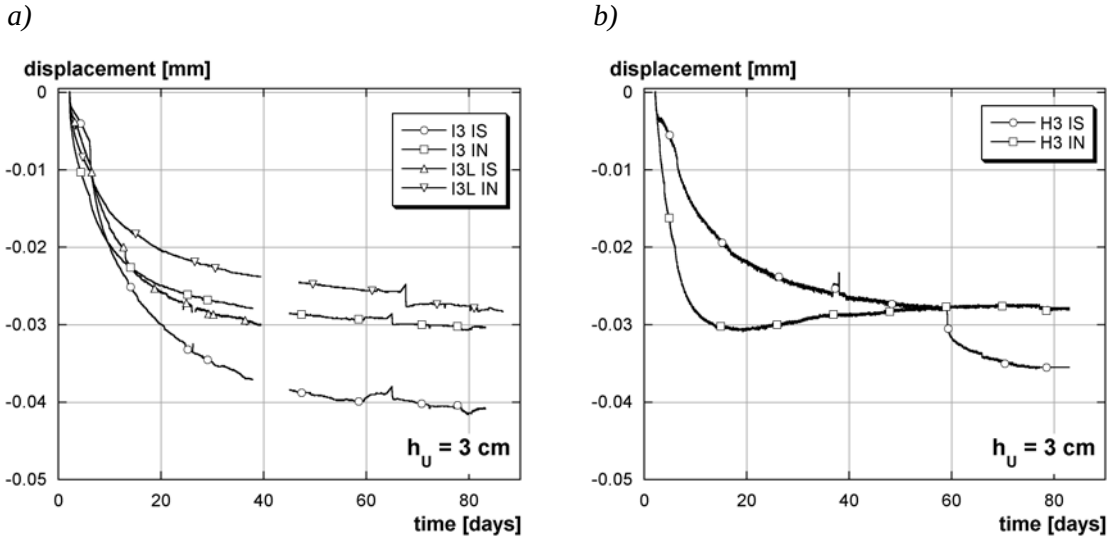

FIGURE 19.31: Debonding of the beams with h_U = 3 cm: a) I3: IS, IN, b) H3: IS, IN

The relative displacements at the interface for the beams with h_U = 5 cm reached a maximum value of 0.03 mm for the LVDTs IS and 0.015 mm for the LVDTs IN (Figure 19.32a and b). The displacements of the LVDTs IS were higher than of IN. The displacements of LVDTs IS were higher for the beams with reinforcement in the UHPFRC layer ($A_{s,U}$) than for the beams without $A_{s,U}$. This tendency was not confirmed by the measurements of the LVDTs IN where one beam with $A_{s,U}$ and one without $A_{s,U}$ had higher displacements at the interface than the other two.

The debonding measurements of the beams with h_U = 10 cm were also higher for the LVDTs IS than for the LVDTs IN (Figure 19.33). The beams with reinforcement in the UHPFRC layer ($A_{s,U}$) showed higher displacements than those without $A_{s,U}$, but, the difference was less pronounced than for h_U = 5 cm. The relative displacements of IN were smaller than for the beams with h_U = 5 cm and

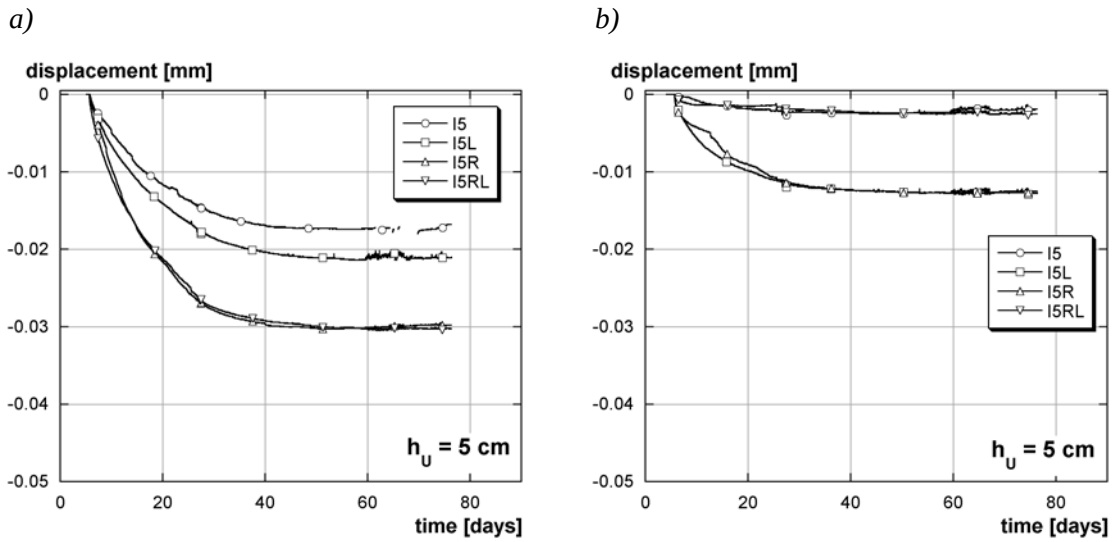

FIGURE 19.32: Debonding of the beams with h_U = 5 cm: a) IS, b) IN

were of the same order of magnitude for all the beams. No sudden increase was observed for the beams with h_U = 5 and 10 cm.

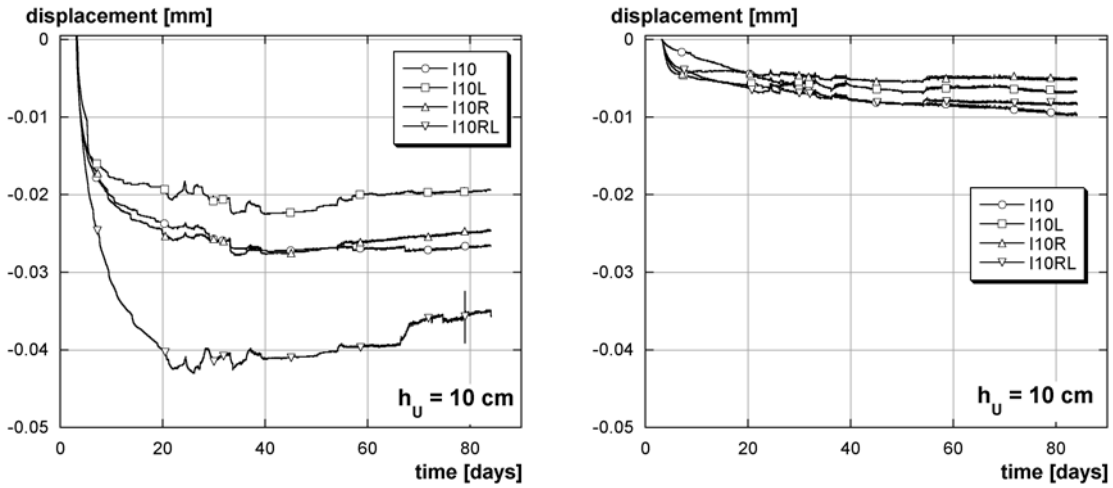

FIGURE 19.33: Debonding of the beams with h_U = 10 cm: a) IS, b) IN

The stronger debonding of the LVDts IS may be explained with the surface preparation of the beams. The last 10 cm of the interface at the side of LVDTs IS had not been prepared by hydrojetting, while the side of LVDTs IN was completely hydrojetted. The bad quality interface at IS favoured interface cracking and the relative displacements at the interface were higher.

The thickness of the UHPFRC layer did not significantly influence the debonding of IS, since the order of magnitude of the deformations was the same for the different thicknesses. However, the thickness influenced the relative deformations at the hydrojetted side (IN). The highest deformations were observed for the thinnest (h_U = 3 cm) and the lowest for the thickest beams (h_U = 10 cm). The higher deformations indicate stronger debonding at the interface.

Reinforcement in the UHPFRC layer led to higher interface cracks on the side of LVDTs IS, however, no influence was observed on the side of LVDTs IN. The increase of debonding was higher for the beams with h_U = 5 cm. The reinforcement stiffened the UHPFRC layer. When the monolithic behaviour of the element was reduced due to interface damage, this additional stiffness favoured interface cracking with increasing deflections. The reinforcement $A_{s,U}$ of the beams with

h_U = 5 cm was nearer to the interface than $A_{s,U}$ of the beams with h_U = 10 cm. The influence of the reinforcement on the behaviour in deformation of the interface was higher for h_U = 5 cm than for the beams with h_U = 10 cm leading to more interface cracking. This effect was not observed with the LVDTs IN because the damage of the interface was less important and the monolithic behaviour of the interface was sufficiently preserved to ensure a monolithic behaviour of the element. In addition, vertical cuts were performed at 12 cm from the non-hydrojetted end and at 5 cm from the hydrojetted end. No interface cracking was observed with the naked eye in the cut cross-sections.

The measurements of debonding are given in Appendix O.

19.4.5 Air permeability of the beams (Torrent tests)

The air permeability of the UHPFRC and the concrete was measured at the end of the long term tests of the first test series (h_U= 5 cm) with the Torrent test. The detailed test results can be found in Appendix P. Figure 19.34 shows the results of the Torrent tests on the non-damaged materials. All the measurements of the concrete were executed on non-damaged sections. Measurements of undamaged UHPFRC were taken on the statically determinate beams (I5, I5L, I5R, I5RL). All the measurements were considered except for one measurement of beam I5L that was taken on a cracked section.

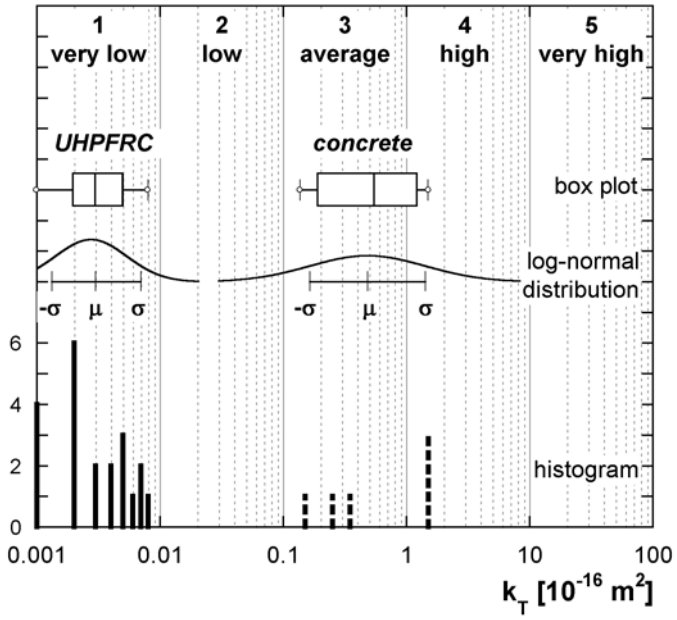

FIGURE 19.34: Results of the Torrent tests (h_U = 5 cm)

The air permeability of the *UHPFRC* was very low. The histogram shows the distribution of the measured values. The box plot shows that no outliers were observed for the UHPFRC. Finally, the test results are modelled with a log-normal distribution with a mean value of $k_T = 0.003 \cdot 10^{-16}$ m^2.

The values of the *concrete* were situated in classes 3 and 4, indicating that the concrete had an average to high permeability. No outliers were found for the concrete either. The mean value of the concrete was $k_T = 0.483 \cdot 10^{-16}$ m^2. Therefore, the air permeability of the concrete was “average” with a tendency to “high”.

Measurements on the UHPFRC were performed in cracked zones on the statically indeterminate beams (H5, H5R). The measured values (Table P.5 and P.6 in Appendix P) had a strong variability. As the crack widths in the tested zone could not be estimated accurately, no correlation was established between the values of the Torrent tests and the damage.

TABLE 19.10: Results of the WENNER tests

Material	Beam	ρ [kΩ cm]							Remarks
UHPFRC	H5	70	*144*	49	55	45	78	73	
UHPFRC	H5R	72	46	29	*158*	55	-	72	
concrete	H5R	infinite values							concrete too dry

The results of the Torrent tests were dependent on the electrical resistivity measured with the test after Wenner. The electrical resistivity was dependent on the moisture content in the cementitious material: the higher the electrical resistivity, the lower was the moisture content in the material. The air permeability of materials with an electrical resistivity lower than ρ = 25 kΩ cm was higher than for materials with an electrical resistivity higher than 25 kΩ cm. The Wenner tests were also modelled with a log-normal distribution. The mean electrical resistivity of the UHPFRC was 66 kΩ cm. All the measured values were higher than 25 kΩ cm. The Wenner test showed infinite values for the concrete, i.e. the concrete was very dry at the time of testing.

19.5 Fracture tests

The results of the fracture tests can also be found in Appendices Q to T.

19.5.1 Beams without reinforcement in the UHPFRC layer (NR)

Force-deflection diagrams. The force-deflection diagrams (Figure 19.35 and 19.36a) show the results of all the tested beams without reinforcement (NR) in the UHPFRC layer ($A_{s,U}$). The deflection at mid-span was calculated with the equation: deflection = $f_1 + 0.5 \cdot (f_6 + f_7)$.

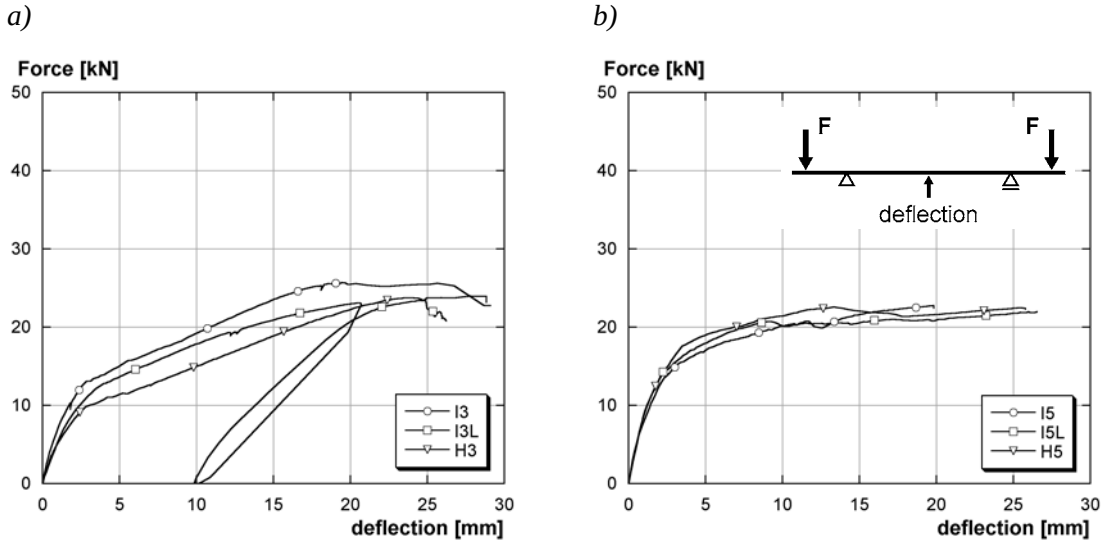

FIGURE 19.35: Force-deflection diagrams of the beams without $A_{s,U}$: a) h_U= 3 cm, b) h_U = 5 cm

Figure 19.35a shows the curves for the beams with h_U= 3 cm (NR3). Three periods could be observed during the test: First, the beams had a high stiffness until a deflection of approximately 2.5 mm. Then, the slope of the curves became smaller until a deflection of approximately 20 mm. Finally, the force remained constant and was reached at a deflection of 20 mm, until a decrease indicated the beginning of the final fracture of the beam. The beam H3 reached the end of the first period at a force of 10 kN and had the lowest stiffness. The highest stiffness was observed for the beam I3. The differences in stiffness may be explained with damage in form of microcracking, induced during the long term tests (cf. 19.4). The beam H3 was the only beam that showed visible bending cracks in the UHPFRC layer during the long term tests. The maximum force was 23 kN.

a) *b)*

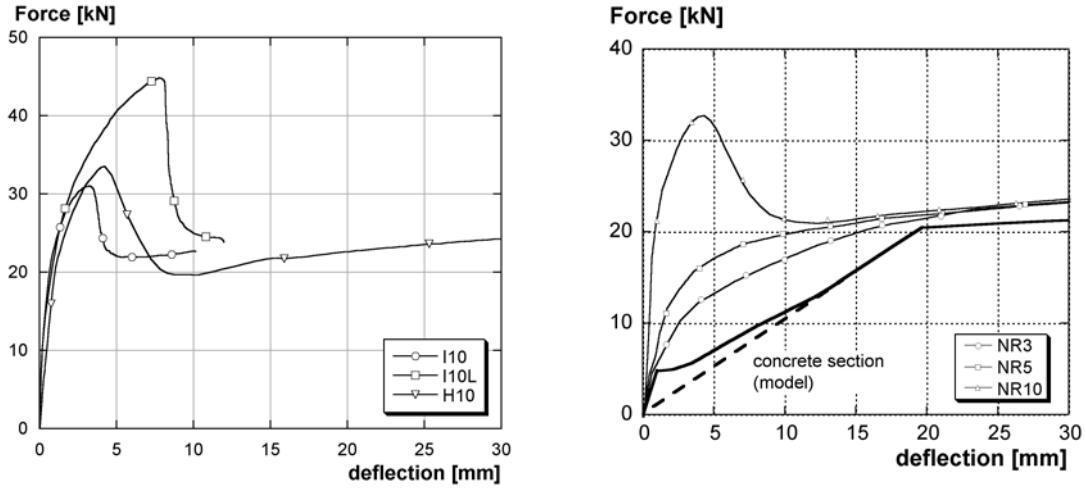

FIGURE 19.36: a) Force-deflection diagrams of the beams without $A_{s,U}$ for h_U = 10 cm, b) comparison of the force-deflection curves with the concrete section (mean curves)

The curves of the beams with h_U= 5 cm (NR5) were nearly identical (Figure 19.35b). The force increased monotonously until the end of the tests, just before the fracture of the tensile reinforcement of the beams. The maximum force was 21 kN at a deflection of 10 mm and remained constant until the final fracture of the beam. The similar curves of the three beams NR5 confirmed the observations during the long term tests with respect to damage.

The force, measured on the beams with h_U= 10 cm (NR10), did not increase monotonously until failure: a maximum was observed at a deflection of approximately 5 mm (Figure 19.36a). The maximum force varied between 31 and 45 kN and was between 30% and 90% higher than for beams NR3 and NR5. The deflection at the maximum force was higher for higher maximum forces (3.3 mm for 31 kN, 7.8 mm for 45 kN). After the maximum, the force decreased until a force of 21 kN. The deflections increased little during the decrease of the force. Finally, the force increased slowly until the final fracture of the beam, corresponding to the resistance of the original reinforced concrete section.

The higher maximum force of the NR3 for deflections higher than 15 mm was due to the higher age of its concrete substrate. The age of the concrete substrate was 250 days for the NR5, 370 days for the NR10 and 465 days for the NR3. The mechanical properties of the old concrete increased during this period (cf. Section 9), leading to a higher force for deflection higher than 15 mm.

The variability of the results was small for the NR5 and higher for the NR10. The variability of the beams NR10 may be explained with the variability of the material characteristics of the UHPFRC. As the UHPFRC layer of the NR10 was the thickest one, the influence of the UHPFRC on the maximum force was the highest. Differences in the fibre distribution led to differences in the resistance of the UHPFRC layer and therefore to different maximum forces.

Comparison with a reinforced concrete beam. Figure 19.36b shows the comparison of the beams without reinforcement in the UHPFRC layer (NR3, NR5 and NR10) with the force-deflection curve of a beam consisting only of the reinforced concrete (RC) layer before the UHPFRC was applied, e. g. a cross section of a 17*30 cm and the reinforcement $A_{s,low}$ and $A_{s,upp}$. The curves NR3, NR5 and NR10 of this figure are representative for the test results. The deflection was calculated with a cross-sectional analytical model for a bending beam; the deflection was determined by using the calculated strains. The dashed line of the analytical model indicates the supposed transition between state I and state II of the beam. The UHPFRC contributed until a deflection of approximately 20 mm (l/120). At this moment, the width of the main crack was so large that the transferred force may be neglected.

The main contribution of the UHPFRC was the increase of stiffness for deflection smaller than 20 mm. The curves of the beams with the UHPFRC layer were convex, the curve of the beam of concrete was concave. The convex curve can be explained with the hardening behaviour of the UHPFRC in tension. The UHPFRC layer acted as tensile reinforcement of the beam. The plasticity limit was smaller than for steel, but compared to traditional concrete with its softening behaviour, the UHPFRC represents a tremendous improvement. The concave behaviour of the RC beam was due to the softening behaviour of concrete that already reduced the stress transfer in the section for small crack widths, leading to a decrease in stiffness.

Measurements of the ODS. The ODS in the UHPFRC layer (ODS U) and in the concrete substrate (ODS L) recorded the mean deformation over a length of 200 cm in the central span of the beam (Figure 19.37). The deformations of ODS U increased during the whole test. The slope of the curve was steep until a deflection of approximately 0.75 to 1 mm. Afterwards, the deformations increased more rapidly. The deformation at the end of the tests were more than 13 mm. As the mean value over a length of 200 cm was measured, the crack openings were included in the measurements of the ODS.

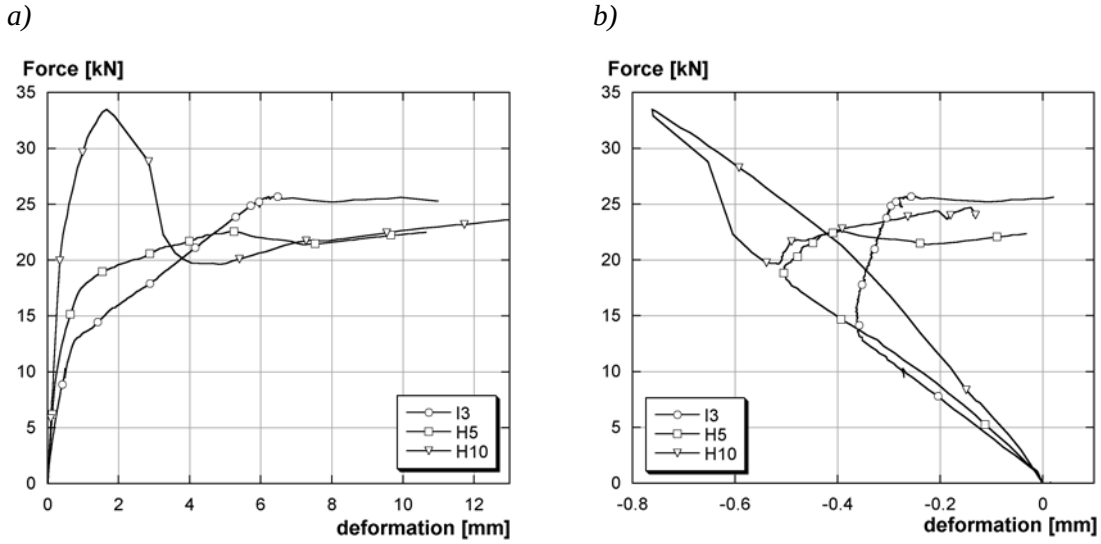

FIGURE 19.37: Force-ODS: a) ODS U, b) ODS L (beams I3, H5, H10)

The deformations, measured in the concrete substrate (ODS L), decreased at the beginning of the test and increased afterwards (Figure 19.37b). For the beams NR3 and NR5, the increase of deformation began shortly after the slope of the curves of ODS U changed (at 13 kN for NR3 and 19 kN for NR5); for the NR10, the increase began at the maximum force. The change of the deflection may be explained with the decreasing thickness of the compression zone of the beam. ODS L was situated at 3.4 cm from the lower side of the beam. When the compression zone became smaller than 3.4 cm, ODS L was in the tension zone of the beam, and its deformations increased. At the end of the tests, deformations of ODS L were an order smaller than those of ODS U. ODS L only measured deformations, while ODS U measured a mixture of deformations and crack openings.

Cracking of the beams NR. *Cracks, distributed* over the beam, developed in the tensile zone of the beam (in the UHPFRC) at a deflection of approximately 2 mm. These distributed cracks had small openings and were typical for a quasi strain-hardening material. When the maximum tensile force in the UHPFRC was reached in one of these small cracks, this crack opened further and developed into a localized crack. The localized cracks were observed with Ω-gages situated on the upper side and on the sides of the beam (plans in Appendix D).

The *localized cracks* of the beams *NR3* occurred at a deflection of 1.7 mm and a force of approximately 10 kN (Figure 19.38a). The force at the localization was less than half of the maximum force. Two cracks were observed with Ω_1 and Ω_7. After a strong increase of the displacement at the

beginning up to a CMOD of 0.4 mm, Ω_7 measured higher crack openings than Ω_1. Beyond the maximum force, the crack openings remained constant, indicating that final fracture occurred in neither of the two cracks.

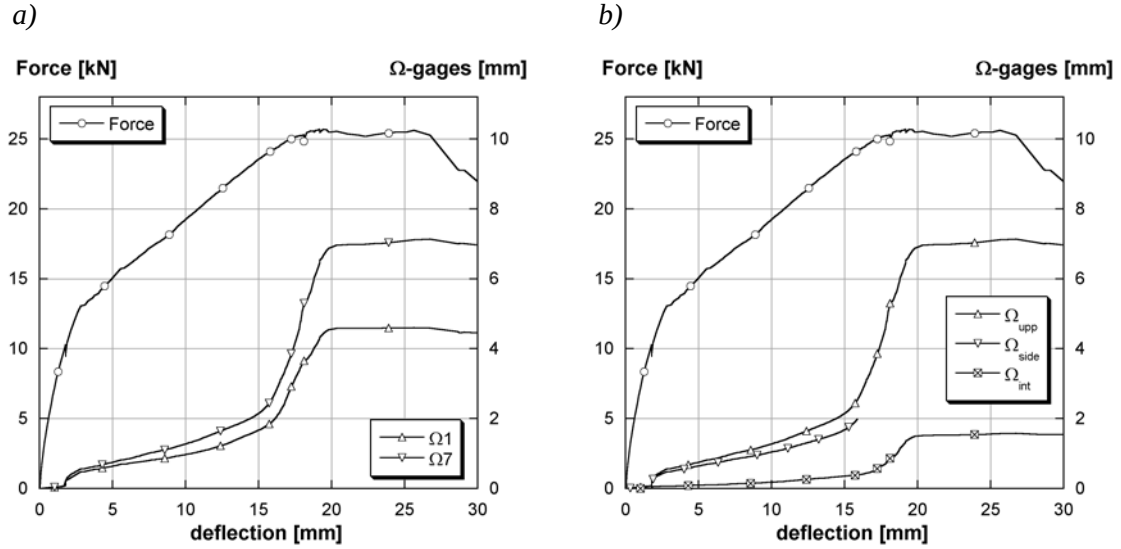

FIGURE 19.38: Crack openings, measured with Ω-gages of beam NR3 (H3): a) on the upper side, b) on the upper side and on the sides

The localized cracks of the NR3 developed over the whole thickness of the UHPFRC layer, as the values of Ω-gage Ω_{side} (at 2 cm from the upper side) increased at the same moment as those of Ω-gage Ω_{upp} (Figure 19.38a). As the Ω-gages on the sides had measuring ranges of 2 mm, they had to be removed during the test. Debonding in the interface zone was also observed from this time on. At a deflection of 16 mm, the rate of the crack opening increased, the crack opening became important with 7 mm at a deflection of 20 mm, and a crack width of 1.5 mm of the horizontal interface crack. Afterwards, the crack width stabilized. As the observed crack was situated above the supports of the beams that were equipped with 10 cm large steel plates, deformations were confined in the compression zone. The final failure (fracture of the rebars $A_{s,upp}$) could not take place in this section; it occurred in a crack in the middle of the beam. This crack formed after the two main cracks (due to the threads) and became only important shortly before the final failure of the beam.

Crack localization of the NR3 occurred always at places that were damaged by the previous long term tests or at weak spots of the beams. As the ODS were fixed with threads to the formwork, the treads ran perpendicular to the axis of the beams above the supports near the upper side in the UHPFRC layer. These threads were weak spots in the UHPFRC layer and forced the main cracks into these sections for the beams I3L and I3. The threads explain also the rapid increase of the crack width, when the cracks began to open. The threads cut the UHPFRC over a thickness of approximately 0.5 mm. When the zone above the threads cracked, there was no resistance over the thickness of the thread and the crack depth increased, with the consequence of larger crack openings (approximately 0.4 mm at the end of the period of fast crack growth). This fast development of the crack led to an energy release that could be heard during the testing. The beam H3 showed cracks perpendicular to the axis after the long term tests (cf. Section 19.4.2). The localized cracks developed out of these cracks.

Localized cracks occurred for the *NR5* and the *NR10* at a deflection of approximately 4 mm (Figure 19.39a) when the maximum force of the NR10 was reached and when the force of the NR5 was near its maximum. For all the beams of the same type (NR5 and NR10), the localization of the cracks started at the same deflection. The crack widths were higher for the NR10 than for the NR5. The higher thickness of the beams NR10 led to the higher crack openings for the same deflection. By comparing the ODS with the Ω-gages, it can be deduced that the localized macrocrack formed at

a deformation of the UHPFRC of 0.8‰ for beam H10. The results of the other beams indicate that crack localization occurred for beams NR at values between approximately 0.5 an 1‰.

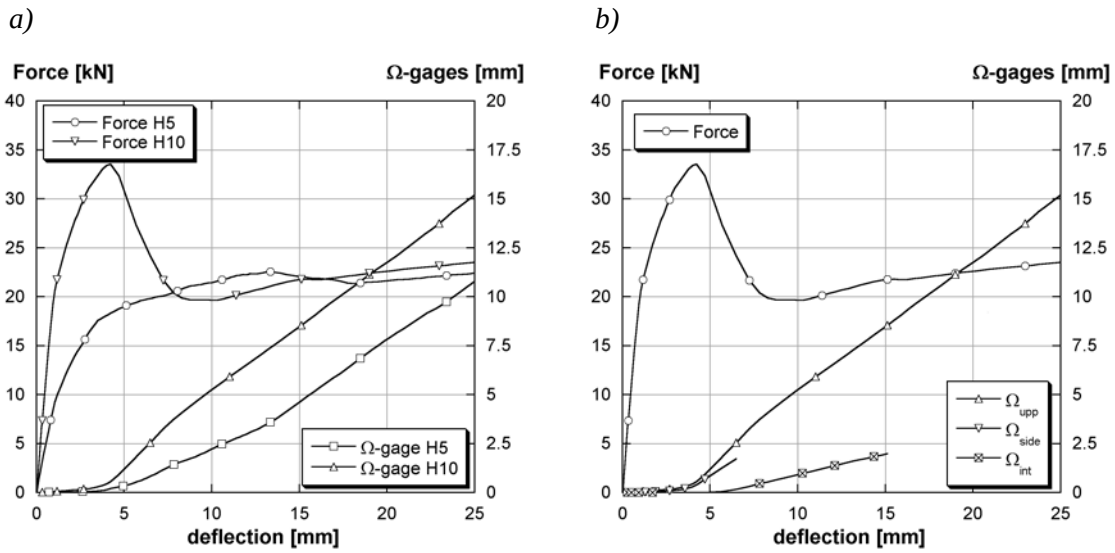

FIGURE 19.39: Crack openings, measured with Ω-gages: a) on the upper side (NR5 (I5), NR10 (I10)), b) on the upper side and on the sides (NR10 (H10))

The crack pattern was followed for one beam NR10 (I10) with three Ω-gages placed on the upper side and on the side of the beam (Figure 19.39b). The displacement, measured with the Ω-gage on the side of the beam (Ω_{side}, at 6 cm from the upper side of the beam), increased simultaneously with the gage fixed on the upper surface (Ω_{upp}), measuring slightly smaller values, e. g. the localized crack developed over the thickness of the UHPFRC layer.

From a deflection of approximately 6 mm on, horizontal *cracking in the interface* zone was observed with the Ω-gage perpendicular to the axis of the beam (Ω_{int}). Ω_{int} was situated at a distance of 5 cm from the vertical crack. The width of the interface crack increased monotonously with further deflection, indicating that no more tensile force could be transferred in this zone and suggesting strong debonding over an increasing length of the beam.

This was also confirmed by the crack patterns that could be observed visually during the testing: Figure 19.40a shows the crack path of a localized crack on beam NR10 at the end of the test with large crack openings. It can be stated that debonding with large crack openings occurred at the level of the upper reinforcement of the concrete substrate ($A_{s,upp}$) (Figure 19.40b), indicating that rebars near the interface weakened the concrete and favoured debonding. It has to be noted that the interface cracking of beams NR10 occurred, after the maximum force had been obtained and did not influence the maximum force.

Bending cracks occurred in the beams. The visible cracks were traced on the upper side of the beams with different colours to follow the evolution of the beams (Appendix T). One representative beam of each thickness of the UHPFRC layer was investigated in detail. The results of the crack evolution were shown in Table 19.11. The diagrams force-deflection f1 show the periods, during which the same colour was used on the beams. The table below gives the limits of the force and the deflection f1 for each period as well as the number of bending cracks in the central span of the beam and the number of cracks per meter.

The first bending cracks occurred at a deflection of approximately 1.3 to 2 mm. More and more cracks developed on the beams until the maximum force was reached. The beam NR3 had 3 major cracks at a force of 12 kN, being half of the maximum force; the beam NR10 had 3 major cracks at a force of 32 kN at 70% of the maximum force. The crack widths of NR3 increased rapidly (see Figure 19.38), whereas the opening of the cracks of the NR10 remained small, until the maximum force was reached (see Figure 19.39). The high crack openings of the NR3 may be explained with

a) *b)*

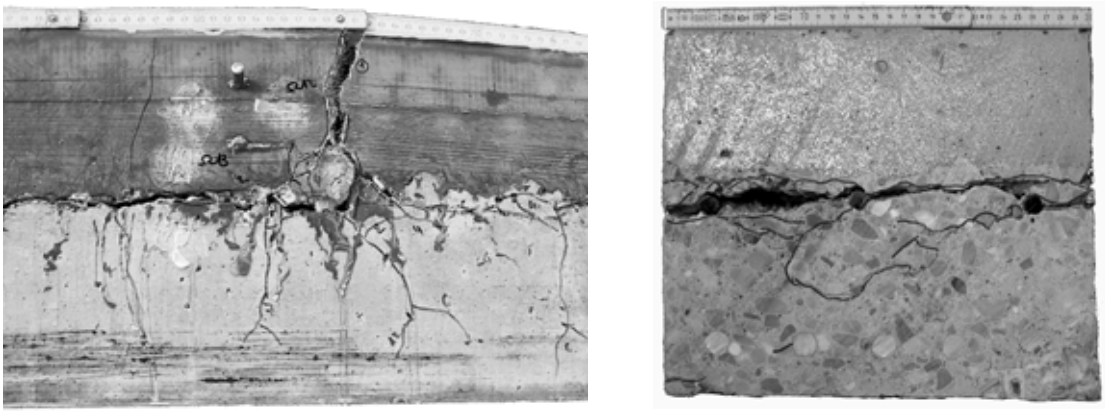

FIGURE 19.40: NR10: a) localized crack at the end of the test, b) debonding at the interface at 5 cm of the localized crack

TABLE 19.11: Cracking of the beams NR

NR3 (I3L)			NR5 (I5)			NR10 (I10L)		
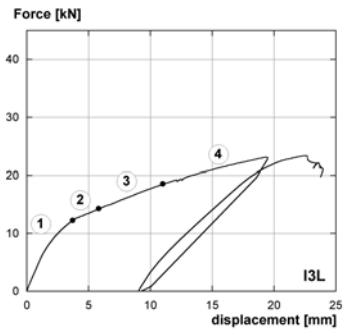			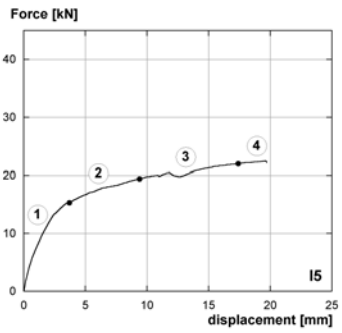			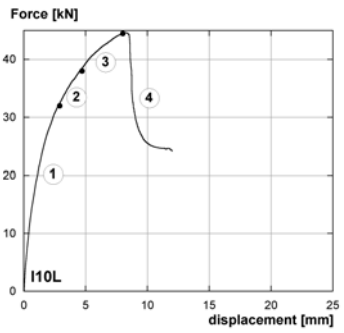		
Force / f1 [kN] / [mm]	cracks [-]	cracks [1/m]	Force / f1 [kN] / [mm]	cracks [-]	cracks [1/m]	Force / f1 [kN] / [mm]	cracks [-]	cracks [1/m]
1) 12.0 / 2.7	3	1.3	1) 15.3 / 3.7	4	1.4	1) 32.0 / 2.9	3	1.3
2) 14.3 / 5.1	7	3				2) 38.0 / 4.9	8	3.3
3) 18.8 / 9.7	14	6	2) 19.4 / 9.4	15	6.2	3) 44.5 / 8	18	7.5
			3) 22.0 / 17.4	17	7.1			
4)	15	6	4)	17	7.1	4)	21	8.8

the weak spots due to threads of the beams. When the maximum force was reached, approximately 6 cracks per meter occurred in the central span of NR3, 7.1 cracks per meter of NR5 and 8.8 cracks per meter of NR10. The higher the thickness of the UHPFRC layer, the more cracks occurred in the central span of the beam.

The crack patterns on the upper side of the beams were very complex (Appendix T). The cracks did not go straight from one side of the beam to the other. A lot of crack bridging and branching was observed. The crack openings stayed small because of the complex crack patterns and the high number of small cracks. The multiple cracking may be attributed to the quasi-strain hardening behaviour of the UHPFRC.

At the end of the development of the distributed cracks, the space between the cracks varied between 11 and 15 cm (Figure 19.41b). The space depended on the maximum stress on the upper side of the UHPFRC layer, on the fibre distribution in the UHPFRC and on the paths of already existing cracks. The fracture behaviour of the beams was accompanied by a strong debonding in the interface zone. When the width of the localized cracks increased, the tensile stress transfer across the

crack was reduced and the tensile stress had to deviate to the reinforcement of the concrete section $A_{s,upp}$. Tensile stresses perpendicular to the interface zone developed. Since the interface zone had the lowest tensile resistance, even relatively low tensile stresses were sufficient to cause debonding cracks. As the tensile stresses could not be transferred across the cracked interface any more, they had to deviate at a greater distance from the vertical localized crack and the debonding crack propagated further (Figure 19.41a).

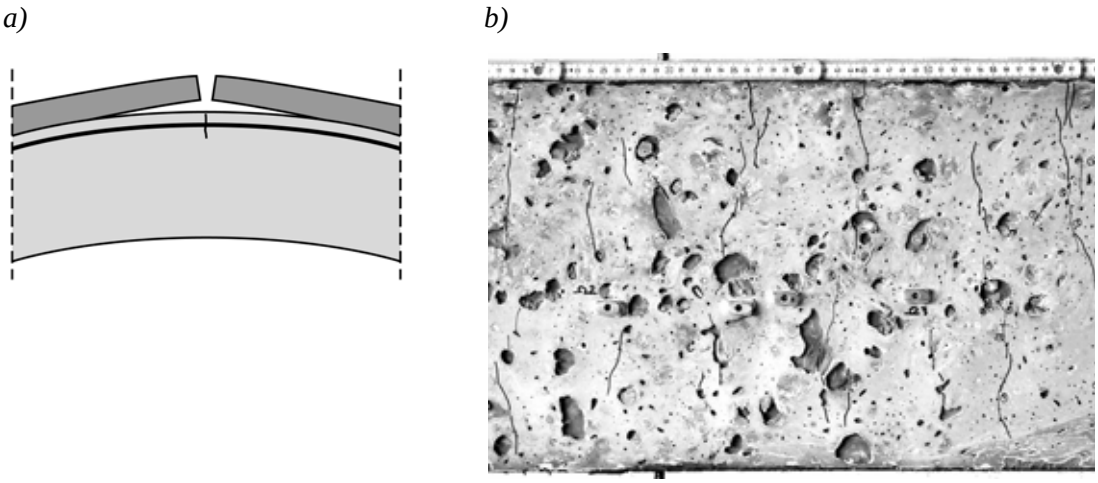

FIGURE 19.41: a) Failure principle, b) crack pattern (at the end of the test) of the beams NR

Fracture Mode. The fracture of the composite beams is described with five stages (Figure 19.42):

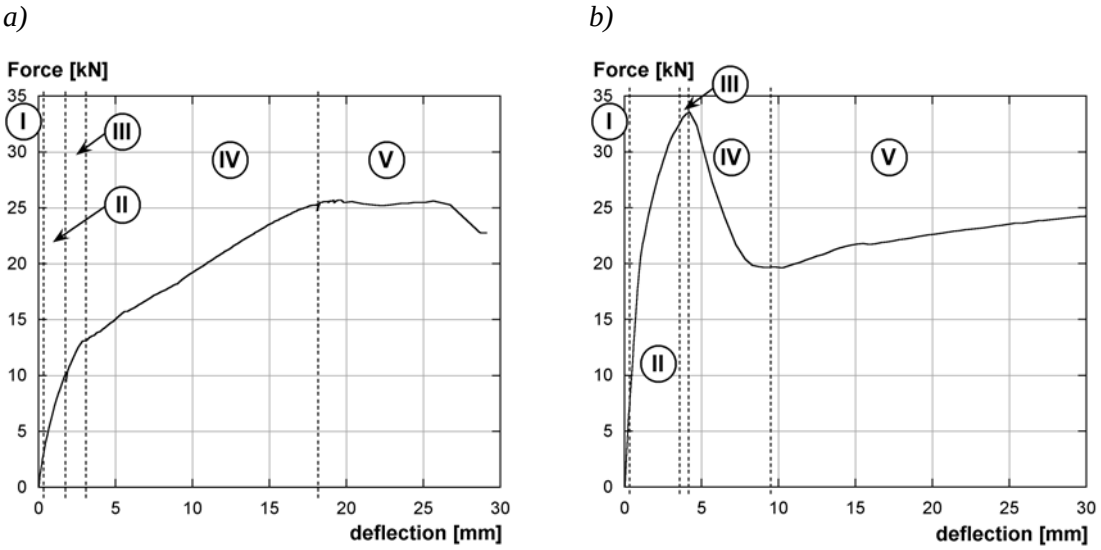

FIGURE 19.42: Schematic diagram of the fracture: a) NR3 (and also for NR5), b) NR10

I. In the beginning, the beams showed linear-elastic behaviour.

II. When the cracking threshold of the UHPFRC matrix was reached, distributed cracks developed in the UHPFRC. Because of the high amount of steel fibres, the force was transferred across the cracks. The tensile stresses continued to increase in the UHPFRC. New distributed cracks occurred until the ultimate resistance of the beam was reached.

III. Localized cracks developed from already existing distributed cracks at one or several places of the beam. These cracks occurred at deflections of 2 to 4 mm.

IV. When the localized cracks reached the interface, they went straight into the concrete substrate. Shortly afterwards, interface cracks developing into debonding in the interface zone were observed. The debonding was strong and increased monotonously.

V. The fracture of the beams was announced by large deformation and spalling in the compression zone. The simultaneous fracture of all the rebars in tension ($A_{s,upp}$) led to the final fracture of the beam.

19.5.2 Beams with reinforcement in the UHPFRC layer

Force-deflection diagrams. The force-deflection diagram (Figure 19.43a) shows the results of all the tested beams with reinforcement (R) in the UHPFRC layer ($A_{s,U}$) and the calculated curve for the concrete section (cf. Figure 19.36b on page 78). The reinforcement ratio of the rebars was constant when referred to the section of the UHPFRC layer and was $\rho_{s,U} = A_{s,U}/(b\ h_U) = 2.1\%$. This corresponded to an additional flexural reinforcement of $\rho_{s,U,bend} = A_{s,U}/(b\ h_{total}) = 0.5\%$ for the beams with h_U= 5 cm (R5) and $\rho_{s,U,bend} = 0.8\%$ for the beams with h_U= 10 cm (R10).

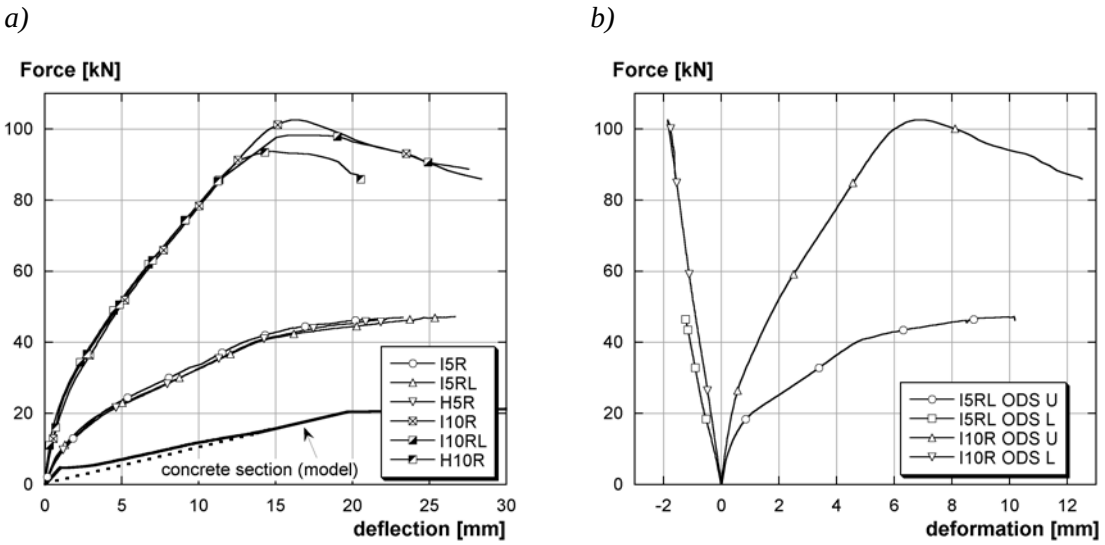

FIGURE 19.43: Beams with $A_{s,U}$: a) force-deflection diagram, b) force-ODS

Three periods were distinguished during the testing: First, the stiffness of the beams was high until a deflection of 2 mm. Then, the stiffness of the beams became lower and stabilized to a constant slope until a deflection of 15 mm. The final period, was characterized by a slowly increasing force for the R5 and a decreasing force for the R10 and led to the final fracture of the beams.

The first period of the beams with R5 finished at a force of 12 kN, the second at a force of 42 kN which was near the maximum force (46 kN) at a deflection of 25 mm. The force increased monotonously until the end of the tests. The maximum force was two times higher when compared to the concrete section. The R10 were stiffer than the R5 due to their higher thickness and the higher reinforcement ratio $\rho_{s,bend}$. The first period ended at a force of 23 kN, i.e. the maximum force of the concrete section. The second period ended at the maximum force which was between 93 and 103 kN - more than four times the maximum force of the concrete section and more than two times the maximum force of the NR10. Afterwards, the force decreased until the final fracture of the beams.

Measurements of the ODS. The deformations, measured with the ODS in the UHPFRC layer (ODS U), (Figure 19.43b) showed a similar behaviour as the force-deflection curves (Figure 19.43a). The measurements of ODS U indicated deformations of 10 mm over a length of 200 cm. The high deformations were a mixture of crack openings and deformations. The measurements of the ODS in the concrete substrate (ODS L) showed a linear decrease of deformations with

increasing force. The deformation at the maximum force was -1.8 mm for the R10 and -1.2 mm for the R5.When the force decreased for the R10, ODS L increased with the slope of the decrease.

The compression zone of the beams with $A_{s,U}$ was always thicker than 34 mm, since ODS L decreased monotonously for an increasing force. The deformation with localized cracks was concentrated in a band around the crack, therefore, ODS U, placed in the tension zone, measured the deformations and the whole crack width, the deformations in the compression zone were concentrated on a small volume of ODS L and did not significantly influence the measurements over the length of 200 cm.

Cracking behaviour. After the first period of high stiffness, *distributed cracks* occurred on the upper surface on the beams. These distributed cracks had small widths and occurred when the UHPFRC was in the quasi strain-hardening behaviour. The deformations, measured with the Ω-gages, were still small and comparable for the whole middle span of the beam (Figure 19.44a). Localized cracks occurred at a deflection of approximately 15 mm (l/120) - a deflection more than three times higher than the one of the beams without $A_{s,U}$ in the UHPFRC layer. At the *localization of cracking*, the force reached its maximum for the R10 and was nearly at its peak value for the R5. At this moment, the space between distributed cracks was 2 to 5 cm (Figure 19.46b). The localized crack opened over the whole thickness of the UHPFRC layer, since the values of the Ω-gage on the side of the beam (Ω_{side}, at 2.5 cm from the upper side) increased simultaneously with the Ω-gage on the upper side (Ω_{upp}) (Figure 19.44b). The comparison of ODS and W-gages showed that crack localization occurred for beams R at approximately 3‰.

a) *b)*

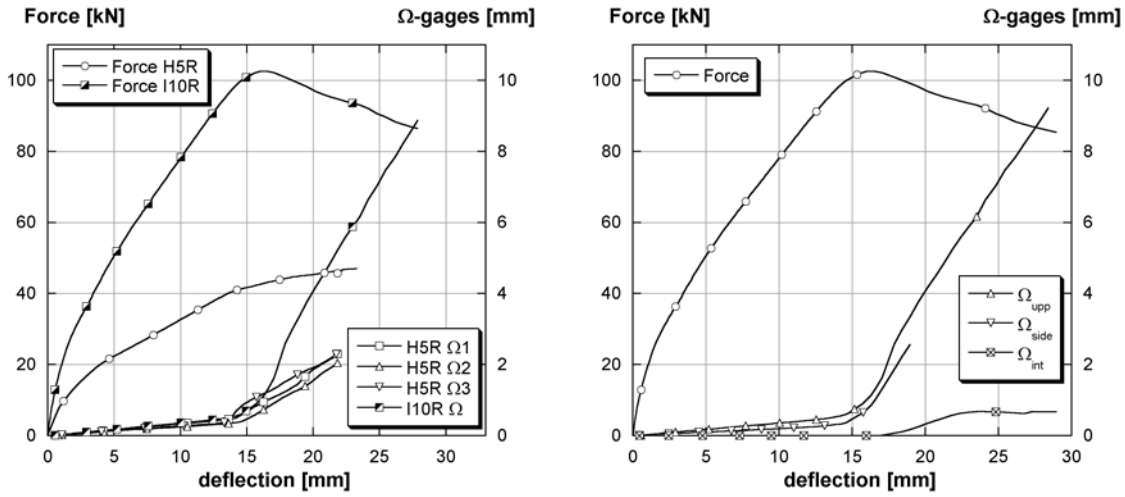

FIGURE 19.44: Crack openings, measured with Ω-gages: a) on the upper side (R5 (H5R), R10 (I10R)), b) on the upper side and on the sides (R10 (I10R))

Interface cracking started at a deflection of 17.5 mm (Figure 19.44b). The width of the interface crack increased until a deflection of 22 mm to a width of 0.6 mm. For higher deflections, the width stayed constant. In contrast to the beams without $A_{s,U}$ in the UHPFRC layer (Figure 19.39b on page 81), where the width of the interface crack increased monotonously, the interface crack of the beams with $A_{s,U}$ in the UHPFRC layer seemed to stabilized (Figure 19.44b).

Less interface cracking was observed for the beams R: the cracks went more directly into the concrete substrate (Figure 19.45a). As a part of the tensile stresses across the localized crack went through $A_{s,U}$, the part of the tensile stresses, which had to deviate to the rebars in the concrete section ($A_{s,upp}$), and the tensile stresses perpendicular to the interface were smaller. So, less debonding occurred for this configuration (Figure 19.46a). The debonding crack was at the level of the upper rebars in the concrete substrate ($A_{s,upp}$) (Figure 19.45b). The opening of the localized cracks led to

yielding in the rebars $A_{s,U}$, and the final fracture of the beam - the fracture of the rebars $A_{s,U}$ and $A_{s,upp}$ - was announced by high deformations of the beam and spalling in the compression zone.

a) *b)*

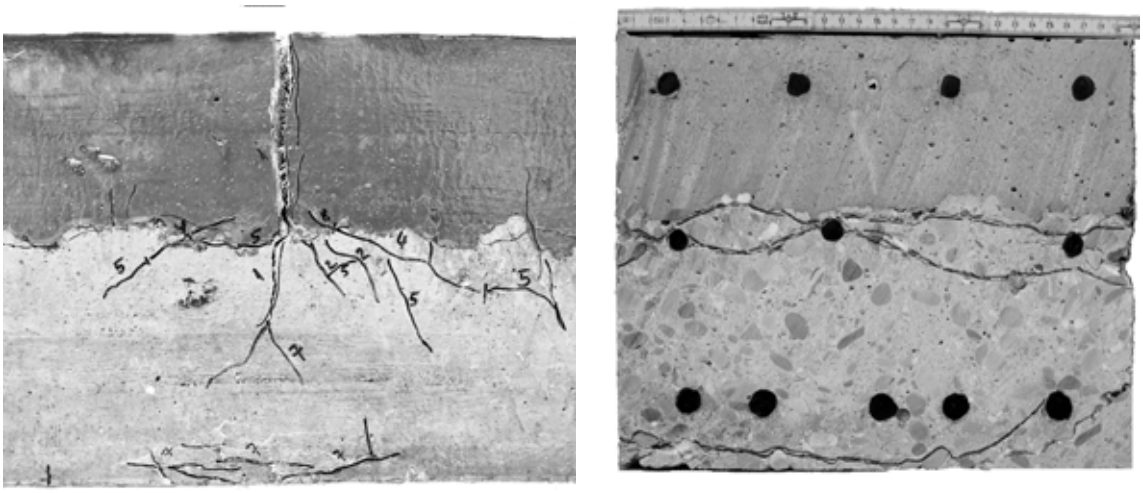

FIGURE 19.45: R10: a) localized crack at the end of the test, b) debonding at the interface at 5 cm of the localized crack

a) *b)*

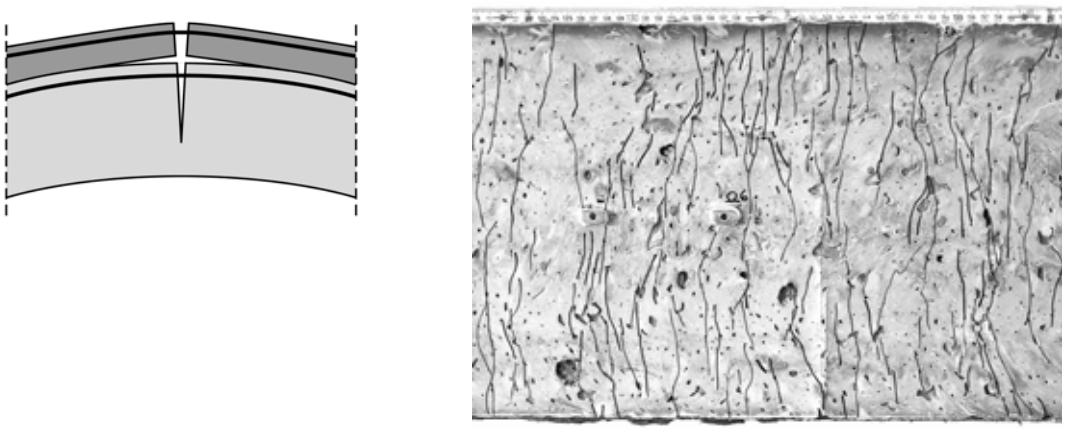

FIGURE 19.46: a) Failure principle, b) crack pattern (at the end of the test) of the beams R

The evolution of the *bending cracks* on the upper side of the beams was followed visually. The summary of the evolution of the crack pattern can be found in Table 19.12, the distribution of the cracks on the upper side of the beam in Appendix T. The values in Table 19.12 referred only to the central span of the beams. Due to pronounced crack bridging and branching, it was impossible to quantify the exact number of cracks. Therefore, the values in Table 19.12 are only approximate to give an idea about the crack pattern.

The beam R5 had 10 main cracks at a force of 20.8 kN, being 50% of the maximum force, the beam R10 had 21 main cracks at a force of 52 kN (50% of the maximum force). The main cracks began to open further at a deflection of approximately 14 mm (cf. Figure 19.44a). At this moment, approximately 14 cracks per meter could be found on beam R5 and approximately 18 to 20 cracks per meter on beam R10. As the crack patterns were complex (bridging and branching), the cracks were found every 3 to 5 cm.

Fracture Mode. The fracture behaviour of the composite beams may be described in five stages (Figure 19.47):

TABLE 19.12: Cracking of the beams R

R5 (H5R)			R10 (I10R)		
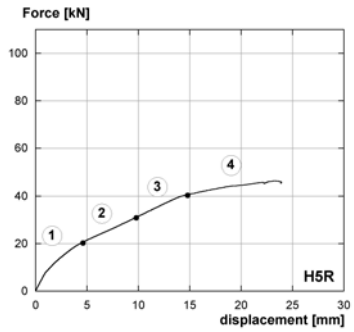			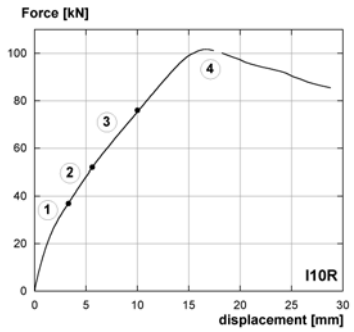		
Force / f1 [kN] / [mm]	cracks [-]	cracks [1/m]	Force / f1 [kN] / [mm]	cracks [-]	cracks [1/m]
1) 20.8 / 4.6	10	4.2	1) 37.0 / 3.3	11	4.6
			2) 52.0 / 5.6	21	8.8
2) 30.9 / 9.8	28	11.7	3) 76.0 / 10.0	29	12.1
3) 40.4 / 14.8	33	13.8			
4)	43	18	4)	50	20.8

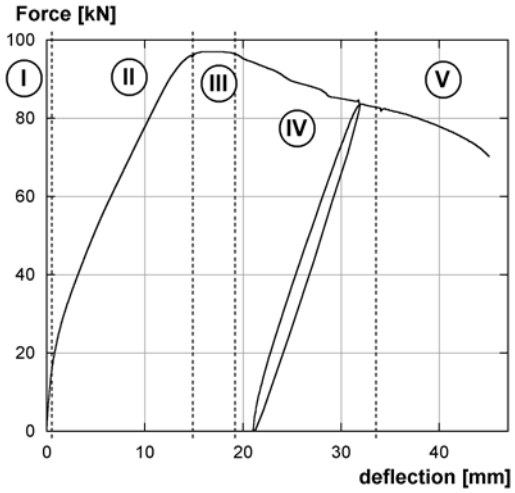

FIGURE 19.47: Schematic diagram of the fracture

I. In the beginning, the beams showed linear-elastic behaviour.

II. When the cracking threshold of the UHPFRC matrix was reached, distributed cracks developed in the UHPFRC. Because of the high amount of steel fibres, the force was transferred across the cracks. The tensile stresses continued to increase in the UHPFRC. New distributed cracks occurred until the ultimate resistance of the beam was reached.

III. Localized cracks developed from already existing distributed cracks at one or several places of the beam. These cracks occurred at deflections of 15 mm.

IV. When the localized cracks reached the interface, they went straight into the concrete substrate. Shortly afterwards, the formation of interface cracks was observed, however, these cracks stabilized and did not lead to local debonding.

V. The fracture of the beams was announced by large deformations and spalling in the compression zone. The simultaneous fracture of all the rebars in tension ($A_{s,U}$, $A_{s,upp}$) provoked the final fracture of the beam.

20 Conclusions from the beam tests

20.1 Processing

- The *fabrication* of composite "UHPFRC-concrete" elements was identical to the one of composite concrete elements. The UHPFRC was produced in a laboratory mixer without difficulty: it was self-compacting and cast with a skip. The steel fibres were slightly orientated in axial direction as a result of the casting mode.
- The *preparation of the contact surface* of the concrete by hydrojetting proved to be a good surface preparation method. No debonding was observed at the contact surface between concrete and UHPFRC. Fracture in the interface zone always occurred in the old concrete. Thus, a surface preparation method should be chosen that induces the least damage in the concrete. As the contact zone proved to be very good, it should also be possible to use surface preparation methods leading to a lower roughness of the contact surface. However, the contact surface has to be prepared before casting an UHPFRC layer, since barely visible interface cracks occurred in all the beams at the small non-hydrojetted surface.
- Adequate *curing* was necessary to minimize damage. It is necessary to prevent water exchange between the cementitious material and the surroundings. The used UHPFRC composition had a *delay of setting* of one day. During this period, the UHPFRC was still soft and had to be protected from drying. Thus, it is proposed to cure the UHPFRC at least by covering free surfaces with plastic sheets. The skin layer of the UHPFRC may even have better properties when humid, but not wet, textile sheets are applied during at least 5 to 7 days.

20.2 Testing

The results on the beam tests gave consistent results. Deformations, forces and cracking could be well followed with the test set-up. However, there were some minor points that should be improved in future tests.

- The ambient *climatic conditions* during the long term tests were aimed to be constant with a temperature of 20 ± 1 °C and a relative humidity of 40%. However, the scatter of the relative humidity was high and had a maximum variability of 15%. Thus, the isolation of the used climatic tents was not sufficient to ensure constant climatic conditions and the climatic control parameters had to be regularly adjusted.
- In the statically indeterminate beams, the major part of the additional restraint was attributed to the *fixation of the supports in vertical direction*. The fixation in vertical direction worked as planned and the bending deformations were restrained by the supports. The vertical restraint increased the bending part of the degree of restraint of 87.5%.
- The *fixation of the central supports in horizontal direction* was only partially efficient due to the insufficient stiffness of the experimental set-up in horizontal direction. So, horizontal deformations were observed in the central span of the statically indeterminate beams, but these deformations were lower than for the statically determinate beams. Total restraint in horizontal direction can only be achieved by using an active system.
- The *measurements* started before casting the UHPFRC layer. Thus, temperatures and deformations could already be recorded for the very early age of the UHPFRC layer. Before setting, the deformations in the UHPFRC layer could be qualitatively followed with the optical deformation sensors (ODS).

- The beams were equipped with two *optical deformation sensors* placed in the UHPFRC and the concrete substrate respectively in order to measure mean central span deformations and curvature. A third optical deformation sensor at the height of the upper reinforcement of the concrete substrate ($A_{s,upp}$) would have been beneficial in order to follow the profile of deformation in the cross-section of the beams and to better determine whether and when debonding occurred.
- The LVDTs that were installed to measure the *horizontal deformations* of the beams during the long term tests did not give valid results, since the measuring system was too much influenced by external factors and by the curling of the beams. The deduction of horizontal deformations and debonding with LVDTs is only possibly when equipping the structural elements with more sensors.
- The deformations of the *statically indeterminate beams* were small. The *reactions* of the supports were not measured and the interaction between stresses and deformations must be investigated by inverse analysis. It would have been beneficial to record the reaction forces at the supports to determine better the interaction between deformations and stresses in the statically indeterminate system.
- Cracking was observed visually during the early age and long term tests. During the fracture tests, cracking was also observed visually and with Ω-gages fixed on the upper side and on the sides of the beams. It would have been interesting to investigate crack patterns and widths more in detail for example with optical methods. However, the high number of fine cracks in the UHPFRC makes an exact mapping and evaluation of cracking difficult.
- The *time span of the creep tests* was short with 7 weeks. The tests started at an age of the UHPFRC layer of 28 days when the properties still changed. Creep should have been measured for at least 3 months and end after the stabilizing of the deformations in the UHPFRC layer which was at approximately 90 days after casting. The measurements of the creep recovery were also too short, since only the elastic part of the recovery could be estimated due to the short period of measurements of creep recovery. However, conclusions could be drawn with regard to microcracking induced by the creep loading.
- The *TORRENT measurements* on the UHPFRC were difficult to conduct due to the uneven surface of the UHPFRC. Air bulbs at the surface made it difficult to place the measuring device. Furthermore, the permeability of the UHPFRC was so low, that the lower limit of the measuring range was reached in some cases.

20.3 Early age and long term tests

20.3.1 Early age of the concrete substrate

- The *temperature evolution in the concrete substrate* at early age shows that the maximum temperature on the beams was between 27 and 38 °C. This was due to the external heating at early age, which led to a temperature rise of approximately 15 °C. The beams cooled down to ambient temperature of approximately 10 °C in a period of 2.5 days.
- No visible cracks were observed on the beams at their arrival at the EPFL 4 days after casting.

20.3.2 Early age of UHPFRC layer

- The *maximum early age deformations* were reached one hour before the maximum temperature was reached. In the beginning, the beams expanded due to the temperature rise, afterwards, the temperature decreased and self-desiccation led to contraction of the beams. The *interaction* of autogenous shrinkage and deformations due to heat of hydration was observed during the beam tests. Self-desiccation started before the maximum temperature was reached and reduced the peak of deformations.
- The *setting point* of the UHPFRC was defined as the point when the measurements with the optical deformation sensors indicated a monolithic behaviour of the beams. The setting point was

reached at the beginning of the temperature rise due to hydration of the UHPFRC at approximately 24 hours after casting.

- The early age was the *critical period* for the beams. Most of the deformations and cracks occurred during this period. In combination with the relatively low strengths of the UHPFRC during this period, cracking was likely to occur during the first 7 to 10 days after casting.

20.3.3 Degree of restraint (influence of the static system)

- The *calculated degree of restraint* at 28 days varied between 0.41 and 0.51 for the statically determinate beams and between 0.53 and 0.76 for the statically indeterminate beams. This values did not consider the additional restraint in horizontal direction, since the fixation of the horizontal supports only worked partially.
- The static system influenced significantly the *bending deformations* of the beams: deflections and curvature were more than 10 times higher for the statically determinate beams (I) than for the statically indeterminate beams (H).
- The influence of the static systems on the *axial deformations* was only 5 to 15%. The small difference in the axial deformations indicated that only partial restraint was obtained with the passive horizontal system of the supports of the statically indeterminate beams.
- The degree of restraint was influenced by the proportion of the *thicknesses* of the concrete and the UHPFRC layer: the higher the thickness of the UHPFRC layer, the lower the degree of restraint.
- The supports of the statically indeterminate beams were loosened at the end of the long term tests. The *recovery* of deflections and curvature after the loosening did not reach the deformations of the statically determinate beams. This may be interpreted as viscoelastic deformations provoked by the statically indeterminate system.

20.3.4 Influence of the thickness of the UHPFRC layer

- An increasing thickness of the UHPFRC layer induced higher *deformations* in the statically determinate beams - the deflections of the beams with h_U = 10 cm were two times higher than for the beams with h_U = 3 cm. This is attributed to the lower degree of restraint and to the higher temperature gradient at early age. A significant increase in longitudinal contraction of the statically indeterminate beams was observed with increasing thickness of the UHPFRC layer: the axial deformations of H10 were four times higher than of H3 and reached a value of -200 μm/m after 70 days.
- *Damage* at early age may be induced in thin layers with high degree of restraint (beam H3). Therefore, the interaction between deformations, loading and restraint has to be investigated when thin layers were used.

20.3.5 Influence of additional reinforcement in the UHPFRC layer

- Reinforcement in the UHPFRC layer $A_{s,U}$ reduced *bending and axial deformations*. The deflection of the statically determinate beams with $A_{s,U}$ and h_U = 10 cm (I10R) was 25% lower than for the beams without $A_{s,U}$ (I10), while no significant difference was observed for the beams with h_U = 5 cm (I5, I5R). The reinforcement in the UHPFRC layer was placed distantly from the concrete substrate. Thus, the restraint of the reinforcement was more important for thicker UHPFRC layers.
- Reinforcement in the UHPFRC layer $A_{s,U}$ induced *additional restraint* at the surface of the UHPFRC and therefore higher stresses in the UHPFRC during the long term tests. When the stresses exceeded the tensile strength of the UHPFRC matrix, cracking occurred in the UHPFRC, leading to a lower stiffness and higher deflections of the structural elements. This was the case for the beams with h_U = 10 cm: The stress level in the UHPFRC layer of beam I10R stayed below the

tensile strength of the UHPFRC matrix and the additional reinforcement $A_{s,U}$ decreased the deformations, while the stress level of beam H10R exceeded the tensile strength of the UHPFRC matrix and the deformations were increased due to damage in the UHPFRC matrix.

- No *stirrups or connectors* between the UHPFRC and the concrete substrate were necessary to guarantee monolithic behaviour of the elements until the maximum load was reached.

20.3.6 Flexural creep

- The *load level* during the creep tests was high, inducing additional tensile stresses of 4.5 MPa (at the upper fibre of the UHPFRC layer) into beams I5L and I5RL and 6 MPa into beams I3L, I10L and I10RL.
- The *creep compliance* was in the range of concrete beams [Bernard00]. Slight damage was observed for the beams with the higher load level (I3L, I10L and I10RL), while no damage was observed for the beams with the lower load level (I5L, I5RL). The creep compliance indicates that the creep deformations did not stabilize during the test period.
- The time span of the *creep recovery* measurements after unloading was short. However, the recorded data was sufficient to evaluate damage in the beams due to the loading. Damage is suspected in beams I3, I10 and I10R, where the deformations at unloading were significantly smaller than at loading. No such clear observations were made for beams I5 and I5R, which remained probably undamaged during creep.

20.3.7 Crack formation

- *Surface cracks* were detected during the tests. Most of the cracks were orientated in transversal direction. The major part of crack formation depended on the casting of the UHPFRC, since no correlation between the test parameters and the crack distribution could be observed. Cracks in longitudinal direction also formed, indicating a slight fibre orientation in longitudinal direction. Only on beam H3, two transverse cracks due to early age deformations were observed which may be attributed to its high degree of restraint.
- The major part of the surface cracks formed until an *age* of the composite beam of 14 days.
- *Debonding* was observed on all the beams at the small non-hydrojetted surface at one end of the beams during the early age and long term tests. The contact surface of the existing concrete must therefore be prepared before the casting of the UHPFRC layer. Slight debonding was observed on the hydrojetted end of the beams. The crack openings stayed small (< 50 μm) and the structural behaviour of the beams was not altered. Debonding always occurred in the existing concrete at a distance of 0 to 2 cm from the contact surface. The adherence between concrete and UHPFRC was perfect in case of surface preparation by hydrojetting, since nearly no fracture occurred at the contact surface (< 5% of the contact surface).
- Reinforcement in the UHPFRC layer $A_{s,U}$ increased the number of surface cracks during the long term tests.

20.3.8 Physical properties

- The *air permeability* of the UHPFRC was very low at the non-damaged zones. It was two to three orders of magnitude lower for the normal strength concrete. The low permeability of UHPFRC significantly hinders the ingress of detrimental substances into the structural elements.

20.4 Fracture tests

20.4.1 Influence of the thickness of the UHPFRC layer

- The *stiffness* of the beams was increased by the UHPFRC layer. The strain hardening behaviour of the UHPFRC, leading to distributed cracks, was responsible for the increased stiffness of the

composite beams. The deformations were distributed over the whole composite beam, i.e. no localized cracks formed.

- *Localized cracks of the NR3* occurred at a force of 10 kN, being less than half of the maximum force. The localized cracks of the NR5 and NR10 formed near the maximum force at a deflection of 4 mm.
- The *maximum force* of the beams was *increased* when the UHPFRC layer was thicker than a threshold value of h_U (between 5 and 10 cm for the tested beams): The increase of the maximum force for the NR10 was always more than 30%. The variability of the force increase was high, ranging from 30 to 90%. These differences may be explained by the inhomogeneity of the fibre distribution in the UHPFRC layer. One section with less fibres orientated in the direction of the tensile stresses was enough to form a weak zone in the layer and to cause cracking in the section.
- The force dropped quickly *after having reached its maximum for the NR10*. After an exceeding of deformation, one to five localized crack formed in the beams and the ultimate resistance was controlled by the reinforced concrete.
- Beam H3 was *damaged* during the long term tests, since it had a lower stiffness than I3 and I3L. No damage could be observed for the beams with thicknesses of the UHPFRC layer of 5 and 10 cm.

20.4.2 Influence of reinforcement in the UHPFRC layer

- Reinforcement in the UHPFRC layer ($A_{s,U}$) increased the *maximum force* of the beams during the fracture tests. A reinforcement of $\rho = 2\%$ of A_{UHPFRC} doubled the maximum force of the beams with $h_U = 5$ cm and quadrupled the maximum force of the beams with $h_U = 10$ cm when compared to the original reinforced concrete section respectively.
- Reinforcement in the UHPFRC layer led to finer *crack distribution* in the UHPFRC layer. The continuous rebars distributed the deformations evenly over the central span. So, inhomogeneities of the UHPFRC were balanced and localized cracks occurred at an average strain of the upper UHPFRC fibre of approximately 3 ‰, corresponding to a mid-span deflection of 15 mm. In comparison, localized cracks occurred on the beams without $A_{s,U}$ at a deflection of 4 mm at less than 1 ‰. Thus, the *interaction of UHPFRC and rebars* proved to be effective. Rebars increase the resistance of the structural element and lead to later occurrence of localized cracks.
- No stirrups or connectors between the UHPFRC and the concrete substrate were necessary to guarantee monolithic behaviour of the elements until the maximum load was reached.

20.4.3 Crack formation

- *Distributed bending cracks* formed during loading until the maximum force. These cracks had small crack openings (< 50 μm) and were spaced regularly in the central span of the beams. At the maximum force, cracks were observed every 10 to 15 cm for the beams NR and every 1 to 5 cm for the beams R.
- The distributed cracks in the UHPFRC layer had complex *crack patterns.* The high amount of steel fibres and their slightly uneven distribution led to this crack formation, since the cracks followed the path with the least amount of fibres and thus the smallest tensile strength.
- *Localized cracks* formed at a mid-span deflection of 4 to 7 mm (L/600) for the beams without $A_{s,U}$ and at 15 mm (L/160) for beams with $A_{s,U}$. Localized cracks formed at lower deflections for the beams with a thickness of the UHPFRC layer of 3 cm, but, these cracks always occurred at weak spots of the layer caused by the fixation of the optical deformation sensors (ODS).
- Monolithic behaviour of the beams was observed until the localized cracks reached the interface. Then, *interface cracks* formed. They developed into local debonding for beams NR and changed the structural behaviour. They stabilized rapidly for beams R and did not change their structural behaviour.

Part V
Conclusions

21 Material characterization of the UHPFRC

The material tests on the UHPFRC and concrete characterized the evolution of their physical properties, its mechanical properties and its time-dependent deformations.

The main *advantages* of the UHPFRC when compared to the concrete were:

- the simplified casting technology, (the UHPFRC was self-compacting, the concrete had to be vibrated)
- the *high compressive strength*,
- the significantly improved *tensile properties*,
- mechanical properties and shrinkage *became virtually constant after 90 days* and
- the *low permeability.*

However, the UHPFRC had also *disadvantageous properties* when compared to the concrete:

- The *heat of hydration* was higher, but it did not lead to a significantly higher temperature rise in the slender elements.
- The *strong self-desiccation* at early age caused *high autogenous shrinkage* of the UHPFRC which is the main driving force for internal UHPFRC deformations. However, drying shrinkage in the concrete was higher than the autogenous shrinkage of the UHPFRC.

Overall, the UHPFRC had significantly improved properties when compared to the concrete. The deformations due to internal thermal and hygral changes (mainly at early age) were higher than for normal strength concrete and may lead to higher stresses in case of restraint or gradients. However, thanks to the high strengths and the hardening behaviour in tension, UHPFRC withstand these actions without damage.

22 Structural testing

22.1 Processing

- The *processing* of composite “UHPFRC-concrete” beams was comparable to the one of composite concrete beams. Since the UHPFRC was self-compacting, casting proved to be easy.
- An adequate *preparation of the contact surface* was necessary to ensure monolithic behaviour of the composite elements. The preparation method should provide sufficient roughness and minimize damage in the existing concrete support. Hydrojetting proved to be an adequate surface preparation method.
- *Curing* was important: drying of the UHPFRC layer must be prevented during the first 5 to 7 days after casting.

22.2 Testing

- The fixation of the *supports* of the statically indeterminate beams was efficient in vertical direction. In horizontal direction, the supports restrained only partially the deformations.
- The *measurements* of deformation and temperature started before the casting of the UHPFRC layer. So, early age temperature changes and deformations could be successfully recorded. The chosen test methods proved to be efficient to describe the time-dependent behaviour and the structural response of the composite beams. However, it would have been interesting to better follow crack patterns and widths, especially in the domain of hardening of the UHPFRC, and to record the support reactions of the statically indeterminate beams (H).

22.3 Main results of the tests on the composite “UHPFRC-concrete” beams

- *Static system:* The bending deformations of the statically indeterminate beams were more than 10 times lower during the long term tests, but, their increased restraint of deformation led to higher stresses. The stresses reached the first cracking strength of the UHPFRC in beam H3, where bending cracks were observed during the long term tests, while no such cracks were observed for the statically determinate beams I3 and I3L.

- *Thickness of the UHPFRC layer (h_U):* The thicker the UHPFRC layer, the higher were the deformations of the beams during the long term tests. The deformations due to thermal changes and autogenous shrinkage in the UHPFRC governed the deformations of the beams.

  During the fracture tests, the stiffness of the beams was increased by a thicker UHPFRC layer. Moreover, the UHPFRC layer increased the resistance of the beams when it was thicker than a threshold value lying between 5 and 10 cm for the given beam configuration. The high fracture energy of UHPFRC led to a higher energy release during the fracture tests of the composite “UHPFRC-concrete” beams.

- *Reinforcement in the UHPFRC layer ($A_{s,U}$):* During the long term tests, reinforcement in the UHPFRC layer reduced the deformations. The decrease of deformations was mainly observed for the beams with h_U = 10 cm. The reinforcement induced supplementary restraint in the UHPFRC layer and induced higher stresses. In combination with a high degree of restraint (e. g. by the static system), damage may occur in the UHPFRC. This damage could be observed on beam H10R that had more visible (surface) bending cracks and higher deformations during the long term tests than H10.

  During the fracture tests, reinforcement in the UHPFRC layer $A_{s,U}$ increased the resistance of the beams, since it was placed in the tension chord. The distributed cracks in the UHPFRC (< 50 μm) were more densely distributed, and localized cracks appeared near the maximum force at three times higher deflections.

- *Creep:* Damage due to loading was induced into the beams with the high load level (beams I3L, I10L, I10RL). The creep compliance indicated that the creep deformations did not stabilize during the test period. The order of magnitude of the creep compliance was in the range of composite concrete elements.

- *Cracking*: During the long term tests, only surface cracks occurred on the beams. H3 - the beam with the highest restraint, was an exception, since two bending cracks formed in the UHPFRC layer.

  During the fracture tests, distributed bending cracks occurred. When the maximum force was reached, one or several cracks with large crack openings formed. Failure occurred in one of these localized cracks.

- *Interface cracks and debonding*: No significant interface cracking was observed during the long term tests.

  During the fracture tests, the beams behaved in a monolithic way, until the maximum force was reached. Then, interface cracks developed that led to local debonding in beams NR. However, the interface cracks remained small and did not change the structural behaviour of beams R.

The advantageous properties of UHPFRC can be exploited in composite “UHPFRC-concrete” elements. The main improvements of UHPFRC when compared to concrete were the tensile behaviour, i.e. strain-hardening and the high fracture energy, and the very low permeability, leading to a higher stiffness and in several cases to a higher resistance as well as an improved cracking behaviour in the composite beams.

Part VI
References

23 References of the test report

[EN196/1] EN196/1, *Methods of testing cement - Part 1: Determination of Strength*, European Standard, 1994, 15 p.

[Bernard00] Bernard O., *Comportement à long term des éléments de structure formés de bétons d'âges différents*, Test report, EPFL-MCS96.01.01, Swiss Federal Institute of Technology (EPFL), Lausanne, Switzerland, November, 2000, 238 p. (in French).

[Broquet99] Broquet C., *Comportement dynamique des dalles de roulement des ponts en béton sollicités par le trafic routier*, Doctoral thesis, No. 1964, Swiss Federal Institute of Technology (EPFL), Lausanne, Switzerland, 1999, 171 p. (in French).

[CEB204] CEB, *CEB-FIP Model Code 1990*, Comité euro-international du béton (CEB), Bulletin d'Information 204, Lausanne, Switzerland, July, 1991, pp. 6-13.

[Charif98] Charif H., Mivelaz P., *Construction de la nouvelle usine GENEX 4 à Genève*, Report 497.023-3.2, ESM Charif & Mivelaz, St Sulpice, Switzerland, 1998 (in French).

[Charron02] Charron J-P., Marchand J., Bissonnette B., Pigeon M., *Test device for studying the early-age stresses and strains in concrete*, American Concrete Institute Fall Convention, Ed. by O. M. Jensen, D. P. Bentz and P. Lura, Phoenix, USA, 2002, 17 p.

[Charron03] Charron J-P., *Contribution à l'étude du comportement au jeune âge des matériaux cimentaires en conditions des déformations libre et restreinte*, PhD thesis, CRIB, University Laval, Québec, Québec, Canada, April, 2003, 373 p. (in French).

[Clement01] Clément J.-L., Le Maou F., *Experimental repeatability of creep and shrinkage concrete tests - data statistical analysis and modelling*, Creep, Shrinkage and Durability Mechanics of Concrete and other Quasi-Brittle Materials, Concreep 6, Ed. by F-J. Ulm, Z. P. Bazant and F. H. Wittmann, Boston, USA, August, 2001, pp 705-714.

[DeSchutter96] De Schutter G., Taerwe L., *Degree of hydration-based description of mechanical properties of early age concrete*, Materials and Structures, Vol. 29, No. 190, July, 1996, pp 335-344.

[Glisic00] Glisic B., *Fibre optic sensors and behaviour in concrete at early age*, Doctoral thesis, No. 2186, Swiss Federal Institute of Technology (EPFL), Lausanne, Switzerland, 2000, 154 p.

[Guandalini04] Guandalini S., Muttoni A., *Essais de poinçonnement symétrique des dalles en béton armé sans armature à l'effort tranchant*, Test report, 00.03-R1, Swiss Federal Institute of Technology (EPFL), Lausanne, Switzerland, 2004, to be published (in French).

[Habel04] Habel K., *Structural Behaviour of Elements Combining Ultra-High Performance Fibre Reinforced Concretes (UHPFRC) and Reinforced Concrete*, Doctoral thesis, No. 3036, Swiss Federal Institute of Technology (EPFL), Lausanne, Switzerland, 2004, 196 p.

[Hammerschlag01] Hammerschlag J-G., *Examen pétrographique de granulats*, Test report, Nyon, Switzerland, June, 2001 (in French), 6 p. (in French).

[Helbling87] Helbling A., Brühwiler E., *Eine neue Halterung für Zugversuche mit Beton-Probekörper*, Material und Technik, No. 4, Switzerland, 1987, pp 103-107 (in German).

[Jensen01] Jensen O. M., Hansen P. F., *Autogenous RH-change and deformation - Exercise*, Behaviour and Performance of Early Age Concrete, Shortcourse organized by D. A. Lange and H. Stang, Technical University of Denmark (DTU), Lyngby, Denmark, July, 2001, 5 p.

[Neville95] Neville A., *Properties of concrete*, Adison Wesley Longman Limited, 4th edition, Harlow, England, 1995.

[RILEM97] RILEM TC 119-TCE, *Avoidance of thermal cracking in concrete at early ages*, Materials and Structures, Vol. 30, October, 1997, pp 451-464.

[Roelfstra89] Roelfstra P. E., *A numerical approach to investigate the properties of concrete - numerical concrete*, Doctoral Thesis, No. 788, Swiss Federal Institute of Technology (EPFL), Lausanne, Switzerland, 1989.

[Rossi02] Rossi P., *Development of new cement composite material for construction*, Innovations and Developments in Concrete Materials and Construction, Proceedings of the International Conference, University of Dundee, Ed. by R. K. Dhir, P. C.Hewlett and L. J. Csetenyi, Dundee, Scotland, September, 2002, pp 17-29.

[SIA162/1] SIA 162/1, *Ouvrages en béton - Essais des matériaux*, Société Suisse des Ingénieurs et des Architectes, Vol. 162/1, Zürich, Switzerland, 1989 (in French).

[Torrent92] Torrent R., *A two-chamber vacuum cell for measuring the coefficient of permeability to air of the concrete cover on site*, Materials and Structures, Vol. 25, No. 150, 1992, pp 358-365.

[Toutlemonde96] Toutlemonde F., Le Maou F., *Protection des éprouvettes de béton vis-à-vis de la dessiccation - Le point sur quelques techniques de laboratoire*, Bulletin des Laboratoires des Ponts et Chaussées, No. 203, France, May - June 1996, pp 105-119 (in French).

[Waller00] Waller V., *Relations entre composition des bétons, exothermie en cours de prise et résistance à la compression*, Doctoral thesis, Laboratoire Central des Ponts et Chaussées (LCPC), Nantes, France, May, 2000, 317 p. (in French).

24 General references

[Aarup04] Aarup B., *CRC - A Special Fibre Reinforced Reinforced High Performance Concrete*, RILEM Symposium, Advances in Concrete Through Science and Engineering, March 22-24, Evanston, USA, March, 2004, 6 p, CD-ROM.

[Abrishami97] Abrishami H. H., Mitchell D., *Influence of Steel Fibers on Tension Stiffening*, ACI Structural Journal, Vol. 94, No. 6, November-December, 1997, pp 769-776.

[Acker01] Acker P., *Micromechanical analysis of creep and shrinkage mechanisms*, Creep, Shrinkage and Durability Mechanics of Concrete and other Quasi-Brittle Materials (Concreep 6), Ed. by F-J. Ulm, Z. P. Bazant and F. H. Wittmann, Boston, USA, August, 2001, pp 15-25.

[Acker01a] Acker P., Ulm F. J., *Creep and shrinkage of concrete: physical origins and practical measurements*, Nuclear Engineering and Design, Vol. 203, No. 2, 2001, pp 143-158.

[AFGC02] Association Française du Génie Civil, *Bétons fibrés à ultra-hautes performances (Ultra high performance fibre-reinforced concretes)*, SETRA - Service d'études techniques des routes et autoroutes, AFGC, France, January, 2002, 152 p.

[Alaee03] Alaee F. J., Karihaloo B., *Retrofitting of Reinforced Concrete Beams with CARDIFRC*, ASCE Journal of Composites for Construction, Vol. 7, No. 3, August, 2003, pp 174-186.

[Alford85] Alford N. McN., Birchall J. D., *The properties and potential applications of Macro-Defect-Free Cement*, Symposium on very high strength cement-based materials, Ed. by J. F. Young, Materials Research Society symposia proceedings, Vol. 42, Pittsburgh, USA, 1985, pp 265-276.

[Alkubaisy75] Al-Kubaisy M.A., Young A.G., *Failure of concrete under sustained tension*, Magazine of Concrete Research, Vol. 27, No. 92, September, 1975, pp. 171-178.

[Altoubat02] Altoubat S. A., Lange D., *The Pickett effect at early age and experiment separating its mechanisms in tension*, Materials and Structures, Vol. 35, No. 248, May, 2002, pp 211-218.

[Attiogbe88] Attiogbe E.K., Darwin D., *Strain due to submicrocracing in cement paste and mortar*, ACI Materials Journal, Vol. 85, No. 1, USA, January-February, 1988, pp 3-11.

[Bache87] Bache H. H., *Introduction to Compact Reinforced Composite*, Nordic concrete research, No. 6, pp 19-33, 1987.

[Baker61] Baker A. L. L., *Note for discussion at Monaco*, Comité euro-international du béton (CEB), Bulletin d'information No. 30, Lausanne, Switzerland, 1961.

[Bangham37] Bangham D. H., *The Gibbs adsorption equation and adsorption on solids*, Transactions of the Faraday Society, London, England, Vol. 33, 1937, pp 805-811.

[Barcelo01] Barcelo L., Boivin S., Acker P., Toupin J., Clavaud B., *Early age shrinkage of concrete: back to physical phenomena*, Concrete Science and Engineering, Vol. 3, No. 10, June, 2001, pp 85-91.

[Barcelo02] *Chemical shrinkage*, Early Age Cracking in Cementitious Systems, Report of Technical Committee 181-EAS: Early age shrinkage induced stresses and cracking in cementitious systems, Ed. by A. Bentur, RILEM Report 25, France, July, 2002, pp 21-25.

[Bazant72] Bazant Z., Najjar L. J., *Nonlinear water diffusion in nonsaturated concrete*, Materials and Structures, Vol. 5, No. 25, 1972, pp 3-20.

[Bazant72a] Bazant Z. P., *Numerical determination of long-range stress history from strain history in concrete*, Materials and Structures, Vol. 5, No. 27, 1972, pp 135-141.

[Bazant74] Bazant Z., Wu S.T., *Rate-type creep law of aging concrete based on Maxwell chain*, Materials and Structures, Vol. 7, No. 37, 1974, pp 45-60.

[Bazant83] Bazant Z. P., Oh B., *Crack band theory for fracture of concrete*, Materials and Structures, Vol. 16, No. 93, 1983, pp 155-177.

[Bazant85] Bazant Z., Chern J.C., *Concrete creep at variable humidity constitutive law and mechanism*, Materials and Construction, Vol. 18, No. 103, 1985, pp 1-20.

[Bazant87] Bazant Z., Chern J.C., *Stress-Induced Thermal and Shrinkage Strains in Concrete*, ASCE Journal of Engineering Mechanics, Vol. 113, No. 10, 1987, pp 1493-1511.

[Bazant98] Bazant Z., Planas J., *Fracture and Size Effect in Concrete and Other Quasibrittle Materials*, New Directions in Civil Engineering, CRC Press, Boca Raton, 1998, pp. 616.

[Behloul03] Behloul M., Kicul C. L., *Ductal® Seonyu footbridge*, Structural concrete, Journal of the fib, Vol. 4, No. 4, December, 2003, pp 195-201.

[Bekaert99] Bekaert A., Behloul M., Dugat J., Adeline R., Lacombe H., *Centrale EDF de Cattenom - Du béton de poudres réactives (BPR) pour le nucléaire*, Travaux, No. 752, April, 2001, pp 69-72 (in French).

[Bentur02]Bentur, A., *Terminology and definitions*, Early Age Cracking in Cementitious Systems, Report of Technical Committee 181-EAS: Early age shrinkage induced stresses and cracking in cementitious systems, Ed. by A. Bentur, RILEM Report 25, France, July, 2002, pp 13-15.

[Bernard00] Bernard O., *Comportement à long terme des éléments de structure formés de bétons d'âges différents*, Doctoral Thesis, No. 2283, Swiss Federal Institute of Technology (EPFL), Lausanne, Switzerland, 2000, 190 p. (in French).

[Bernard00a] Bernard O., *Comportement à long term des éléments de structure formés de bétons d'âges différents*, Test report, EPFL-MCS96.01.01, Swiss Federal Institute of Technology (EPFL), Lausanne, Switzerland, November, 2000, 238 p (in French).

[Bernard01] Bernard O., Denarié E., Brühwiler E., *Comportement au jeune âge du béton et limitation de la fissuration traversante des structures hybrides*, Report VSS, 1997/064 (82/97), Swiss Federal Roads Authority, Swiss Association of Road and Transportation Experts, Lausanne, Switzerland, October, 2001, 116 p. (in French).

[Bernard02] Bernard O., Brühwiler E., *Influence of autogenous shrinkage on early age behaviour of structural elements consisting of concretes of different ages*, Materials and Structures, Vol. 35, No. 235, November, 2002, pp 550-556.

[Bernard03] Bernard O., Brühwiler E., *The effect of reinforcement in the new layer on hygral cracking in hybrid structural elements*, Materials and Structures, Vol. 36, No. 256, March, 2003, pp 118-126.

[Bissonnette00] Bissonnette B., Pigeon M., *Le comportement viscoélastique du béton en traction et la compatibilité déformationelle des réparations*, Materials and Structures, Vol. 33, No. 226, March, 2000, pp 108-118 (in French).

[Bonneau97] Bonneau O., Lachemi M., Dallaire E., Dugat J., Aïtcin P-C., *Mechanical Properties and Durability of Two Industrial Reactive Powder Concretes*, ACI Materials Journal, Vol. 94, No. 4, July-August, 1997, pp 286-290.

[Boulay03] Boulay C., Arca A., Tailhan J-L., Rossi P., Sananes J., *Comportement mécanique d'un nouveau composite cimentaire à écrouissage positif. II : Caractérisation du comportement en traction uniaxiale*, Bulletin des Laboratoires des Ponts et Chaussées, No. 243, LCPC, France, March-April, 2003, pp 19-30 (in French).

[Brenni95] Brenni P., *Il comportamento al taglio di una struttura a sezione mista in calcestruzzo a getti successivi*, IBK-Report, No. 211, Swiss Federal Institute of Technology (ETHZ), Zürich, Switzerland, September, 1995, 150 p. (in Italian).

[Broquet99] Broquet C., *Comportement dynamique des dalles de roulement des ponts en béton sollicités par le trafic routier*, Doctoral thesis, No. 1964, Swiss Federal Institute of Technology (EPFL), Lausanne, Switzerland, 1999, 171 p. (in French).

[Brühwiler88] Brühwiler E., *Bruchmechanik von Staumauerbeton unter quasi-statischer und erdbebendynamischer Belastung*, Doctoral thesis, No. 739, Swiss Federal Institute of Technology (EPFL), Lausanne, Switzerland, 1988, 169 p. (in German).

[Brühwiler00] Brühwiler E., Bernard O., Wolf S., *Beton-Beton Verbundbauteil bei der Verbreiterung eines Brückenüberbaus - Massnahmen zur Begrenzung der Rissbildung im neuen Beton*, Beton- und Stahlbetonbau, Vol.95, No. 3, March, 2000, pp 158-166 (in German).

[Brühwiler04] Brühwiler E., Denarié E., Wälchli T., Maitre M., Conciatori D., *Dauerhafte Kunstbauten bei geringem Unterhalt (Ouvrages d'art durables à entretien minimal)*, final draft, Report VSS, 2000/173 (88/00), Swiss Federal Roads Authority, Swiss Association of Road and Transportation Experts, Lausanne, Switzerland, April, 2004 (in German).

[Brunauer73] Brunauer S., Yudenfreund M., Odler I., Skalny J., *Hardened Portland Cement Pastes of Low Porosity, VI. Mechanism of the Hydration Process*, Cement and Concrete Research, Vol. 3, No. 2, 1973, pp 129-147.

[Brunauer73a] Brunauer S., Skalny J., Odler I., Yudenfreund M., *Hardened Portland Cement Pastes of Low Porosity, VII. Further Remarks about Early Hydration. Composition and Surface Area of Tobermorite Gel. Summary*, Cement and Concrete Research, Vol. 3, No. 3, 1973, pp 279-293.

[Byfors82] Byfors J., *Mechanical properties*, International Conference on Concrete at Early Ages, Vol. 2, Ecole Nationale des Ponts et Chaussées (ENPC), Paris, France, April, 6-8, 1982, pp 13-33.

[Carino94] Carino N. J., *The Maturity Method: Theory and Application*, Cement, Concrete and Aggregates, Vol. 6, No. 2, 1984, pp 61-73.

[Casanova94] Casanova P., Le Maou F., Renwez S., Rossi P., *Calcul du béton de fibres métalliques: poutre en flexion simple*, Bulletin de liaison des laboratoires des ponts et chaussées, No. 191, France, May-June, 1994, pp 73-85 (in French).

[CEB204] CEB, *CEB-FIP Model Code 1990*, Comité euro-international du béton (CEB), Bulletin d'Information 204, Lausanne, Switzerland, July, 1991.

[CEB242] CEB, *Ductility of reinforced concrete structures - Synthesis Report and Individual Contributions*, Comité euro-international du béton (CEB), Bulletin d'Information 242, Lausanne, Switzerland, May, 1998, 332 p.

[Charif98] Charif H., Mivelaz P., *Construction de la nouvelle usine GENEX 4 à Genève*, Report 497.023-3.2, ESM Charif & Mivelaz, St Sulpice, Switzerland, 1998 (in French).

[Charron02] Charron J-P., Marchand J., Bissonnette B., Pigeon M., *Test device for studying the early-age stresses and strains in concrete*, American Concrete Institute Fall Convention, Ed. by O. M. Jensen, D. P. Bentz and P. Lura, Phoenix, USA, 2002, 17 p.

[Charron03] Charron J-P., *Contribution à l'étude du comportement au jeune âge des matériaux cimentaires en conditions des déformations libre et restreinte*, PhD thesis, CRIB, University Laval, Québec, Québec, Canada, April, 2003, 373 p. (in French).

[Charron04] Charron J-P., Denarié E., Brühwiler E., *Permeability of UHPFRC under high stresses*, RILEM Symposium, Advances in Concrete Through Science and Engineering, March 22-24, Evanston, USA, 2004, 12 p. CD-ROM.

[Chausson97] Chausson H., Granju J.-L., *Optimized design of fiber reinforced thin bonded overlays*, 5th International Symposium on Brittle Matrix Composites, Warsaw, Poland, October, 1997, pp 133-142.

[Cheyrezy95] Cheyrezy M., Maret V., Frouin L., *Microstructural analysis of RPC (Reactive Powder Concrete)*, Cement and Concrete Research, Vol. 25, No. 7, July, 1995, pp 1491-1500.

[Cheyrezy97] Cheyrezy M., *Structural Applications of RPC*, International Conference - New technologies in structural engineering, Vol. 1, Lisbon, Portugal, July, 1997, pp 5-14.

[Cheyrezy01] Cheyrezy M., Behloul M., *Creep and Shrinkage of Ultra-High Performance Concrete*, Creep, Shrinkage and Durability Mechanics of Concrete and other Quasi-Brittle Materials (Concreep 6), Ed. by F.-J. Ulm, Z. P. Bazant and F. H. Wittmann, Boston, USA, August, 2001, pp 527-538.

[Cosenza91] Cosenza E., Greco C., Pecce M., *Nonlinear design of Reinforced Concrete Continuous beams*, Structural Engineering International, Vol. 1 No. 1, February, 1991, pp 19-27.

[Courard99] Courard L., *Contribution à l'analyse des paramètres influençant la création de l'interface entre un béton et un système de réparation*, University of Liège, Collection des Publications de la Faculté des Sciences Appliquées, No. 192, Liège, Belgium, 1999, 198 p. (in French).

[DeLarrard94] De Larrard F., Sedran T., *Optimization of Ultra-High-Performance Concrete by the Use of a Packing Model*, Cement and Concrete Research, Vol. 24, No. 6, June, 1994, pp 997-1009.

[DeLarrard99] De Larrard F., *Concrete mixture Proportioning - A scientific approach*, Modern concrete technology 9, E & FN SPON, London, England, 1999, 421 p.

[Denarie00] Denarié E., *Etude expérimentale des couplages viscoélasticité-croissance des fissures dans les bétons de ciment*, Doctoral Thesis, No. 2195, Swiss Federal Institute of Technology (EPFL), Lausanne, Switzerland, 2000 207 p. (in French).

[Denarie01] Denarié E., Brühwiler E., *Comportement d'Eléments de Structure Hybrides formés de béton Traditionnel et de Matériaux Cimentaires Avancés*, Regroupement Francophone pour la Recherche et la Foration sur le Béton ($(RF)_2B$), Québec, Canada, August, 2001, 4 p. (in French).

[Denarie03] Denarié E., Habel K., Brühwiler E., *Structural behavior of hybrid elements with Advanced Cementitious Materials (HPFRCC)*, RILEM Proceedings PRO 30, 4th International Workshop on High Performance Fiber Reinforced Cement Composites (HPFRCC-4), Ed. by A. E. Naaman and H. W. Reinhardt, Ann Arbor, USA, June, 2003, pp 301-312.

[Denarie04] Denarié. E., *personal communication*, Swiss Federal Institute of Technology (EPFL), Lausanne, Switzerland, 2004.

[DeSchutter96] De Schutter G., Taerwe L., *Degree of hydration-based description of mechanical properties of early age concrete*, Materials and Structures, Vol. 29, No. 190, July, 1996, pp 335-344.

[DeSchutter00] De Schutter G., *Fictitious degree of hydration method for the basic creep of early age concrete*, Materials and Structures, Vol. 33, No. 230, July, 2000, pp 370-380.

[DeSchutter02] De Schutter G., *Short-term mechanical properties*, Early Age Cracking in Cementitious Systems, Report of Technical Committee 181-EAS: Early age shrinkage induced stresses and cracking in cementitious systems, Ed. by A. Bentur, RILEM Report 25, France, July, 2002, pp 101-109.

[DeSchutter02a] De Schutter G., *Visco-elastic response*, Early Age Cracking in Cementitious Systems, Report of Technical Committee 181-EAS: Early age shrinkage induced stresses and cracking in cementitious systems, Ed. by A. Bentur, RILEM Report 25, France, July, 2002, pp 111-120.

[Ducret97] Ducret J-M., *Etude du comportement réel des ponts mixtes et modélisation pour le dimensionnement*, Swiss Federal Institute of Technology (EPFL), Doctoral thesis, No. 1738, Lausanne, Switzerland, 1997, 185 p. (in French).

[Dugat96] Dugat J., Roux N., Bernier G., *Mechanical Properties of Reactive Powder Concretes*, Materials and Structures, Vol. 29, No. 188, May, 1996, pp 233-240.

[Dupont03] Dupont D., *Modelling and experimental validation of the constitutive law (σ-ε) and cracking behaviou rof steel fibre reinforced concrete*, Doctoral thesis, Faculty of Applied Science, Catholic University of Leuven, Leuven, Belgium, October, 2003, 256 p.

[EC01] *Eurocode 1, Draft pr EN 1990 - Eurocode: Basis of Structural Design*, European Committee of Standardization (CEN), Stage 34, Brussels, Belgium, December, 2000, 88 p.

[Emberson96] Emberson N. K., Mays G. C., *Significance of property mismatch in the patch repair of structural concrete, Part 3: Reinforced concrete members in flexure*, Magazine of Concrete Research, Vol. 48, No. 174, March, 1996, pp 45-57.

[Emborg89] Emborg M., *Thermal stresses in concrete structures at early ages*, Doctoral thesis, Division of structural engineering, Lulea University of Technology, 189:73 D, Lulea, Sweden, 1989, 285 p.

[Emmons00] Emmons P. H., Vaysburd A. M., McDonald J. E., Poston R.W., Kesner K., *Selecting Durable Repair Materials: Performance Criteria*, Concrete International, Vol. 22, No. 3, March, 2000, pp 38-45.

[EN206] *EN206, Beton - Teil 1: Festlegung, Eigenschaften, Herstellung und Konformität*, EN 206-1:2000, SIA, Zürich, Switzerland, 2000, 83 p. (in German).

[Feldmann68] Feldmann R. F., Sereda P. J., *A model for hydrated Portland cement paste as deduced from sorption-length change and mechanical properties*, Materials and Structures, Vol. 1, Nr. 6, 1968, pp 509-520.

[Femmasse04] *Finite Element Modules for Materials Science and Structural Engineering*, website, Retrieved: April 20, 2004, from http://www.femmasse.com.

[Ferraris87] Ferraris C.F., Wittmann F.H., *Shrinkage mechanisms of hardened cement paste*, Cement and Concrete Research, Vol. 17, No. 3, 1987, pp. 453-463.

[fib10] *Bond of reinforcement in concrete: state-of-art report prepared by Task Group Bond models*, Fédération Internationale du Béton (fib), fib Bulletin, No. 10, Lausanne, Switzerland, August, 2000, 427pp.

[Fischer02] Fischer G., Li V. C., *Influence of Matrix Ductility on Tension-Stiffening Behavior of Steel Reinforced Engineered Cementitious Composites (ECC)*, ACI Structural Journal, Vol. 99, No. 1, January-February, 2002, pp 104-111.

[Gamble78] Gamble B. R., Parrott L. J., *Creep of Concrete in Compression during Drying and Wetting*, Magazine of Concrete Research, Vol. 30, No. 104, September, 1978, pp 129-138.

[Gartner89] Gartner E. M., Gaidis J. M., Grace W. R., *Hydration mechanisms I*, Materials Science of Concrete I, Ed. by J. Skalny, American Ceramics Society, Westerville, USA, 1989, pp 95-125.

[Gibbon98] Gibbon G. J., Ballim Y., *Determination of the thermal conductivity of concrete during the early age stages of hydration*, Magazine of Concrete Research, Vol. 50, No. 3, September, 1998, pp 229-235.

[Goto71] Goto Y., *Cracks formed in concrete around deformed tension bars*, ACI Journal Proceedings, Vol. 68, No. 4, April, 1971, pp 244-251.

[Granju01] Granju J.-L., *Debonding of Thin Cement-Based Overlays*, ASCE Journal of Materials in Civil Engineering, Vol. 13, No. 2, March-April, 2001, pp 114-120.

[Guandalini04] Guandalini S., Muttoni A., *Essais de poinçonnement symétrique des dalles en béton armé sans armature à l'effort tranchant*, Test report, 00.03-R1, Swiss Federal Institute of Technology (EPFL), Lausanne, Switzerland, 2004, to be published (in French).

[GuenotDelahaie97] Guénot-Delahaie I., *Contribution à l'analyse physique et à la modélisation du fluage propre du béton*, Doctoral thesis, Laboratoire Central des Ponts et Chaussées (LCPC), France, April, 1997, 180 p. (in French).

[Haardt91] Haardt P., *Zementgebundene und kunststoffvergütete Beschichtungen auf Beton*, Doctoral thesis, Massivbau und Baustofftechnologie, University of Karlsruhe, Karlsruhe, Germany, 1991, 201 p. (in German).

[Habel00] Habel K., Bernard O., Brühwiler E., *The Numerical Investigation of Delamination in Hybrid Reinforced Concrete Elements*, 3rd International PhD Symposium in Civil Engineering, fib, Ed. K. Bergmeister, Vol. 2, Vienna, Austria, October, 2000, pp 221-228.

[Habel04] Habel K., *Structural behaviour of "UHPFRC - concrete" elements*, Test report, MCS99.04, Swiss Federal Institute of Technology (EPFL), Lausanne, Switzerland, 2004.

[Hamza96] Hamza A. M., Naaman A. E., *Bond Characteristics of Deformed Reinforcing Steel Bars Embedded in SIFCON*, ACI Materials Journal, Vol. 93, No. 6, November-December, 1996, pp 578-588.

[Hansen86] Hansen T. C., *Physical structure of hardened cement paste. A classical approach*, Materials and Structures, Vol. 19, No. 114, 1986, pp 423-436.

[Hauggaard99] Hauggaard A.B., Damkilde L., Hansen P. F., *Transitional Thermal Creep of Early Age Concrete*, ASCE, Journal of Engineering Mechanics, April, 1999, pp 458-465.

[Helbling87] Helbling A., Brühwiler E., *Eine neue Halterung für Zugversuche mit Beton-Probekörper*, Material und Technik, No. 4, Switzerland, 1987, pp 103-107 (in German).

[Hillerborg83] Hillerborg A., *Analysis of a single crack*, Fracture mechanics of concrete Ed. by F.H.Wittmann, Elsevier science Publishers B.V., Amsterdam, Netherlands, 1983, pp 223-249.

[Holschemacher03] Holschemacher K., Dehn F., *Ultrahochfester Beton (UHFB) - Stand der Technik und Entwicklungsmöglichkeiten*, Ultrahochfester Beton, Innovationen im Bauwesen - Beiträge aus Praxis und Wissenschaft, Ed. by G. König, K. Holschemacher, F. Dehn, Bauwerk, Berlin, Leipzig, Germany, 2003 pp 1-12 (in German).

[Hua95] Hua C., Acker P., Ehrlacher A., *Analyses and Models of the Autogenous Shrinkage of Hardening Cement Paste, I. Modelling at macroscopic scale*, Cement and Concrete Research, Vol. 25, No. 7, 1995, pp 1457-1468.

[Jennings00] Jennings H. M., *A model for the microstructure of calcium silicate hydrate in cement paste*, Cement and Concrete Research, Vol. 30, No. 1, 2000, pp 101-116.

[Jennings04] Jennings H. M., *Colloid model of C-S-H and implications to the problem of creep and shrinkage*, Materials and Structures, Vol. 27, No. 265, January-February, 2004, pp 59-70.

[Jensen95] Jensen O. M., *Thermodynamic limitation of self-desiccation*, Cement and Concrete Research, Vol. 25, No. 1, January, 1995, pp 157-164.

[Jensen96] Jensen O. M., Hansen P. F., *Autogenous deformation and change of the relative humidity in silica fume-modified cement paste*, ACI Materials Journal, Vol. 93, No. 6, 1996, pp 539-543.

[Jensen01] Jensen O. M., Hansen P. F., *Autogenous RH-change and deformation - Exercise*, Behaviour and Performance of Early Age Concrete, Shortcourse organized by D. A. Lange and H. Stang, Technical University of Denmark (DTU), Lyngby, Denmark, July, 2001, 5 p.

[Jensen01a] Jensen O. M., Hansen P. F., *Autogenous deformation and RH-change in perspective*, Cement and Concrete Research, Vol. 31, No. 12, December, 2001, pp 1859-1865.

[Jones02] Jones M. R., Zheng L., Newlands M. D., *Comparison of particle packing models for porportioning concrete constituents for minimum voids ratio*, Materials and Structures, Vol. 35, No. 249, June, 2002, pp 301-309.

[Kada02] Kada H., Lachemi M., Petrov N., Bonneau O., Aïtcin P.-C., *Determination of the coefficient of thermal expansion of high performance concrete from initial setting*, Materials and Structures, Vol. 35, No. 245, January-February, 2002, pp 35-41.

[Kendall83] Kendall K., Howard A. J., Birchall J. D., *The relation between porosity, microstructure and strength, and the approach to advanced cement-based materials*, Philosophical Transactions of the Royal Society of London, A 310, London, England, 1983, pp 139-153.

[Kim03] Kim K.-H., Jeon S-E., Kim J.-K., Yang S., *An experimental study on thermal conductivity of concrete*, Cement and Concrete Research, Vol. 33, No. 3, 2003, pp 363-371.

[Kosa91] Kosa K., Naaman A. E., Hansen W., *Durability of Fiber Reinforced Mortar*, ACI Materials Journal, Vol. 88, No. 3, May-June, 1991, pp 310-319.

[Kranz99] Kranz St., *Lokale Schwind- und Temperaturgradienten in bewehrten, oberflächennahen Zonen von Betonstrukturen*, Doctoral thesis, Heft 35, Massivbau und Baustofftechnologie, University of Karlsruhe, Karlsruhe, Germany, 1999, 377 p. (in German).

[Krstulovic96] Krstulovic-Opara N., Toutanji H., *Infrastructural repair and retrofit with HPFRCCs*, High Performance Fiber Reinforced Concrete Composites 2 (HPFRCC 2), Ed. by A. E. Naaman and H. W. Reinhardt, RILEM, Proceedings 31 Ann Arbor, USA, June, 1996, pp 423-442,.

[Krstulovic97] Krstulovic-Opara N., Dogan E., Uang C.-M., Haghayeghi A. R., *Flexural Behavior of Composite R.C.-Slurry Infiltrated Mat Concrete (SIMCON) Members*, ACI Structural Journal, Vol. 94, No. 5, September - October, 1997, pp 502-512.

[Laplante94] Laplante P., Boulay C., *Evolution du coefficient de dilatation thermique du béton en fonction de sa maturité aux tout premiers âges.*, Materials and Structures, Vol. 27, No. 174, USA, 1994, pp 596-605.

[Laube90] Laube M., *Werkstoffmodell zur Berechnung von Temperaturspannungen in massigen Betonbauteilen in jungen Alter*, Doctoral thesis, University of Braunschweig, Braunschweig, Germany, May, 1990, 251 p. (in German).

[Lemberg96] Lemberg M., *Dichtschichten aus hochfestem Faserbeton*, Deutscher Ausschuss für Stahlbeton, (DAfStb), Beuth Verlag GmbH, No. 465, Berlin, Germany, 1996, pp 1-163 (in German).

[Li00] Li V. C., Horii H., Kabele P., Kanda T., Lim Y. M., *Repair and retrofit with engineered cementitious composites*, Engineering fracture mechanics, Vol. 65, No. 2-3, 2000, pp 317-334.

[Lim02] Lim Y. M., Kim M. K., Kim J. H. J., Shin S. K., *Is ductility important for repair application?*, Proceedings of the JCI international Workshop on Ductile Fiber Reinforced Cementitious Composites (DFRCC) - Application and Evaluation (DFRCC-02), Takayama, Japan, October, 2002, pp 199-208.

[Locher76] Locher F. W., Richartz W., Sprung S., *Erstarren von Zement - Teil 1: Reaktion und Gefügeentwicklung (Setting of cement - Part 1: Reaction and development of structure)*, Zement, Kalk, Gips, Vol. 29, No. 10, October, 1976, pp 435-442 (in German).

[Loukili96] Loukili A., *Etude du retrait et du fluage de Bétons à Ultra-Hautes Performances*, Doctoral thesis, Ecole Centrale Nantes, Nantes, France, November, 1996, 155 p (in French).

[Martinola01] Martinola G., Sadouki H., Wittmann F. H., *Numerical model for minimizing risk of damage in repair systems*, ASCE Journal of Materials in Civil Engineering, Vol. 13, No. 2, March-April, 2001, pp 121-129.

[Martinola02] Martinola G., Bäuml M. F., Wittmann F. H., *Modified ECC applied as an effective chloride barrier*, Proceedings of the JCI international Workshop on Ductile Fiber Reinforced Cementitious Composites (DFRCC) - Application and Evaluation (DFRCC-02), Takayama, Japan, October, 2002, pp 171-180.

[Massicotte03] Massicotte B., *Design of SFRC members in flexure: application to a building floor*, Dimensionato de estruturas de betão reforçado com fibras de aço, Ed. by J. Barros, P. Rossi, B. Massicotte, DEC-UM, Portugal, 2003, p. 4.1-4.17.

[Mensi88] Mensi R, Acker P., Attolou A, *Séchage du béton: analyse et modélisation*, Materials and Structures, Vol. 21, No. 121, 1988, pp 3-12 (in French).

[Morin01] Morin V., Cohen Tounedji F., Feylessoufi A., Richard P., *Superplasticizer effects on setting and structuration mechanisms of ultrahigh-performance concrete*, Cement and Concrete Research, Vol. 31, No. 1, 2001, pp 63-71.

[Morin02] Morin V., Cohen-Tenoudji F., Feylessoufi A., Richard P., *Evolution of the capillary network in a reactive powder concrete during hydration process*, Cement and Concrete Research, Vol. 32, No. 12, 2002, pp 1907-1914.

[Muttoni97] Muttoni A., Schwartz J., Thürlimann B., *Bemessung von Betontragwerken mit Spannungsfeldern*, Birkhäuser, Basel, Switzerland, 1997, 145 pp (in German).

[Naaman02] Naaman A. E., *Toughness, ductility, surface energy and deflection-hardening FRC composites*, Proceedings of the JCI international Workshop on Ductile Fiber Reinforced Cementitious Composites (DFRCC) - Application and Evaluation (DFRCC-02), Takayama, Japan, October, 2002, pp 33-57.

[Neville70] Neville A., *Creep of Concrete: Plain, Reinforced and Prestressed*, North-Holland Publishing Company, Amsterdam, the Netherlands, 1970, 622 p.

[Neville95] Neville A., *Properties of concrete*, Adison Wesley Longman Limited, 4th edition, Harlow, England, 1995.

[Odler72] Odler I., Yudenfreund M., Skalny J., Brunauer S., *Hardened Portland Cement Pastes of Low Porosity, III. Degree of Hydration. Expansion of Paste, Total Porosity*, Cement and Concrete Research, Vol. 2, No. 4, 1972, pp 463-480.

[Odler72a] Odler I., Hagymassy J., Bodor E. E., Yudenfreund M., Brunauer S., *Hardened Portland Cement Pastes of Low Porosity, IV. Surface Area and Pore Structure*, Cement and Concrete Research, Vol. 2, No. 5, 1972, pp 577-589.

[Orange00] Orange G., Dugat J., Acker P., *DUCTAL: New Ultra High Performance Concretes. Damage, Resistance and Micromechanical Analysis*, Fifth RILEM Symposium on Fiber-Reinforced Concretes (FRC) (BEFIB 2000), Ed. by P. Rossi and G. Chanvillard, Lyon, France, September, 2000, pp 781-790.

[Parant03] Parant E., *Mécanismes d'endommagement et comportements mécaniques d'un composite cimentaire fibré multi-échelles sous sollicitations sévères: fatigue, choc, corrosion*, Doctoral thesis, Laboratoire Central des Ponts et Chaussées (LCPC), France, December, 2003, 245 p. (in French).

[Pfyl03] Pfyl Th., *Tragverhalten von Stahlfaserbeton*, Doctoral thesis, IBK-Report, No. 279, Swiss Federal Institute of Technology (ETHZ), Zürich, Switzerland, February, 2003, 140 p. (in German).

[Pickett42] Pickett G., *The Effect of Change in Moisture-Content on the Creep of Concrete Under a Sustained Load*, Research Laboratory of the Portland Cement Association, Bull. 11, Detroit, USA, March, 1942, 80 p.

[Pigeon92] Pigeon M. , Saucier F. , *Durability of repaired concrete structures*, International Symposium on Advances in Concrete Technology, Ed. by V. M. Malhotra, Athens, Greece, May, 1992, pp 741-773.

[Powers48] Powers T. C., Brownyard T. L., *Studies of the Physical Properties of Hardened Portland Cement Paste*, Research Laboratories of the Portland Cement Association, Bull. 22, Detroit, USA, March, 1948, 356 p.

[Randl00] Randl N., Wicke M., *Schubübertragung zwischen Alt- und Neubeton*, Beton- und Stahlbetonbau, Vol. 95, No. 8, August, 2000, pp 461-473 (in German).

[Reich97] Reich R., Cervenka J., Saouma V. E., *MERLIN, A Three-Dimensional Finite Element Program Based on a Mixed-Iterative Solution Strategy for Problems in Elasticity,*

Plasticity, and Linear and Nonlinear Fracture Mechanics, EPRI Report, Palo Alto, USA, 1997.

[Richard95] Richard P., Cheyrezy M., *Composition of Reactive Powder Concretes*, Cement and Concrete Research, Vol. 25, No. 7, October, 1995, pp 1501-1511.

[RILEM02] RILEM TC 181-EAS, *Early Age Cracking in Cementitious Systems*, RILEM report, Technical Committee 181-EAS: Early age shrinkage induced stresses and cracking in cementitious systems, Ed. by A. Bentur, Report 25, France, July, 2002, 337 p.

[Roelfstra89] Roelfstra P. E., *A numerical approach to investigate the properties of concrete - numerical concrete*, Doctoral Thesis, No. 788, Swiss Federal Institute of Technology (EPFL), Lausanne, Switzerland, 1989.

[Rossi87] Rossi P., Acker P., Malier Y., *Effect of steel fibres at two different stages: the material and the structure*, Materials and Structures, Vol. 20, No. 120, 1987, pp 436-439.

[Rossi97] Rossi P., *High Performance Multimodal Fiber Reinforced Cement Composites (HPMFRCC): The LCPC Experience*, ACI Materials Journal, Vol. 94, No. 6, November - December, 1997, pp 478-483.

[Rossi02] Rossi P., *Development of new cement composite material for construction*, Innovations and Developments in Concrete Materials and Construction, Proceedings of the International Conference, University of Dundee, Ed. by R. K. Dhir, P. C.Hewlett and L. J. Csetenyi, Dundee, Scotland, September, 2002, pp 17-29.

[Roux96] Roux N., Andrade C., Sanjuan M. A., *Experimental Study of Durability of Reactive Powder Concretes*, ASCE Journal of Materials in Civil Engineering, Vol. 8, No. 1, February, 1996., pp 1-6

[Roy72] Roy D. M., Gouda G. R., Bobrowsky A., *Very high strength cement pastes prepared by hot pressing and other high pressure techniques*, Cement and Concrete Research, Vol. 2, No. 3, 1972, pp 349-366.

[Roy73] Roy D. M., Gouda G. R., *High strength generation in cement pastes*, Cement and Concrete Research, Vol. 3, No. 6, 1973, pp 807-820.

[Rüsch60] Rüsch H., *Researches towards a general flexural theory for structural concrete*, ACI Journal Proceedings, Vol. 57, July, 1960, pp 1-28.

[Sadouki97] Sadouki H., Van Mier J. G. M., *Simulation of hygral crack growth in concrete repair systems*, Materials and Structures, Vol. 30, no. 203, November, 1997, pp 518-526.

[Saucier90] Saucier F., *Contribution à l'étude de la durabilité de l'adhérence des réparations en béton*, PhD thesis, University Laval, Québec, Québec, Canada, December, 1990, 144 p. (in French)

[Schachinger03] Schachinger I., Schmidt K., Heinz D., *Zeitabhängiges Verformungsverhalten von UHFB*, Ultrahochfester Beton, Innovationen im Bauwesen - Beiträge aus Praxis und Wissenschaft, Ed. by G. König, K. Holschemacher, F. Dehn, Bauwerk, Berlin, Leipzig, Germany, 2003, pp 67-77 (in German).

[Schenkel98] Schenkel M., *Zum Verbundverhalten von Bewehrung bei kleiner Betondeckung*, Doctoral Thesis, IBK-Report, No. 237, Swiss Federal Institute of Technology (ETHZ), Zürich, Switzerland, September, 1998, 162pp. (in German).

[Schläfli99] Schläfli M., *Ermüdung von Brückenfahrbahnplatten aus Stahlbeton*, Doctoral thesis, No.1998, Swiss Federal Institute of Technology (EPFL), Lausanne, Switzerland, 1999, 113 p. (in German).

[Schneider92] Schneider B., *Development of SIFCON through applications*, Proceedings of the International Workshop, "High Performance Fiber Reinforced Cement Composites (HPFRCC), Ed. by H. W. Reinhardt and A. E. Naaman, E & FN Spon, RILEM Proceedings 15, Stuttgart, Germany, June, 1992, pp 177-194.

[Schrader92] Schrader K. E., *Mistakes, Misconceptions, and Controversial Issues Concerning Concrete and Concrete Repairs, part 1, 2, 3*, Concrete International, Vol. 14, No. 9, 10, 11, September, October, November, 1992, pp 52-56, 48-52, 54-59.

[Scrivener89] Scrivener K., *The Microstructure of Concrete*, Materials Science of Concrete I, Ed. by J. Skalny, American Ceramics Society, Westerville, USA, 1989, pp 127-161.

[Sedran94] Sedran T., de Larrard F., Angot D., *Prévision des mélanges granulaires par le modèle de suspension solide, I - Fondements théoriques et étalonnage du modèle*, Bulletin de liaison des laboratoires des ponts et chaussées, No. 194, France, November-December, 1994, pp 59-70 (in French).

[SIA260] *SIA 260, Grundlagen der Projektierung von Tragwerken (Swisscode 0)*, SIA, Zürich, Switzerland, 2003, 44 p. (in German).

[SIA261] *SIA 161, Einwirkungen auf Tragwerke (Swisscode 1)*, SIA, Zürich, Switzerland, 2003, 110 p. (in German).

[SIA262] *SIA 262, Betonbauten (Swisscode 2)*, SIA, Zürich, Switzerland, 2002, 76 p. (in German).

[SIA469] *SIA 469, Erhaltung von Bauwerken*, SIA, Zürich, Switzerland, 1997, 20 p. (in German).

[Siebel03] Siebel E., Müller Chr., *Geeignete Zemente für die Herstellung von UHFB*, Ultrahochfester Beton, Innovationen im Bauwesen - Beiträge aus Praxis und Wissenschaft, Ed. by G. König, K. Holschemacher, F. Dehn, Bauwerk, Berlin, Leipzig, Germany, 2003, pp 13-24 (in German).

[Sigrist95] Sigrist V., *Zum Verformungsvermögen von Stahlbetonträgern*, Doctoral thesis, IBK-Report, No. 210, Swiss Federal Institute of Technology (ETHZ), Zürich, Switzerland, 1995, 160 p. (in German).

[Silfwerbrand87] Silfwerbrand J., *Effekter av differenskrympning, krypning och fogytans egenskaper på bärförmågan hos samverkanplattor av gammal och pågjuten betong (Effects of differential shrinkage, creep and properties of the contact surface on the strength of composite concrete slabs of old and new concrete)*, Research Report, No. 147, TRITA-BST-0147, Institutionen för Byggnedsstatik, Royal Institute of Technology, KTH, Stockholm, Sweden, 1987, 131 p. (in Swedish).

[Silfwerbrand90] Silfwerbrand J., *Improving concrete bond in repaired bridge deck*, Concrete International, Vol. 12, No. 9, September, 1990, pp 61-66.

[Silfwerbrand97] Silfwerbrand J., *Stresses and Strains in Composite Concrete Beams Subjected to Differential Shrinkage*, ACI Structural Journal, Vol. 94, No. 4, July-August, 1997, pp 347-353.

[Tazawa98] Tazawa E., *Autogenous shrinkage of concrete*, Proceedings of the International Workshop organized by JCI (Japan Concrete Institute), Hiroshima, Japan, June, E & FN SPON, London, 1998, 411 p.

[Torrent92] Torrent R., *A two-chamber vacuum cell for measuring the coefficient of permeability to air of the concrete cover on site*, Materials and Structures, Vol. 25, No. 150, 1992, pp 358-365.

[Trausch01] Trausch J-L., *Verhalten der grenzflächennahen Zone von Instandsetzungs- und Schutzsystemen für Stahlbeton*, Doctoral thesis, Swiss Federal Institute of Technology (ETHZ), Building Material Reports, No. 13, Aedificatio Publishers, Zürich, Switzerland, 2001, 209 p. (in German).

[VanBreugel92] Van Breugel K., *Numerical Simulation of Hydration and Microstructural Development in Hardening Cement-Based Materials*, Heron, Vol. 37, No. 3, the Netherlands, 1992, 62 p.

[VanMier97] Van Mier J. G. M., *Fracture Processes of Concrete - Assessment of Material Parameters for Fracture Models*, CRC press, Boca Raton, USA, 1997, 448 p.

[Vandewalle00] Vandewalle L., *Cracking behaviour of concrete beams reinforced with a combination of ordinary reinforcement and steel fibers*, Materials and Structures, Vol. 33, No. 227, April, 2000, pp 164-170.

[Vaysburd01] Vaysburd A. M., Sabnis G. M., Emmons P. H., McDonald J. E., *Interfacial bond and surface preparation in concrete repair*, The Indian Concrete Journal (ICJ-journal), January, 2001, pp 27-33.

[Viviani04] Viviani, M., *personal communication*, Swiss Federal Institute of Technology (EPFL), Lausanne, Switzerland, 2004.

[Waller00] Waller V., *Relations entre composition des bétons, exothermie en cours de prise et résistance à la compression*, Doctoral thesis, Laboratoire Central des Ponts et Chaussées (LCPC), Nantes, France, May, 2000, 317 p. (in French).

[Warner98] Warner J., Bhuyan S., Smoak W. G., Hindo K. R., Sprinkel M. M., *Surface preparation for overlays*, Concrete International, Vol. 20, No. 5, May, 1998, pp 43-46.

[Weimann03] Li V. C., Weimann M. B., *Hygral Behavior of Engineered Cementitious Composites (ECC)*, International Journal for Restoration of Buildings and Monuments, Vol. 9, No. 5, 2003, pp 513-534.

[Weiss02] Weiss, J., *Experimental determination of the 'time zero' t_0 (maturity-zero M_0)*, Early Age Cracking in Cementitious Systems, Report of Technical Committee 181-EAS: Early age shrinkage induced stresses and cracking in cementitious systems, Ed. by A. Bentur, RILEM Report 25, France, July, 2002, pp 195-206.

[Wittmann82] Wittmann F. H., *Creep and shrinkage mechanisms*, Concrete and shrinkage in concrete structures, Ed. by Z. P. Bazant and F. H. Wittmann, John Wiley & Sons, 1982, pp 129-162.

[Wittmann83] Wittmann F. H., *Structure of concrete with respect to crack formation*, Fracture mechanics of concrete, Ed. by F.H.Wittmann, Developments in Civil Engineering 7, Elsevier science Publishers B.V., Amsterdam, Netherlands, 1983, pp 43-74.

[Wuest04] Wuest J., *Etude Exploratoire des Propriétés Mécaniques de Bétons de Fibres Ultra Performants de Structures*, Diploma thesis, MCS, Swiss Federal Institute of Technology (EPFL), Lausanne, Switzerland, March, 2004, 137 p. (in French).

[Yuan94] Yuan Y. , Marosszeky M., *Restrained shrinkage in repaired reinforced concrete elements*, Materials and Structures, Vol. 27, No. 171, 1994, pp 375-382.

[Yudenfreund72] Yudenfreund M., Odler I., Brunauer S., *Hardened Portland Cement Pastes of Low Porosity, I. Materials and Experimental Methods*, Cement and Concrete Research, Vol. 2, No. 3, May, 1972, pp 313-330.

[Yudenfreund72a] Yudenfreund M., Skalny J., Mikhail R. S., Brunauer S., *Hardened Portland Cement Pastes of Low Porosity, II. Exploratory Studies. Dimensional Changes*, Cement and Concrete Research, Vol. 2, No. 3, May, 1972, pp 331-348.

[Yudenfreund72b] Yudenfreund M., Hanna K, M., Skalny J., Odler I., Brunauer S., *Hardened Portland Cement Pastes of Low Porosity, V. Compressive Strength*, Cement and Concrete Research, Vol. 2, No. 6, 1972, pp 731-743.

[Zhu91] Zhu Y., *Evaluation of bond strength between new and old concrete by means of fracture mechanics method*, Doctoral thesis, Royal Institute of Technology (KTH), Bull. 157, Stockholm, Sweden, May, 1991, 102 p.

Appendices

Appendix A: Uniaxial tensile test (UHPFRC)

*TABLE A.1: Uniaxial tensile tests on notched plate specimens (50*20*5 cm^3, notched section: 16*5 cm^2)*

Name	Age [days]	maximum force			force at 1st crack			maximum force hardening			E_t [GPa]	G_F [kJ/m^2]	Remarks
		F_{max} [kN]	σ_{max} [MPa]	$disp_{1st}$ [mm]	F_{1st} [kN]	σ_{1st} [MPa]	$disp_{1st}$ [mm]	F_{hard} [kN]	σ_{hard} [MPa]	$disp_{hard}$ [mm]			
A57T01	3.8	62.1	7.8	0.354	39.8	5	0.015	62.1	7.8	0.354	38.8	10.2	cyclic test
A57T02	4.2	49.6	6.2	0.065	45.5	5.7	0.02	49.6	6.2	0.065	38.4	6.7	
A57T03	4.9	57.4	7.2	0.042	53.4	6.7	0.029	57.4	7.2	0.042	34.9	12.8	
A55T01	7.8	52.9	6.6	0.025	52.3	6.5	0.025	49.6	6.2	0.082	36.1	8.7	cyclic test
A55T02	8.1	46.6	5.8	0.088	41.4	5.2	0.018	46.6	5.8	0.088	38.8	7.1	
A55T03	8.9	39.8	5	0.014	39.8	5	0.014	37.7	4.7	0.074	37.1	7.9	
A55T04	14.2	62.4	7.8	0.087	62.0	7.8	0.024	62.4	7.8	0.087	38.8	13.5	
A55T05	14.9	58.6	7.3	0.026	58.6	7.3	0.026	54.4	6.8	0.078	39.3	8.8	
A18T01	26.7	88.4	11.1	0.202	69.4	8.7	0.024	88.4	11.1	0.202	40.8	12.2	early fracture
A44T01	26.8	87.7	11	0.252	66.5	8.3	0.026	87.7	11.0	0.252	39.2	22.1	
A18T02	27.7	88.4	11.1	0.279	79.5	9.9	0.035	88.4	11.1	0.279	36.7	19.5	
A44T02	27.8	80.9	10.1	0.207	69.3	8.7	0.025	80.9	10.1	0.207	39.4	20.8	
A44T03	28.7	76.6	9.6	0.039	73.9	9.2	0.027	76.6	9.6	0.039	43.2	-	cyclic test, early fracture
A18T03	28.7	93.9	11.7	0.337	81.1	10.1	0.029	93.9	11.7	0.337	40.3	26.7	
A44T04	30.9	80.7	10.1	0.031	80.7	10.1	0.031	-	-	-	32.7	-	early fracture
A18T04	96.7	95.1	11.9	0.062	83.7	10.5	0.027	95.1	11.9	0.062	45.6	19.9	
A18T05	97.7	104	13	0.285	94.1	11.8	0.031	104	13	0.285	45.8	23.1	
A18T06	98.7	106.6	13.3	0.236	90.7	11.3	0.031	106.6	13.3	0.236	46.1	28.3	
A18T07	364	98.5	13.1	0.274	74.1	9.8	0.025	98.5	13.1	0.274	44.1	23.4	
A18T08	365	101.4	13.4	0.214	82.9	11	0.026	101.4	13.4	0.214	48.1	28.7	
A18T09	368	92.7	12.3	0.248	74.3	9.8	0.026	92.7	12.3	0.248	43.7	20.5	

*TABLE A.1. Uniaxial tensile tests on dogbone plate specimens (70*20*5 cm^3, reduced section: 16*5 cm^2)*

		maximum force		force at 1st crack		
Name	**Age [days]**	**F_{max} [kN]**	**σ_{max} [MPa]**	**F_{1st} [kN]**	**σ_{1st} [MPa]**	**E_t [GPa]**
A44JPC1	19.8	72.2	9.6	64.4	8.6	50.0
A44JPC2	20.1	47.4	6.3	39.4	5.3	49.4
A45JPC3	27	85.9	11.5	65.0	8.7	54.2
A45JPC4	28	87.4	11.7	71.4	9.5	52.7
A55T06L	244	95.8	12.0	88.2	11.0	59.8
A55T07L	245	81.8	10.2	81.8	10.2	56.4

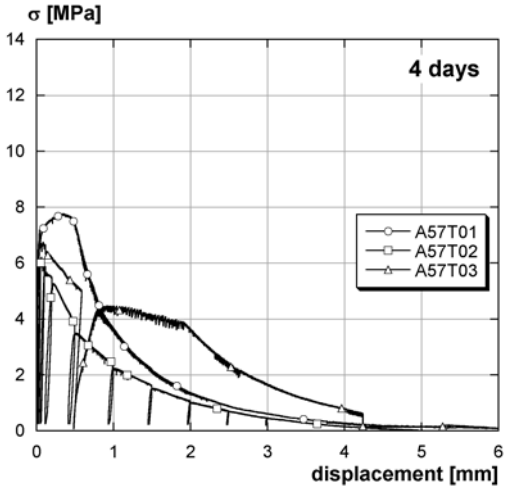

FIGURE A.2: Stress-disp. curves - 4 days

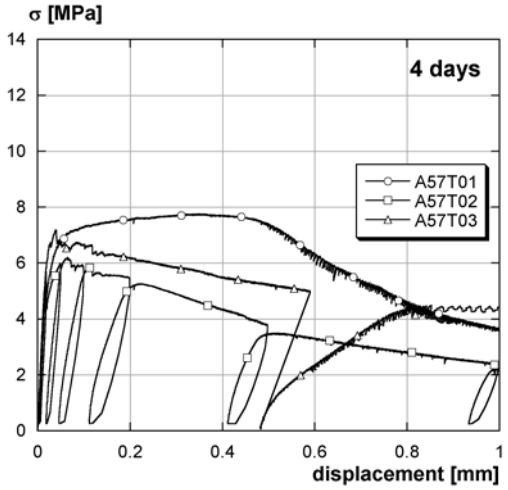

FIGURE A.3: Stress-disp. curves - 4 days (detail)

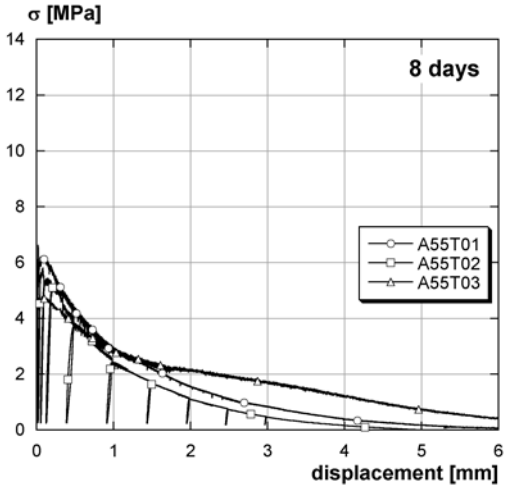

FIGURE A.4: Stress-disp. curves - 8 days

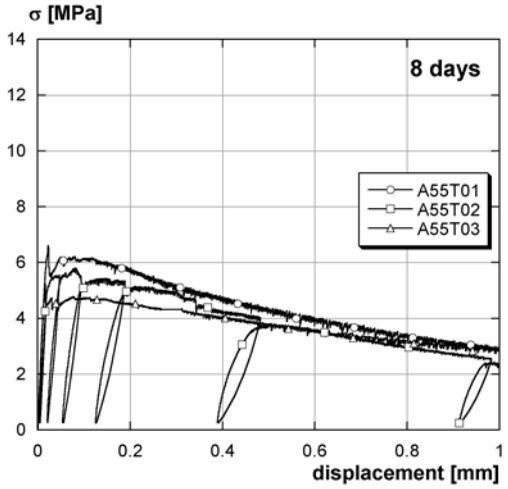

FIGURE A.5: Stress-disp. curves - 8 days (detail)

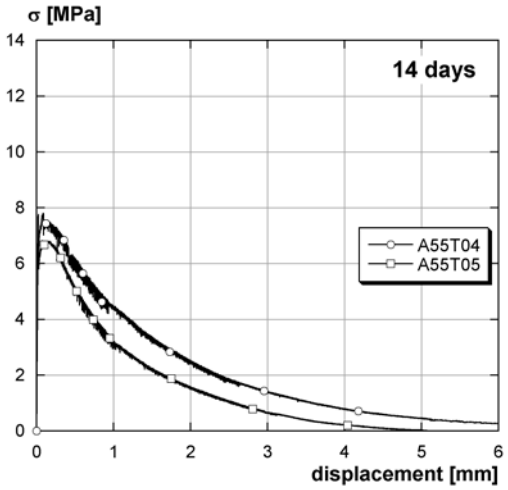

FIGURE A.6: Stress-disp. curves - 14 days

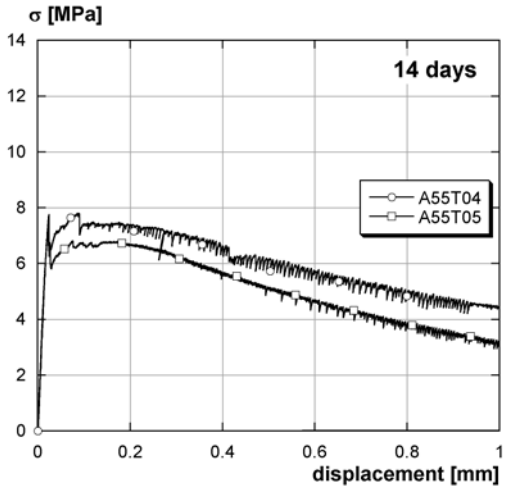

FIGURE A.7: Stress-disp. curves - 14 days (detail)

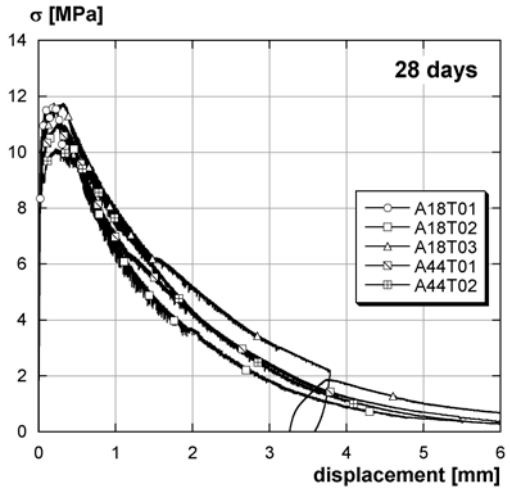

FIGURE A.8: Stress-disp. curves - 28 days

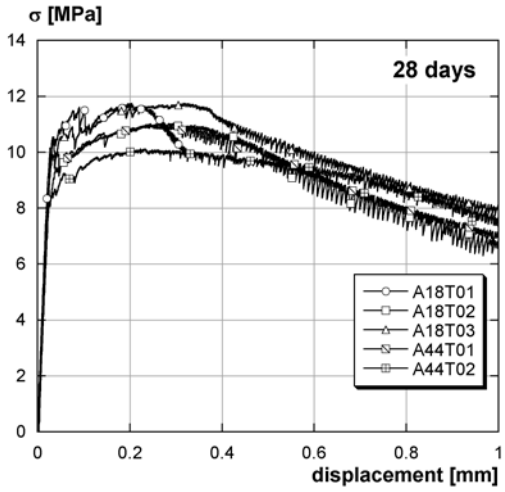

FIGURE A.9: Stress-disp. curves - 28 days (detail)

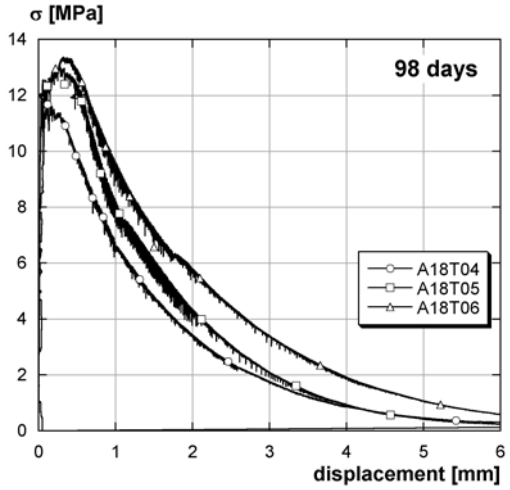

FIGURE A.10: Stress-disp. curves - 98 days

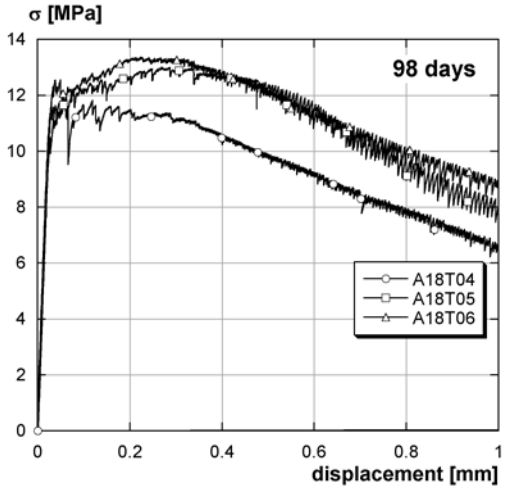

FIGURE A.11: Stress-disp. curves - 98 days (detail)

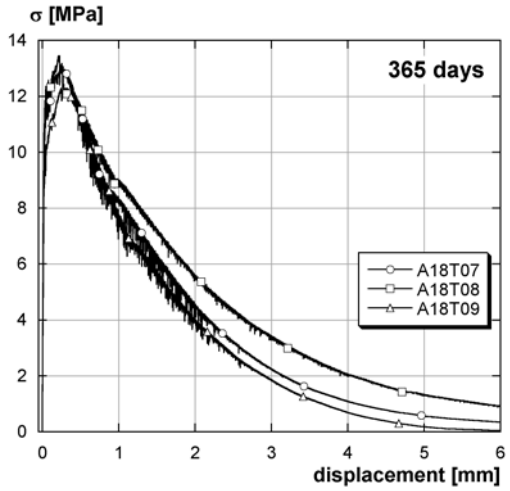

FIGURE A.12: Stress-disp. curves - 365 days

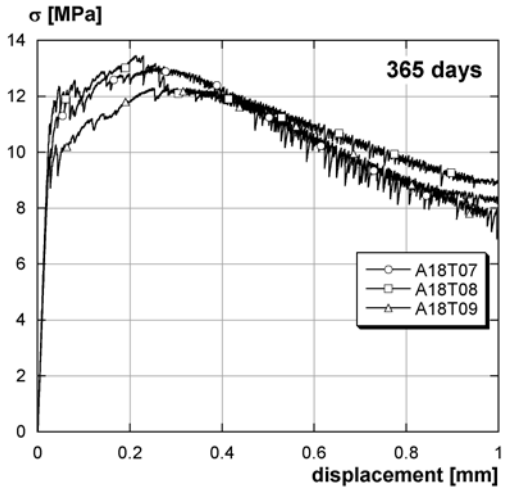

FIGURE A.13: Stress-disp. curves - 365 days (detail)

Fracture of the 4 days old specimens

FIGURE A.14: A57T01 - side 1

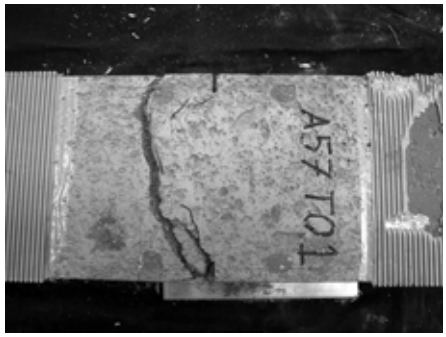

FIGURE A.15: A57T01 - side 2

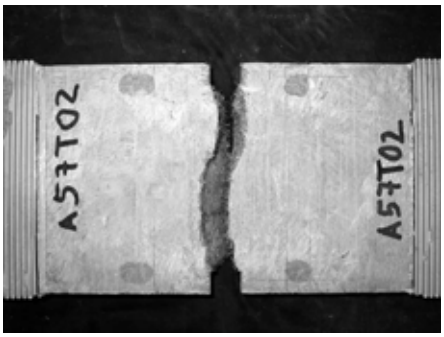

FIGURE A.16: A57T02 - side 1

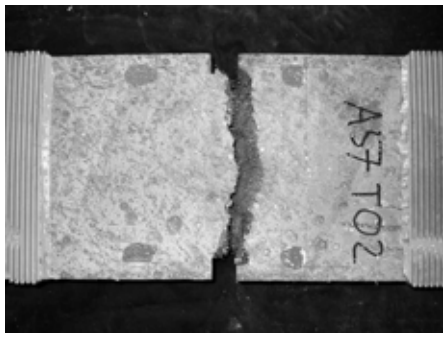

FIGURE A.17: A57T02 - side 2

FIGURE A.18: A57T03 - side 1

FIGURE A.19: A57T03 - side 2

Fracture of the 8 days old specimens

FIGURE A.20: A55T01 - side 1

FIGURE A.21: A55T01 - side 2

FIGURE A.22: A55T02 - side 1

FIGURE A.23: A55T02 - side 2

FIGURE A.24: A55T03 - side 1

FIGURE A.25: A55T03 - side 2

Fracture of the 14 days old specimens

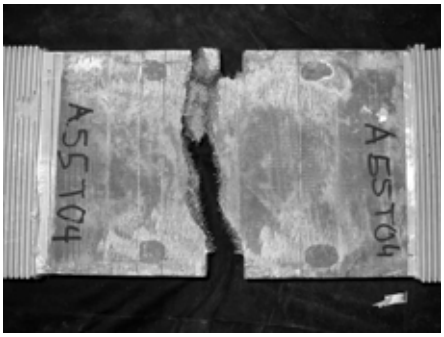

FIGURE A.26: A55T04 - side 1

FIGURE A.27: A55T04 - side 2

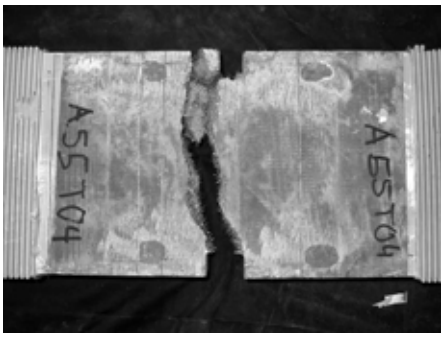

FIGURE A.28: A55T05 - side 1

FIGURE A.29: A55T05 - side 2

Fracture of the 28 days old specimens

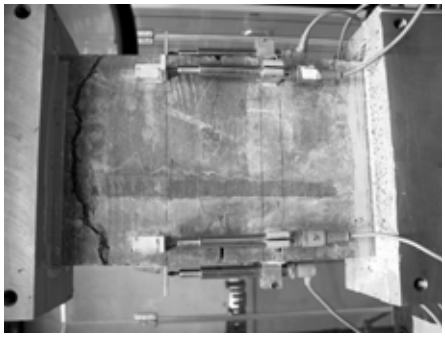

FIGURE A.30: A18T01 - side 1

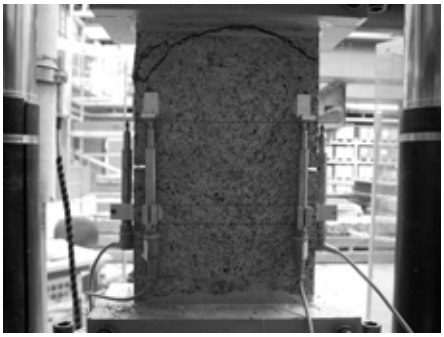

FIGURE A.31: A18T01 - side 2

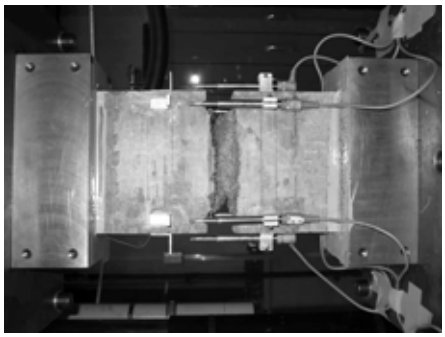

FIGURE A.32: A18T02 - side 1

FIGURE A.33: A18T02 - side 2

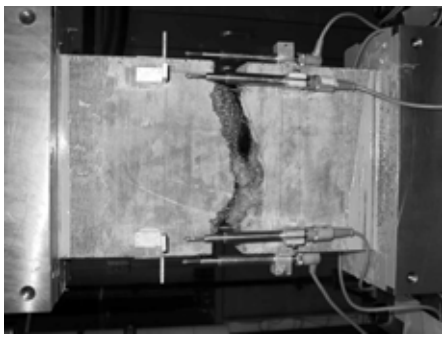

FIGURE A.34: A18T03 - side 1

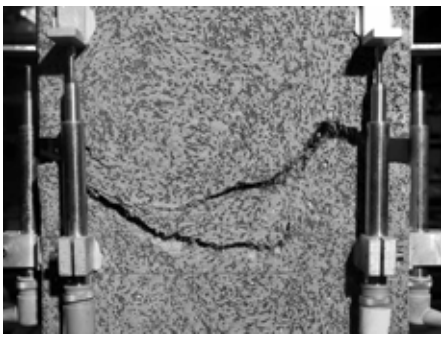

FIGURE A.35: A18T03 - side 2

FIGURE A.36: A44T01 - side 1

FIGURE A.37: A44T01 - side 2

FIGURE A.38: A44T02 - side 1

FIGURE A.39: A44T02 - side 2

Fracture of the 98 days old specimens

FIGURE A.40: A18T05 - side 1

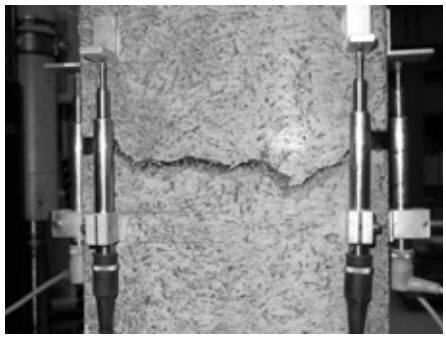

FIGURE A.41: A18T05 - side 2

Fracture of the 365 days old specimens

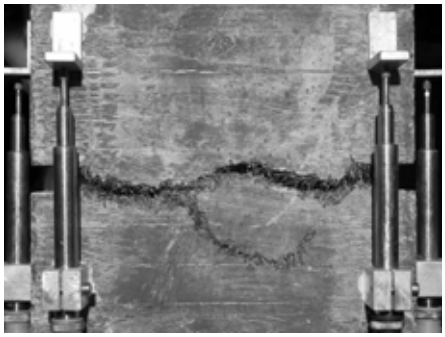

FIGURE A.42: A18T08 - side 1

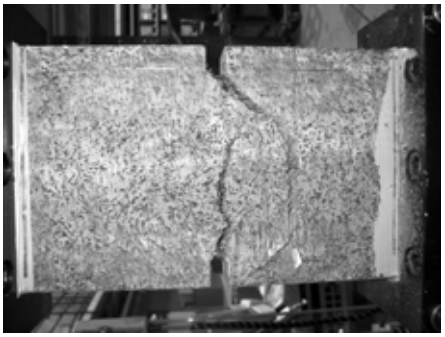

FIGURE A.43: A18T08 - side 2

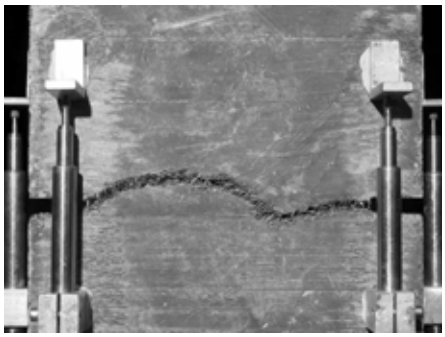

FIGURE A.44: A18T09 - side 1

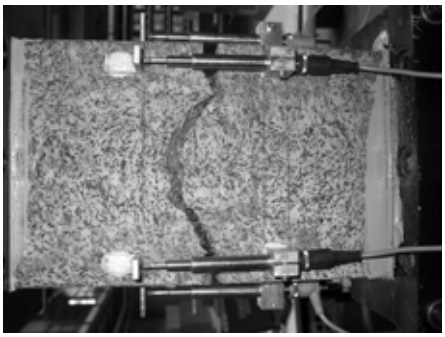

FIGURE A.45: A18T09 - side 2

Fit of the different model parameters

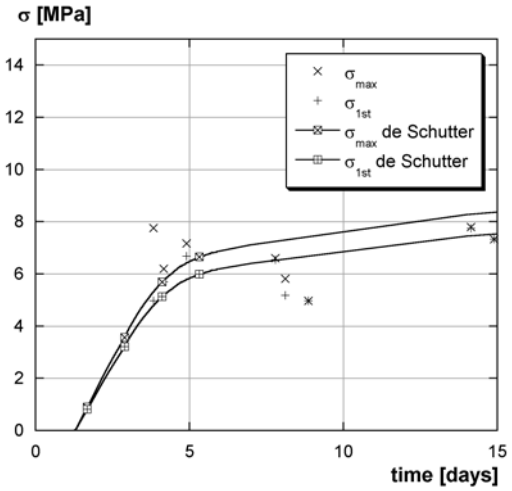

FIGURE A.46: Tensile strength of the UHPFRC: fit to the de Schutter model

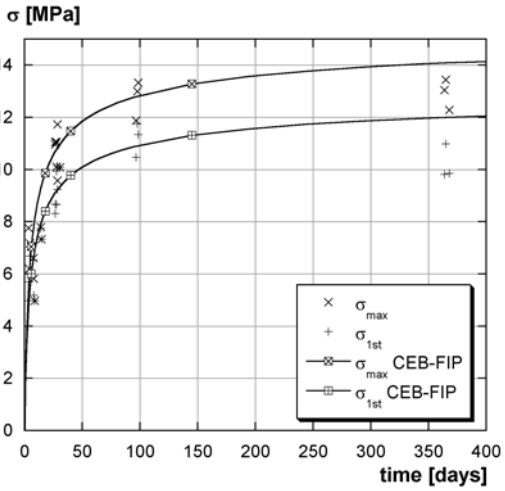

FIGURE A.47: Tensile strength of the UHPFRC: fit to the CEB-FIP model

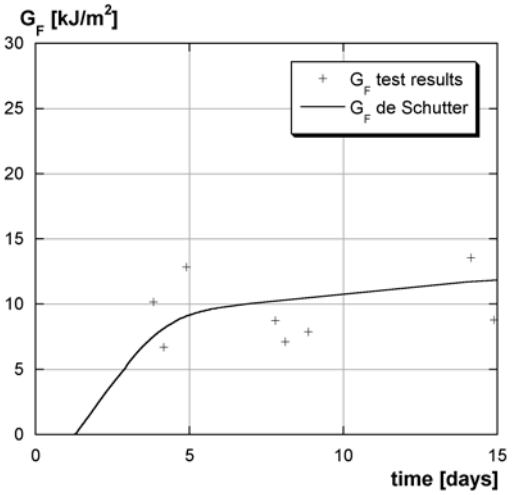

FIGURE A.48: Fracture energy of the UHPFRC: fit to the de Schutter model

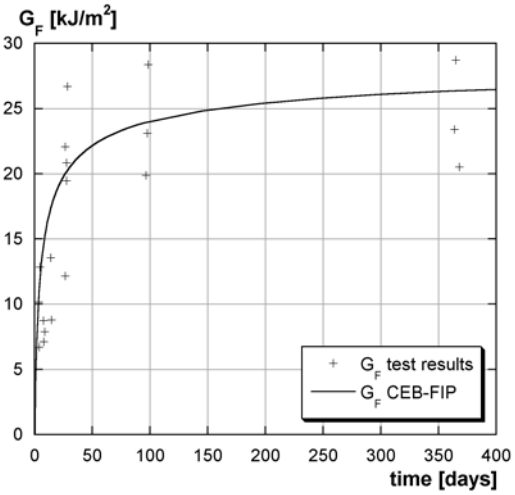

FIGURE A.49: Fracture energy of the UHPFRC: fit to the CEB-FIP model

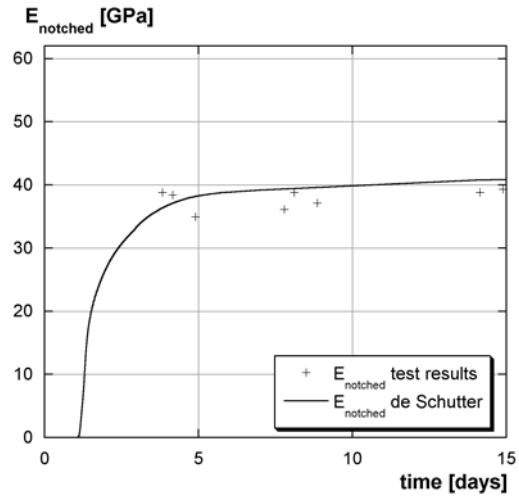

FIGURE A.50: $E_{notched}$ (UHPFRC): fit to the de Schutter model

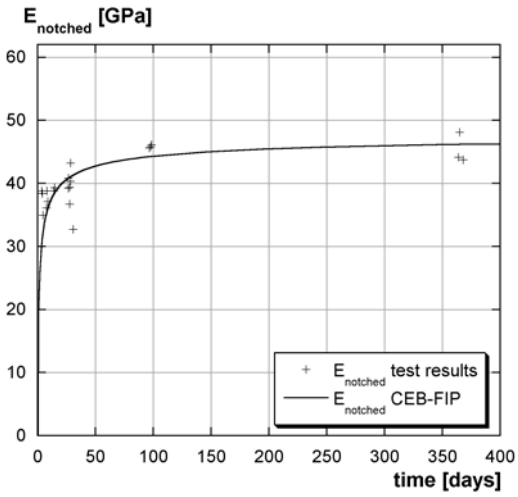

FIGURE A.51: $E_{notched}$ (UHPFRC): fit to the CEB-FIP model

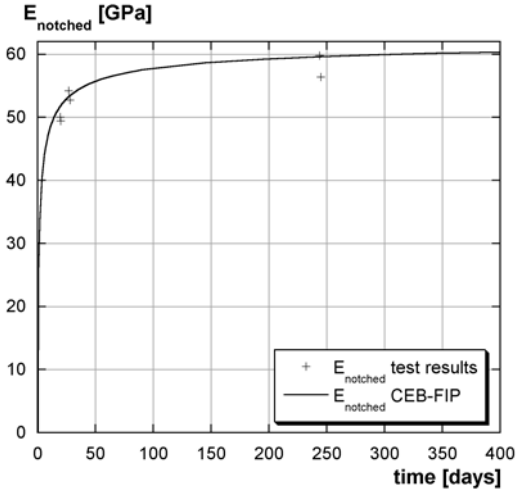

FIGURE A.52: $E_{dogbone}$ (UHPFRC): fit to the CEB-FIP model

Appendix B: Experimental program of the beam tests

	Date	Age of the old layer [days]	Age of the new layer [days]
Old layer			
casting	7.2.2002	0	-
removal of the formwork	11.2.2002	4	-
transport to the EPFL	12.2.2002	5	-
application of the epoxide resin on the sides (2 layers)	14./15.2.2002	6/7	-
hydrojetting	14./15.5.2002	96/97	-
re-application of the epoxide resin (2 layers)	16./17.5.2002	98/99	-
Series 1 (h_U = 5 cm)			
installation of the beams (statically determinate beams, ISO)	2.7.2002	145	-
(statically indeterminate beams, HYP)	3.7.2002	146	-
fixation of the supports of the HYP	11.7.2002	154	-
casting of the new layer (ISO)	24.7.2002	167	0
(HYP)	16.7.2002	159	0
removal of the formwork (ISO)	29.7.2002	172	6
(HYP)	22.7.2002	165	6
application of epoxide resin on the sides (2 layers) (ISO)	29./30.7.2002	172/173	5/6
(HYP)	22./23.7.2002	165/166	6/7
loading (ISO)	22.8.2002	196	29
unloading (ISO)	8.10.2002	243	76
loosening of the supports of the HYP	2.10.2002	237	78
end of the measurements (ISO)	10.10.2002	245	78
(HYP)	2.10.2002	237	78
fracture tests (ISO)	16./17.10.2002	251/252	84/85
(HYP)	18.10.2002	253	94

	Date	Age of the old layer [days]	Age of the new layer [days]
Series 2 (h_U = 10 cm)			
installation of the beams (statically determinate beams, ISO)	22.10.2002	257	-
(statically indeterminate beams, HYP)	23.10.2002	258	-
fixation of the supports of the HYP	24.10.2002	259	-
casting of the new layer (ISO)	12.11.2002	278	0
(HYP)	5.11.2002	271	0
removal of the formwork (ISO)	15.11.2002	281	3
(HYP)	8.11.2002	274	3
application of epoxide resin on the sides (2 layers) (ISO)	15./16.11.2002	281/282	3/4
(HYP)	8./10.11.2002	274/276	3/5
loading (ISO)	12.12.2002	308	30
unloading (ISO)	30.1.2003	357	79
loosening of the supports of the HYP	21.1.2003	348	77
end of the measurements (ISO)	4.2.2003	362	84
(HYP)	29.1.2003	356	85
fracture tests (ISO)	12.-14.2.2003	370-372	92-94
(HYP)	10./11.2.2003	368/369	97/98
Series 3 (h_U = 3 cm)			
installation of the beams (statically determinate beams, ISO)	4.2.2003	362	-
(statically indeterminate beams, HYP)	29.1.2003	356	-
fixation of the supports of the HYP	24.2.2003	382	-
casting of the new layer (ISO, HYP)	25.2.2003	383	0
removal of the formwork (ISO, HYO)	27.2.2003	385	2
application of epoxide resin on the sides (2 layers, ISO, HYP)	27.2./2.3.2003	385/388	2/5
loading (ISO)	25.3.2003	411	28
unloading (ISO)	13.5.2003	460	77
loosening of the supports of the HYP	14.5.2003	461	78
end of the measurements (ISO and HYP)	19.5.2003	466	83
fracture tests (ISO, HYP)	21.-23.5.2003	468-470	85-87

TABLE B.1. Sensors of the statically determinate beams

Denomination	Type	Place	Remarks
f1	LVDT 20 mm	mid-span deflection, central span	
f2	LVDT 20 mm	deflection cantilever south	
f3	LVDT 20 mm	deflection cantilever north	
HS	LVDT 10 mm	horizontal displacement south	
HN	LVDT 10 mm	horizontal displacement north	
IS	LVDT 1 mm	relative displacement between the concrete and the UHPFRC layer south	
IN	LVDT 1 mm	relative displacement between the concrete and the UHPFRC layer north	
AM	LVDT 10 mm	displacement of the freely movable support	
ODS U	optical deformation sensor	central span, UHPFRC layer (measuring length: 2 m)	
ODS L	optical deformation sensor	central span, concrete substrate (measuring length: 2 m)	
TC_U	thermocouple, type K	UHPFRC layer	
TC_{upp}	thermocouple, type K	concrete substrate, near the interface	
TC_{low}	thermocouple, type K	concrete substrate, near the lower surface	
HumU	humidity sensor	concrete substrate	only in beams I5 and I10L
HumL	humidity sensor	concrete substrate	only in beams I5 and I10L
RH1	humidity and temperature sensor ROTRONIC	UHPFRC layer	only in beam I5

TABLE B.2. Sensors of the statically indeterminate beams

Denomination	Type	Place	Remarks
f1	LVDT 20 mm	mid-span deflection, central span	
f2	LVDT 20 mm	mid-span deflection, end span, south	
f3	LVDT 20 mm	mid-span deflection, end span, north	
HS	LVDT 10 mm	horizontal displacement south	
HN	LVDT 10 mm	horizontal displacement north	
IS	LVDT 1 mm	relative displacement between the concrete and the UHPFRC layer south	
IN	LVDT 1 mm	relative displacement between the concrete and the UHPFRC layer north	
AS	LVDT 1 mm	displacement of the fixed support south	
AN	LVDT 1 mm	displacement of the fixed support north	
ODS U	optical deformation sensor	central span, UHPFRC layer (measuring length: 2 m)	
ODS L	optical deformation sensor	central span, concrete substrate (measuring length: 2 m)	
TC_U	thermocouple, type K	UHPFRC layer	
TC_{upp}	thermocouple, type K	concrete substrate, near the interface	
TC_{low}	thermocouple, type K	concrete substrate, near the lower surface	

TABLE B.3. Sensors used during the fracture tests

Denomination	Type	Place	Remarks
f1	LVDT 20 mm	mid-span displacement, central span	
f2	LVDT 20 mm	third point displacement (South), central span	
f3	LVDT 20 mm	third point displacement (North), central span	
f4	LVDT 50 mm	displacement cantilever south, under hydraulic jack	
f5	LVDT 50 mm	displacement cantilever north, under hydraulic jack	
f6	LVDT 10 mm	displacement support (South)	
f7	LVDT 10 mm	displacement support (North)	
F1	force sensor, 200 kN	force of the hydraulic jack, south	
F2	force sensor, 200 kN	force of the hydraulic jack, north	
ODS U	optical deformation sensor	central span, UHPFRC layer (measuring length: 2 m)	
ODS L	optical deformation sensor	central span, concrete substrate (measuring length: 2 m)	
Ω1 to Ω7	Ω-gages, base 100 mm	on the upper side of the beam, according to plans	
Ω10 to Ω15	Ω-gages, base 50 mm	on the sides of the beam, according to plans	

Appendix C: Reinforcement drawings

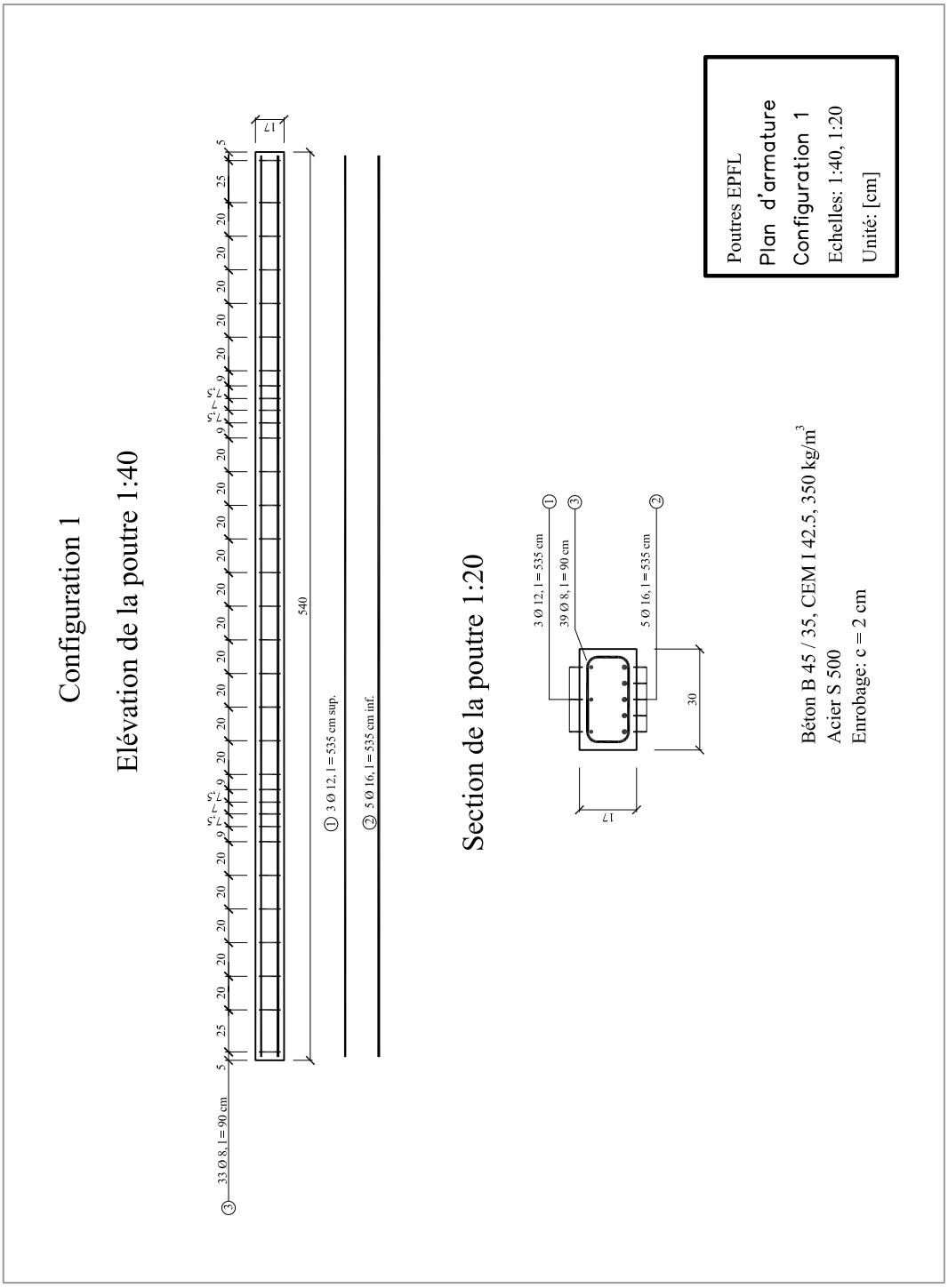

FIGURE C.1: Reinforcement drawing of the concrete substrate of the statically determinate beams

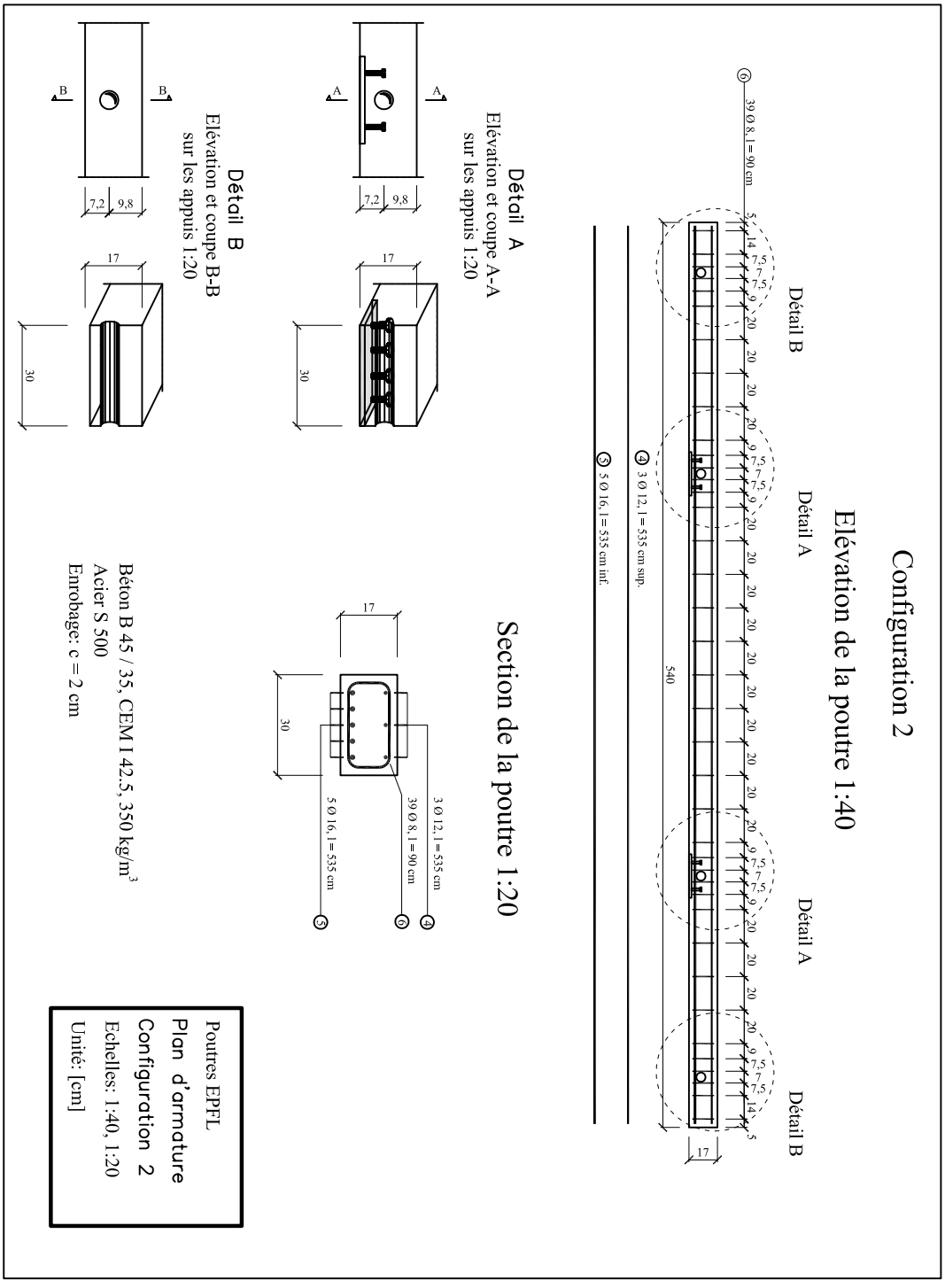

FIGURE C.2: Reinforcement drawing of the concrete substrate of the statically indeterminate beams

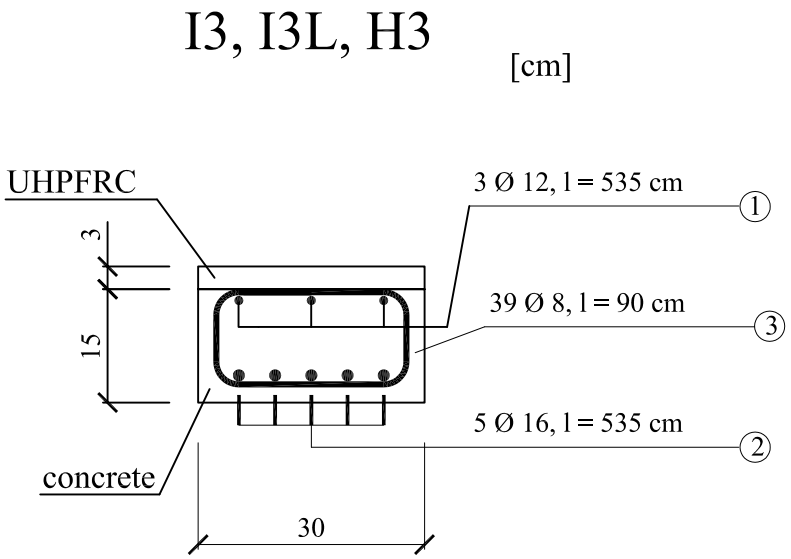

FIGURE C.3: Cross section of the beams with h_U = 3 cm, scale 1:10

I5, I5L, H5

[cm]

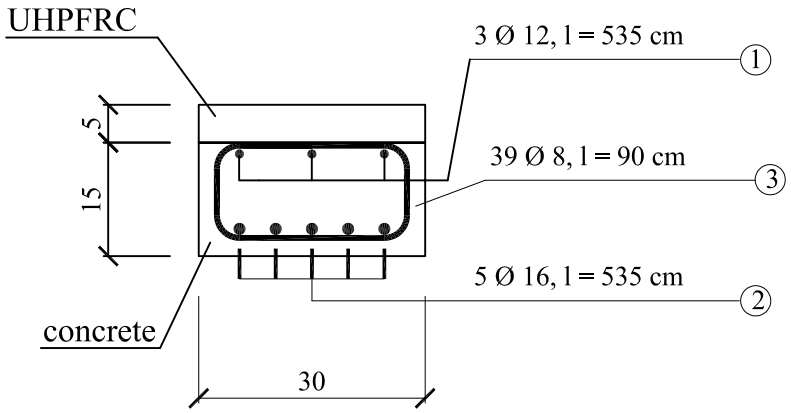

I5R, I5RL, H5R

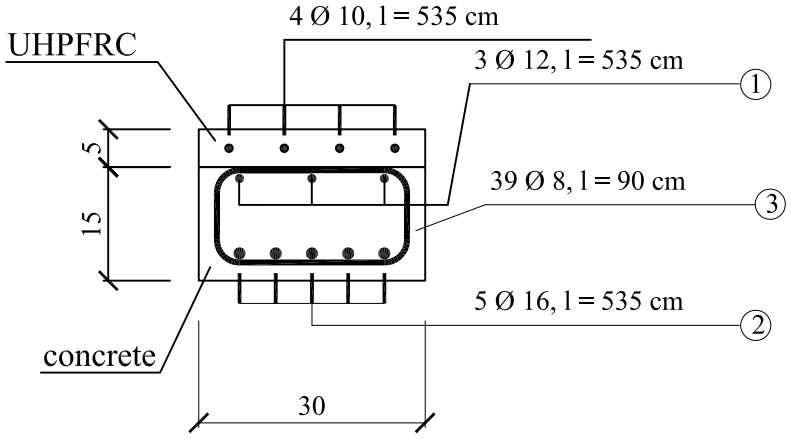

FIGURE C.4: Cross section of the beams with h_U = 5 cm, scale 1:10

I10, I10L, H10 [cm]

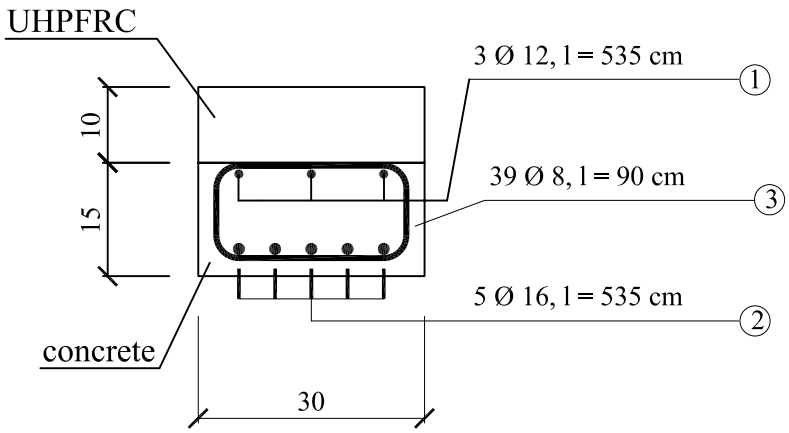

I10R, I10RL, H10R

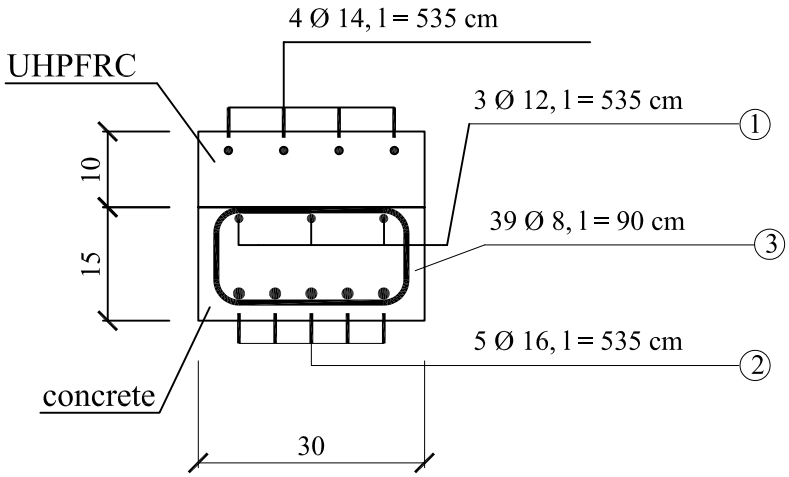

FIGURE C.5: Cross section of the beams with h_U = 10 cm, scale 1:10

Appendix D: Position of the Ω-gages during the fracture tests (scale 1:25)

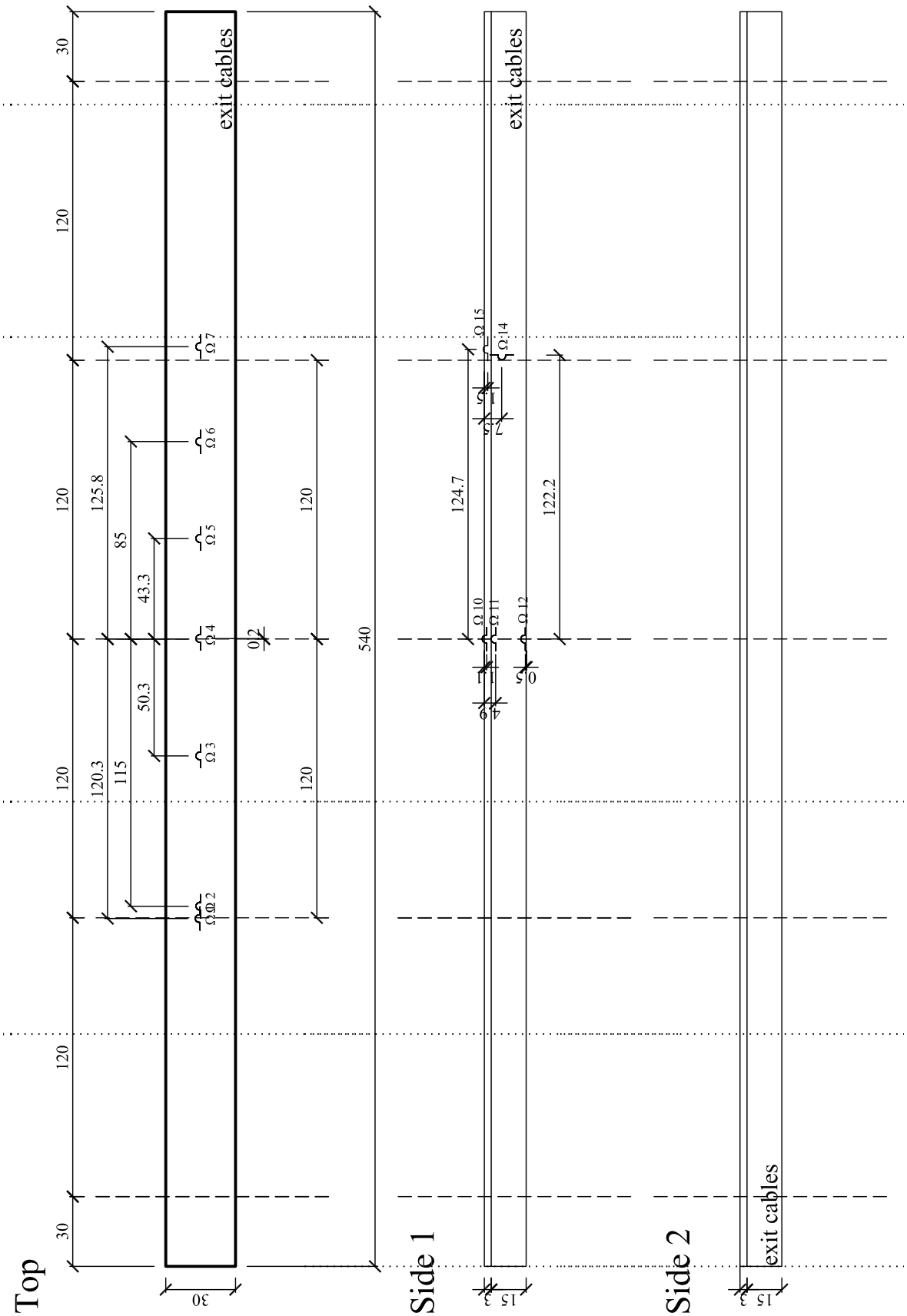

FIGURE D.1: Position of the Ω-gages during the fracture test: I3

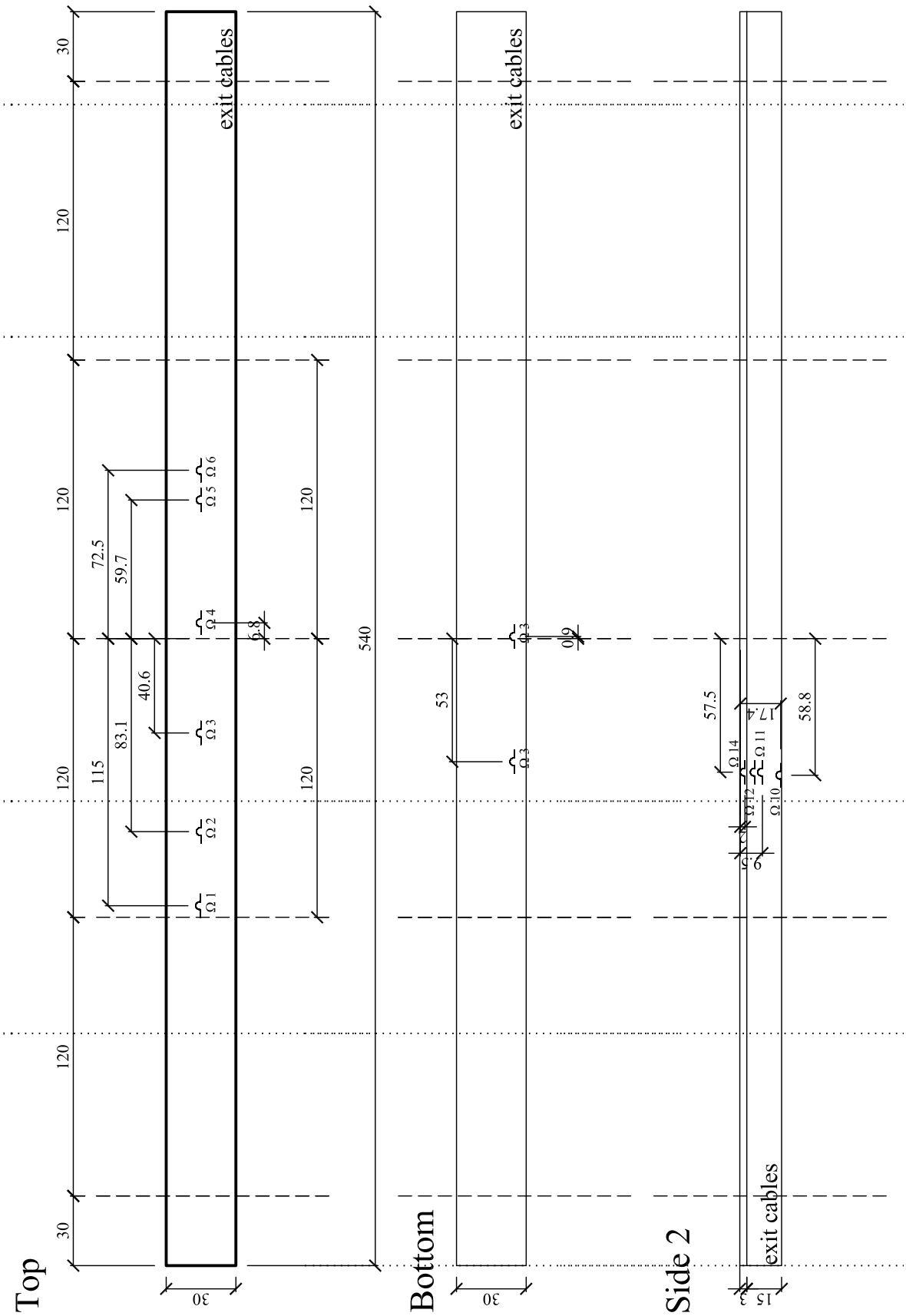

FIGURE D.2: Position of the Ω-gages during the fracture test: I3L

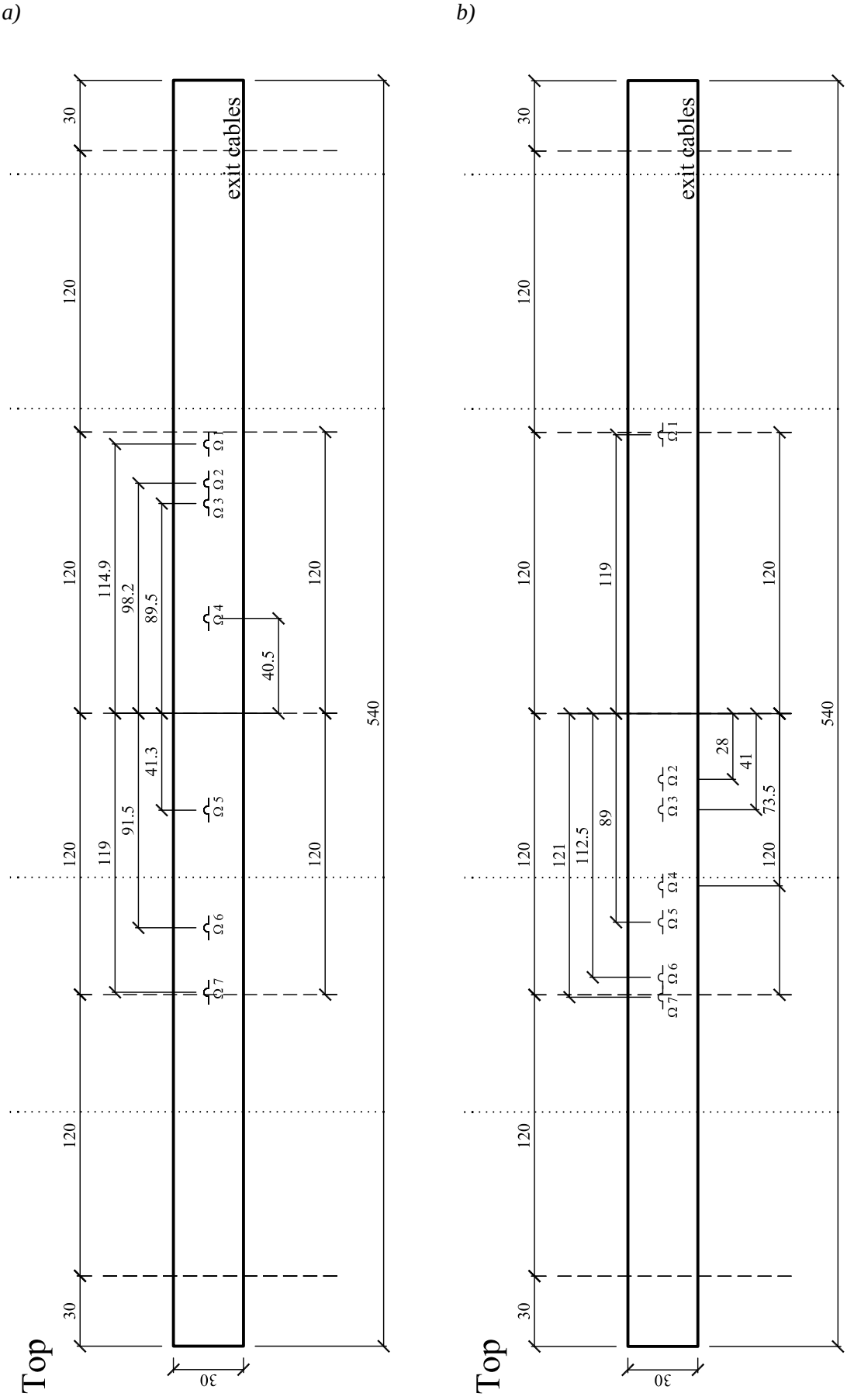

FIGURE D.3: Position of the Ω-gages during the fracture test: a) I5, b) I5L

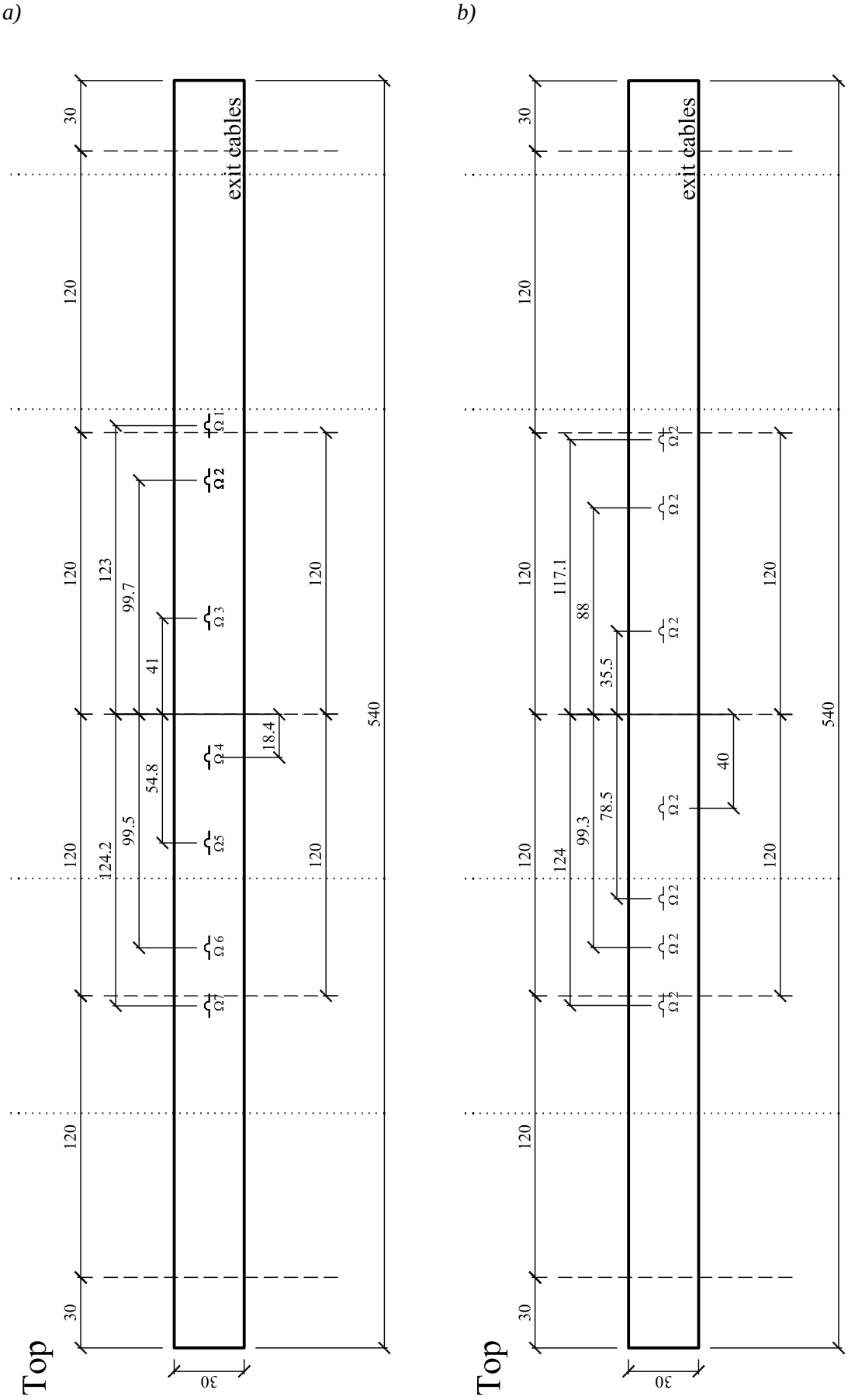

FIGURE D.4: Position of the Ω-gages during the fracture test: a) I5R, b) I5RL

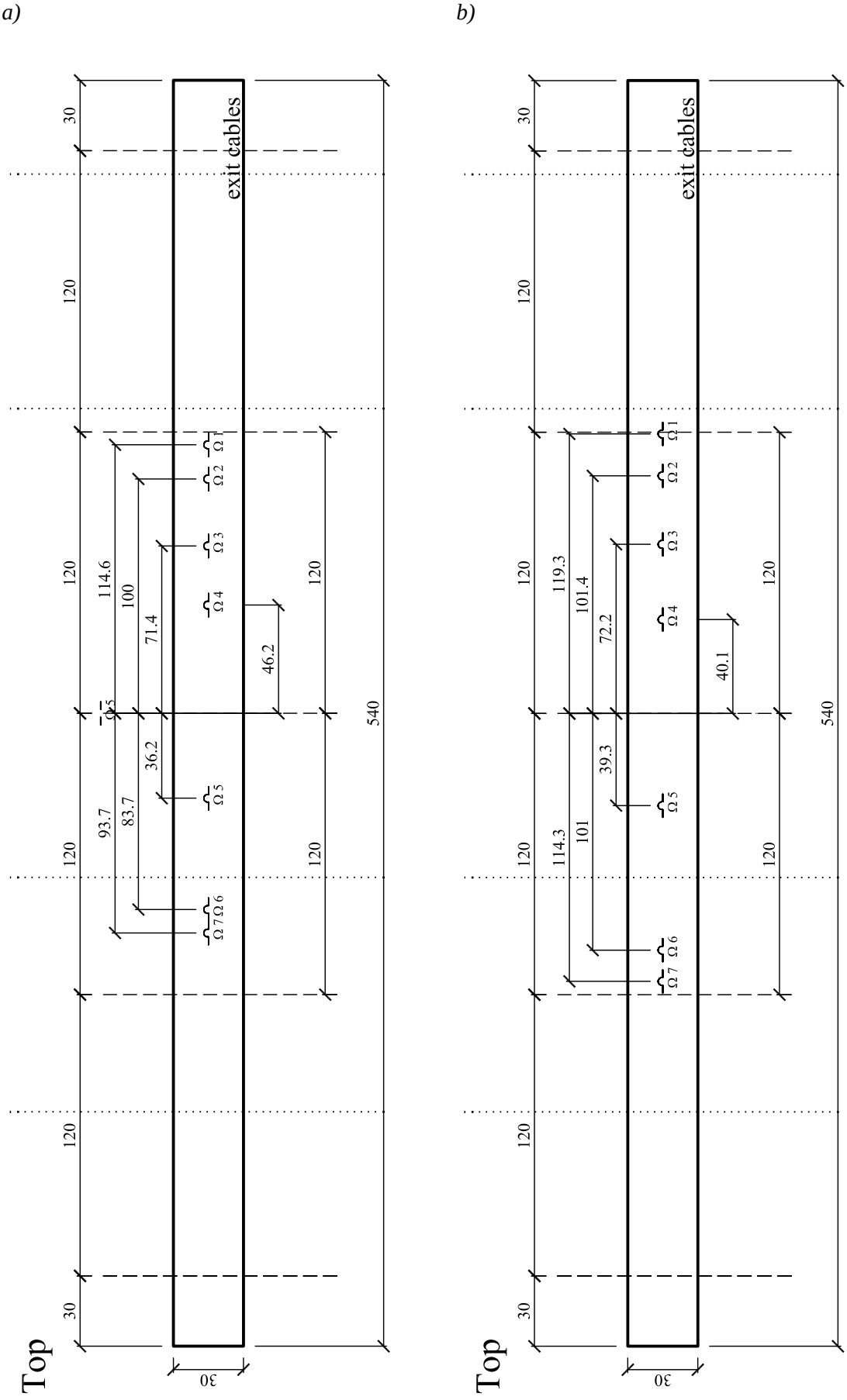

FIGURE D.5: Position of the Ω-gages during the fracture test: a) H5, b) H5R

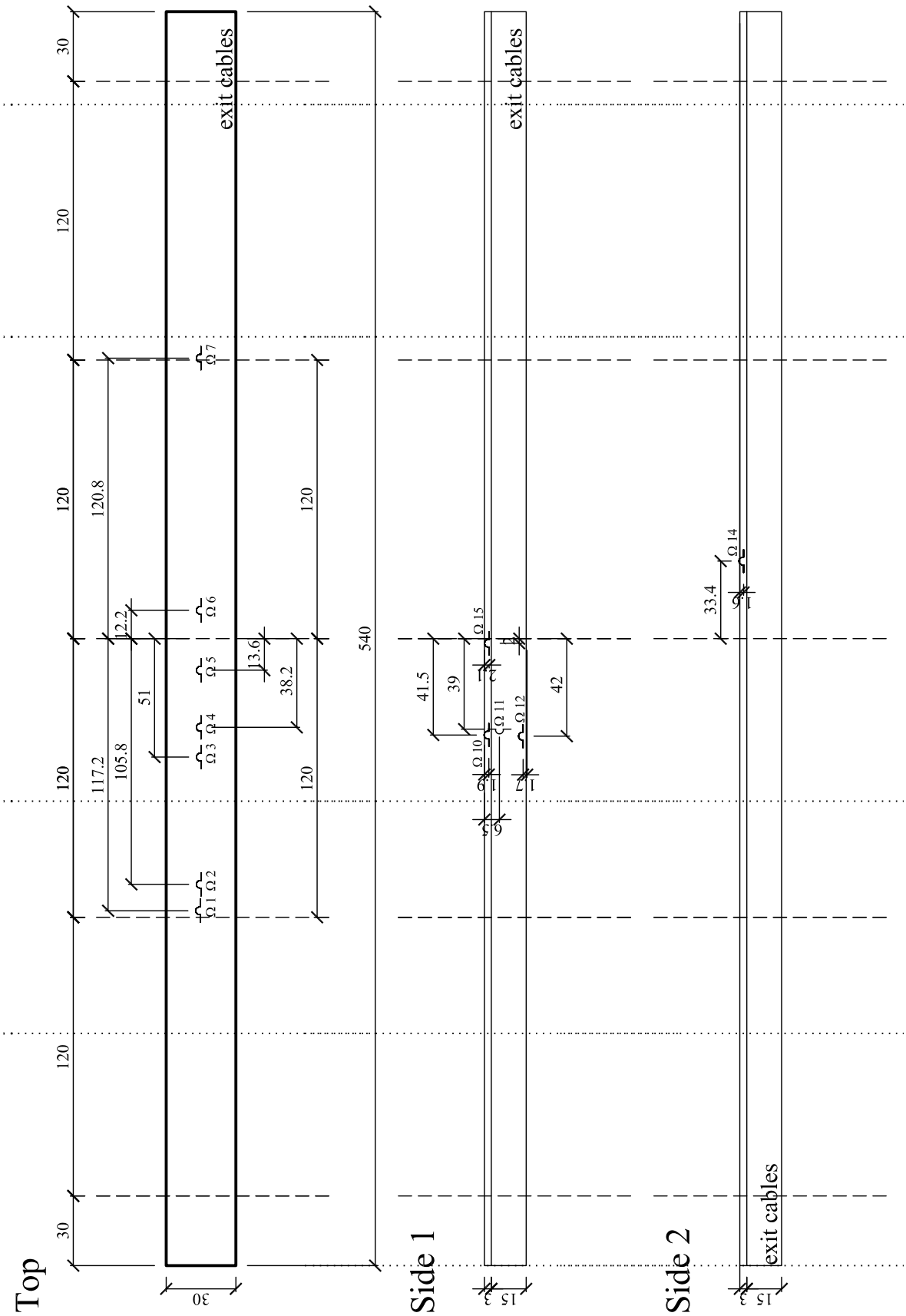

FIGURE D.6: Position of the Ω-gages during the fracture test: H3

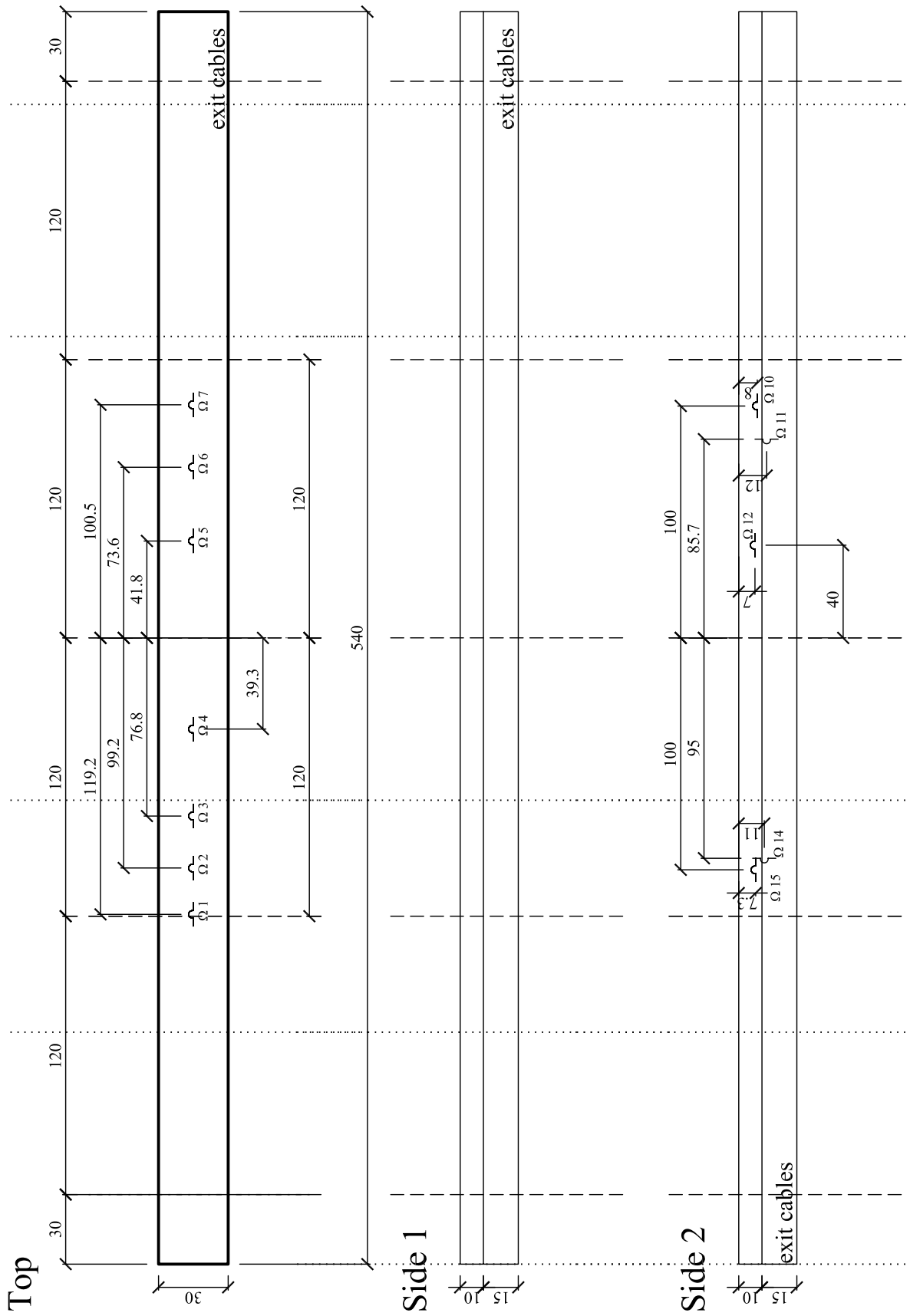

FIGURE D.7: Position of the Ω-gages during the fracture test: I10

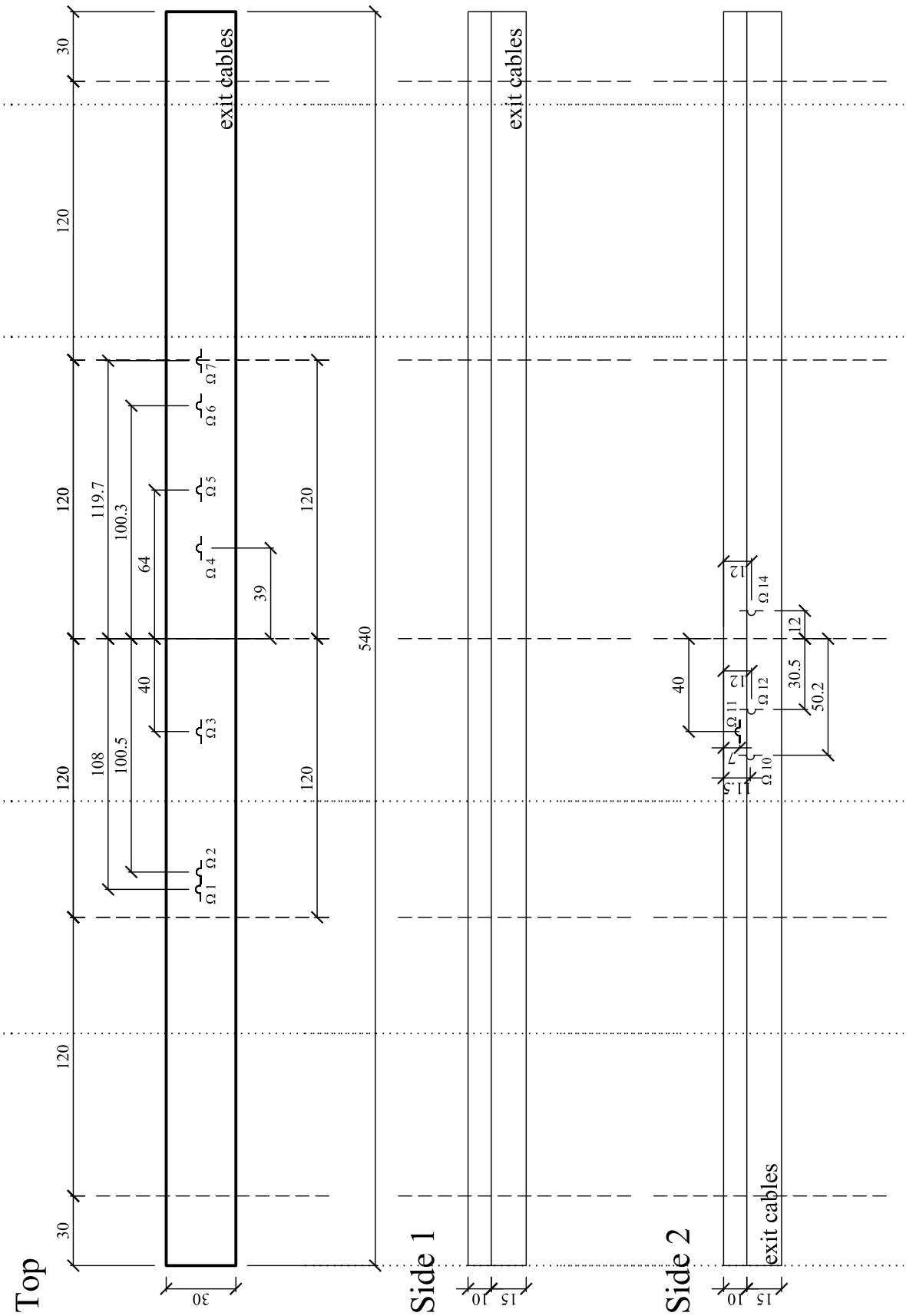

FIGURE D.8: Position of the Ω-gages during the fracture test: I10L

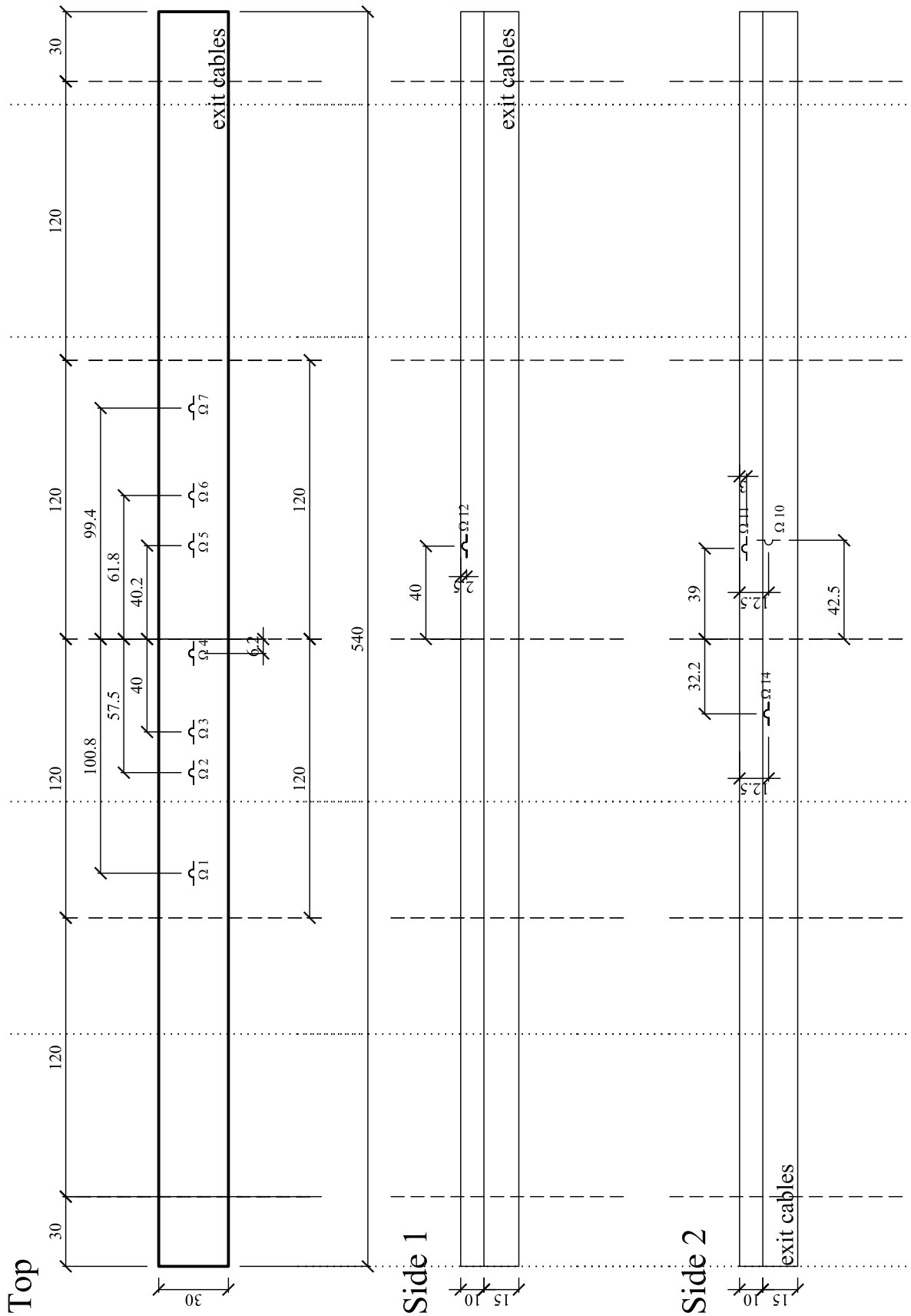

FIGURE D.9: Position of the Ω-gages during the fracture test: I10R

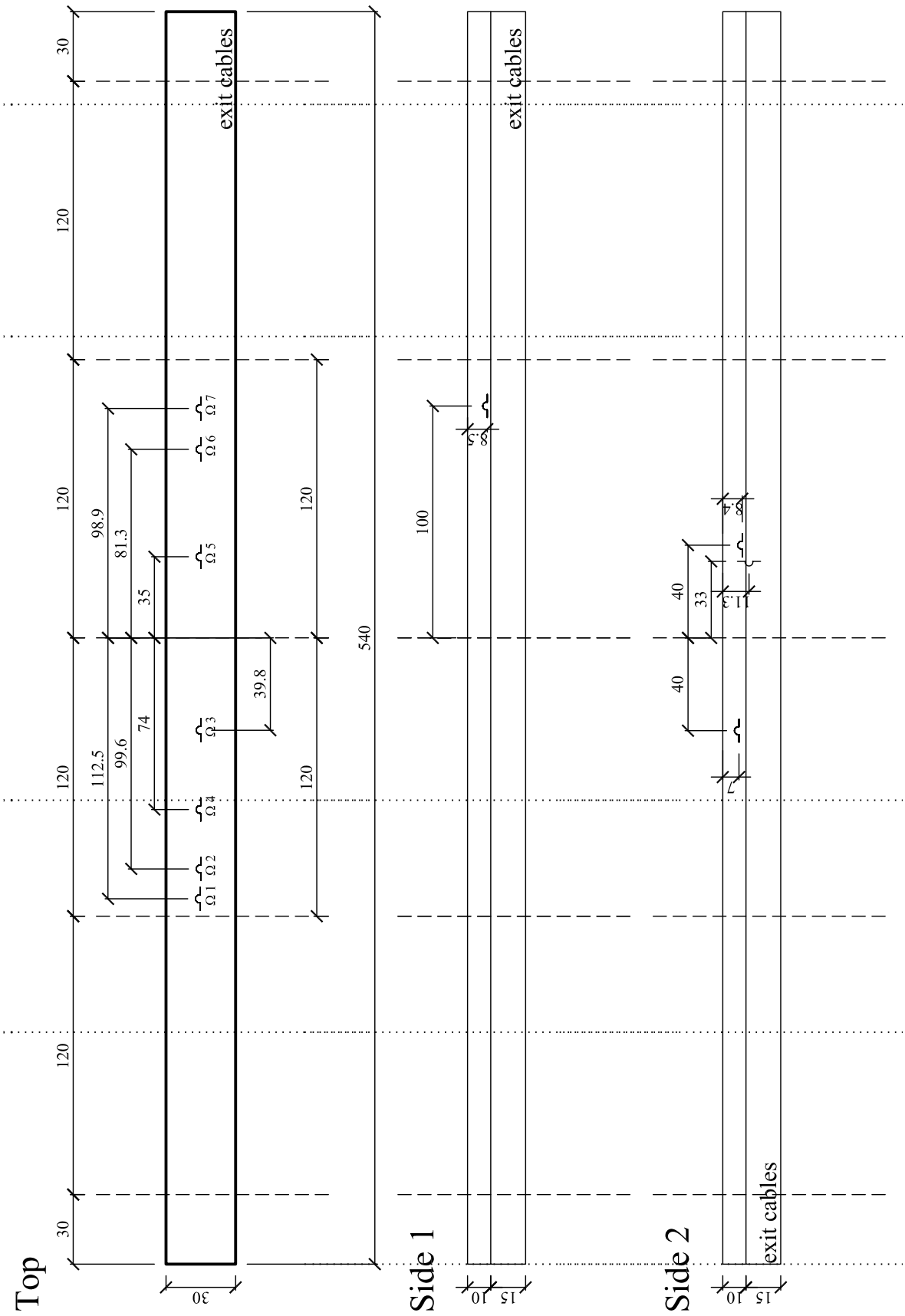

FIGURE D.10: Position of the Ω-gages during the fracture test: I10RL

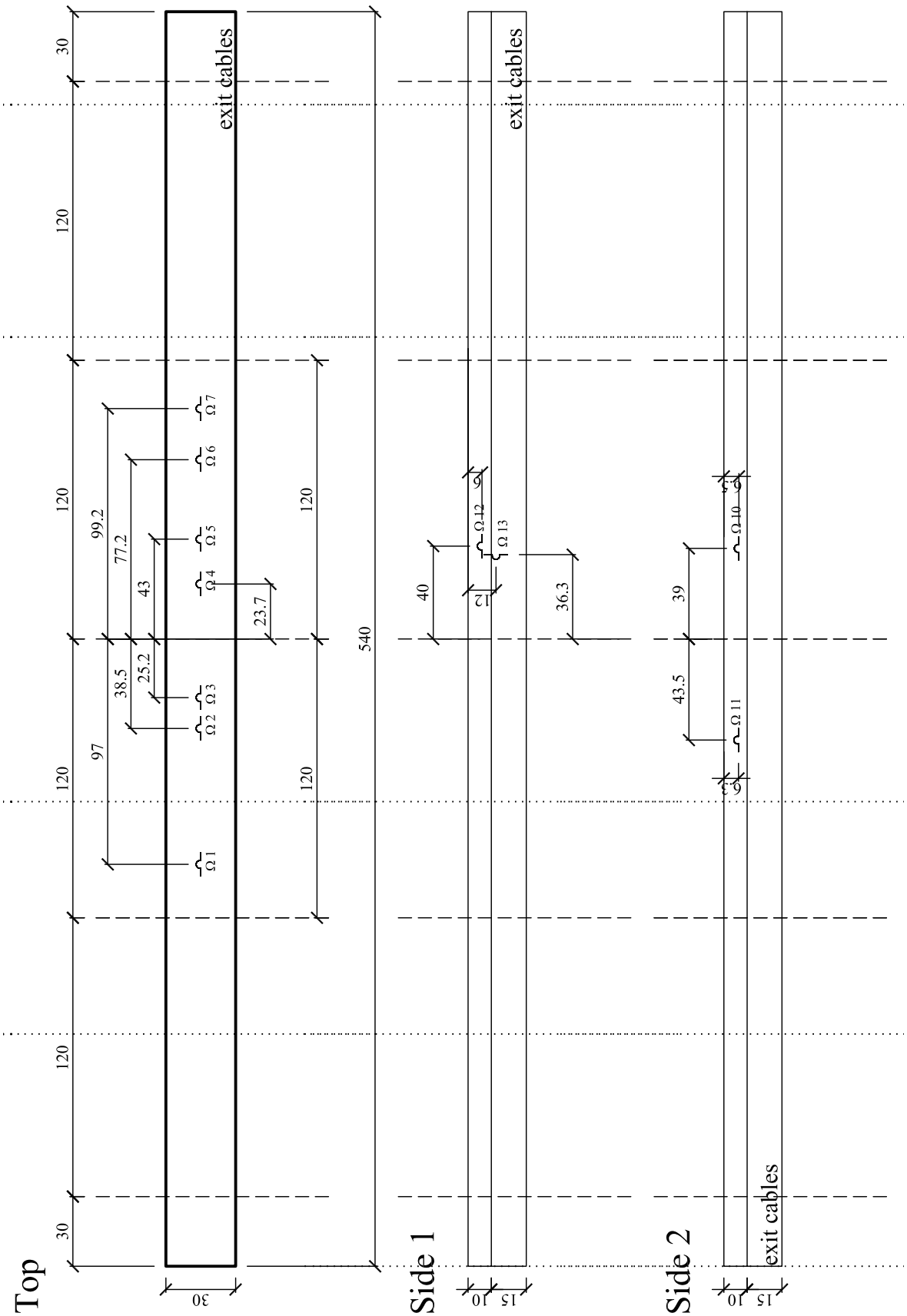

FIGURE D.11: Position of the Ω-gages during the fracture test: H10

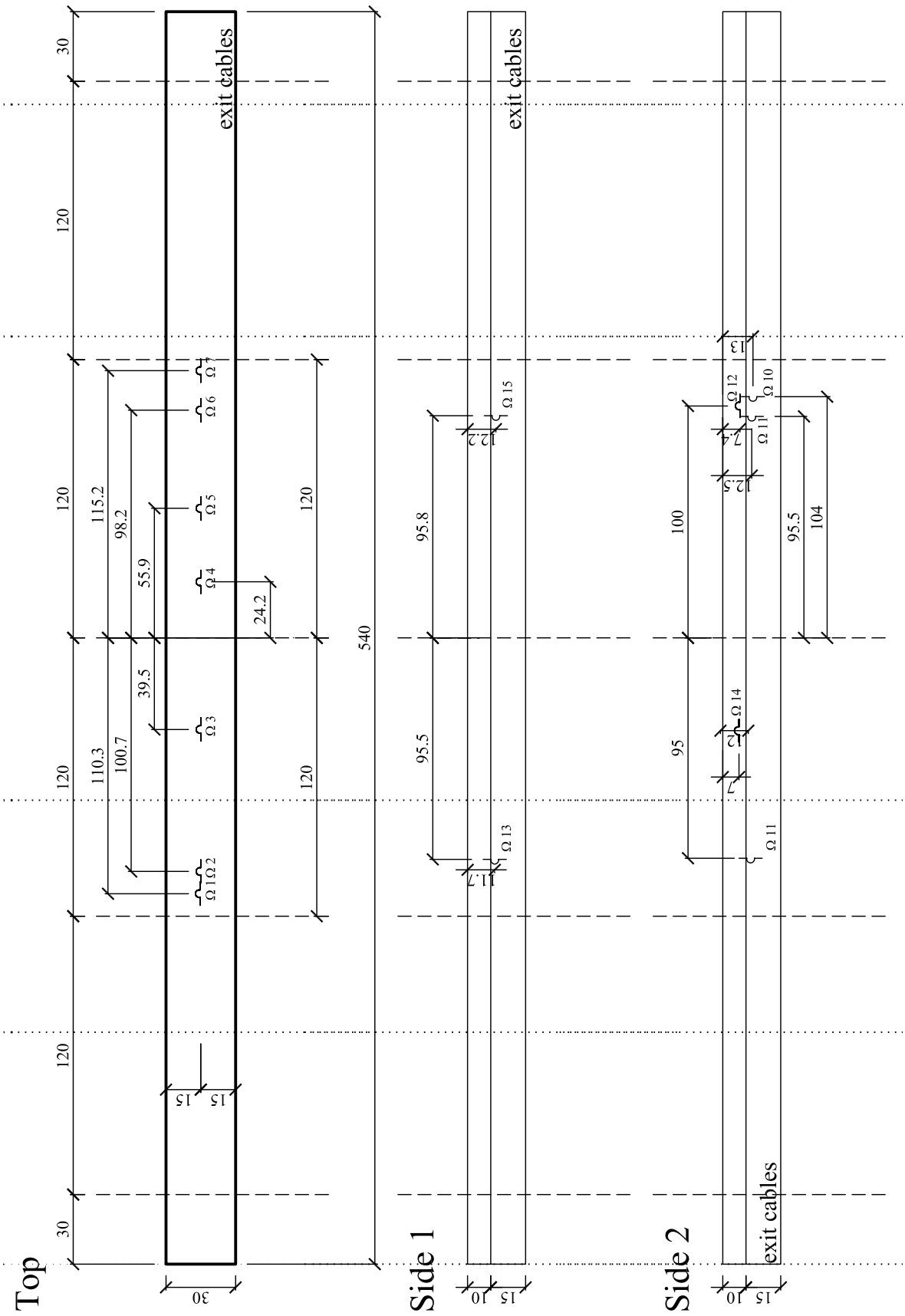

FIGURE D.12: Position of the Ω-gages during the fracture test: H10R

Appendix E: Temperature and relative humidity in the climatic tents

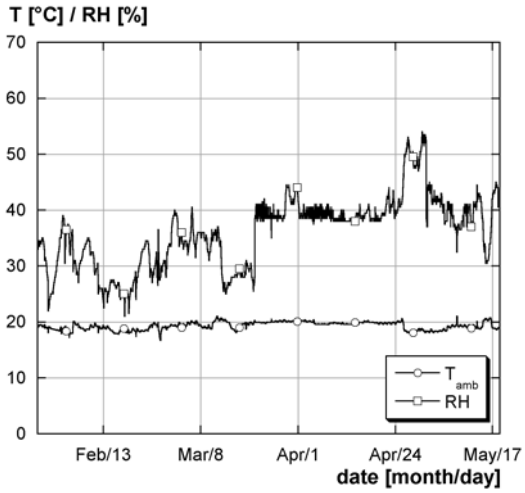

FIGURE E.1: Temperature and RH, statically determinate beams h_U = 3 cm

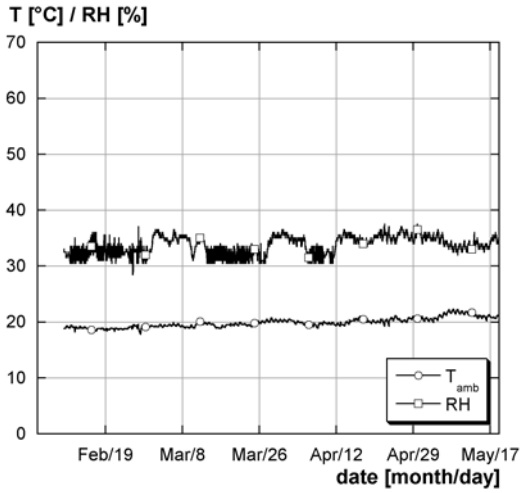

FIGURE E.2: Temperature and RH, statically indeterminate beams h_U = 3 cm

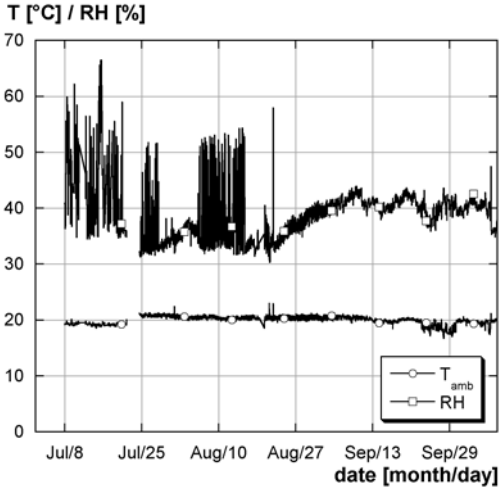

FIGURE E.3: Temperature and RH, statically determinate beams h_U = 5 cm

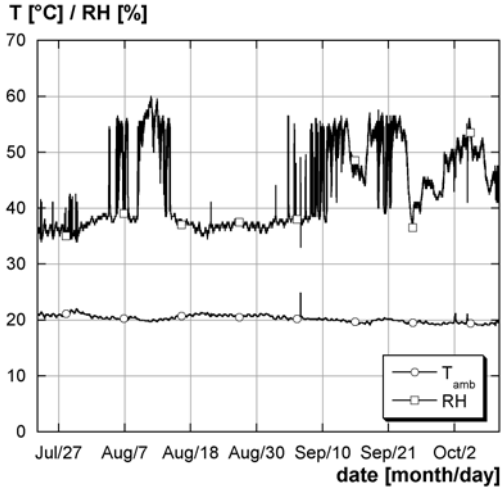

FIGURE E.4: Temperature and RH, statically indeterminate beams h_U = 5 cm

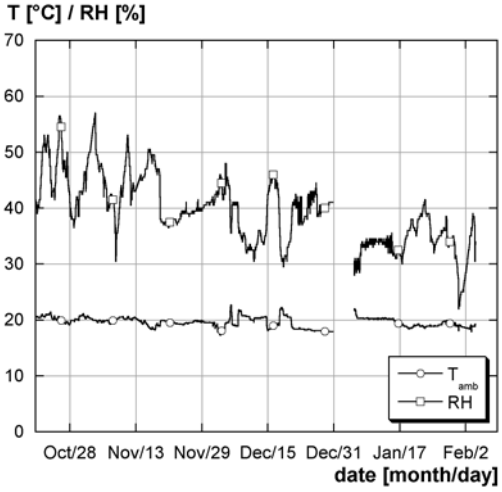

FIGURE E.5: Temperature and RH, statically determinate beams h_U = 10 cm

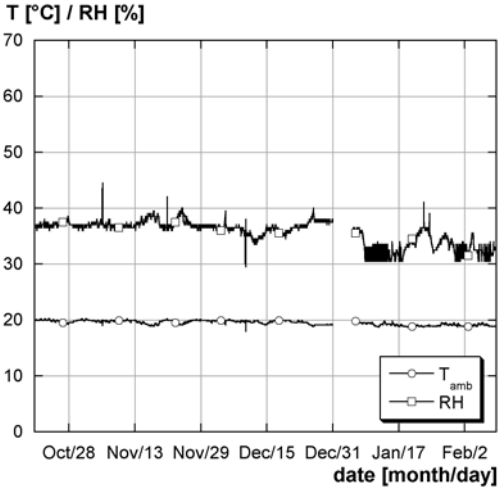

FIGURE E.6: Temperature and RH, statically indeterminate beams h_U = 10 cm

Appendix F: Temperature evolution at the early age of the concrete substrate

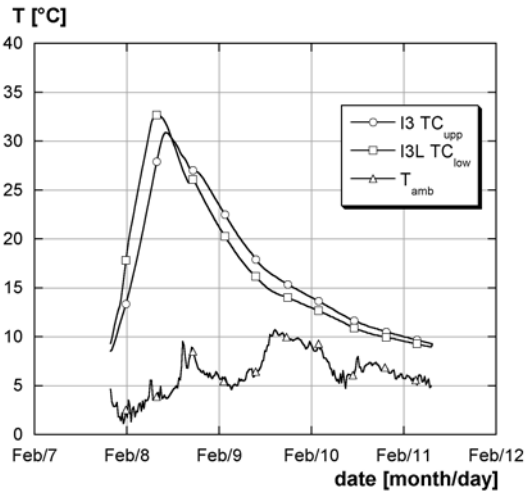

FIGURE F.1: TC_{upp} of I3 and I3L

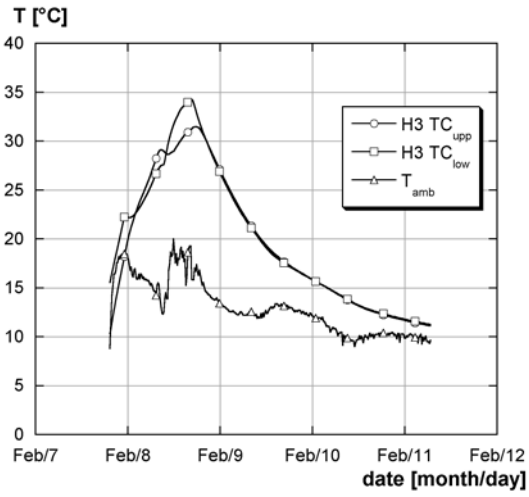

FIGURE F.2: TC_{upp} of H3

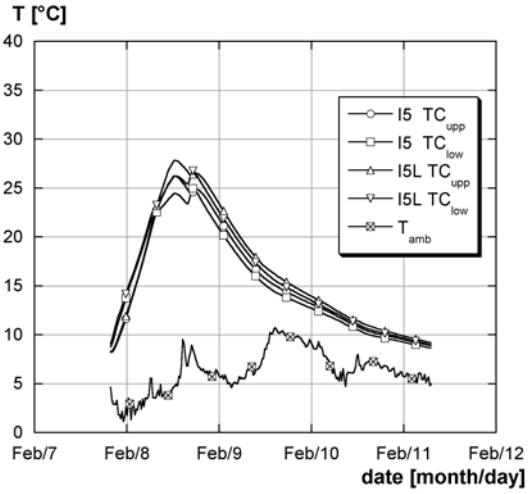

FIGURE F.3: temperature evolution of I5 and I5L

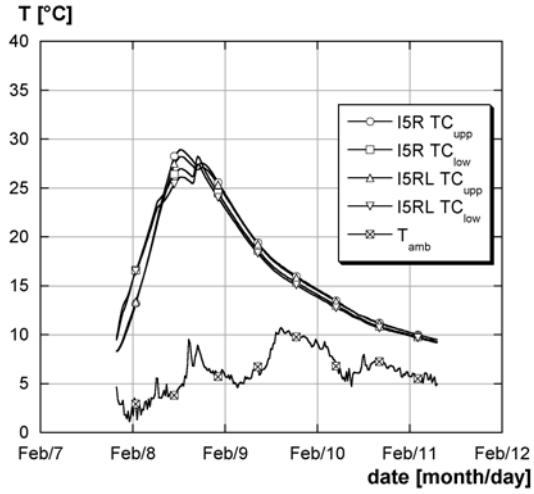

FIGURE F.4: temperature evolution of I5R and I5RL

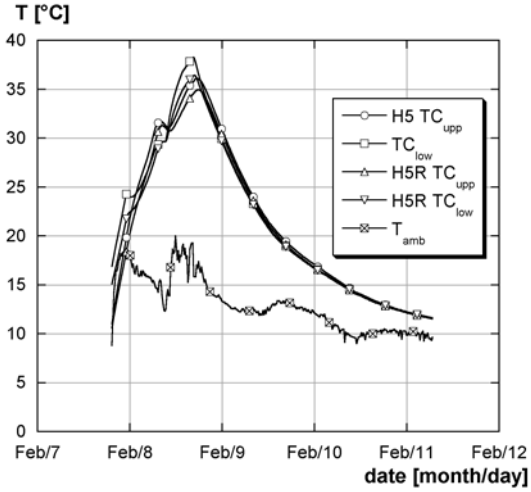

FIGURE F.5: temperature evolution of H5 and H5R

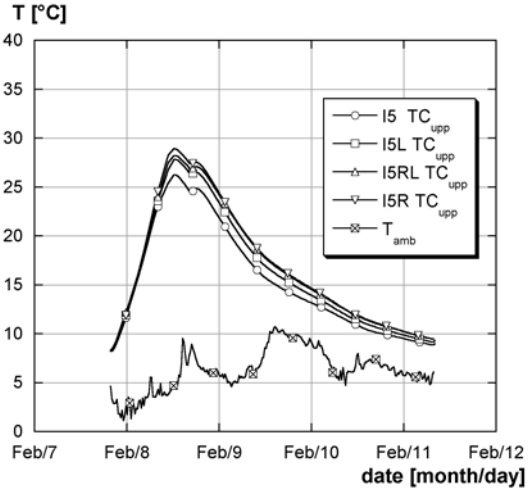

FIGURE F.6: TC_{upp} of I5, I5L, I5R, I5RL

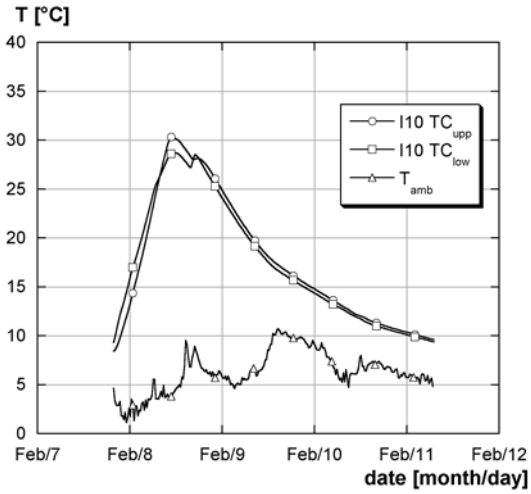

FIGURE F.7: temperature evolution of I10

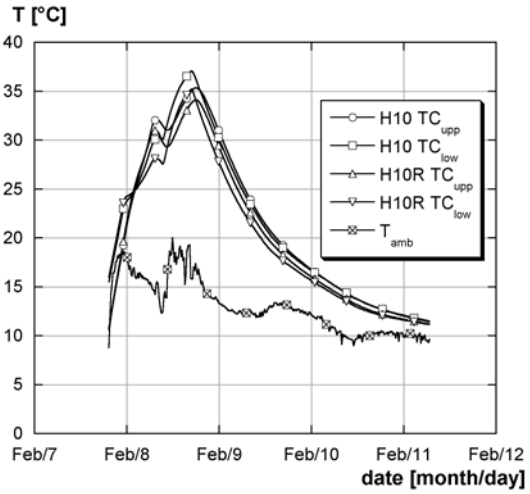

FIGURE F.8: temperature evolution of H10 and H10R

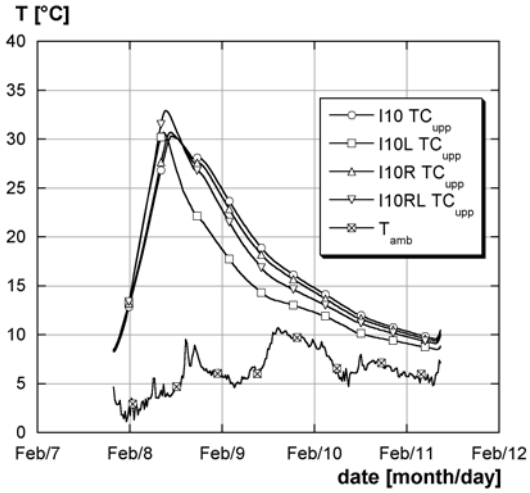

FIGURE F.9: TC_{upp} of I10, I10L, I10R, I10RL

Appendix G: Temperature at the early age of the UHPFRC layer

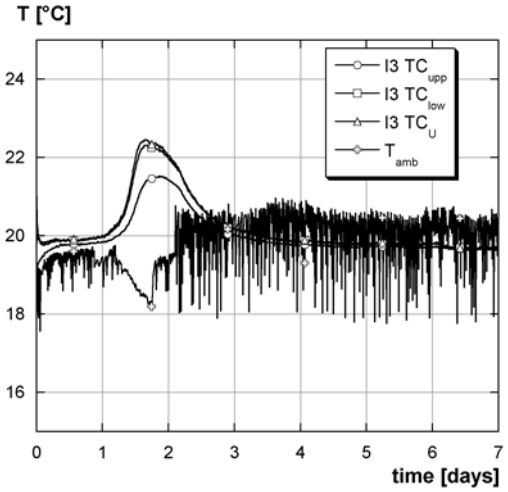

FIGURE G.1: I3 - temperature evolution at the early age of the UHPFRC layer

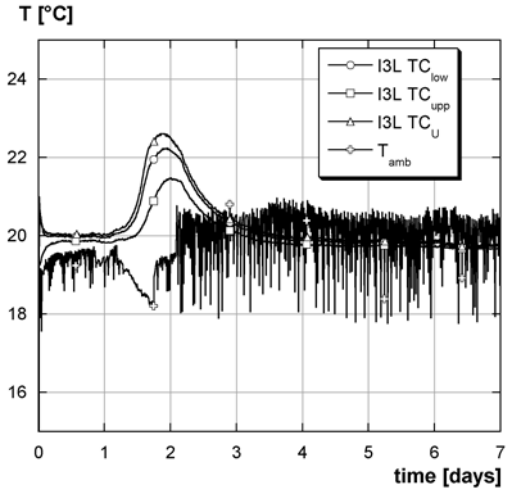

FIGURE G.2: I3L - temperature evolution at the early age of the UHPFRC layer

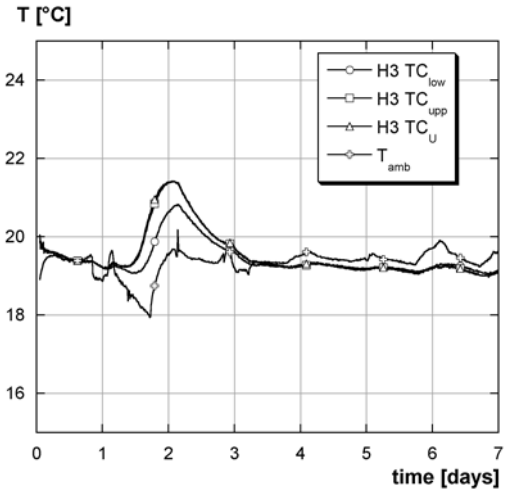

FIGURE G.3: H3 - temperature evolution at the early age of the UHPFRC layer

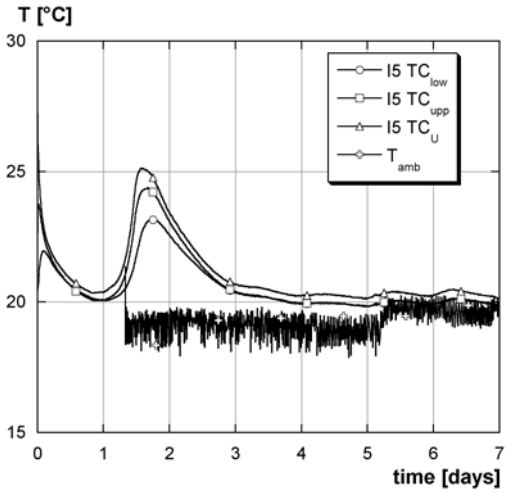

FIGURE G.4: I5 - temperature evolution at the early age of the UHPFRC layer

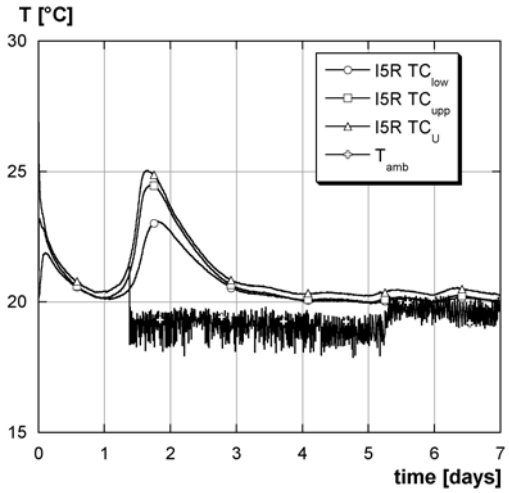

FIGURE G.5: I5R - temperature evolution at the early age of the UHPFRC layer

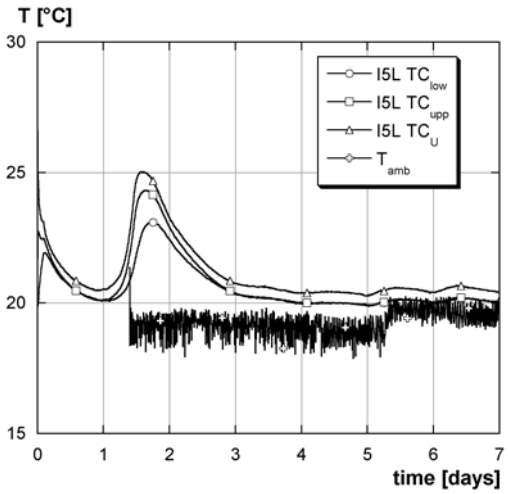

FIGURE G.6: I5L - temperature evolution at the early age of the UHPFRC layer

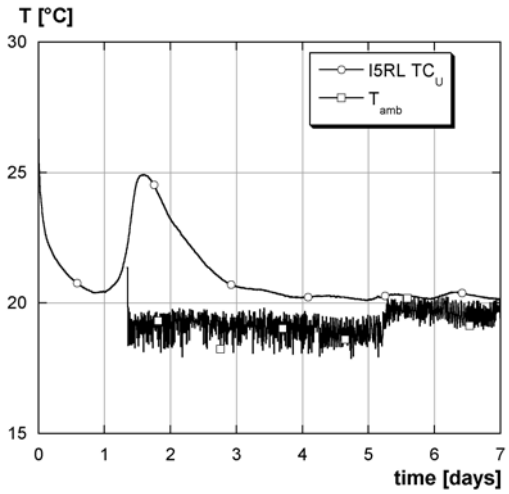

FIGURE G.7: I5RL - temperature evolution at the early age of the UHPFRC layer

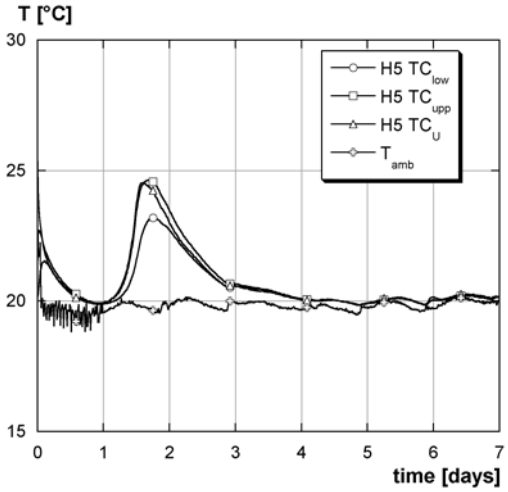

FIGURE G.8: H5 - temperature evolution at the early age of the UHPFRC layer

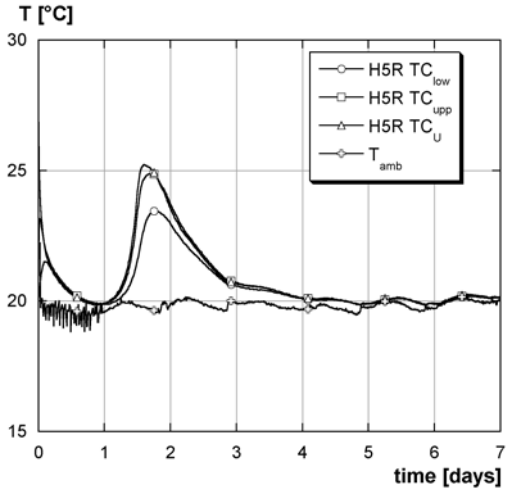

FIGURE G.9: H5R - temperature evolution at the early age of the UHPFRC layer

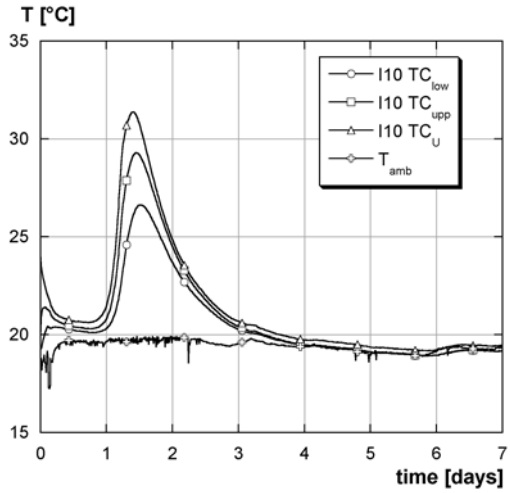

FIGURE G.10: I10 - temperature evolution at the early age of the UHPFRC layer

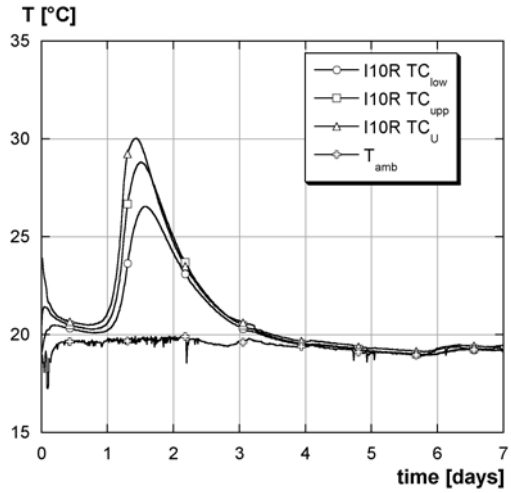

FIGURE G.11: I10R - temperature evolution at the early age of the UHPFRC layer

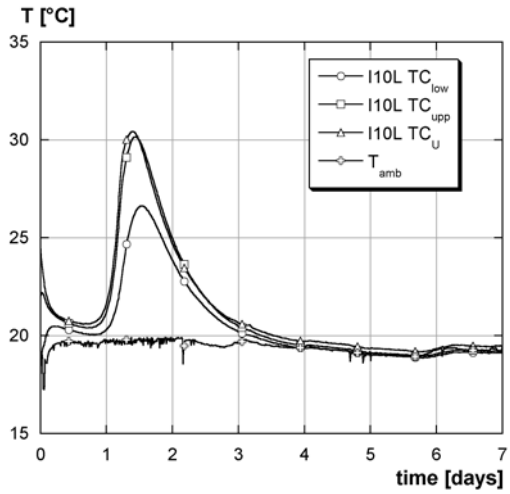

FIGURE G.12: I10L - temperature evolution at the early age of the UHPFRC layer

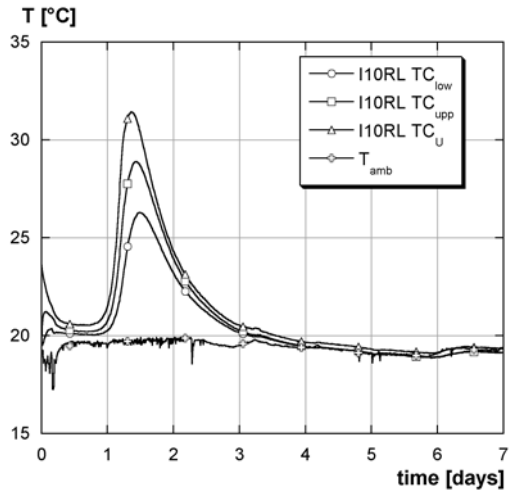

FIGURE G.13: I10RL - temperature evolution at the early age of the UHPFRC layer

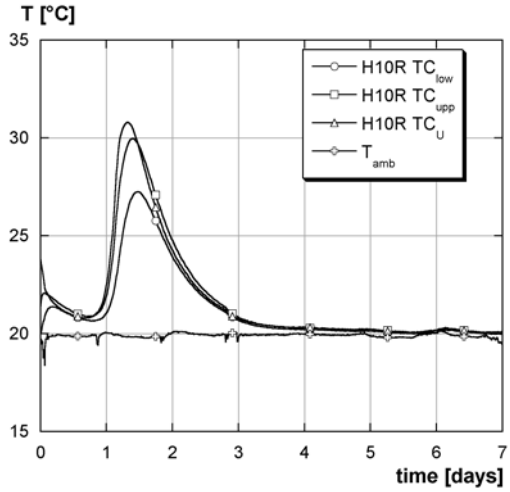

FIGURE G.14: H10 - temperature evolution at the early age of the UHPFRC layer

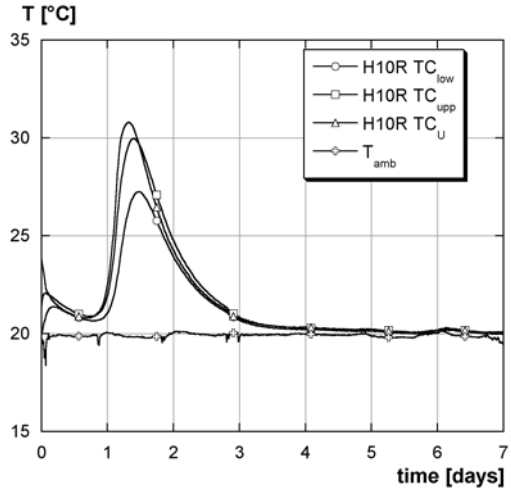

FIGURE G.15: H10R - temperature evolution at the early age of the UHPFRC layer

Appendix H: Measurements of the deflections (f1, f2, f3) during the long-term tests

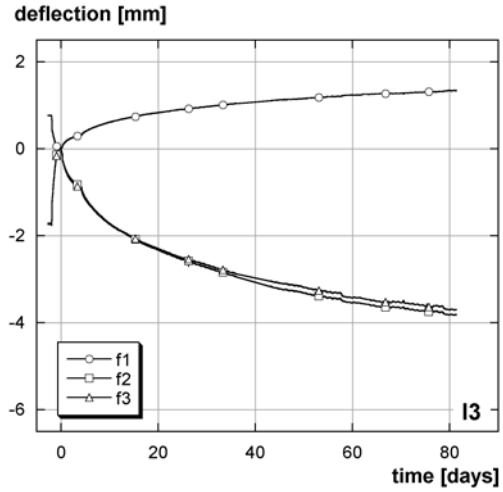

FIGURE H.1: I3 - deflections f1, f2, f3

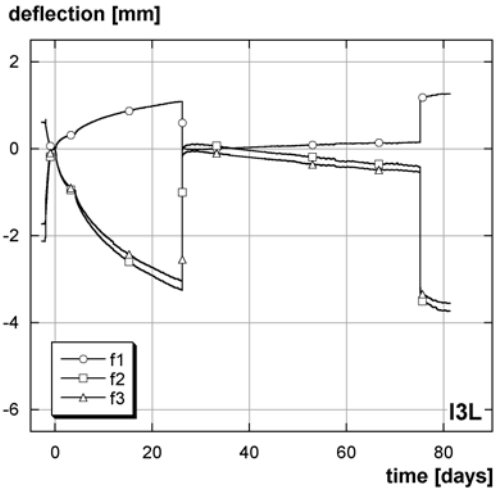

FIGURE H.2: I3L - deflections f1, f2, f3

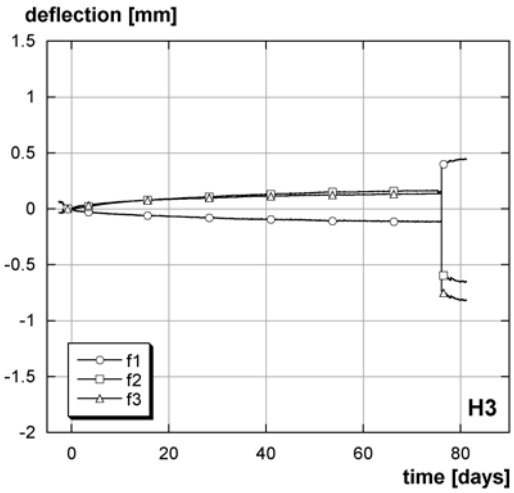

FIGURE H.3: H3 - deflections f1, f2, f3

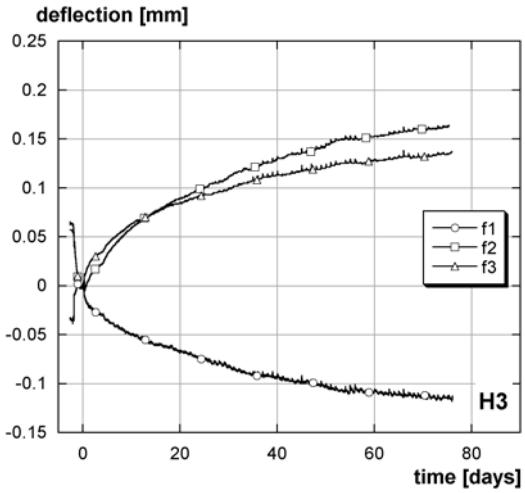

FIGURE H.4: H3 - deflections f1, f2, f3, detail

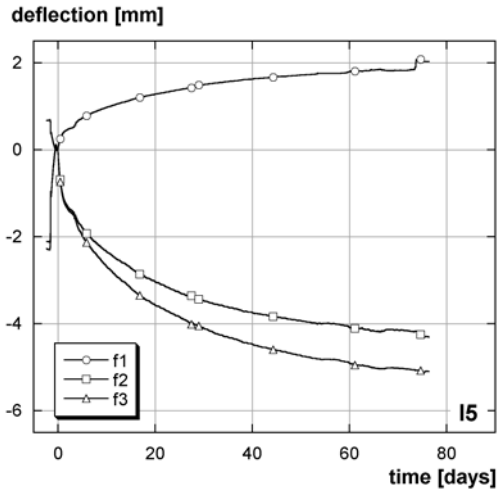

FIGURE H.5: I5 - deflections f1, f2, f3

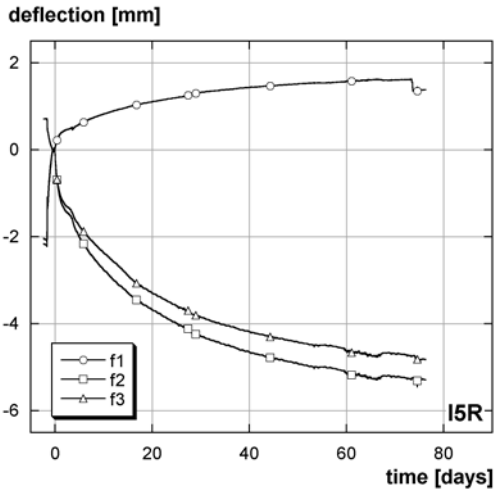

FIGURE H.6: I5R - deflections f1, f2, f3

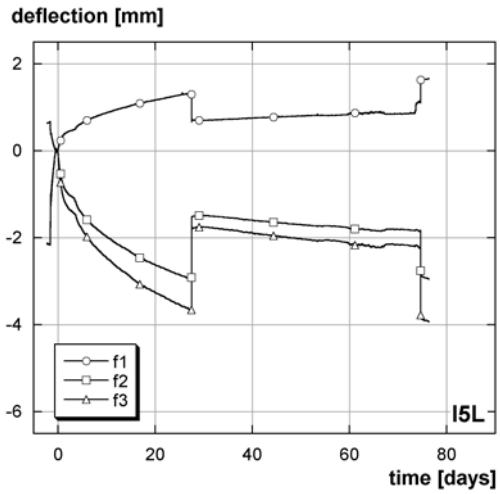

FIGURE H.7: I5L - deflections f1, f2, f3

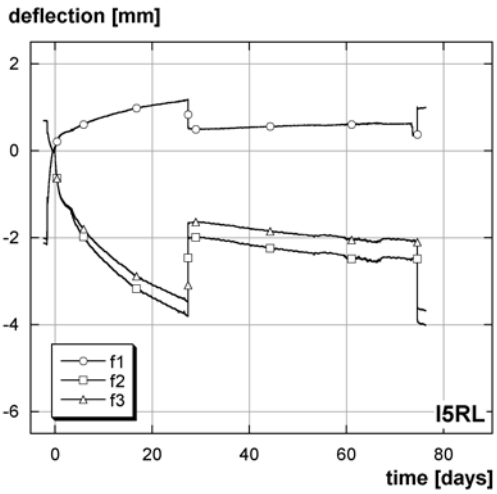

FIGURE H.8: I5RL - deflections f1, f2, f3

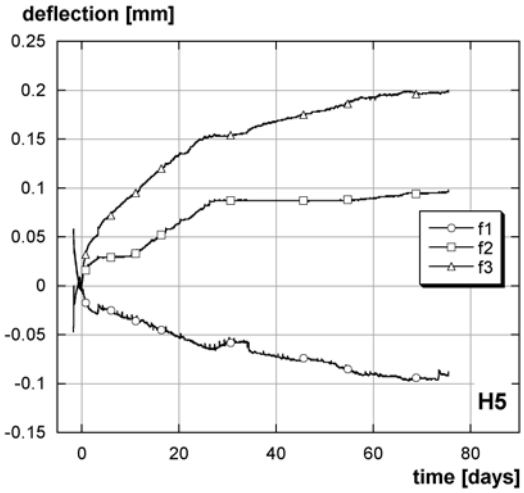

FIGURE H.9: H5 - deflections f1, f2, f3

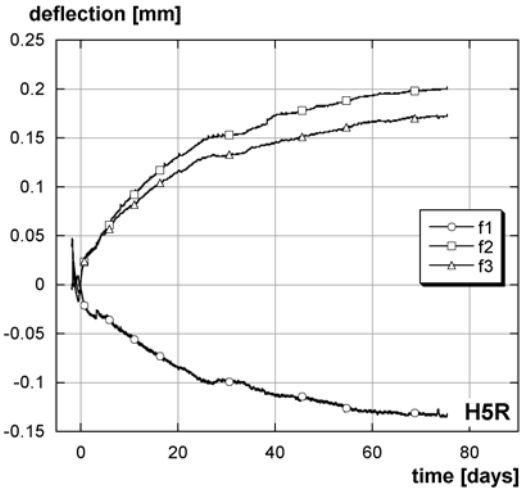

FIGURE H.10: H5R - deflections f1, f2, f3

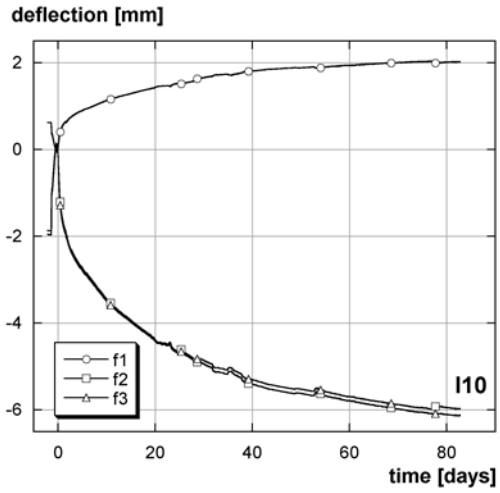

FIGURE H.11: I10 - deflections f1, f2, f3

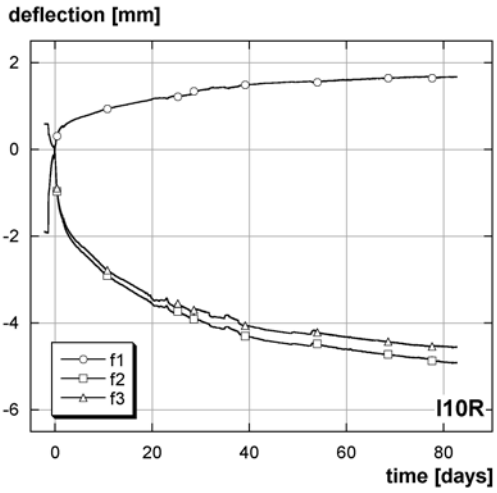

FIGURE H.12: I10R - deflections f1, f2, f3

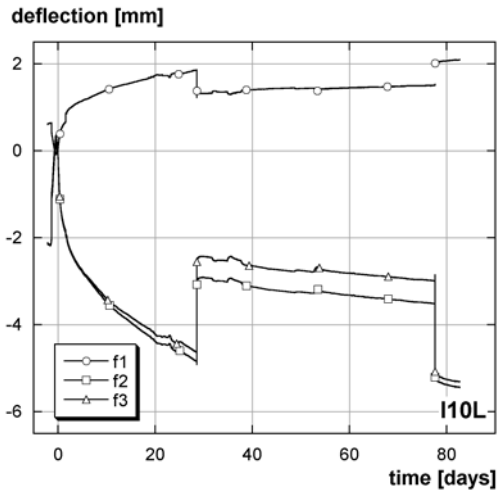

FIGURE H.13: I10L - deflections f1, f2, f3

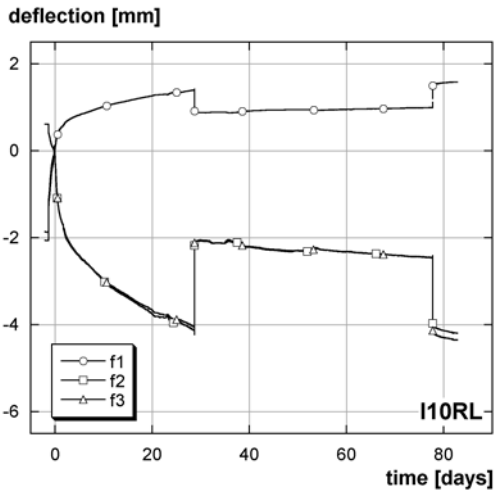

FIGURE H.14: I10RL - deflections f1, f2, f3

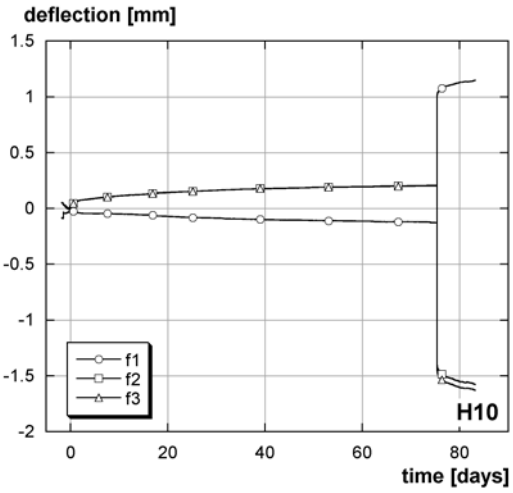

FIGURE H.15: H10 - deflections f1, f2, f3

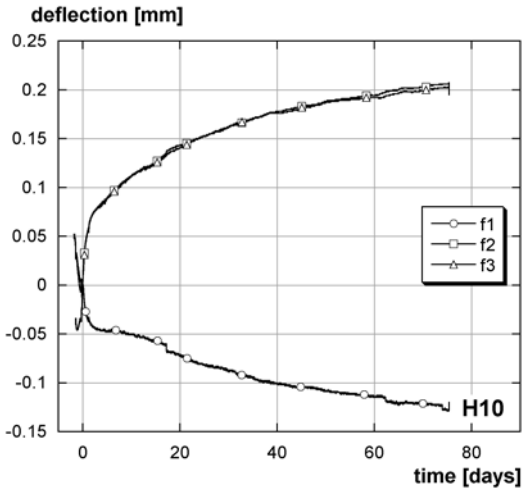

FIGURE H.16: H10 - deflections f1, f2, f3, detail

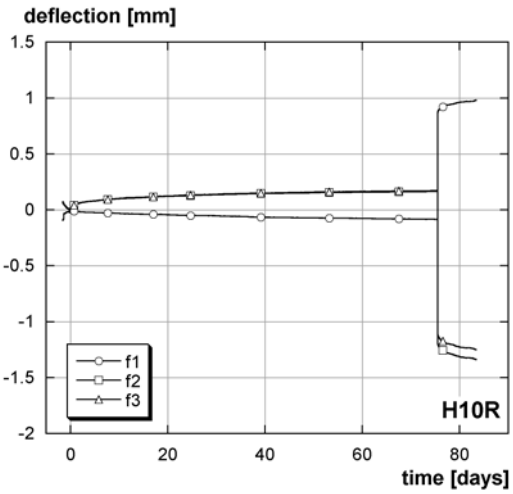

FIGURE H.17: H10R - deflections f1, f2, f3

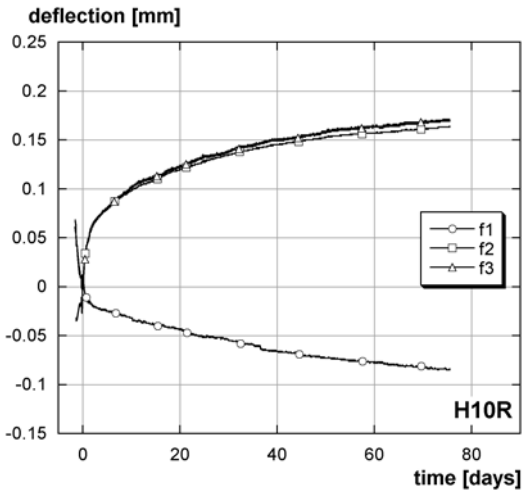

FIGURE H.18: H10R - deflections f1, f2, f3, detail

Appendix I: Measurements of the optical deformation sensors (ODS L, ODS U) during the long-term tests

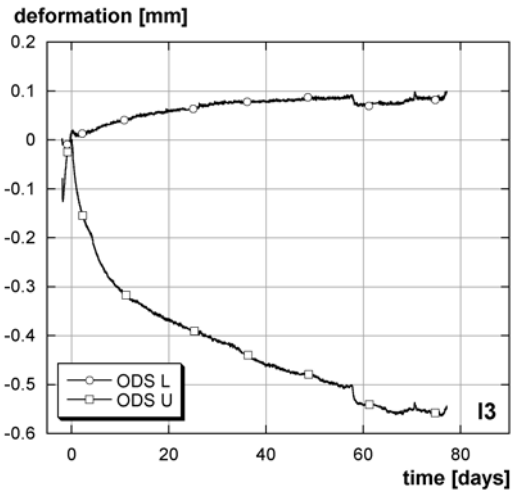

FIGURE I.1: I3 - ODS deformations

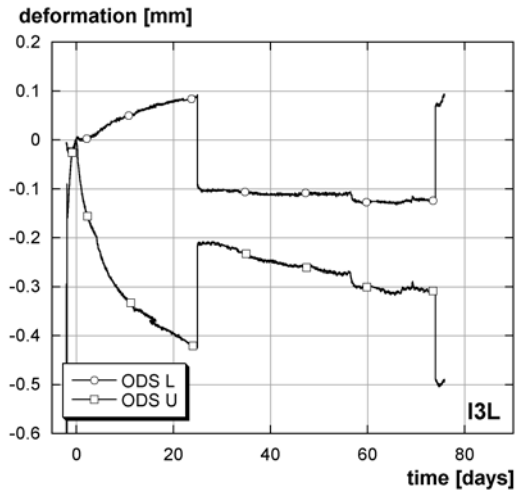

FIGURE I.2: I3L - ODS deformations

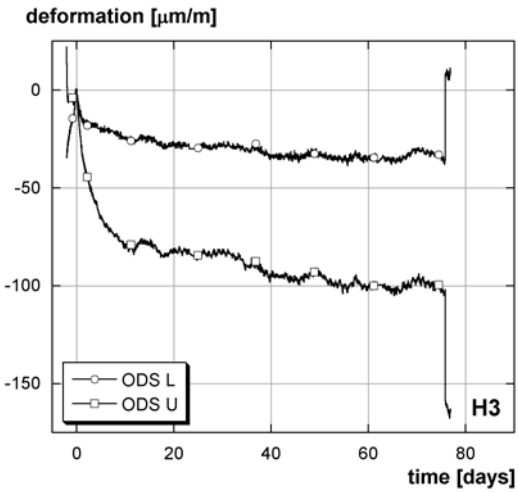

FIGURE I.3: H3 - ODS deformations

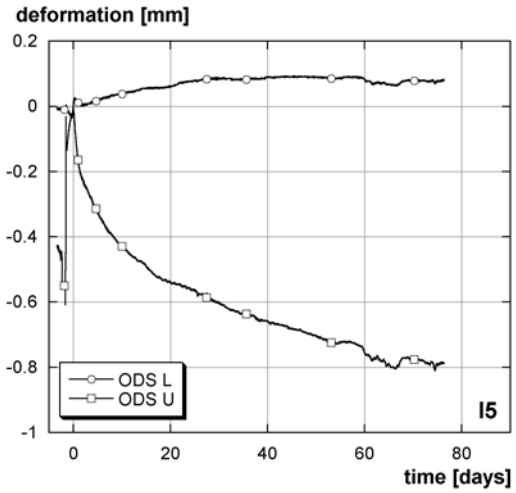

FIGURE I.4: I5 - ODS deformations

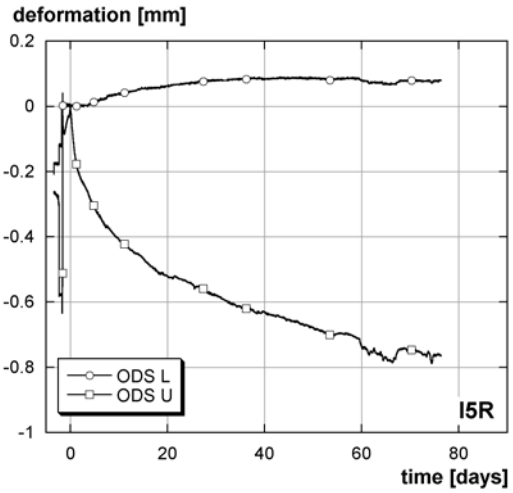

FIGURE I.5: I5R - ODS deformations

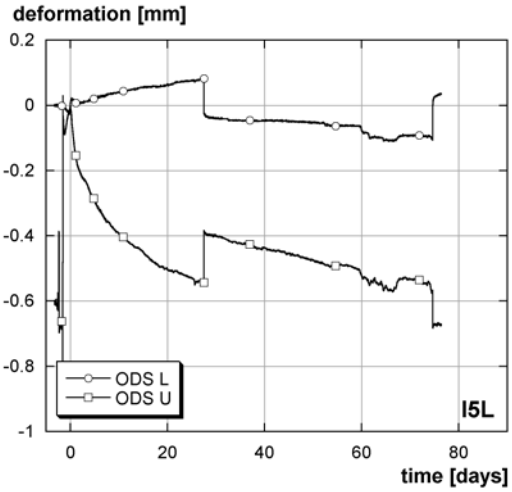

FIGURE I.6: I5L - ODS deformations

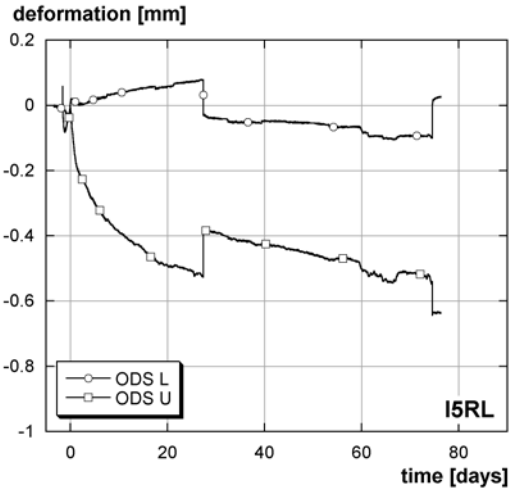

FIGURE I.7: I5RL - ODS deformations

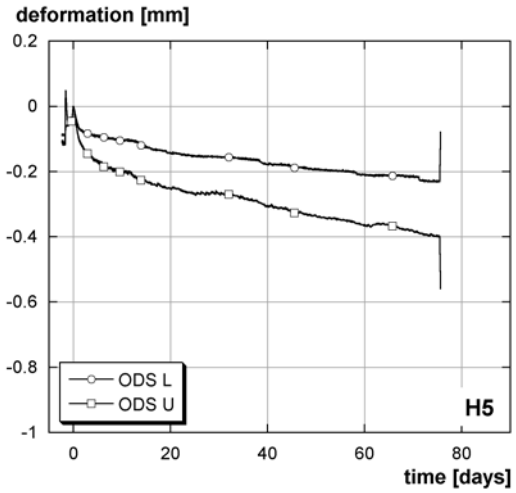

FIGURE I.8: H5 - ODS deformations

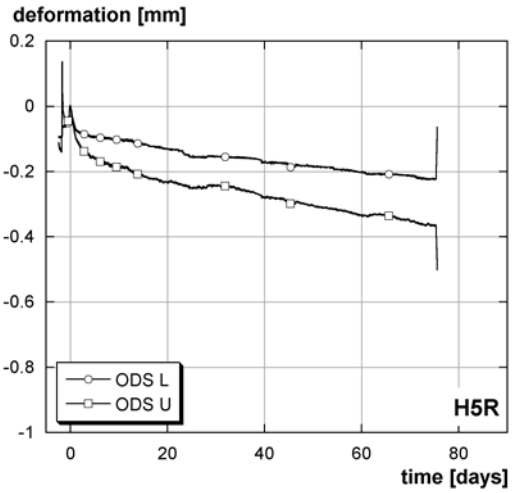

FIGURE I.9: H5R - ODS deformations

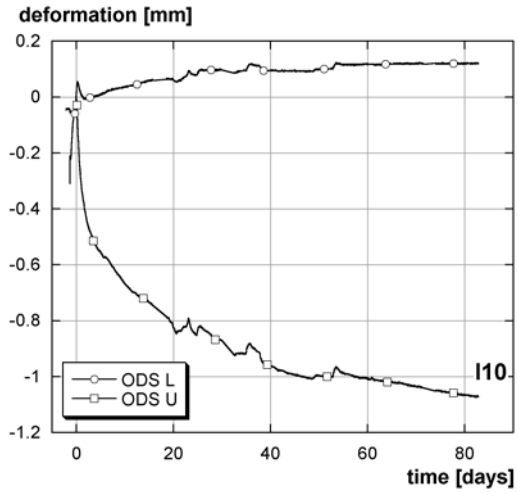

FIGURE I.10: I10 - ODS deformations

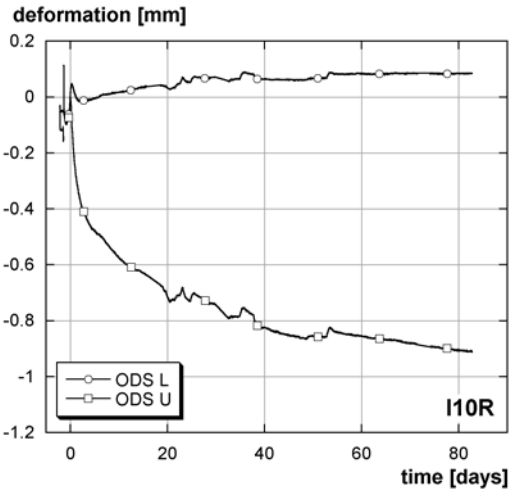

FIGURE I.11: I10R - ODS deformations

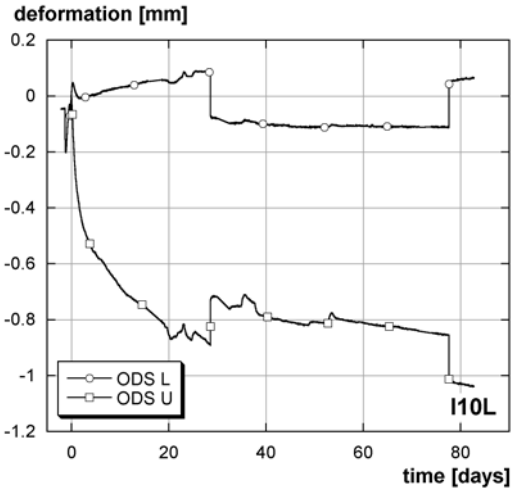

FIGURE I.12: I10L - ODS deformations

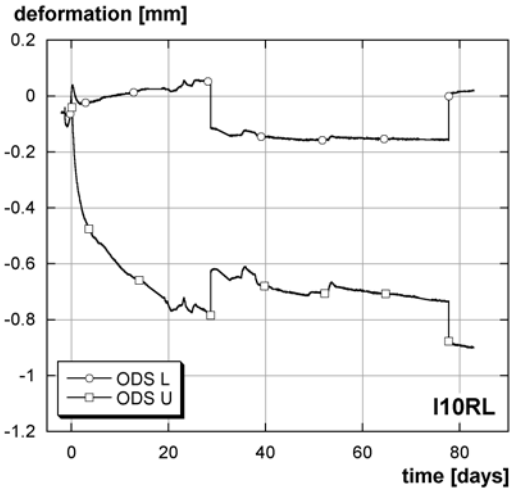

FIGURE I.13: I10RL - ODS deformations

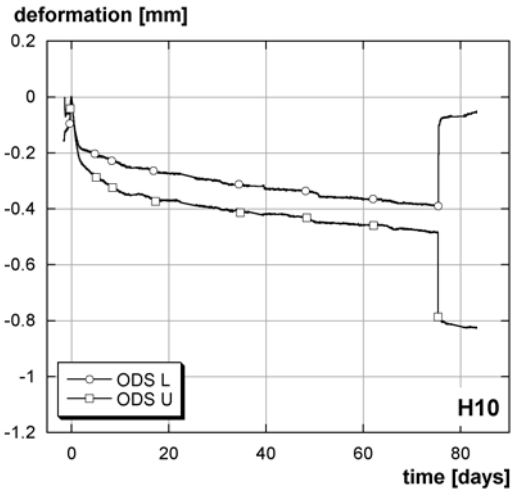

FIGURE I.14: H10 - ODS deformations

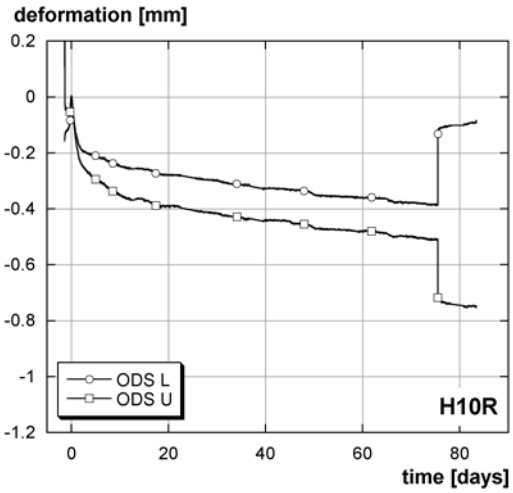

FIGURE I.15: H10R - ODS deformations

Appendix J: Curvature ODS during the long-term tests

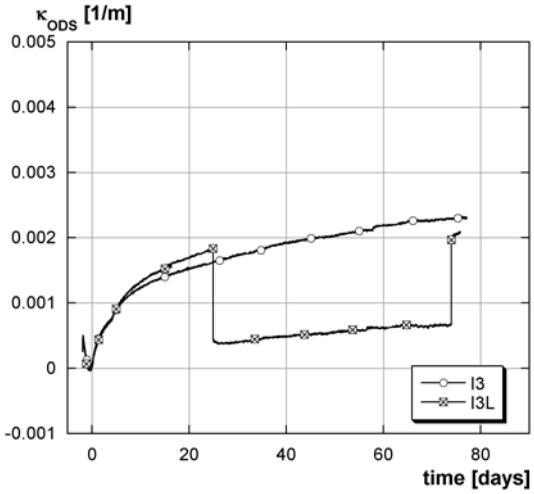

FIGURE J.1: I3 - curvature ODS

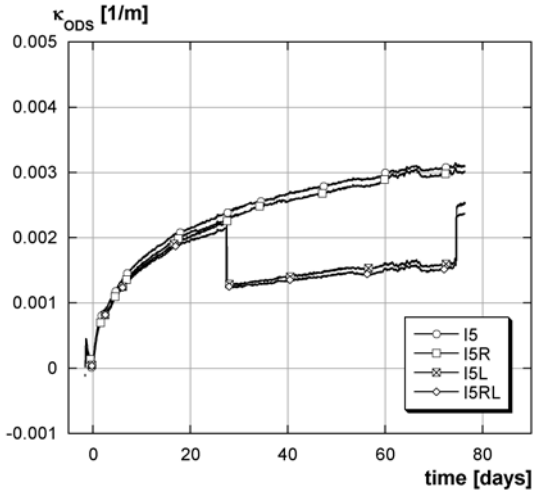

FIGURE J.2: I5 - curvature ODS

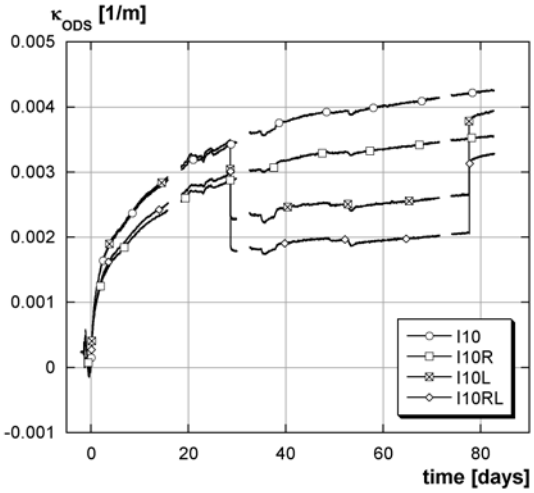

FIGURE J.3: I10 - curvature ODS

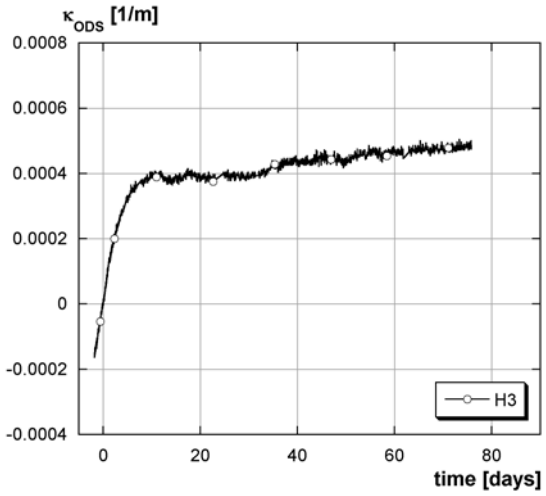

FIGURE J.4: H3 - curvature ODS, detail

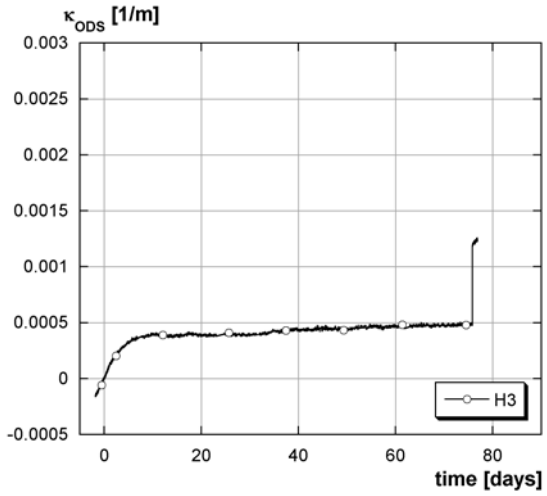

FIGURE J.5: H3 - curvature ODS

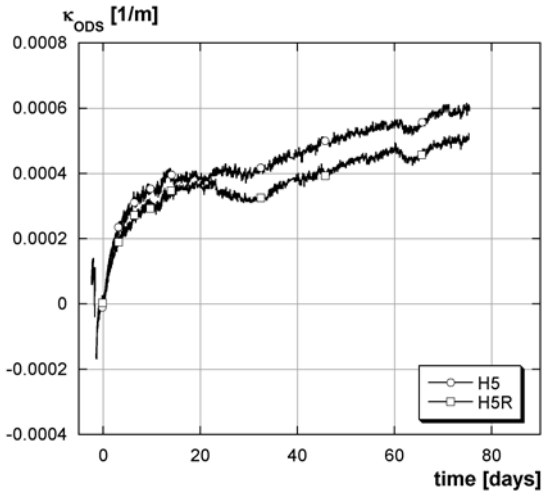

FIGURE J.6: H5 - curvature ODS, detail

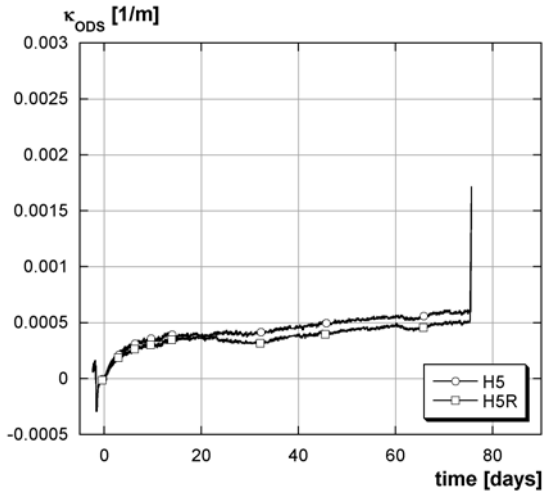

FIGURE J.7: H5 - curvature ODS

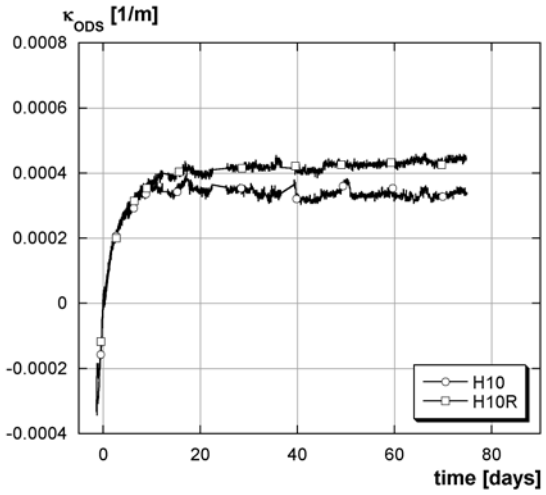

FIGURE J.8: H10 - curvature ODS, detail

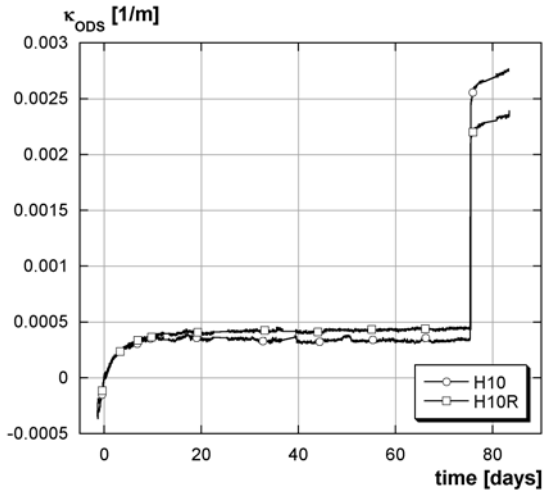

FIGURE J.9: H10 - curvature ODS

Appendix K: Influence of the reinforcement during the long-term tests

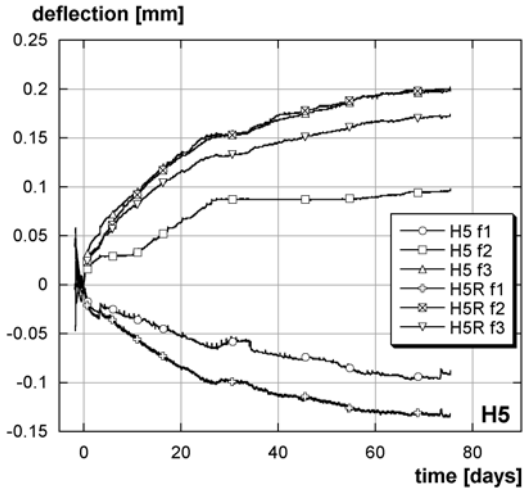

FIGURE K.1: H5 - deflection - influence of the reinforcement

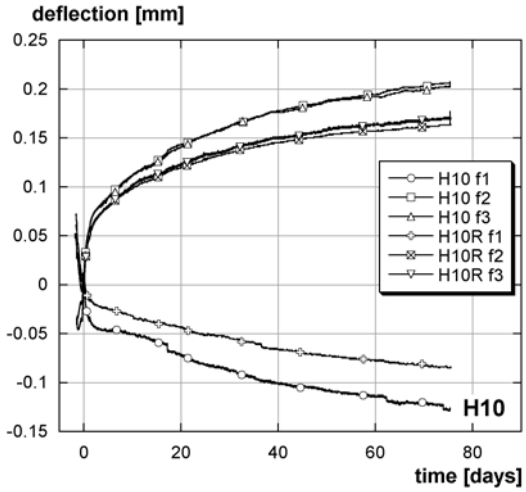

FIGURE K.2: H10 - deflection - influence of the reinforcement

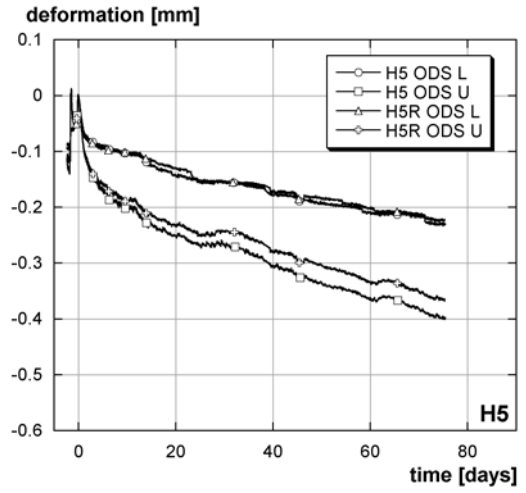

FIGURE K.3: H5 - ODS - influence of the reinforcement

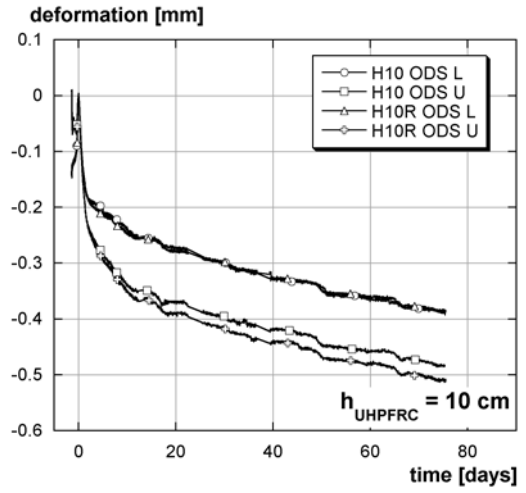

FIGURE K.4: H10 - ODS - influence of the reinforcement

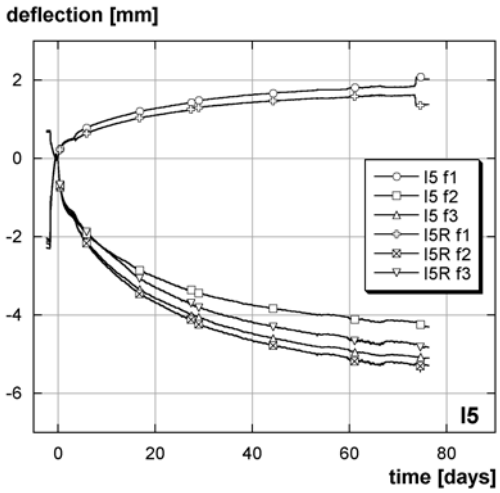

FIGURE K.5: I5 - deflection - influence of the reinforcement

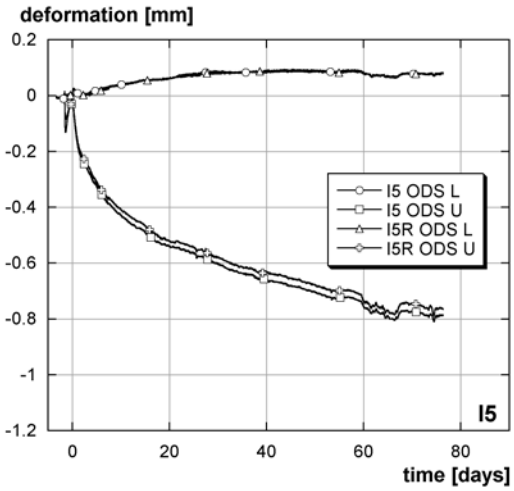

FIGURE K.6: I5 - ODS - influence of the reinforcement

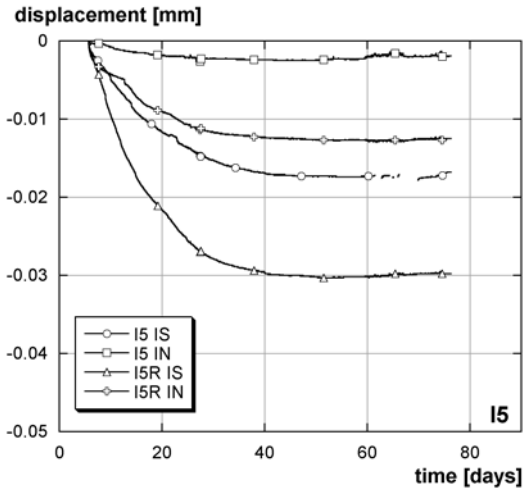

FIGURE K.7: I5 - debonding - influence of the reinforcement

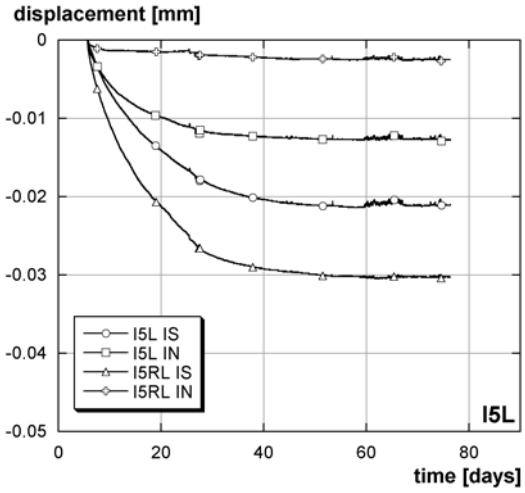

FIGURE K.8: I5L - debonding - influence of the reinforcement

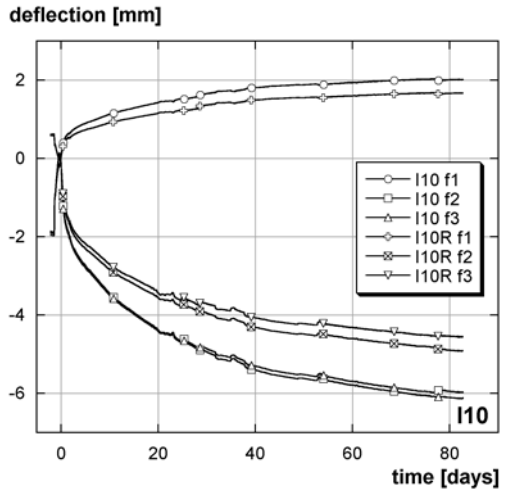

FIGURE K.9: I10 - deflection - influence of the reinforcement

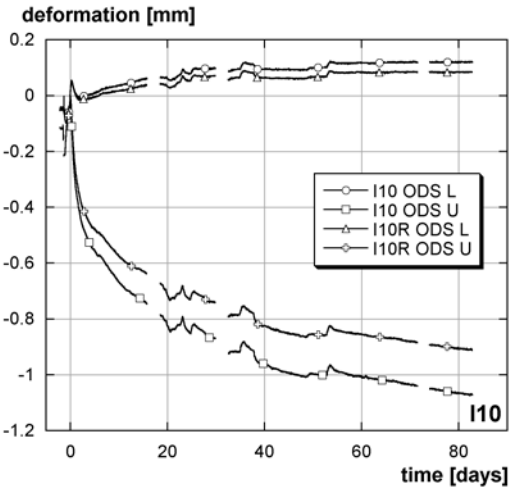

FIGURE K.10: I10R - ODS deformations

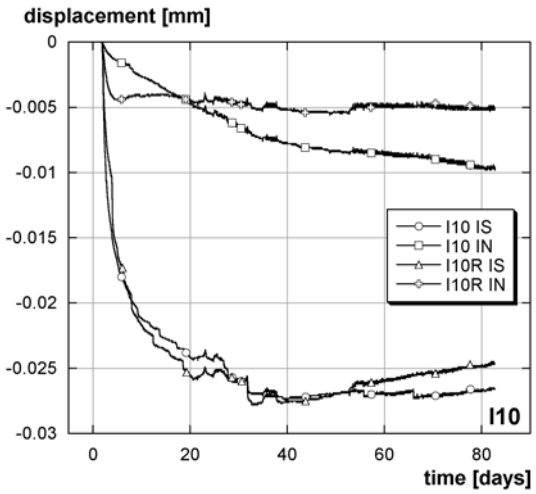

FIGURE K.11: I10 - debonding - influence of the reinforcement

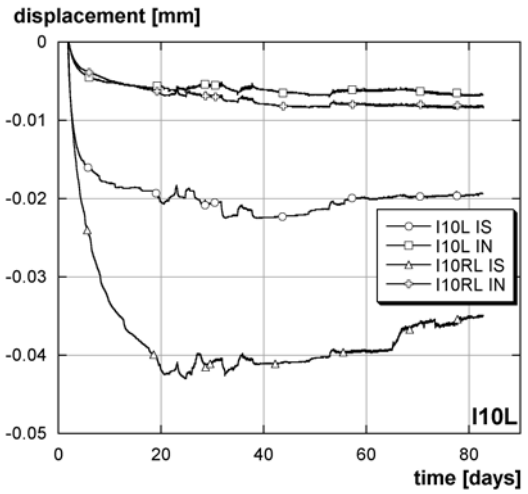

FIGURE K.12: I10L - debonding - influence of the reinforcement

Appendix L: Influence of the thickness of the UHPFRC layer (h_U) during the long-term tests

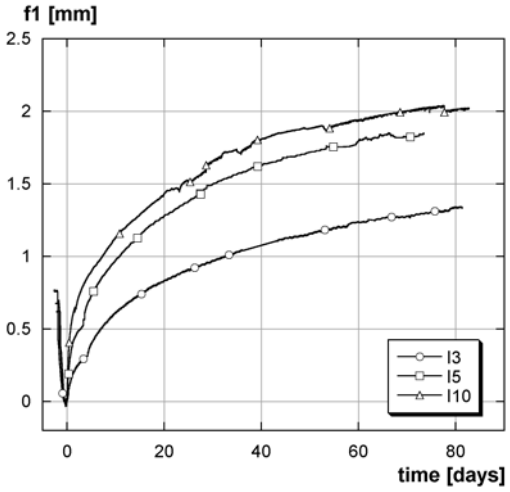

FIGURE L.1: Comparison f1 - I3, I5, I10

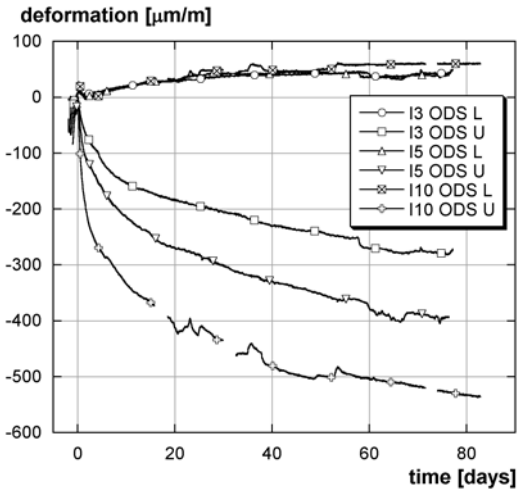

FIGURE L.2: Comparison ODS - I3, I5, I10

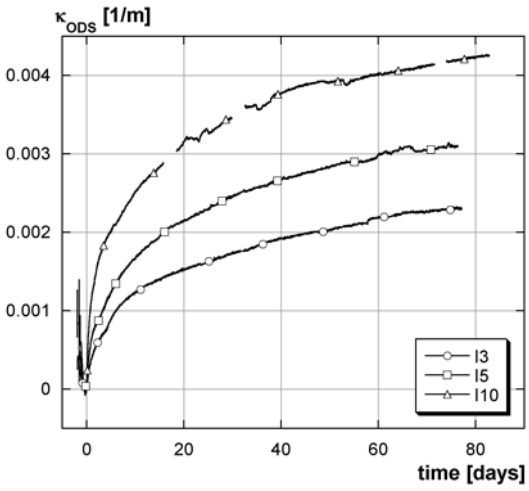

FIGURE L.3: Comparison curvature - I3, I5, I10

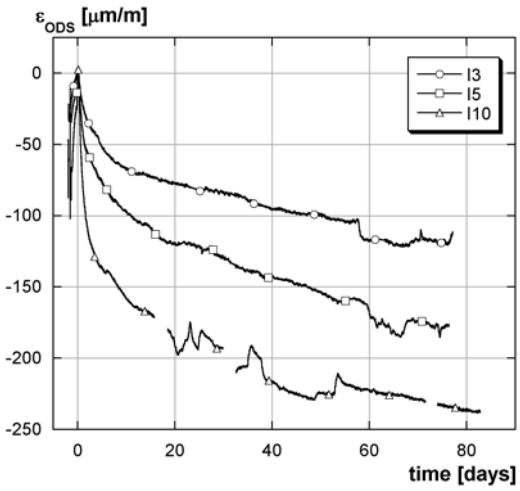

FIGURE L.4: Comparison elongation - I3, I5, I10

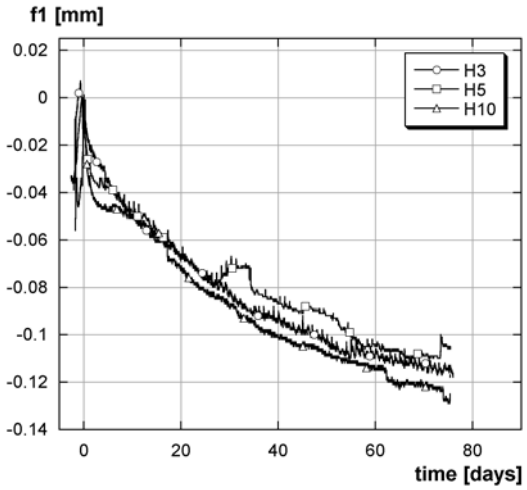

FIGURE L.5: Comparison f1 - H3, H5, H10

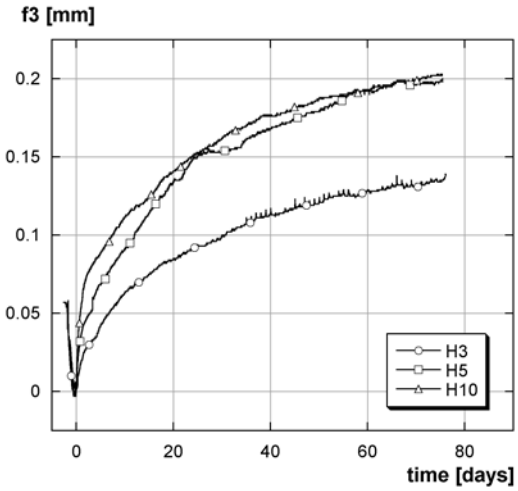

FIGURE L.6: Comparison f3 - H3, H5, H10

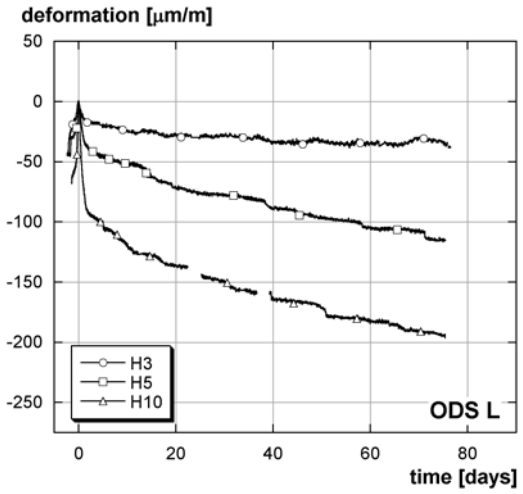

FIGURE L.7: Comparison ODS L - H3, H5, H10

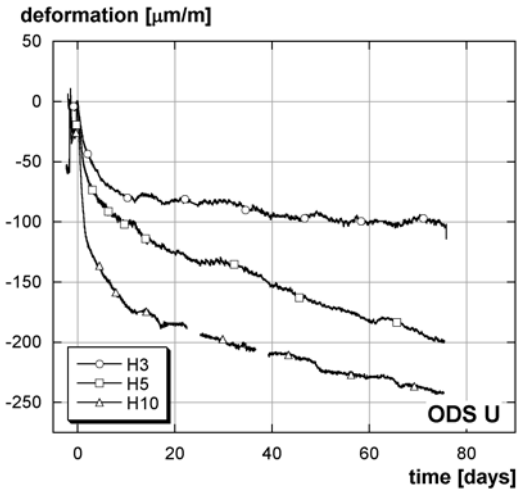

FIGURE L.8: Comparison ODS U - H3, H5, H10

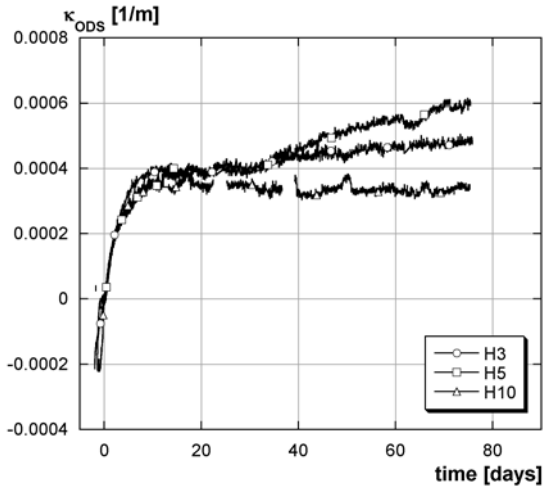

FIGURE L.9: Comparison curvature - H3, H5, H10

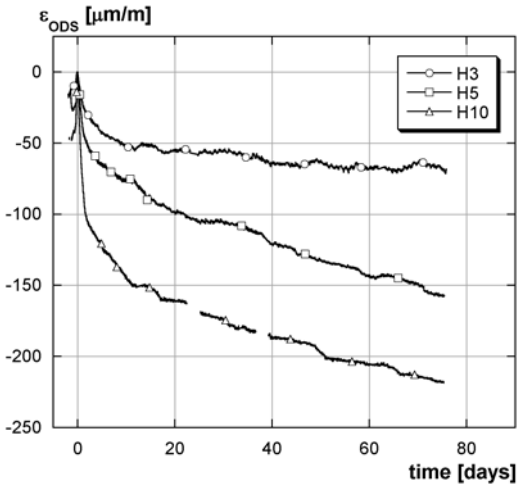

FIGURE L.10: Comparison elongation - H3, H5, H10

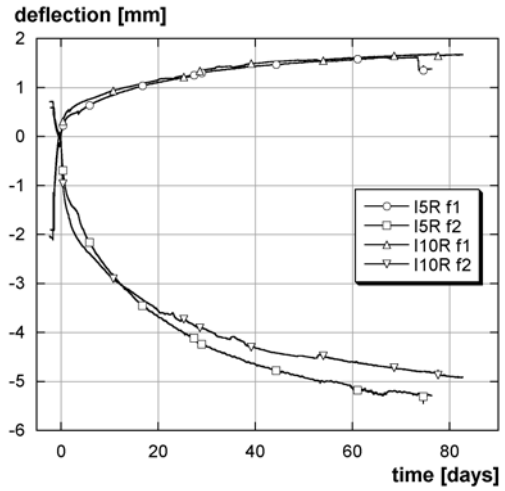

FIGURE L.11: Comparison f1, f2 - I5R, I10R

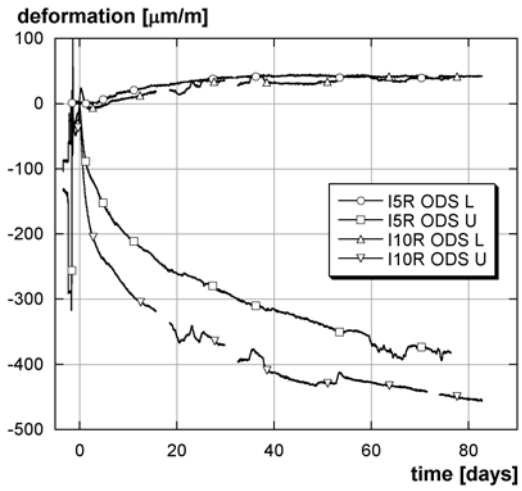

FIGURE L.12: Comparison ODS - I5R, I10R

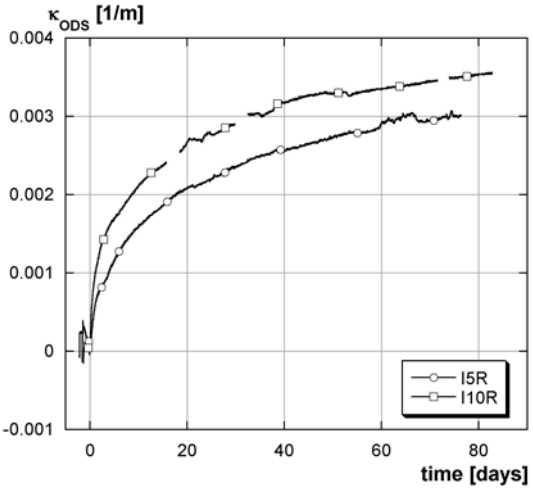

FIGURE L.13: Comparison curvature - I5R, I10R

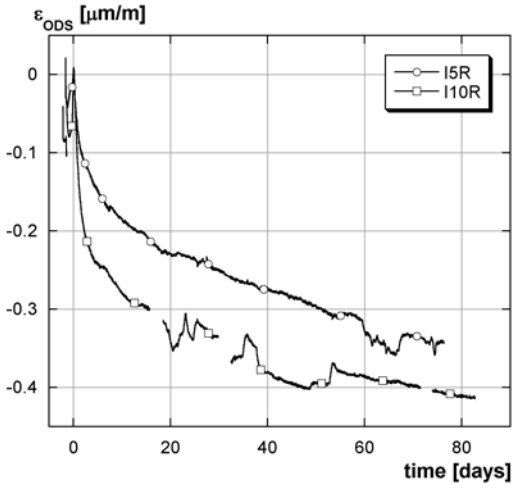

FIGURE L.14: Comparison elongation - I5R, I10R

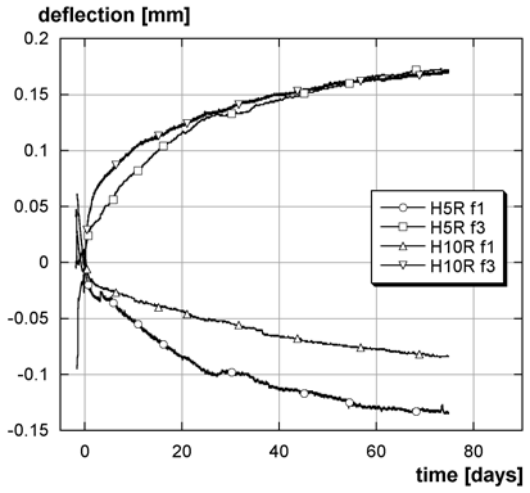

FIGURE L.15: Comparison f1, f2 - H5R, H10R

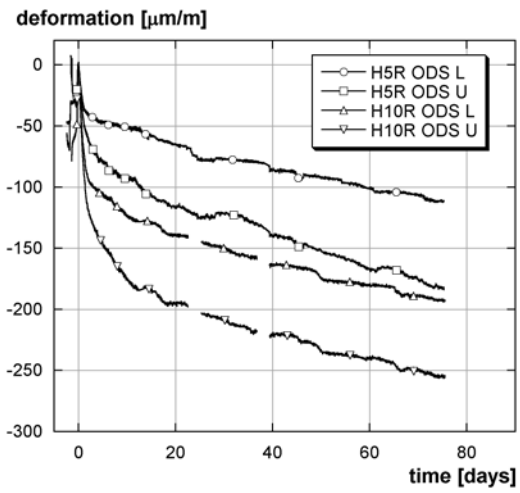

FIGURE L.16: Comparison ODS - H5R, H10R

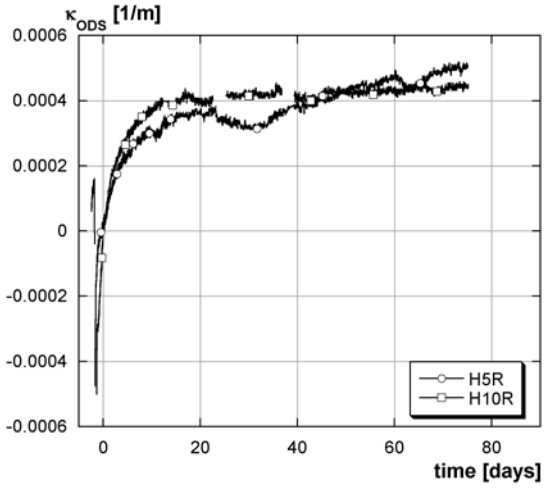

FIGURE L.17: Comparison curvature - H5R, H10R

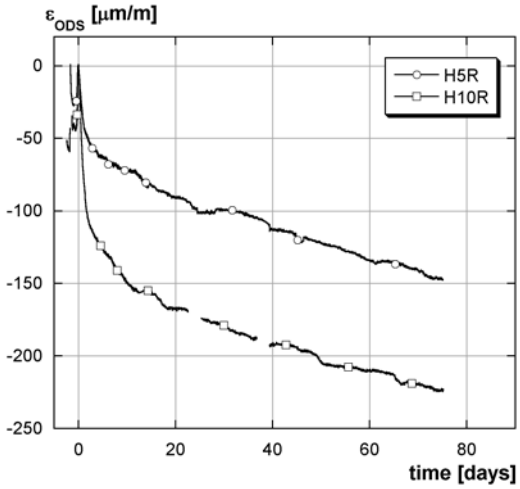

FIGURE L.18: Comparison elongation - H5R, H10R

Appendix M: Flexural creep

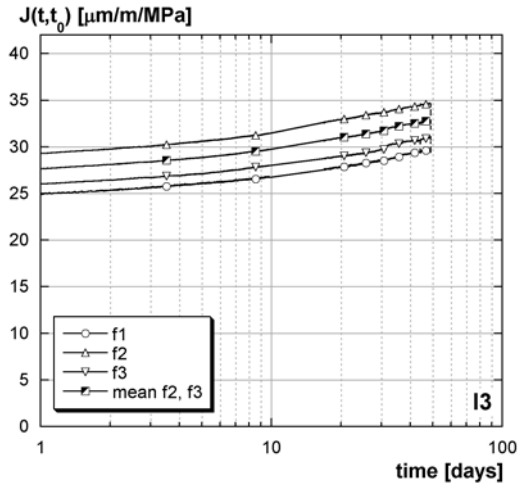

FIGURE M.1: I3 - creep compliance f1, f2, f3

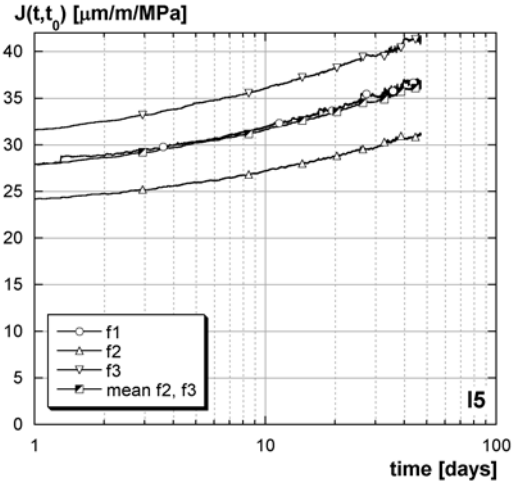

FIGURE M.2: I5 - creep compliance f1, f2, f3

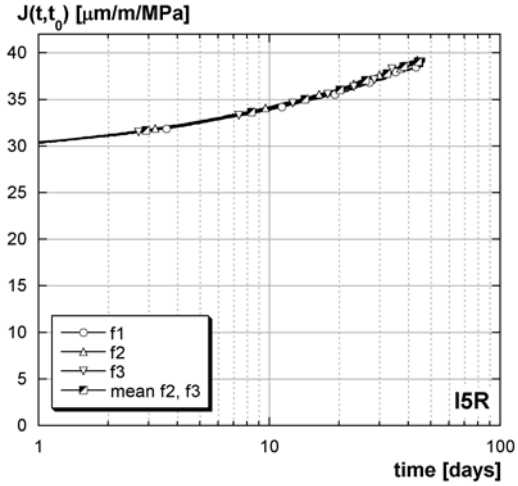

FIGURE M.3: I5R - creep compliance f1, f2, f3

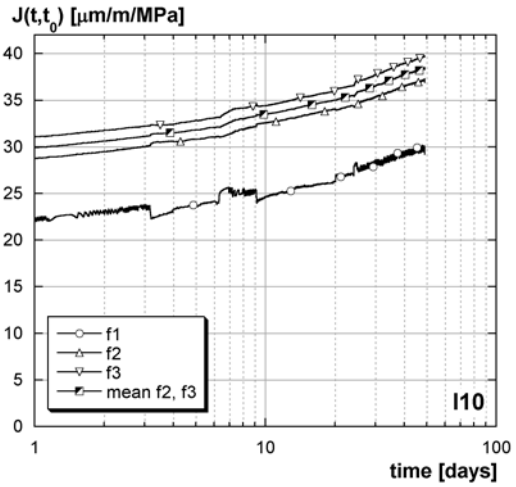

FIGURE M.4: I10 - creep compliance f1, f2, f3

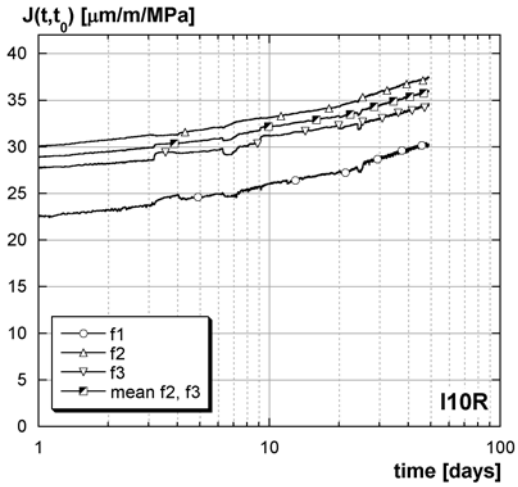

FIGURE M.5: I10R - creep compliance f1, f2, f3

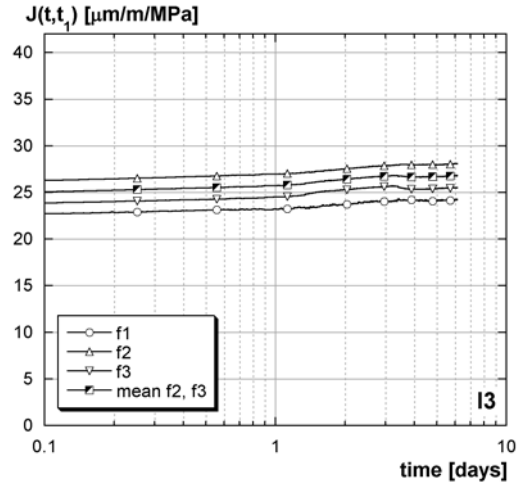

FIGURE M.6: I3 - recovery compliance f1, f2, f3

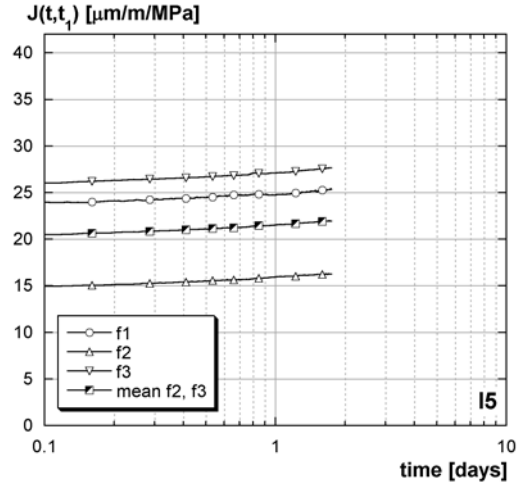

FIGURE M.7: I5 - recovery compliance f1, f2, f3

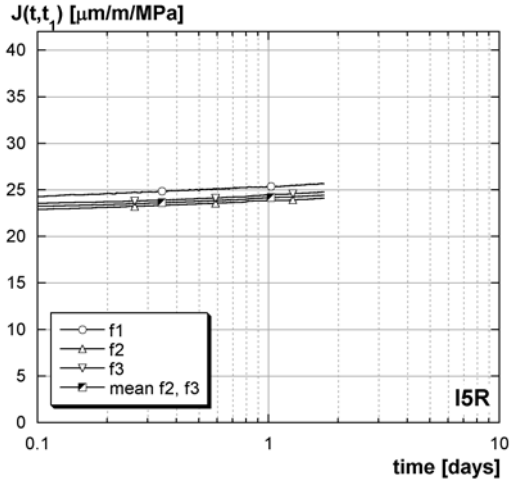

FIGURE M.8: I5R - recovery compliance f1, f2, f3

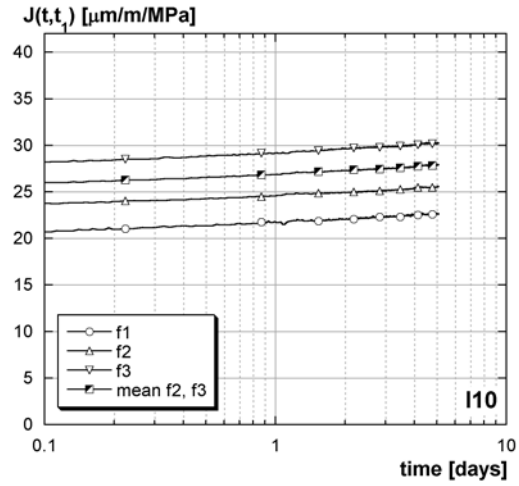

FIGURE M.9: I10 - recovery compliance f1, f2, f3

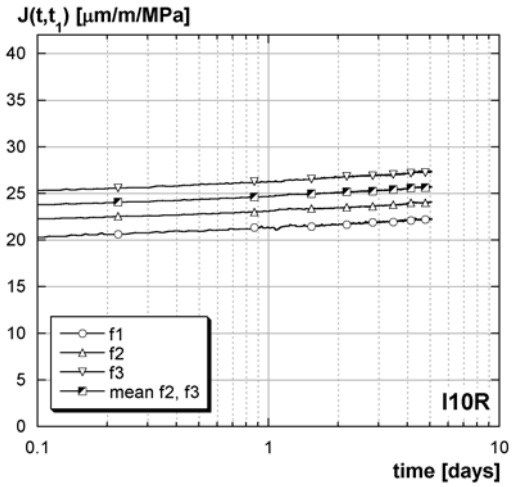

FIGURE M.10: I10R - recovery compliance f1, f2, f3

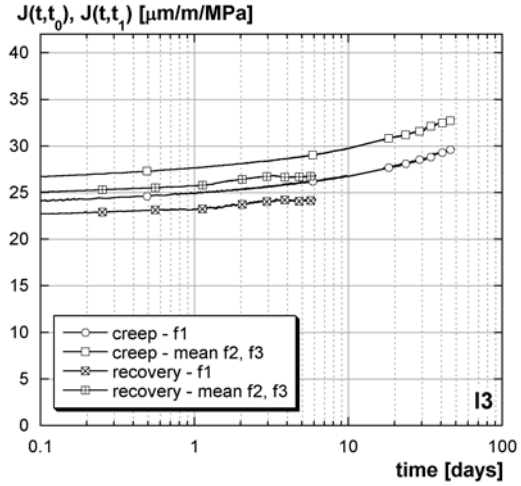

FIGURE M.11: I3 - comparison creep - recovery

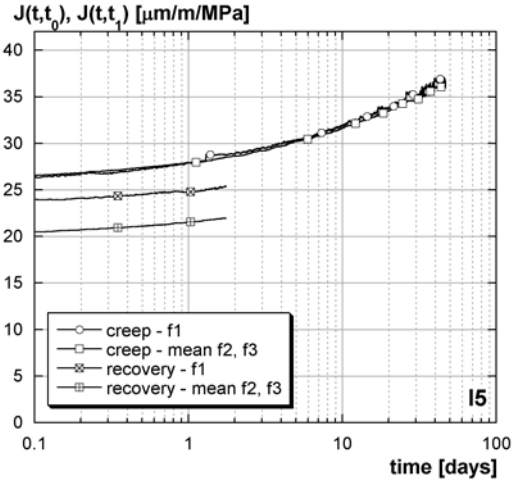

FIGURE M.12: I5 - comparison creep - recovery

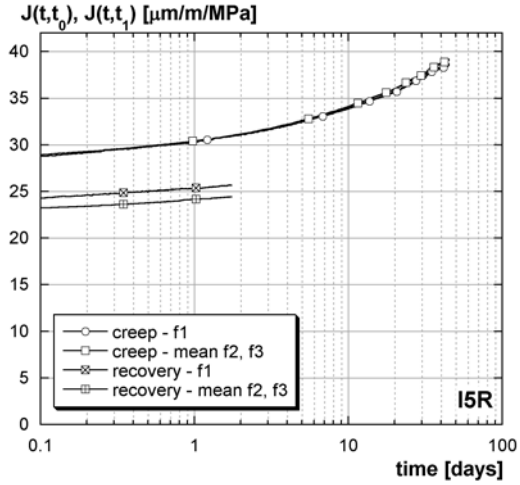

FIGURE M.13: I5R - comparison creep - recovery

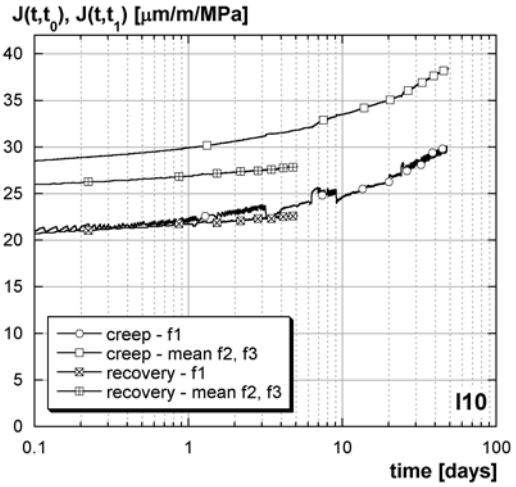

FIGURE M.14: I10 - comparison creep - recovery

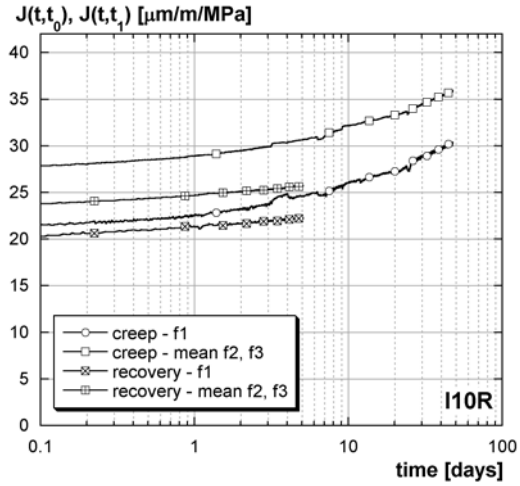

FIGURE M.15: I10R - comparison creep - recovery

Appendix N: Crack patterns on the upper side during the long-term tests

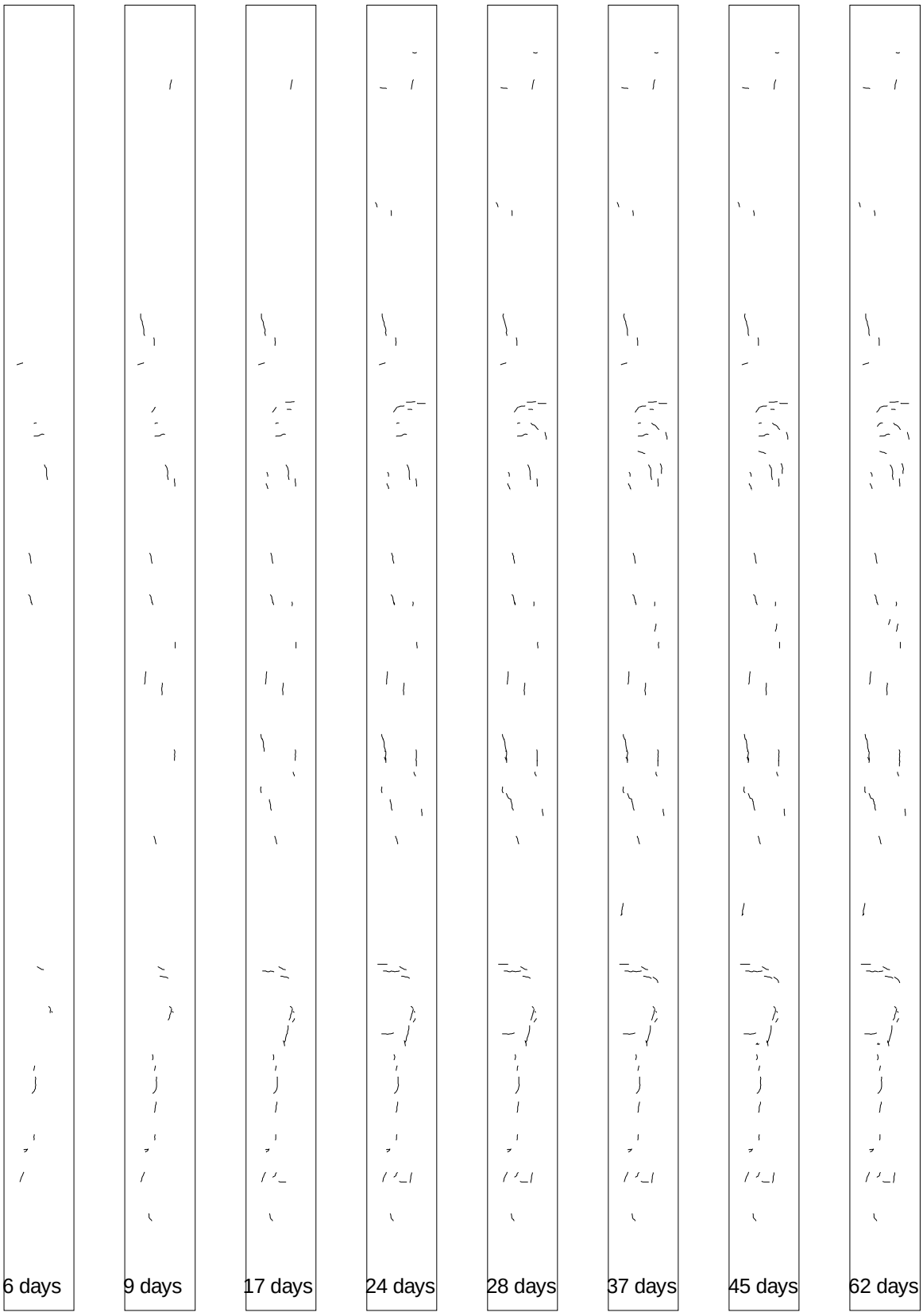

FIGURE N.1: Beam I3 - crack pattern during the long term tests

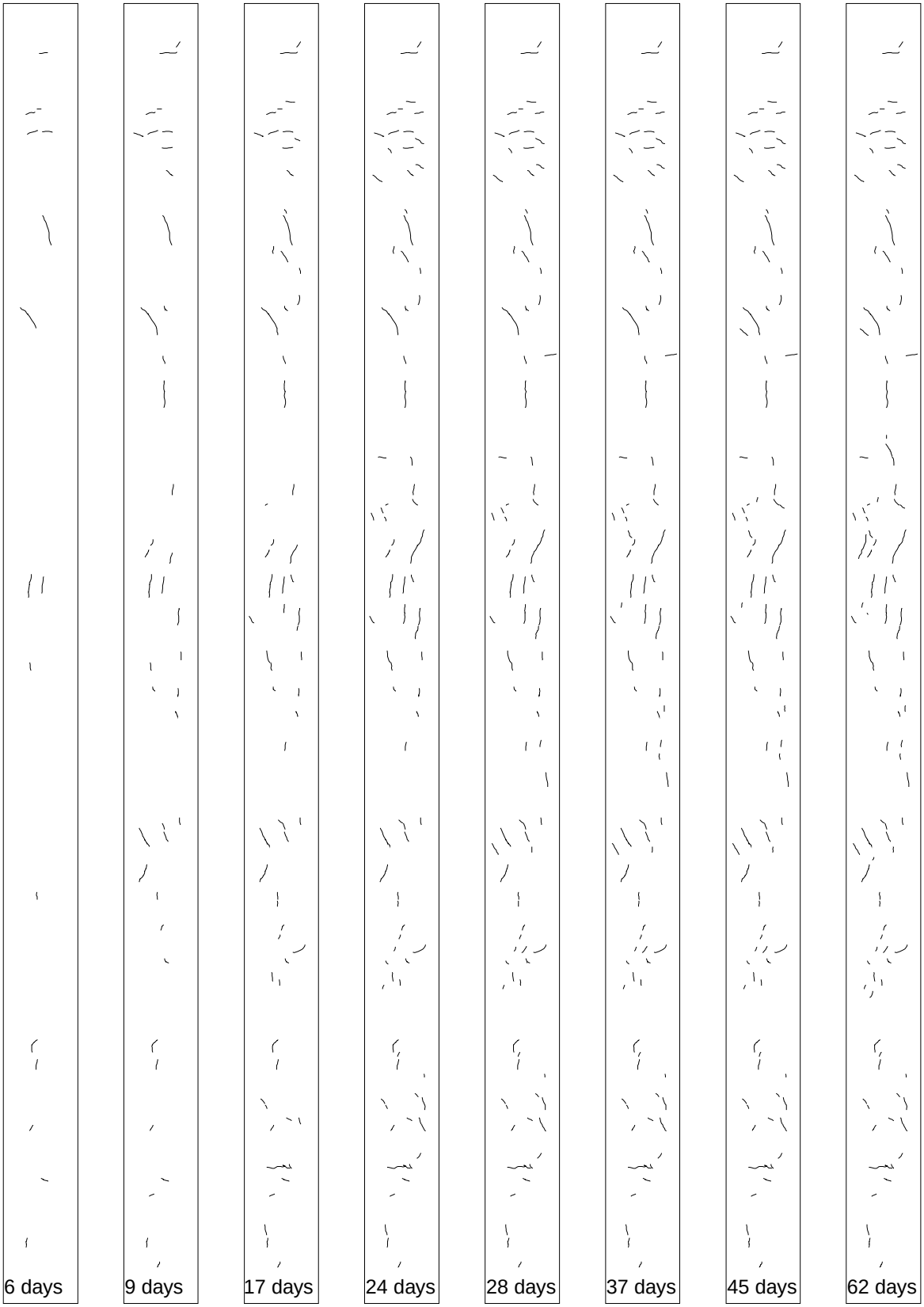

FIGURE N.2: Beam I3L - crack pattern during the long term tests

FIGURE N.3: Beam H3 - crack pattern during the long term tests

Appendix O: Measurements of the debonding (IS, IN) during the long-term tests

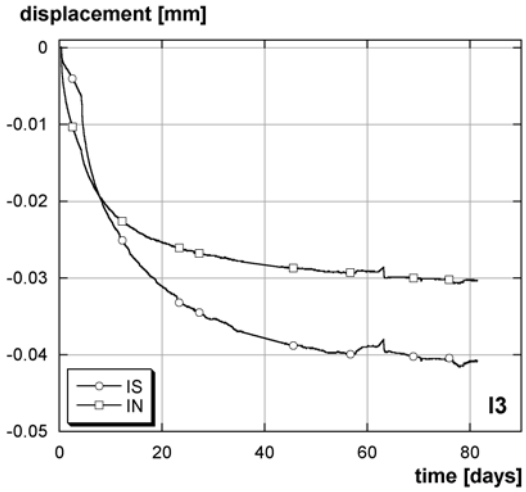

FIGURE O.1: I3 - debonding

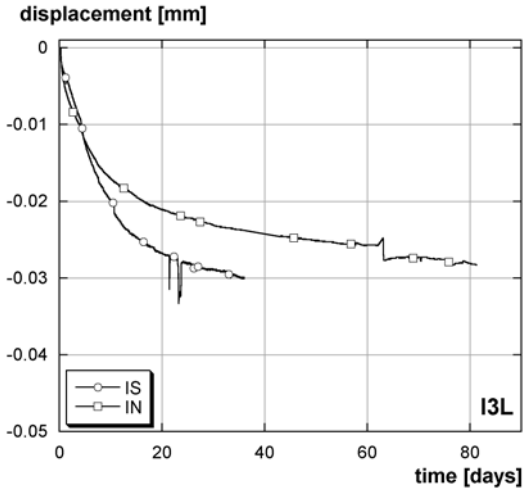

FIGURE O.2: I3L - debonding

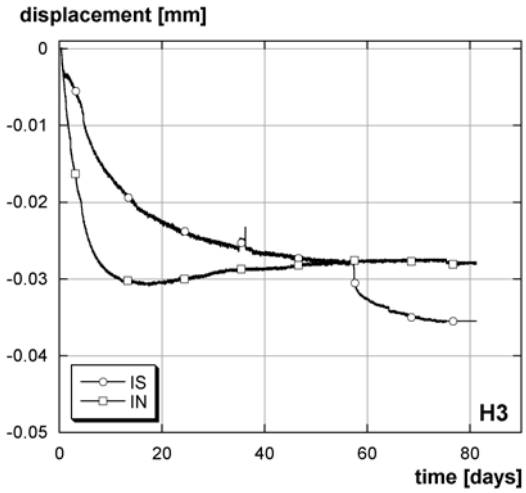

FIGURE O.3: H3 - debonding

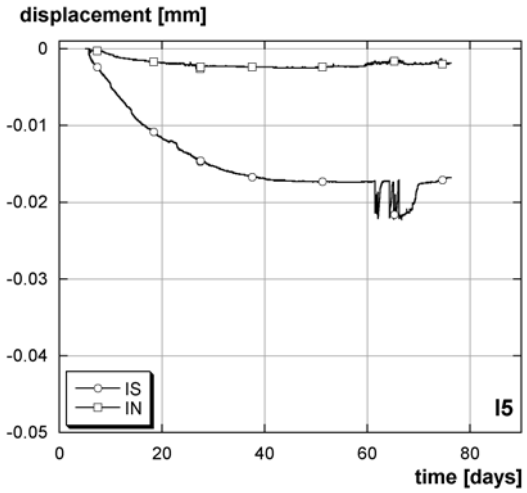

FIGURE O.4: I5 - debonding

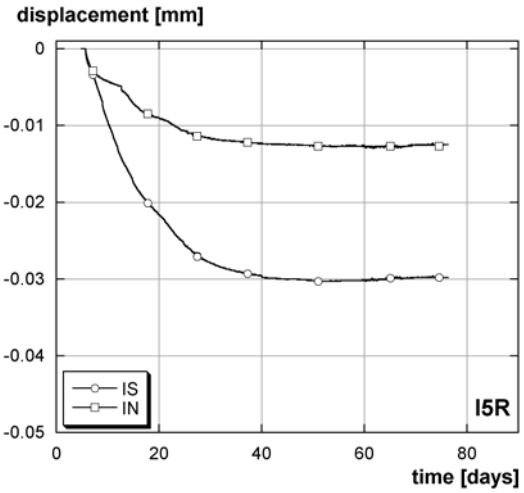

FIGURE O.5: I5R - debonding

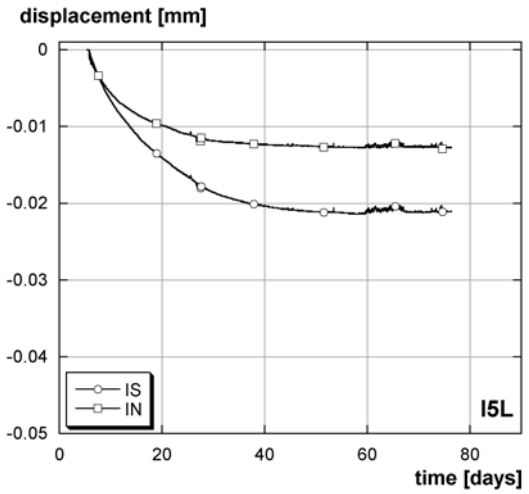

FIGURE O.6: I5L - debonding

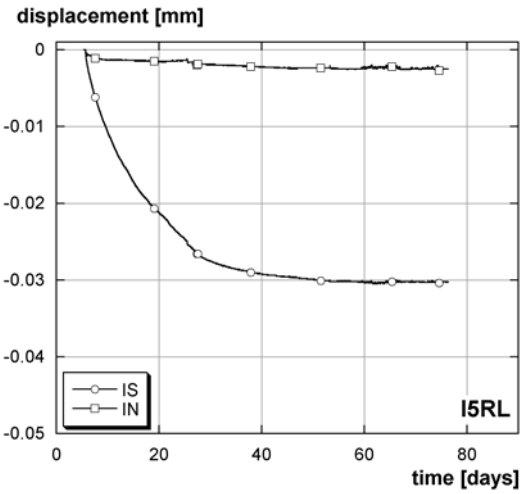

FIGURE O.7: I5RL - debonding

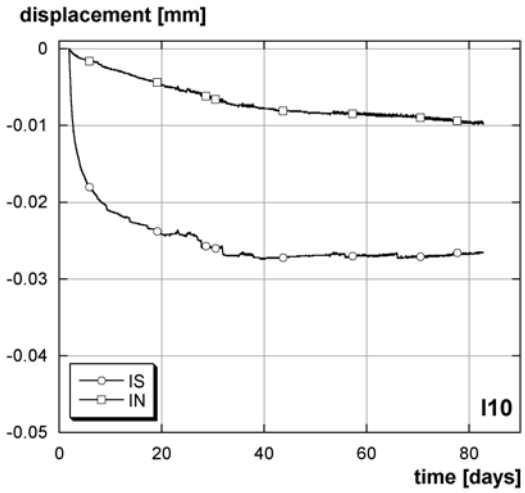

FIGURE O.8: I10 - debonding

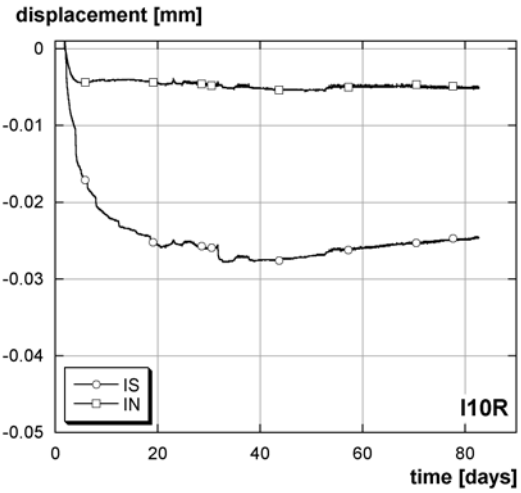

FIGURE O.9: I10R - debonding

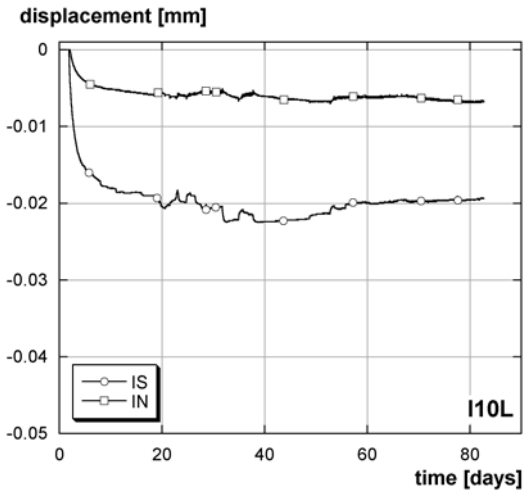

FIGURE O.10: I10L - debonding

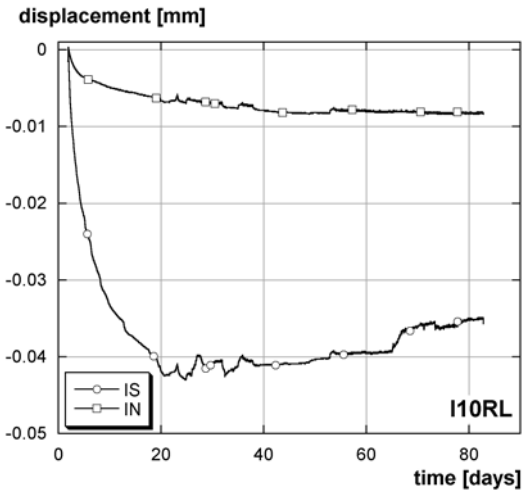

FIGURE O.11: I10RL - debonding

Appendix P: TORRENT tests on series 1 (h_U = 5 cm)

TABLE P.1. Results of the TORRENT tests (UHPFRC) - beam I5

Place	pi [mbar]	k_T [10^{-16} m^2]	l [mm]	Remarks
end of the beam	17	0.003	3.8	
	12	0.001	2.0	
	13	0.006	5.1	
above support	52	0.004	4.2	
	14	0.002	3.1	
	21	0.002	3.1	
mid-span	17	0.001	2.0	
	16	-	-	no values
	14	0.002	2.7	

TABLE P.2. Results of the TORRENT tests (UHPFRC) - beam I5L

Place	pi [mbar]	k_T [10^{-16} m^2]	l [mm]	Remarks
above support	14	0.007	5.6	
	16	0.008	6.2	
	15	0.002	3.1	
mid-span	14	0.004	4.4	
	14	0.003	4.0	
	18	0.043	14.0	cracks

TABLE P.3. Results of the TORRENT tests (UHPFRC) - beam I5R

Place	pi [mbar]	k_T [10^{-16} m^2]	l [mm]	Remarks
end of the beam	17	-	-	no values
	11	0.006	5.1	at the specially cured surface
	22	0.005	4.7	at the specially cured surface
above support	15	0.002	2.7	
	14	0.001	2.2	
	13	0.002	3.3	
mid-span	13	0.003	3.8	
	13	0.001	2.4	
	12	0.001	1.5	

TABLE P.4. Results of the TORRENT tests (UHPFRC) - beam I5RL

Place	pi [mbar]	k_T [10^{-16} m^2]	l [mm]	Remarks
above support	12	0.002	3.1	
	14	0.005	4.9	
	13	0.004	4.2	
mid-span	18	0.002	3.3	
	13	0.005	4.7	
	14	0.007	5.6	

TABLE P.5. Results of the TORRENT tests (UHPFRC) - beam H5

Place	pi [mbar]	k_T [10^{-16} m^2]	l [mm]	Remarks
end of the beam	55	0.001	2.2	no cracks
above support	19	0.005	5.0	one crack
-	22	0.01	4.8	one crack
-	49	2.548	61.2	one crack, test stopped after 250 sec
-	15	0.014	8.1	small cracks
end of the beam	13	0.004	4.5	no cracks

TABLE P.6. Results of the TORRENT tests (UHPFRC) - beam H5R

Place	pi [mbar]	k_T [10^{-16} m^2]	l [mm]	Remarks
end of the beam	17	0.012	7.4	no cracks, but pores
	14	0.006	5.5	several small cracks
	17	0.001	2	
mid-span	19	0.006	5.2	some small cracks
	29	0.209	31.2	cracks
above support	27	0.129	24.4	some cracks, pores
	14	0.01	6.7	some small cracks

TABLE P.7. Results of the TORRENT tests (concrete)

Beam	pi [mbar]	k_T [10^{-16} m^2]	l [mm]	Remarks
I5R	37	1.237	55.5	test stopped after 390 sec.
H5R	24	0.137	25.3	
	29	0.280	36.2	
	33	1.076	52.2	
	33	1.492	56.3	
	25	0.167	27.9	

Appendix Q: Force-deflection diagrams of the fracture tests

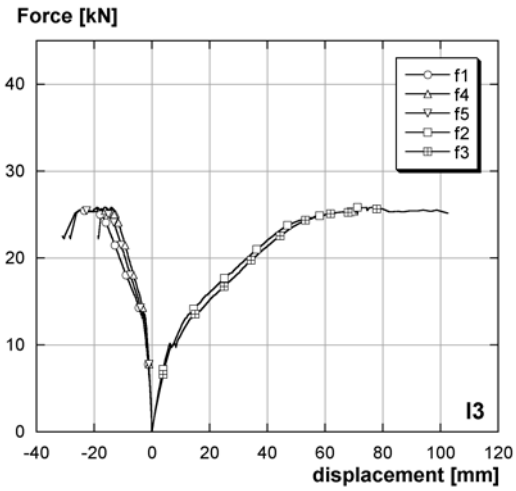

FIGURE Q.1: Force - deflections: I3

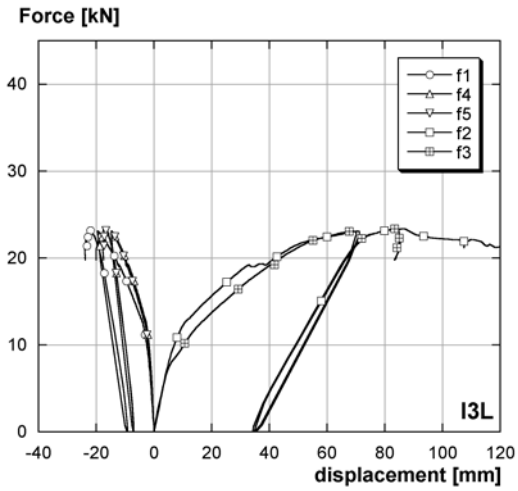

FIGURE Q.2: Force - deflections: I3L

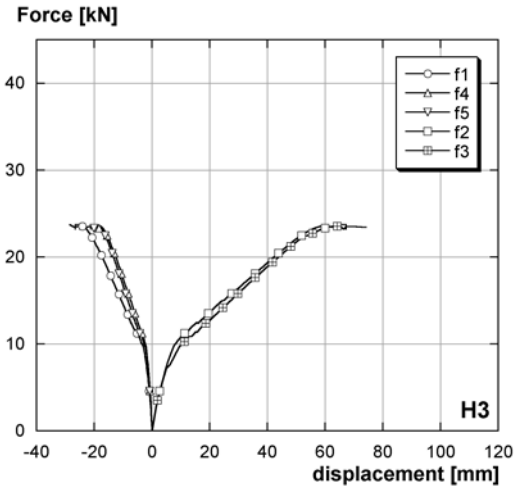

FIGURE Q.3: Force - deflections: H3

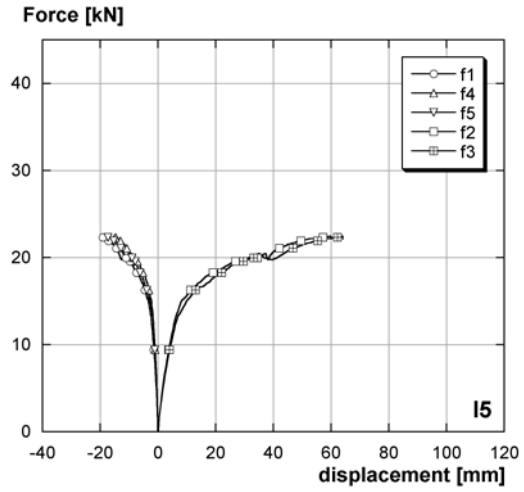

FIGURE Q.4: Force - deflections: I5

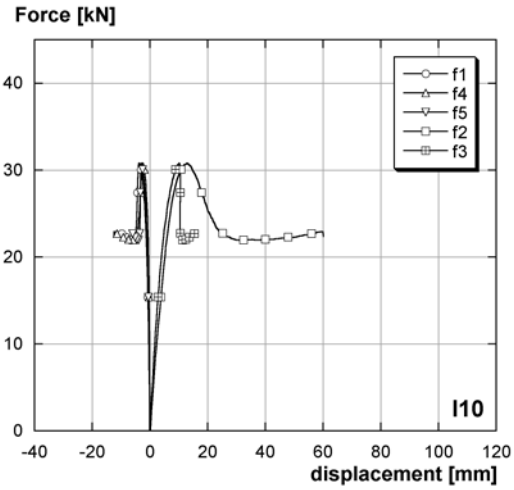

FIGURE Q.5: Force - deflections: I10

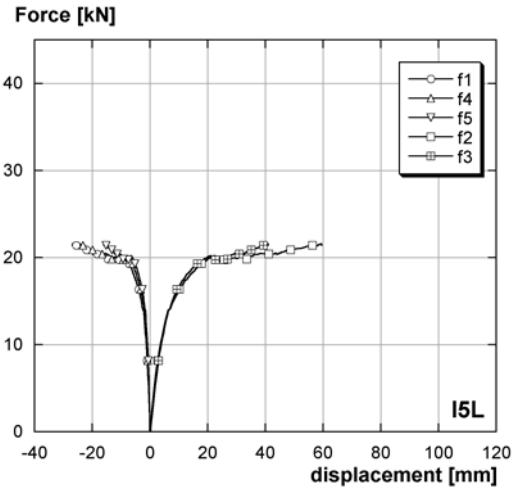

FIGURE Q.6: Force - deflections: I5L

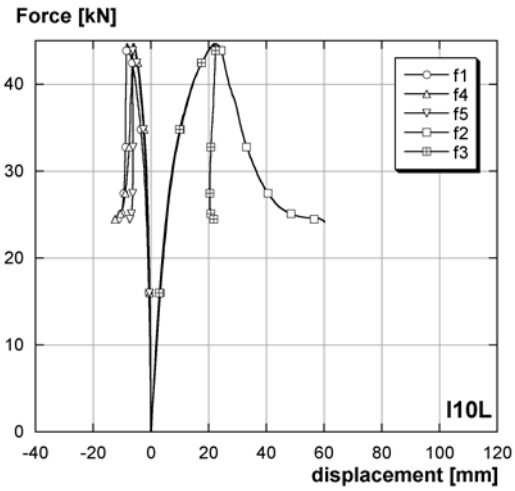

FIGURE Q.7: Force - deflections: I10L

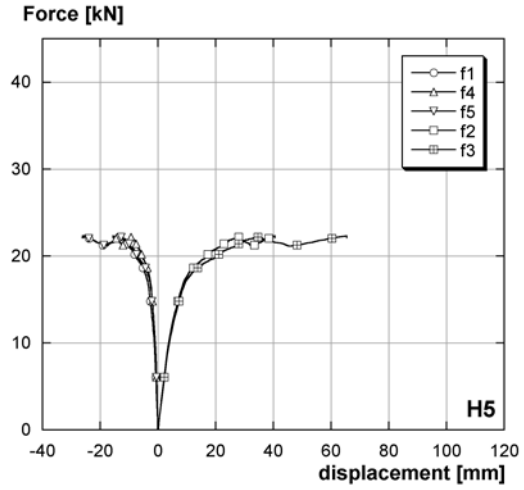

FIGURE Q.8: Force - deflections: H5

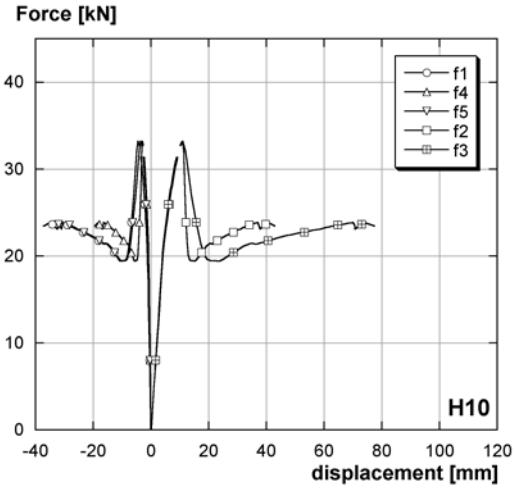

FIGURE Q.9: Force - deflections: H10

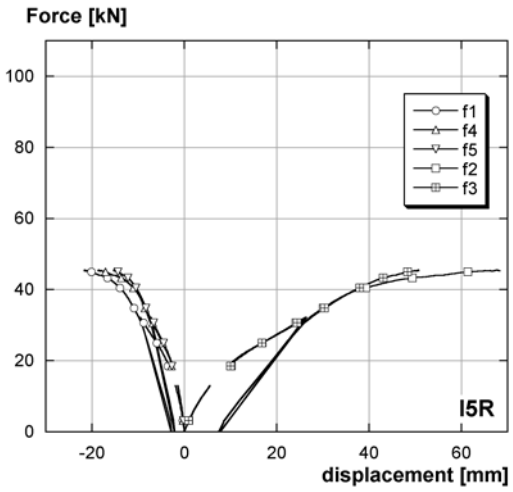

FIGURE Q.10: Force - deflections: I5R

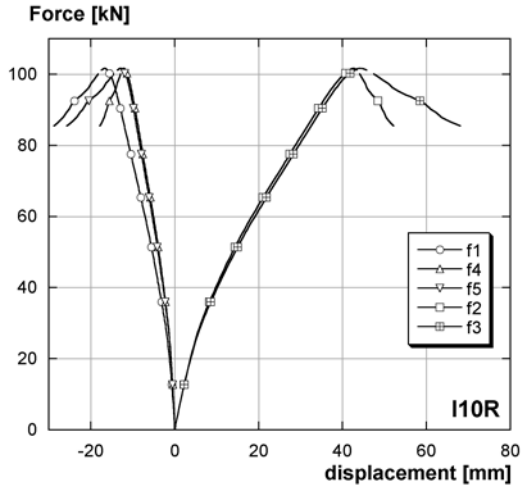

FIGURE Q.11: Force - deflections: I10R

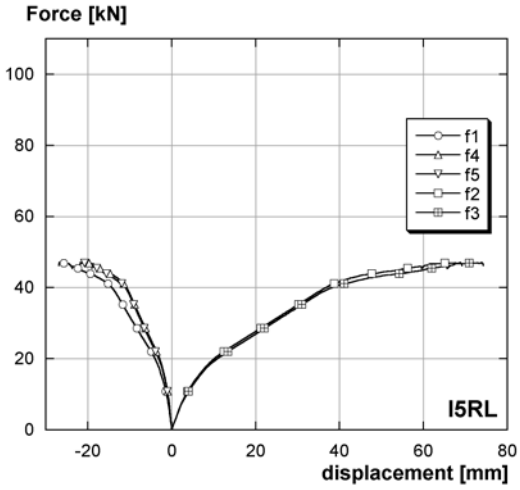

FIGURE Q.12: Force - deflections: I5RL

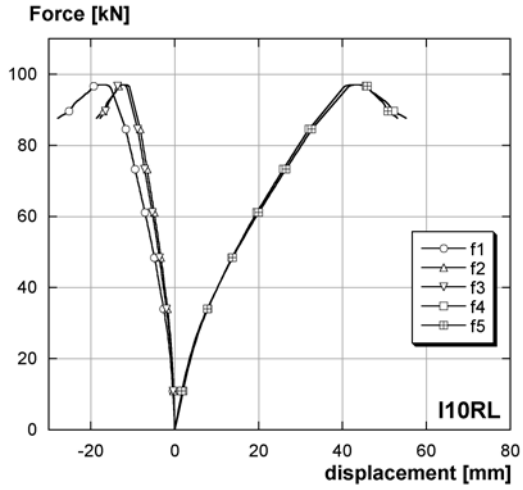

FIGURE Q.13: Force - deflections: I10RL

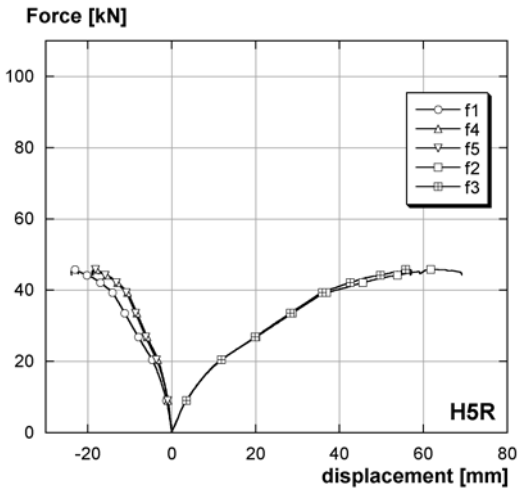

FIGURE Q.14: Force - deflections: H5R

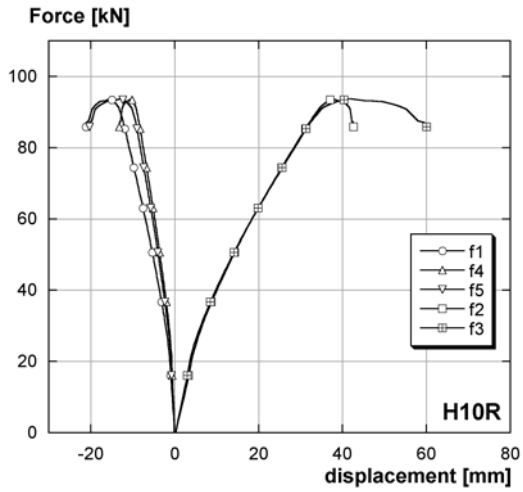

FIGURE Q.15: Force - deflections: H10R

Appendix R: Force-ODS diagrams of the fracture tests

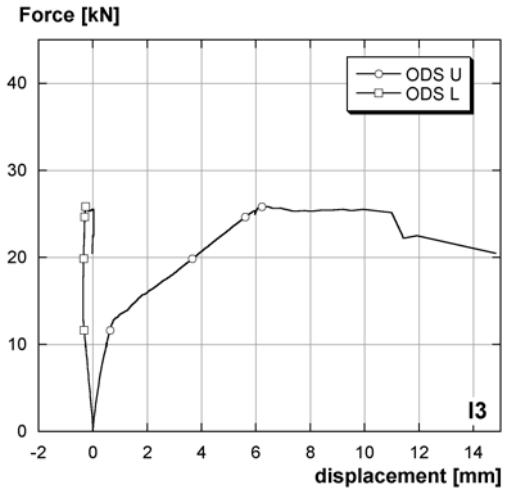

FIGURE R.1: Force - ODS: I3

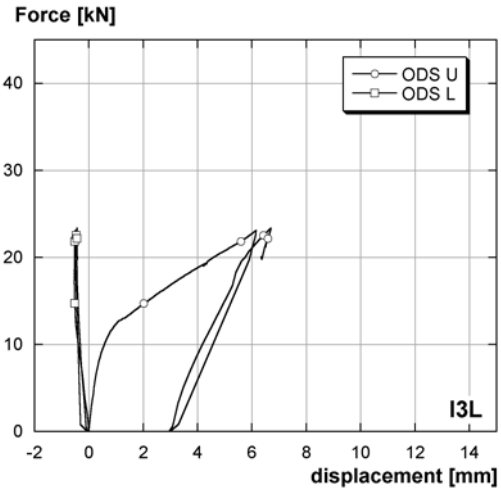

FIGURE R.2: Force - ODS: I3L

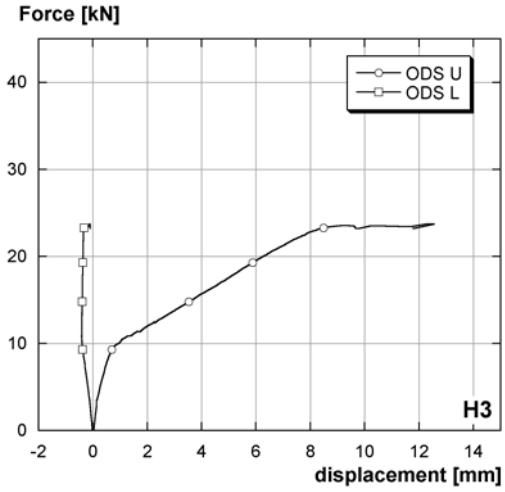

FIGURE R.3: Force - ODS: H3

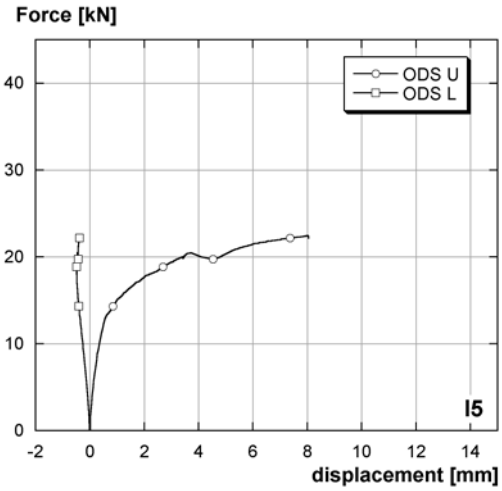

FIGURE R.4: Force - ODS: I5

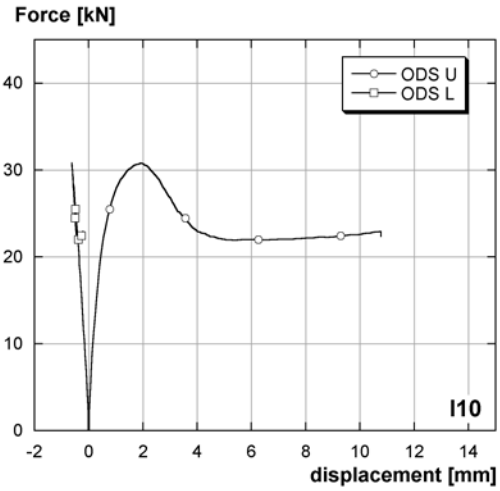

FIGURE R.5: Force - ODS: I10

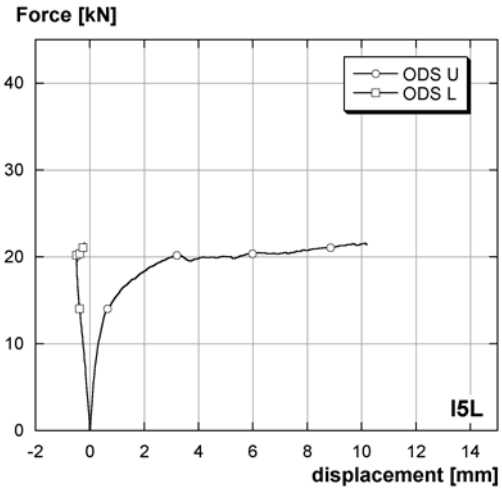

FIGURE R.6: Force - ODS: I5L

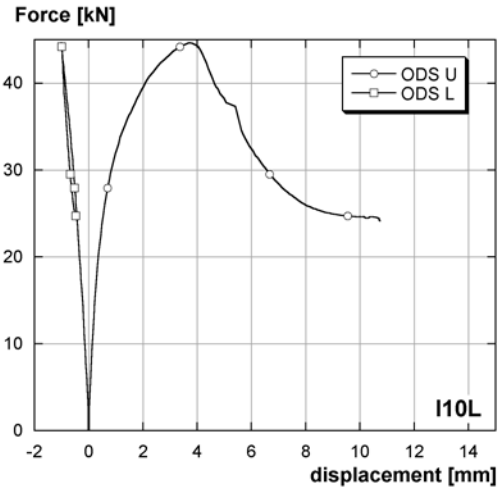

FIGURE R.7: Force - ODS: I10L

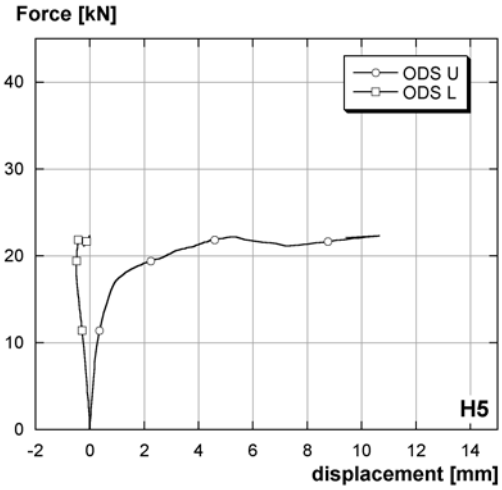

FIGURE R.8: Force - ODS: H5

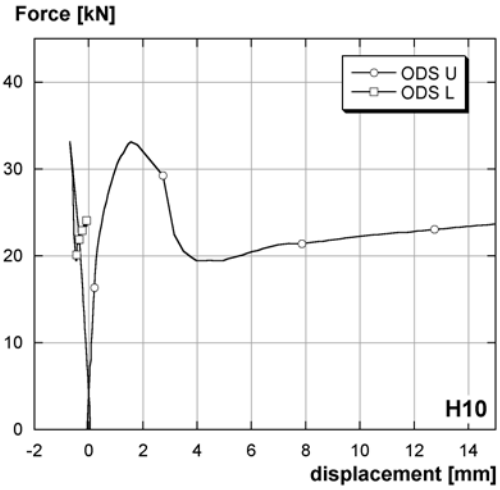

FIGURE R.9: Force - ODS: H10

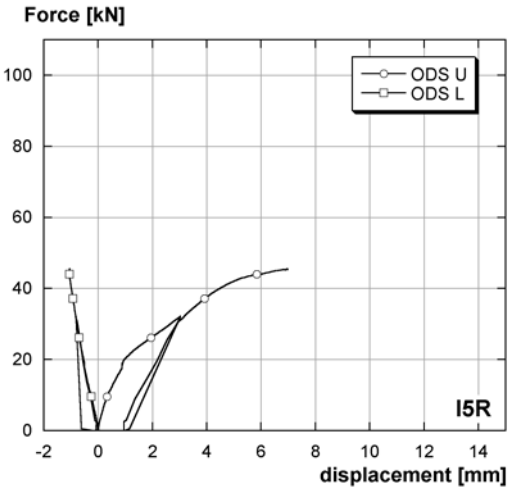

FIGURE R.10: Force - ODS: I5R

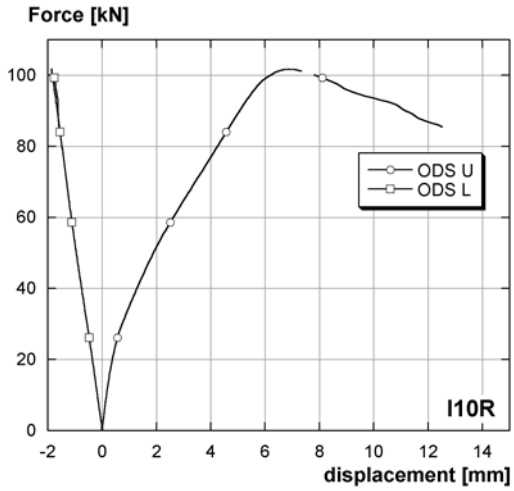

FIGURE R.11: Force - ODS: I10R

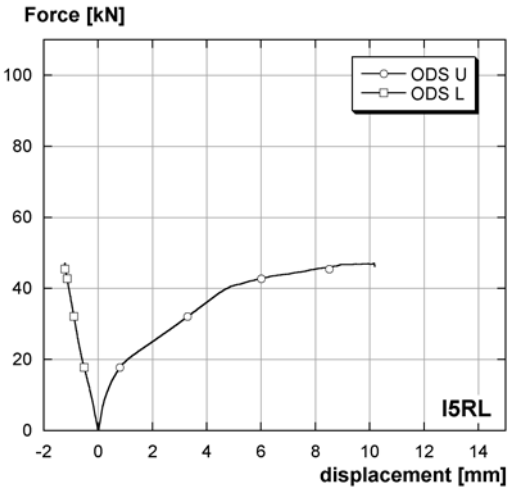

FIGURE R.12: Force - ODS: I5RL

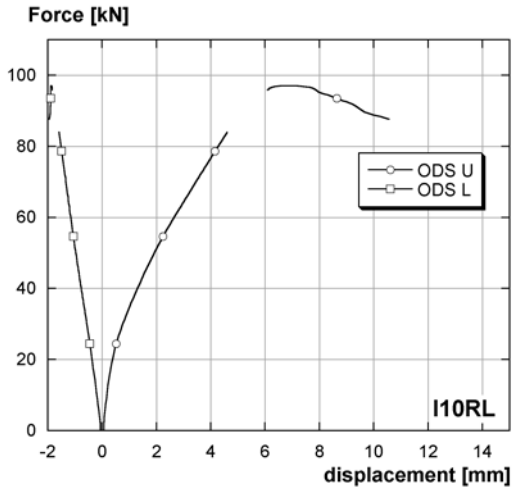

FIGURE R.13: Force - ODS: I10RL

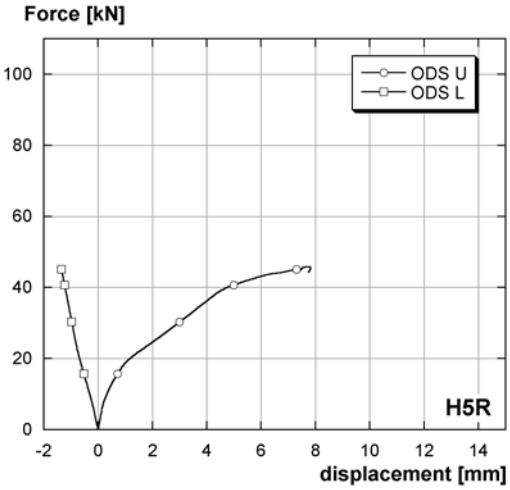

FIGURE R.14: Force - ODS: H5R

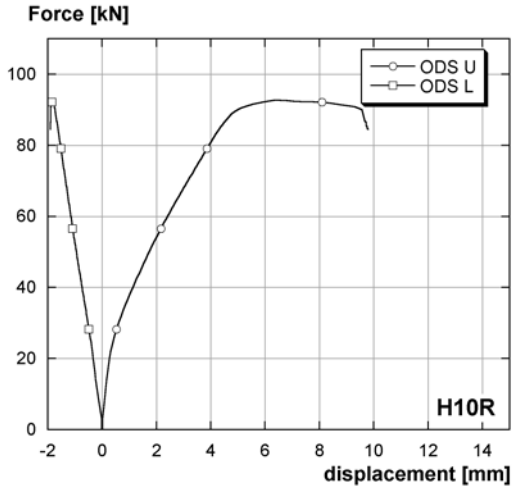

FIGURE R.15: Force - ODS: H10R

Appendix S: Force-Ω-gages diagrams of the fracture tests

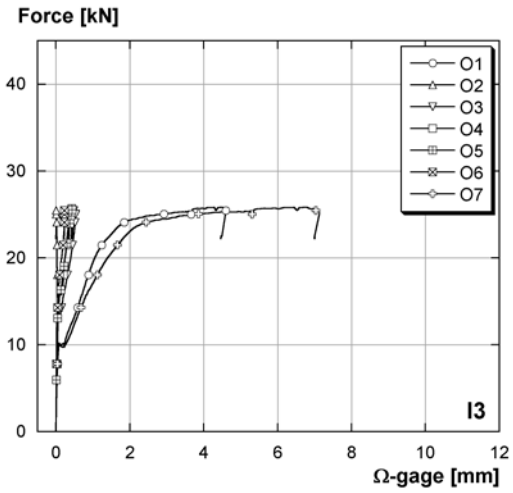

FIGURE S.1: Force-Ω-gages: I3

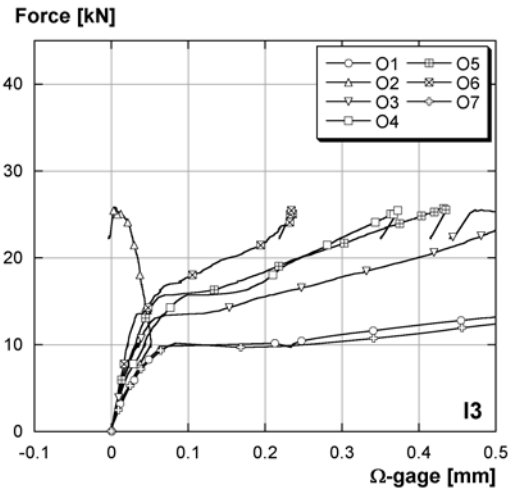

FIGURE S.2: Force-Ω-gages: I3 - detail

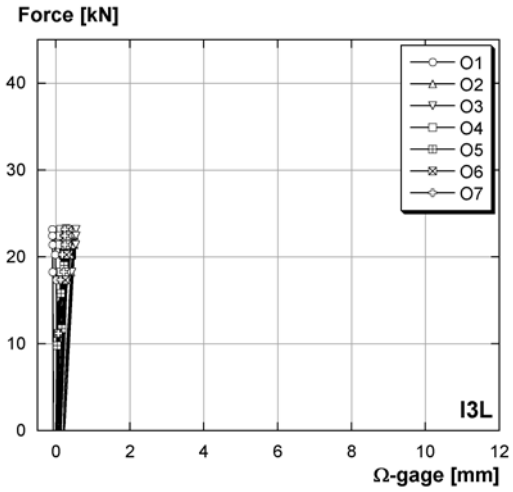

FIGURE S.3: Force-Ω-gages: I3L

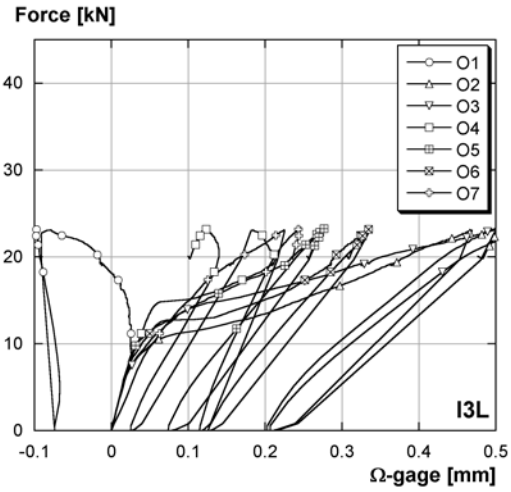

FIGURE S.4: Force-Ω-gages: I3L - detail

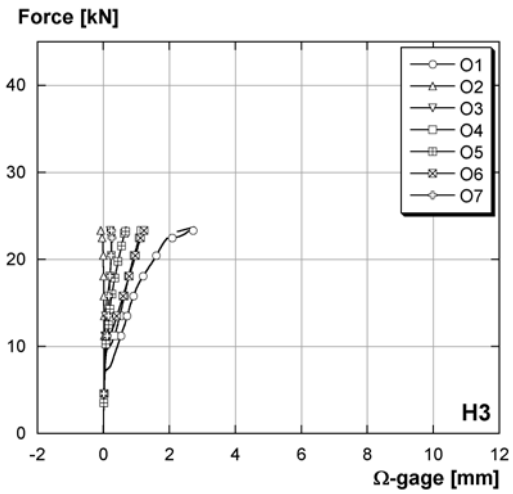

FIGURE S.5: Force-Ω-gages: H3

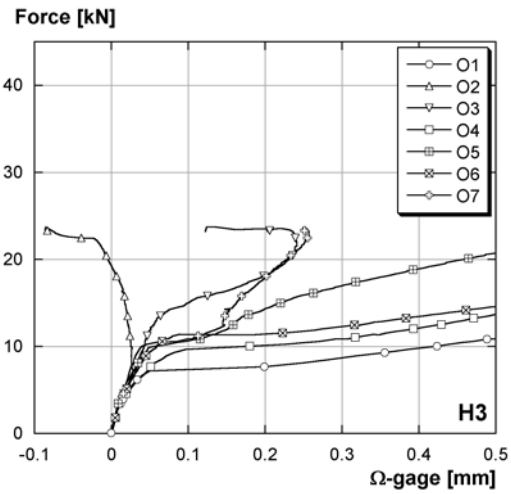

FIGURE S.6: Force-Ω-gages: H3 - detail

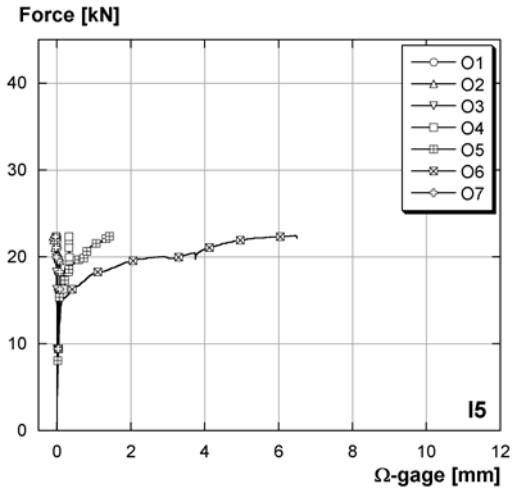

FIGURE S.7: Force-Ω-gages: I5

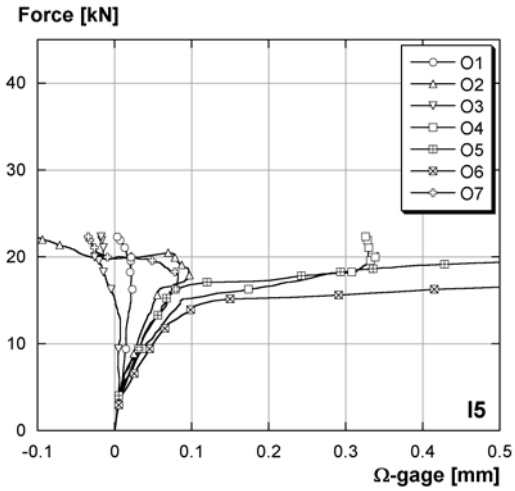

FIGURE S.8: Force-Ω-gages: I5 - detail

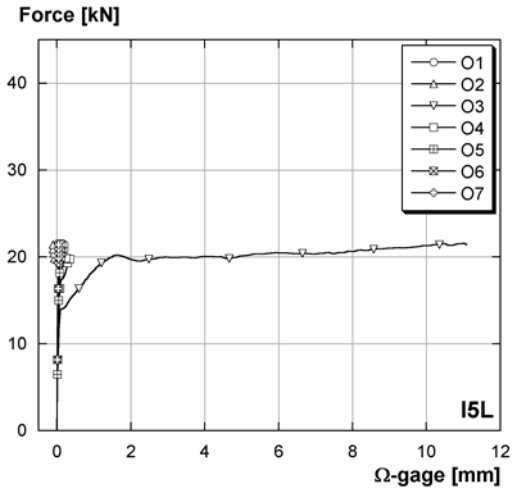

FIGURE S.9: Force-Ω-gages: I5L

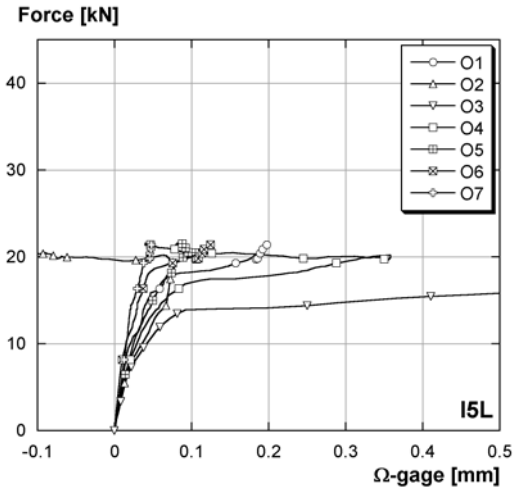

FIGURE S.10: Force-Ω-gages: I5L - detail

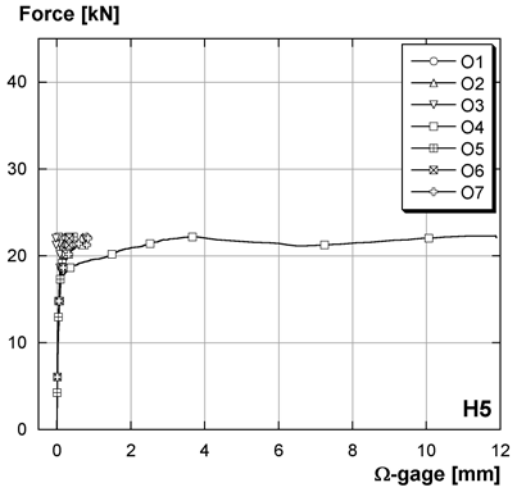

FIGURE S.11: Force-Ω-gages: H5

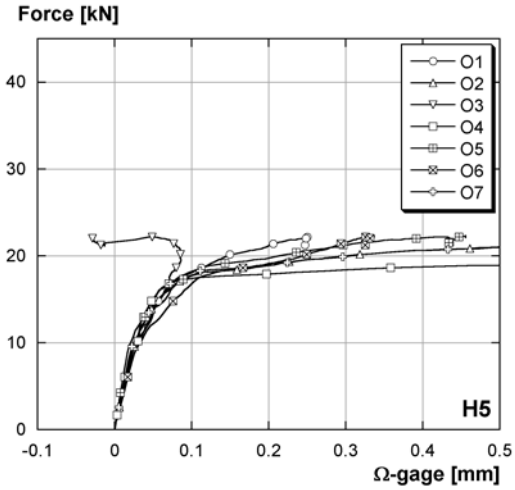

FIGURE S.12: Force-Ω-gages: H5 - detail

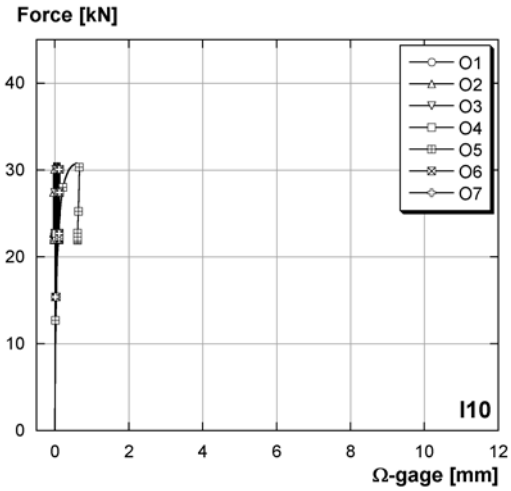

FIGURE S.13: Force-Ω-gages: I10

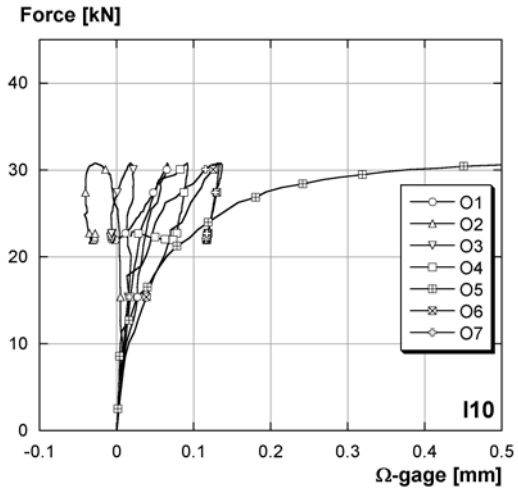

FIGURE S.14: Force-Ω-gages: I10 - detail

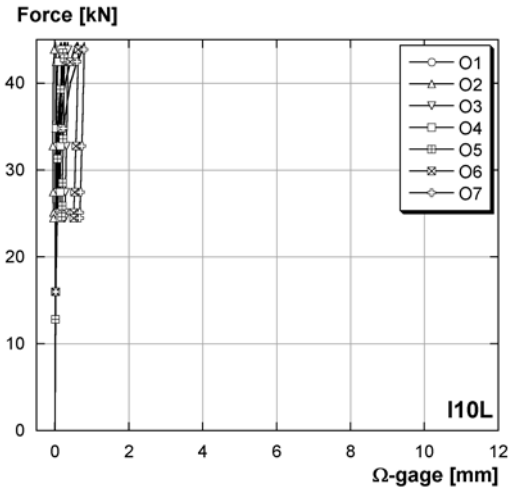

FIGURE S.15: Force-Ω-gages: I10L

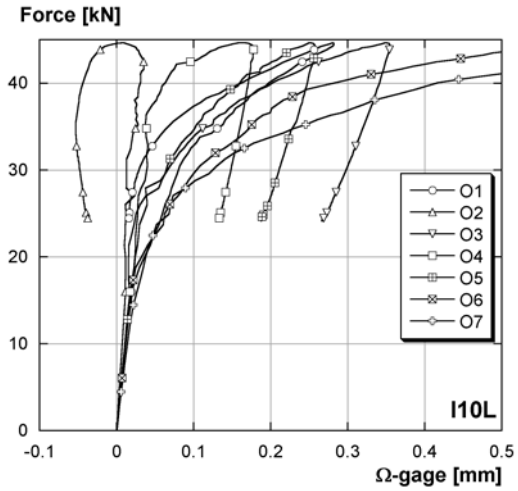

FIGURE S.16: Force-Ω-gages: I10L - detail

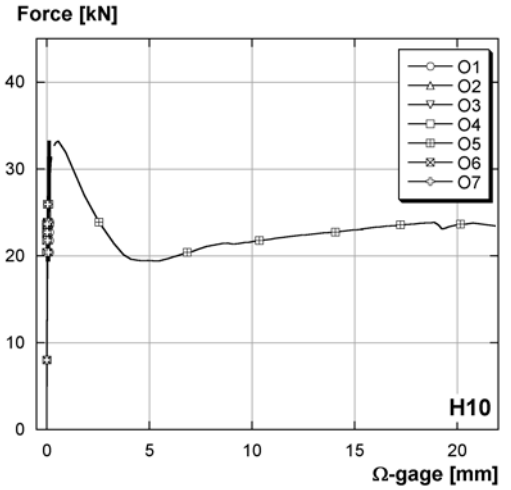

FIGURE S.17: Force-Ω-gages: H10

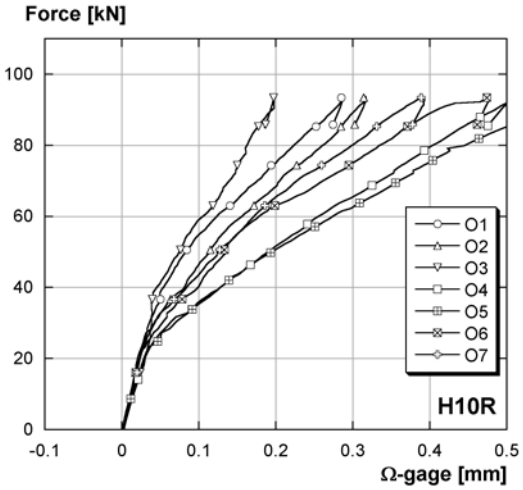

FIGURE S.18: Force-Ω-gages: H10 - detail

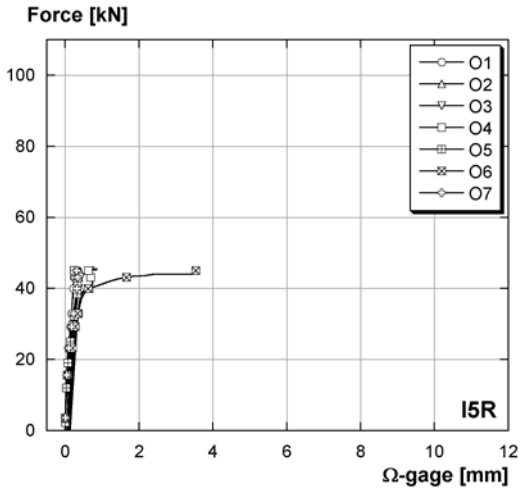

FIGURE S.19: Force-Ω-gages: I5R

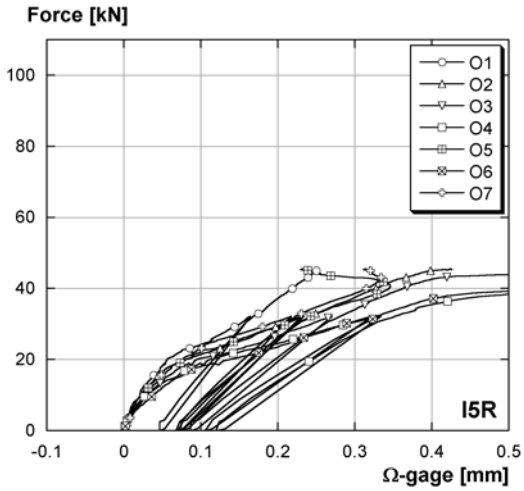

FIGURE S.20: Force-Ω-gages: I5R - detail

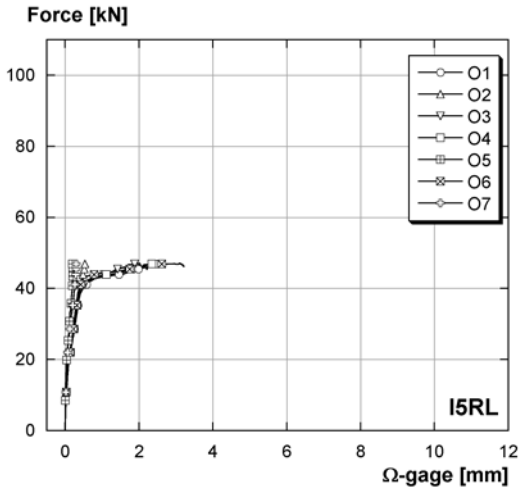

FIGURE S.21: Force-Ω-gages: I5RL

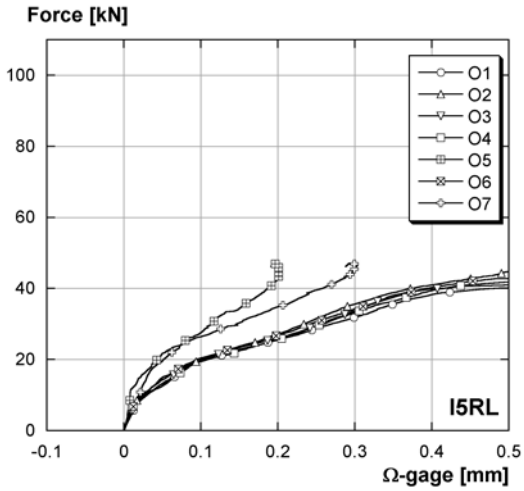

FIGURE S.22: Force-Ω-gages: I5RL - detail

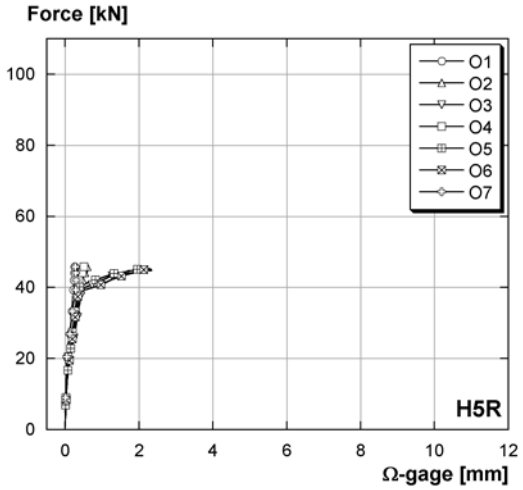

FIGURE S.23: Force-Ω-gages: H5R

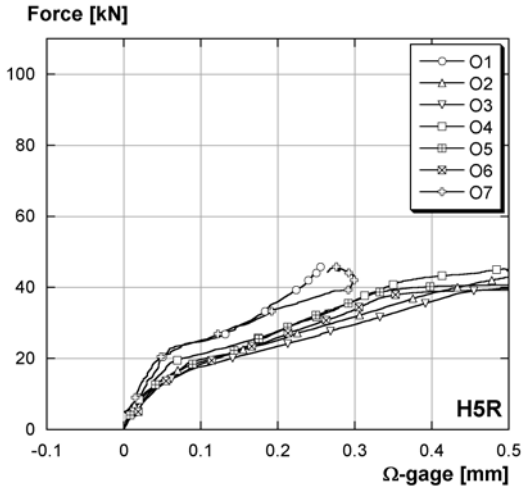

FIGURE S.24: Force-Ω-gages: H5R - detail

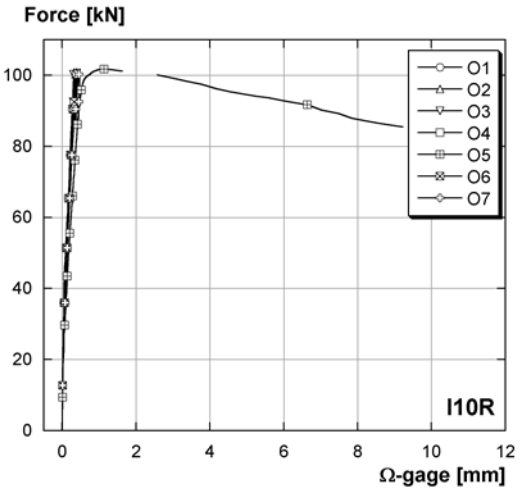

FIGURE S.25: Force-Ω-gages: I10R

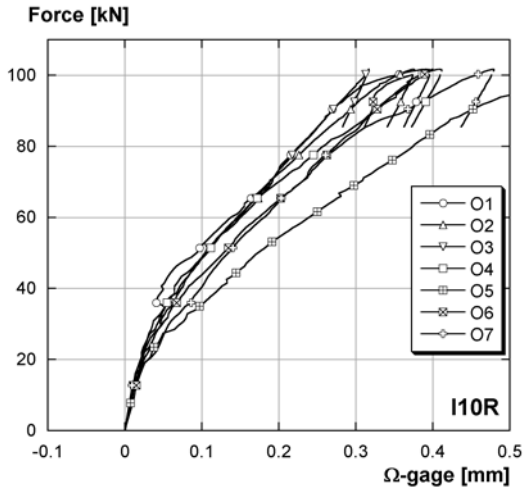

FIGURE S.26: Force-Ω-gages: I10R - detail

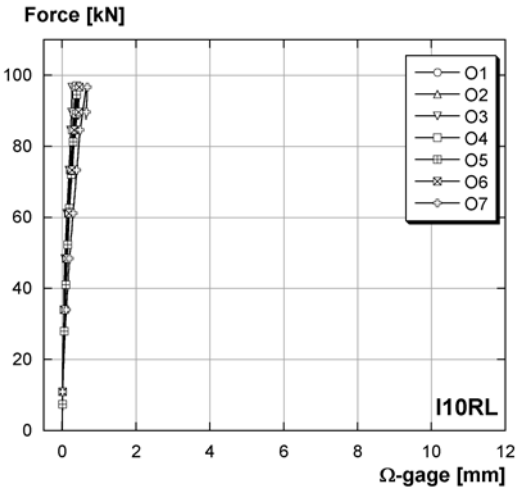

FIGURE S.27: Force-Ω-gages: I10RL

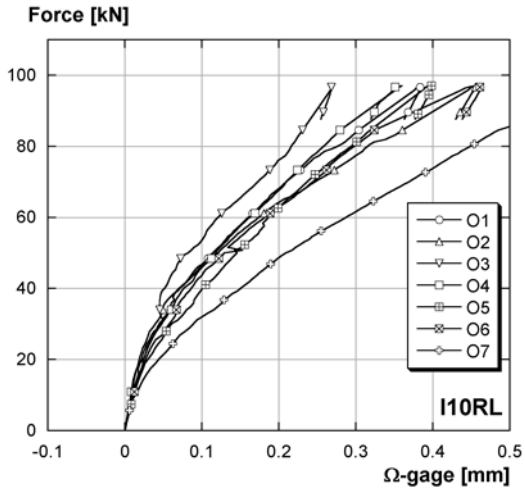

FIGURE S.28: Force-Ω-gages: I10RL - detail

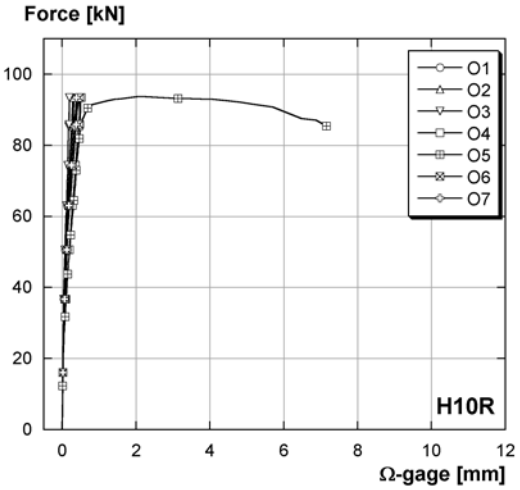

FIGURE S.29: Force-Ω-gages: H10R

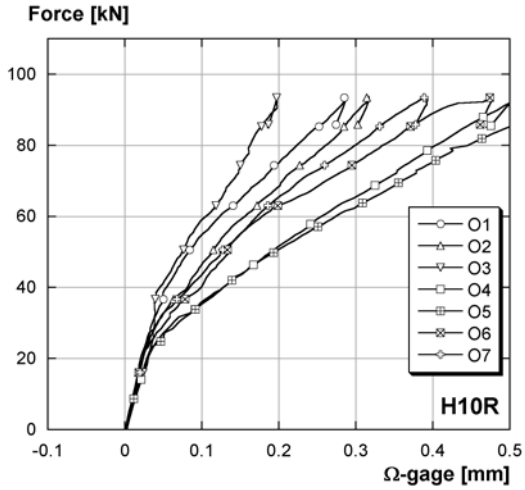

FIGURE S.30: Force-Ω-gages: H10R - detail

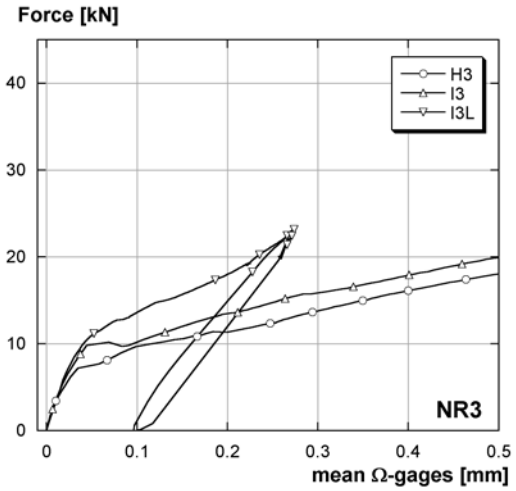

FIGURE S.31: Mean deformation of the Ω-gages (NR3)

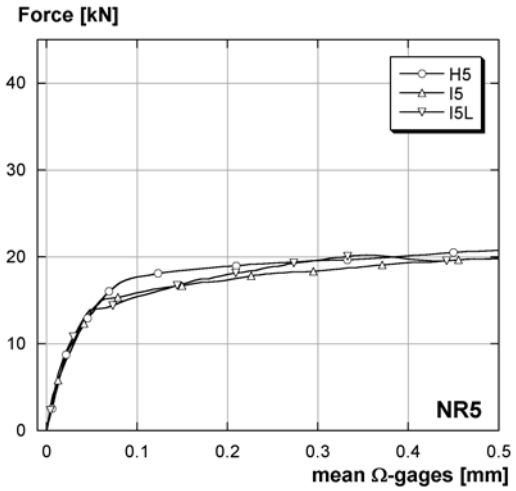

FIGURE S.32: Mean deformation of the Ω-gages (NR5)

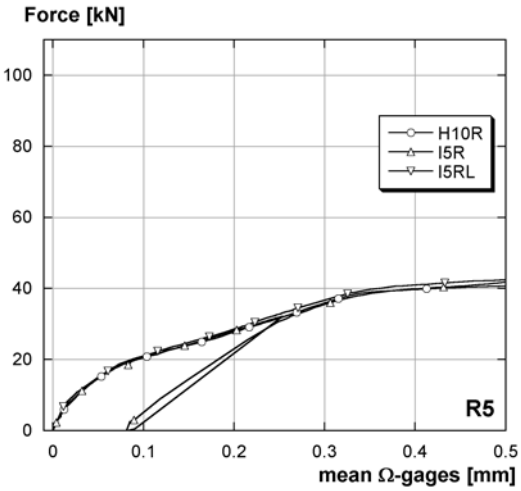

FIGURE S.33: Mean deformation of the Ω-gages (R5)

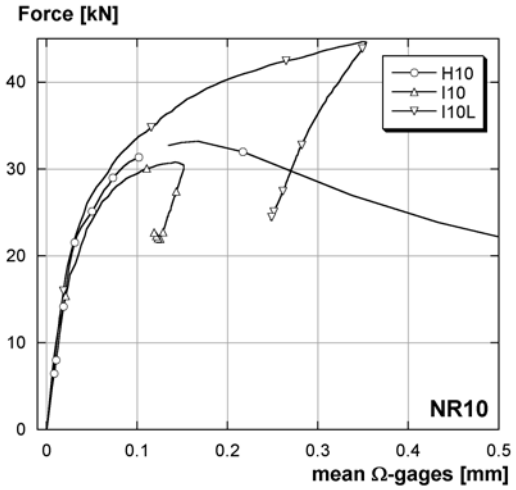

FIGURE S.34: Mean deformation of the Ω-gages (NR10)

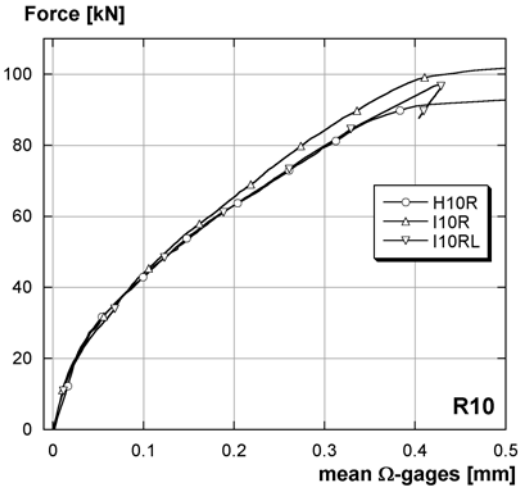

FIGURE S.35: Mean deformation of the Ω-gages (R10)

Appendix T: Crack pattern on the upper face of the fracture tests

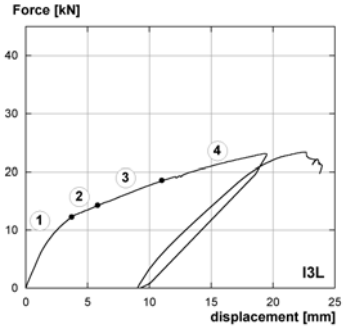

Periods of cracking:

	F [kN]	w [mm]
1	0.0 - 12.3	0.0 - 3.7
2	12.3 - 14.3	3.7 - 5.8
3	14.3 - 18.6	5.8 - 11.0
4	18.6 -	11.0 -

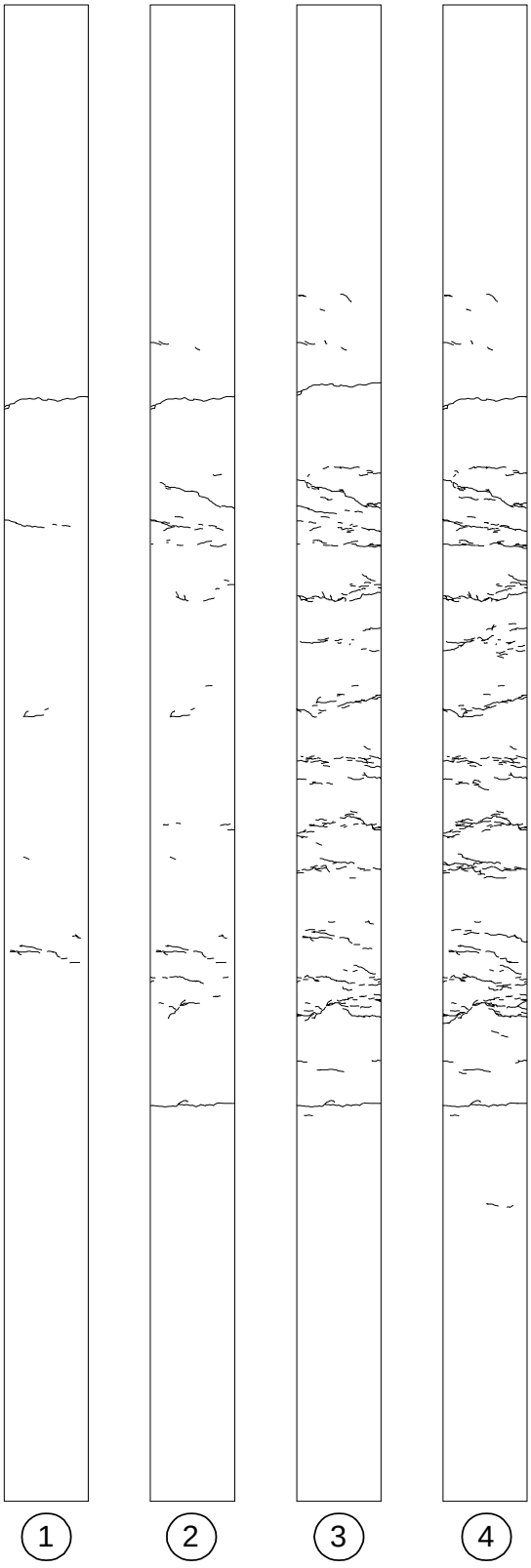

FIGURE T.1: Beam I3L(NR3) - crack pattern on the upper face

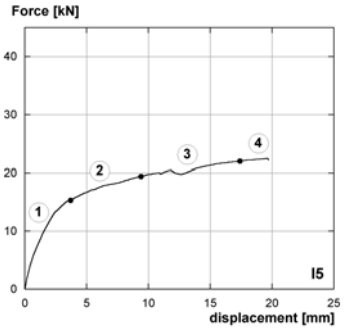

Periods of cracking:

	F [kN]	w [mm]
0	after long term tests	
1	0.0 - 15.3	0.0 - 3.7
2	15.3 - 19.4	3.7 - 9.4
3	19.4 - 22.0	9.4 - 17.4
4	22.0 -	17.4 -

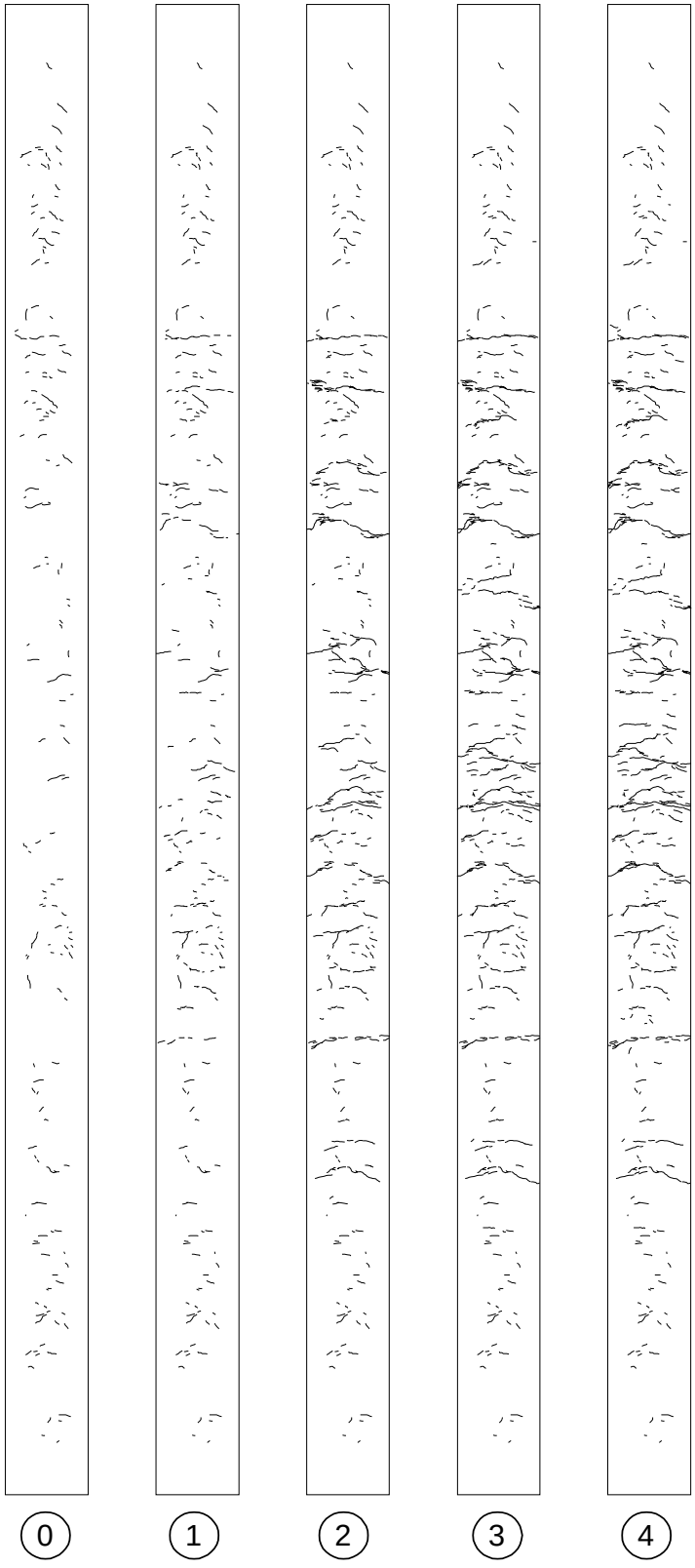

FIGURE T.2: Beam I5 (NR5) - crack pattern on the upper face

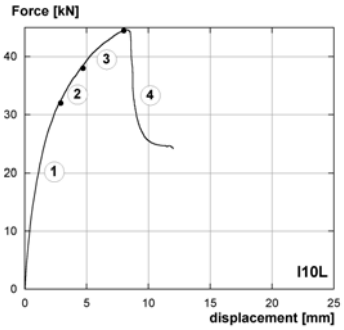

Periods of cracking:

	F [kN]	w [mm]
1	0.0 - 22.0	0.0 - 2.9
2	22.0 - 38.0	2.9 - 4.7
3	38.0 - 44.5	4.7 - 8.0
4	44.5 -	8.0 -

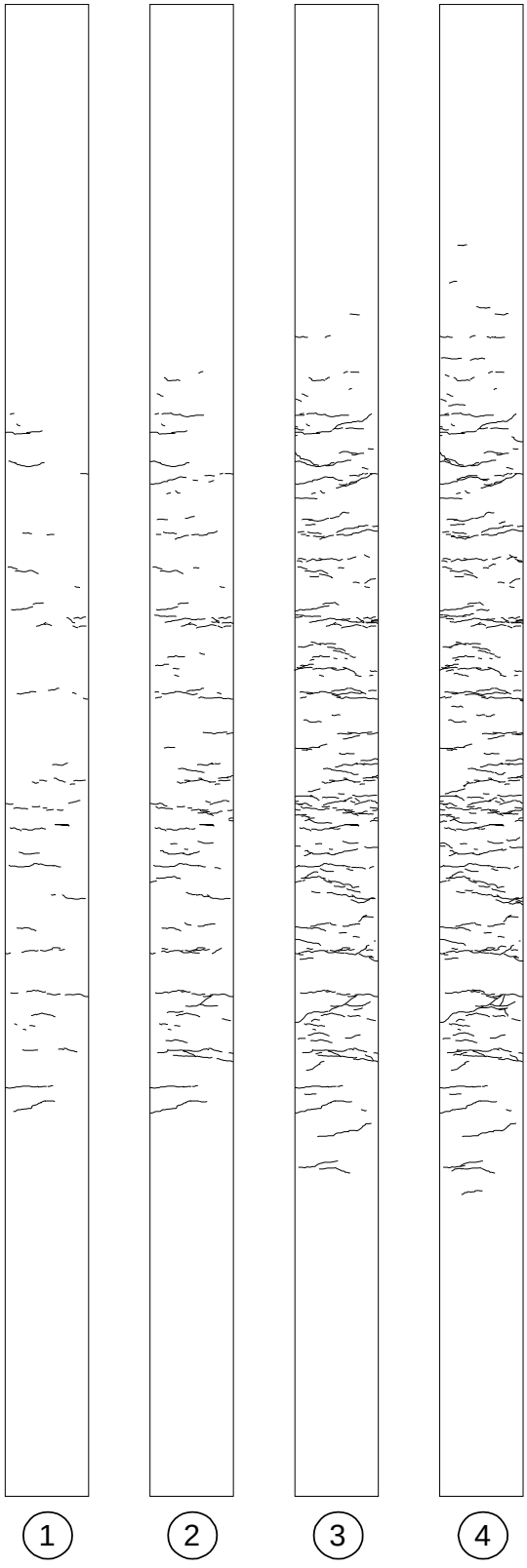

FIGURE T.3: Beam I10L (NR10) - crack pattern on the upper face

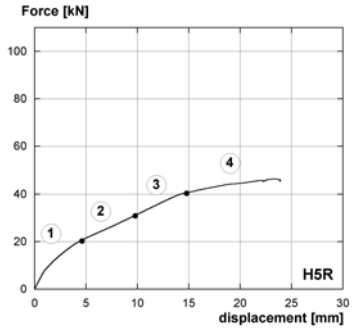

Periods of cracking:

	F [kN]	w [mm]
0	after long term tests	
1	0.0 - 20.3	0.0 - 4.6
2	20.3 - 30.9	4.6 - 9.8
3	30.9 - 40.4	9.8 - 14.8
4	40.4 -	14.8 -

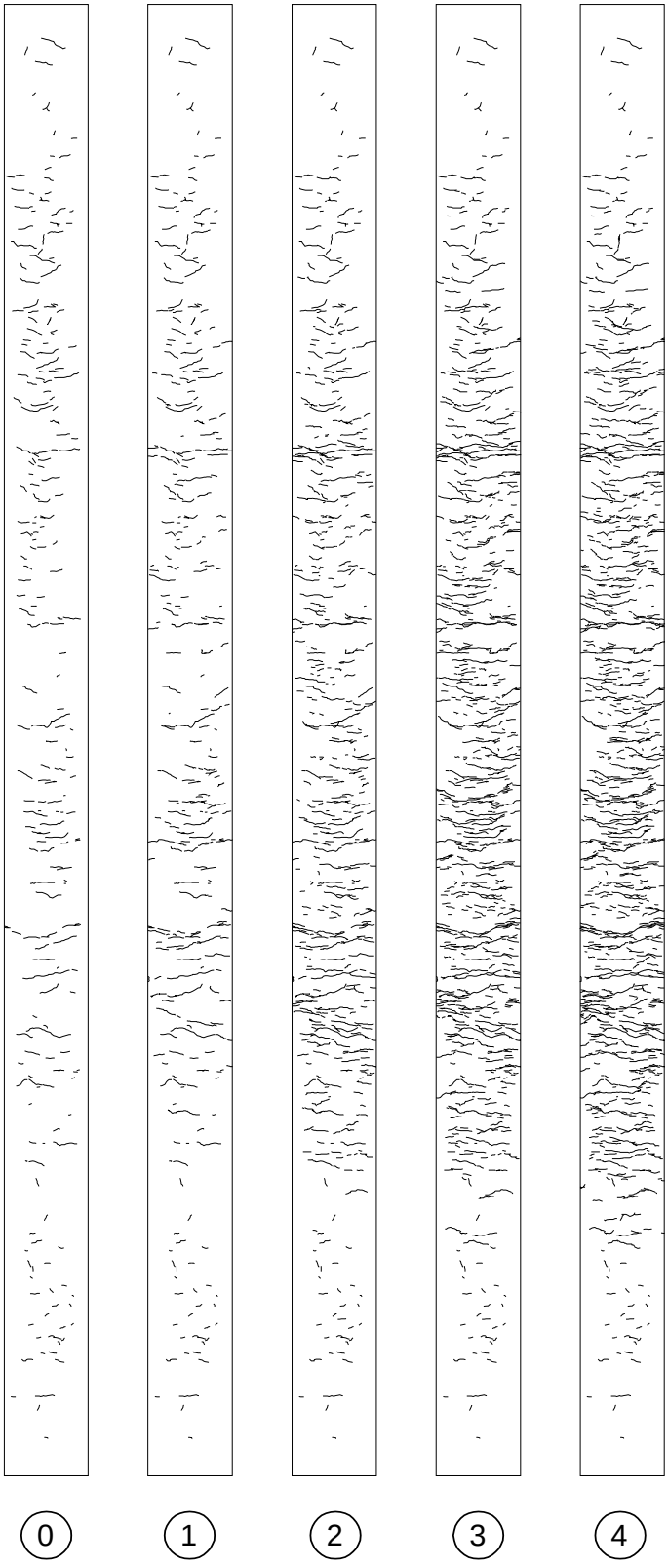

FIGURE T.4: Beam H5R (R5) - crack pattern on the upper face

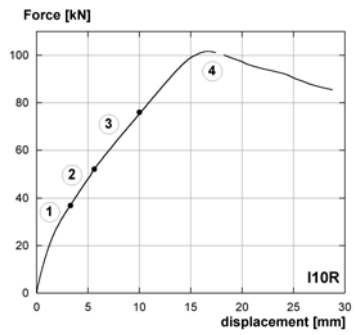

Periods of cracking:

	F [kN]	w [mm]
0	after long term tests	
1	0.0 - 27.0	0.0 - 3.3
2	27.0 - 52.0	3.3 - 5.6
3	52.0 - 76.0	5.6 - 10.0
4	76.0 -	10.0 -

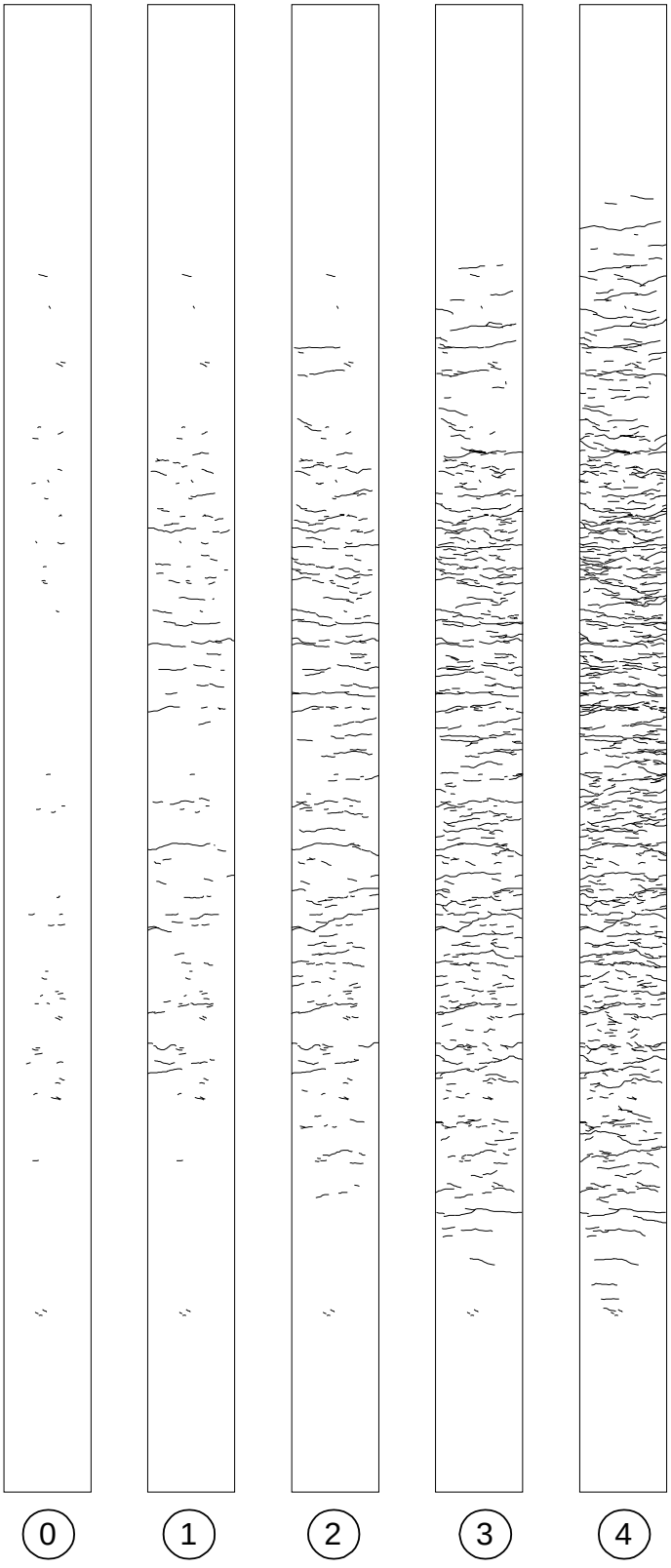

FIGURE T.5: Beam I10R (R10) - crack pattern on the upper face

Appendix U: UHPFRC recipes

TABLE 24.1: Composition of material CM0

Component	Vol. Percent of fibres [%]	ρ [kg/m^3]	Mass [kg/m^3]	Volume [l/m^3]
Powders			1846.2	
Cement		3.140	1051.1	334.7
Silica Fume		2.200	273.3	124.2
(Fine sand + quartz)		2.680	732.5	273.3
Added water		1.000	164.6	164.6
Steel wool		7.850		
Fibres 5 mm		7.850		
Fibres 10 mm	6	7.850	468	59.6
Fibres 20 mm		7.850		
Admixture		1.055	35.1	33.3
Dry extract 30%			10.5	
Liquid part 70%			24.6	
Total water		1.000		189.2
Air				10.2
Total	**6**		**2724.7**	**1000.0**

TABLE 24.2:

Component	Type
Cement	CEM I 52.5 N CE PM-ES-CP 2, Lafarge, Le Teil
Silica fume	SEPR (average diameter 0.5 μm)
	Specific surface 12 m^2/g, SiO2 > 93.5 %
Fine sand + quartz	SIFRACO (SiO_2>5%), D_{max} < 0.5 mm
Steel fibres	Steel wool (micro fibres) from Gervois
	Straight, l_f=5 mm, d_f=0.15 mm
	Straight l_f=10 mm, d_f=0.2 mm
	Straight l_f=20 mm, d_f=0.25 mm
Superplasticizer	Chrysofluid OPTIMA 175